Doctoral Dissertation

Liquid xenon detector with highly granular scintillation readout to search for $\mu^+ \to e^+\gamma$ with sensitivity of 5×10^{-14} in MEG II experiment

MEG II $\qquad\qquad\qquad 5 \times 10^{-14} \qquad \mu^+ \to e^+\gamma$

10

Department of Physics, Graduate School of Science,
The University of Tokyo

Shinji Ogawa

Abstract

A charged lepton flavor violating decay of a muon, $\mu \rightarrow e\gamma$, is an interesting probe in the search of physics beyond the Standard Model. Current upper limit on the branching ratio of this decay is 4.2×10^{-13} (90% confidence level) given by the MEG experiment. An upgrade experiment of MEG called MEG II is planned aiming to improve the sensitivity by one order of magnitude.

For this purpose, a new liquid xenon detector has been developed to measure γ-rays with a good resolution. It utilises new large area VUV-sensitive Multi-Pixel Photon Counters (MPPC). A high granularity and a good uniformity of the scintillation readout realized by the MPPCs enable us to achieve a good position and energy resolution especially for the shallow events near the γ-ray entrance face. Performance of the detector was measured in a series of pilot runs. Better position and energy resolutions for the shallow events are demonstrated. An improvement on the timing resolution is also achieved by an optimized analysis.

On the other hand, the energy resolution for the deep events is found to be worse than expected, probably due to an unknown contribution also observed in the previous experiment. In addition, a degradation was found on the photon detection efficiency of the MPPCs for xenon scintillation light by a radiation damage, while it was neither reported nor expected.

The branching ratio sensitivity of MEG II with this detector is estimated based on the measured detector performances. Even though the worse energy resolution and the degradation of the photon detection efficiency deteriorate the branching ratio sensitivity of MEG II, the planned sensitivity of 5×10^{-14} is found to be still achievable by a realistic extension of the data-taking period. Therefore, it is concluded that the liquid xenon detector has a sufficient performance to search for a $\mu \rightarrow e\gamma$ decay with a sensitivity of 5×10^{-14}.

Contents

Preface

Background

The Standard Model is a fundamental model in the particle physics validated by many experiments up to the electroweak energy scale. Even with its success, it is thought to be a low energy approximation of more fundamental physics due to the existence of some unexplained phenomena and some theoretical difficulties. Therefore, physics beyond the Standard Model is actively searched.

A charged lepton flavor violating decay of a muon, $\mu \to e\gamma$, is an interesting probe in the search of the new physics. Experimentally reachable branching ratio of this decay is predicted by many extensions of the Standard Model, while this decay is prohibited in the Standard Model by the lepton flavor conservation law. Since this decay emits a coincident pair of monochromatic e and γ in the back-to-back direction, a signal event is efficiently distinguishable from many other background events by searching for an event satisfying this criteria. Current upper limit on the branching ratio of this decay is set to be 4.2×10^{-13} (90% confidence level) by the MEG experiment [1]. An upgrade of the MEG experiment called MEG II experiment is planned for a further improvement of the branching ratio sensitivity by one order of magnitude. Since the sensitivity in MEG was limited by the number of the accidental backgrounds, an improvement of the detector resolutions is a key to achieve the goal of MEG II.

Structure of this thesis

This thesis focuses on a liquid xenon γ-ray detector developed for this purpose. Chapter 1 gives a basic knowledge on the MEG II experiment needed to understand the discussion in following chapters. Chapter 2 explains the developed liquid xenon detector. A new photosensor developed for this detector is also introduced. A series of pilot runs was performed to evaluate the detector performance. A details is given in Chapter 3, and a detail of the simulation used for the analysis is given in Chapter 4. Chapter 5 and 6 summarize measured performances of the photosensors in the pilot runs. An unexpected radiation damage is observed on the new photosensors, and this is also shown in Chapter 6. Each measured detector resolution is shown in Chapter 7, 8, 9, and 10. In Chapter 11, the MEG II branching ratio sensitivity achievable with the liquid xenon detector is discussed based on the results shown in the previous chapters. A modification of the MEG II data-taking plan is proposed to deal with the radiation damage of the photosensor. This thesis is concluded in Chapter 12.

The author's contribution

The liquid xenon detector has been developed by the liquid xenon group of the MEG II collaboration. The author participated in the group at the middle of 2014, and contributed to the finalization of the development of the photosensor whose performance summarized in Section 2.1. The author joined the construction of the liquid xenon detector on site described in Section 2.2–2.7.

In the beam test for the demonstration of the detector performance, the author played a central role both in the data-taking and the analysis of the data. The calibration of the photosensors described in Chapter 5 and 6 was carried out by a few members of the group. The major contribution of the author is an observation of a radiation damage (Section 6.2.2). The demonstration of the detector performance (Chapter 7–10) and the discussion of the effect on the branching ratio sensitivity (Chapter 11) was mainly done by the author except for the position resolution measurement written in Chapter 7. In addition to the performance improvement expected at the design stage, the offline analysis is also improved by the author for even better detector performance as described in Section 8.3, 9.3.6, and 10.3.

Chapter 1

Introduction to MEG II experiment

1.1 Physics motivation: Charged lepton flavor violation

The Standard Model (SM) is a fundamental model in the particle physics. It is validated by many experiments up to the electroweak energy scale ($O(100)\,\mathrm{GeV}$). Even with its success, there are several unexplained phenomena such as the existence of the dark matter. It also has some theoretical problems such as too many parameters and hierarchy problem. The existence of the generations is also a mystery in the SM. The SM contains three generations for the quarks and the leptons, while they are not theoretically required. Therefore, the SM is thought to be an approximation of a more fundamental law of nature. Many theoretical extensions of the SM are proposed, and the physics beyond Standard Model (BSM) is eagerly searched by many experiments.

Charged lepton flavor violating processes are interesting probes to search for the BSM. In the SM, flavor mixing is allowed for the quark sector, while it is prohibited for the lepton sector by the lepton flavor conservation law. Since the flavor mixing between neutrinos called neutrino oscillation is recently found, flavor mixing between charge leptons, namely a charged lepton flavor violation (CLFV) process, is the only the flavor mixing process which has not yet been observed.

The purpose of the MEG II experiment is to search for a CLFV decay of a muon, $\mu \to e\gamma$, with a very good branching ratio sensitivity to find a clue for the new physics.

In the SM taking the neutrino oscillation into account, the $\mu \to e\gamma$ decay occurs by a Feynman diagram shown in Fig. 1.1. Its branching ratio is calculated to be as follows [2]:

$$\mathcal{B}(\mu \to e\gamma) = \frac{3\alpha}{32\pi} \left| \sum_{i=2,3} U_{\mu i}^* U_{ei} \frac{\Delta m_{i1}^2}{M_W^2} \right| \sim 10^{-55},$$

where U is the PMNS matrix. Due to the small mass difference of the neutrinos Δm^2 compared to the mass of W boson, the branching ratio is largely suppressed, and is too small to be detected in the experiment.

In contrast, some of the BSM models predict a branching ratio of $O(10^{-13}$–$10^{-14})$, which is experimentally detectable [3]. Supersymmetry (SUSY) is one promising candidate for the BSMs.
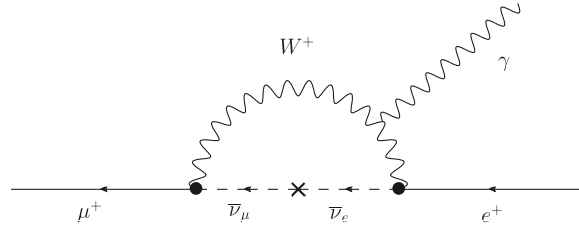
Figure 1.1   Feynman diagram of $\mu \to e\gamma$ in the SM with the neutrino oscillation.
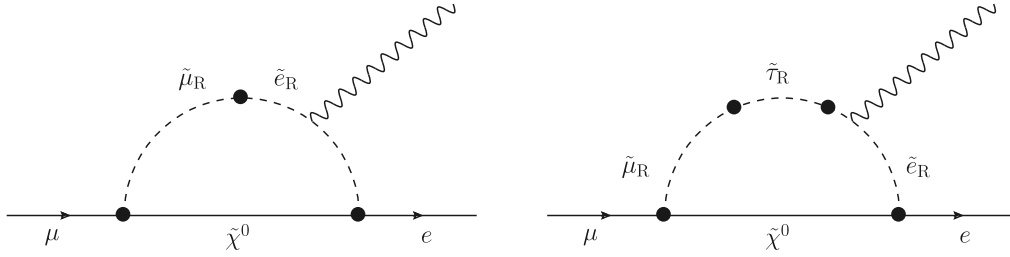
Figure 1.2   Feynman diagram of $\mu \to e\gamma$ in the SU(5) SUSY GUT [3].

In the minimal extension of the SM with SUSY called MSSM, a SUSY partner is introduced to each SM particle. This model is attractive since it can cancel the quadratic divergence in the radiative corrections of the Higgs mass. In the BSM models with SUSY, if the off-diagonal elements on the slepton mass matrix is non-zero in the basis which diagonalize the lepton mass matrix, it becomes a source of the CLFV.

One example is SU(5) SUSY GUT model [4]. In this model, electromagnetic, weak, and strong interactions are unified into a single gauge group at the grand unification (GUT) energy scale. This model is attractive in the sense that coupling constants of three interactions become unified at the GUT scale thanks to the contribution from the SUSY particles. In this model, when the (SM) lepton mass matrix is diagonalized

$$V_R y_e V_L^\dagger = diagnonal,$$

the off-diagonal terms of the right-handed slepton mass matrix is written as follows:

$$(m_{\tilde{e}R}^2)_{ij} \simeq -\frac{3}{8\pi^2}(V_R)_{i3}(V_R)_{j3}^*|y_u^{33}|^2 m_0^2(3+|A_0|^2)\ln\frac{M_P}{M_G},$$

where y_e and y_u are the Yukawa coupling constant for leptons and up-type quarks, m_0 is the universal scaler mass, A_0 is the trilinear coupling, M_P is the reduce Planck mass, and M_G is the GUT energy scale. This off-diagonal term leads to the CLFV through Feynman diagrams shown in Fig. 1.2.

Another example is SUSY seesaw model [5][6]. This model introduces right-handed heavy neutrinos with a Majorana mass term to explain the observed tiny mass of neutrinos by a seesaw mechanism. By introducing Majorana neutrinos into the SUSY model, a new Yukawa coupling constant for the neutrinos y_ν is introduced. Since the Yukawa coupling constant for the neutrinos and that for the leptons are independent, an off-diagonal term appears in the

(a)   (b)   (c)
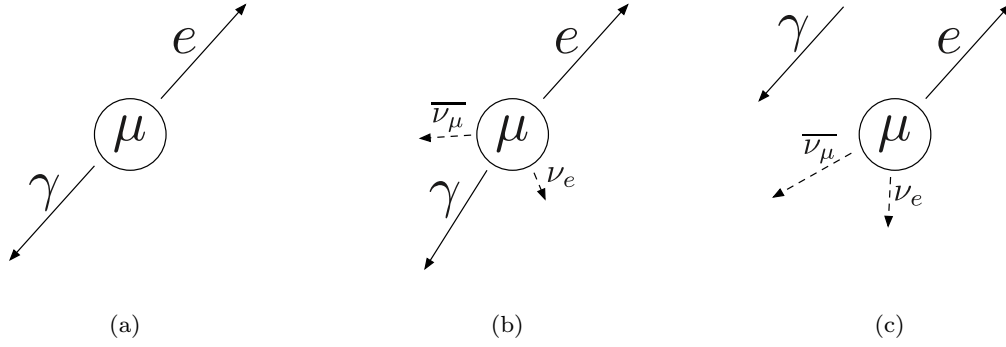
Figure 1.3   Event signature of (a) Signal, (b) Physics background (RMD), and (c) Accidental background.

left-handed slepton mass matrix as follows, and can be another source of the CLFV:

$$(m_{\tilde{l}L}^2)_{ij} \simeq -\frac{1}{8\pi^2}(y_\nu)_{ki}^*(y_\nu)_{kj}m_0^2(3+|A_0|^2)\ln\frac{M_P}{M_R},$$

where M_R is the mass of the right-handed Majorana neutrino.

1.2   Previous experiment: MEG experiment

The current best upper limit to the branching ratio of the $\mu \to e\gamma$ decay is set to 4.2×10^{-13} at 90% confidence level by the MEG experiment [1]. The MEG experiment measured many muon decays from the world's most intense continuous muon beam available at Paul Scherrer Institute (PSI) in Switzerland with good detector resolution and efficiency. In the search of the $\mu \to e\gamma$ decay, a signal event has to be identified from many other background events by utilizing its signature. This section describes how the MEG experiment searched for the $\mu \to e\gamma$ event, and what was a limiting factor of its physics performance. This will be a basis to discuss how to improve the branching ratio sensitivity in MEG II in the next section.

Principle of $\mu \to e\gamma$ search

The signal decay $\mu \to e\gamma$ is a two-body decay of a stopped muon to the nearly massless particles. Therefore, a signal decay emits a time coincident pair of a positron and a γ-ray having an energy of the half of the muon mass ($m_\mu/2 = 52.8\,\mathrm{MeV}$) to the back-to-back direction (Fig. 1.3). Their energies E_e and E_γ, opening angle $\Theta_{e\gamma}$, and time difference $t_{e\gamma}$ were measured by the positron and γ-ray detectors shown in Fig. 1.4. Signal events which satisfy $E_e = E_\gamma = 52.8\,\mathrm{MeV}$, $\Theta_{e\gamma} = \pi$, $t_{e\gamma} = 0$ were searched for.

Single event sensitivity

The expected number of signal events N_{sig} is calculated as follows:

$$N_{\mathrm{sig}} = \mathcal{B} \times k,$$
$$k := R_\mu \times T \times \Omega \times \epsilon_e \times \epsilon_\gamma \times \epsilon_{cut},$$
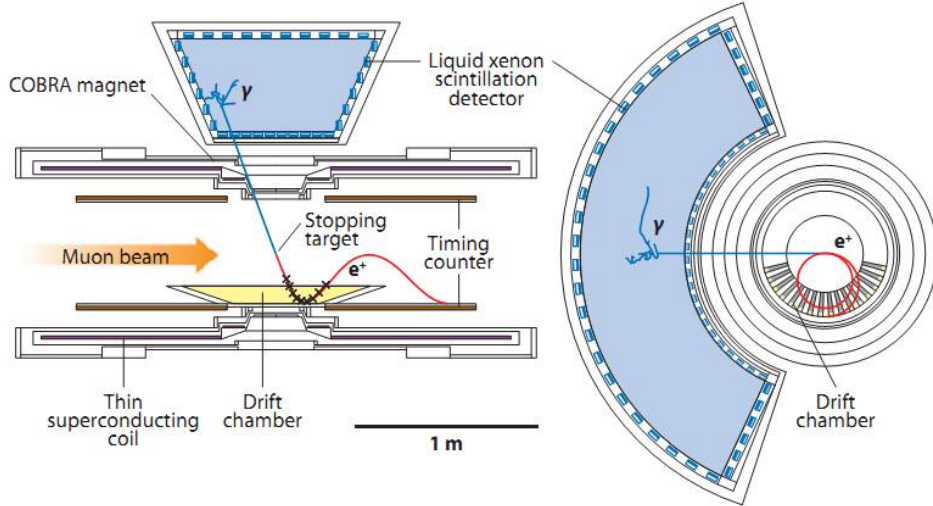
Figure 1.4   Schematic of the MEG experiment [7].

where $\mathcal{B}$ is the branching ratio of the signal decay, and k is the inverse of the single event sensitivity. R_μ is the muon beam intensity, T is the total data-taking time, Ω is the geometrical acceptance of the detectors, ϵ_e is the detection efficiency for signal positron, ϵ_γ is the detection efficiency for signal γ-ray, and ϵ_{cut} is a product of the trigger efficiency and the event selection efficiency in the offline analysis. In the MEG experiment, about $R_\mu \times T = 8 \times 10^{14}$ muons were decayed on the target in five years data-taking. These events were measured by the detectors of $\Omega = 10.8\%$, $\epsilon_e = 30\%$, $\epsilon_\gamma = 63\%$, $\epsilon_{cut} = 91\%$(from 2009-2010), 96%(from 2011-2013), and the single event sensitivity $k^{-1} = 0.58 \times 10^{-13}$ was achieved.

Background events

Events which satisfy the signal event criteria by chance become background events. There are two types of background events as shown in Fig. 1.3: physics background and accidental background.

One is the physics background coming from a radiative muon decay (RMD), $\mu^+ \rightarrow e\overline{\nu_\mu}\nu_e\gamma$. A pair of a positron and a γ-ray both of which carry signal-like energies can be emitted nearly back-to-back direction from the RMD, when two neutrinos carry only a small amount of the energy. The effective branching ratio of the physics background is calculated to be only about 0.1×10^{-13} from the theoretical spectrum of the RMD folded with the detector resolutions in MEG. This is smaller than the single event sensitivity, and thus the physics background was negligible.

The other is an accidental coincidence of a positron and a γ-ray. If a pair of positron and γ-ray near the signal energy originated from independent muon decays are accidentally emitted back-to-back at the same time, it looks like a signal event. Positrons near the signal energy comes from the Michel decays. Fig. 1.5(a) shows the spectrum of the Michel positron. Michel positron near the signal energy can be emitted with a rather high probability. Gamma-rays near the signal energy come from two types of events. One is the γ-ray from the RMD. Fig. 1.5(b) shows

(a)   (b)
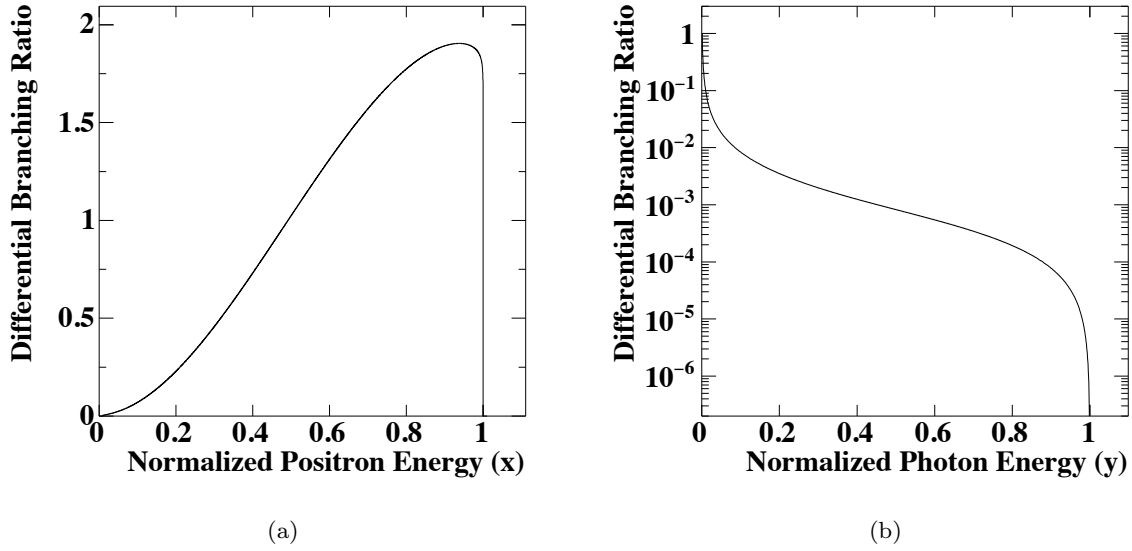
Figure 1.5   (a) Simulated energy spectrum of the Michel positron [8]. (b) Simulated energy spectrum of the RMD γ-ray. Energies on the x-axis are normalized to the half of the muon mass ($m_\mu/2 = 52.8\,\mathrm{MeV}$).

its energy spectrum of γ-ray. Contrary to the Michel positron, its spectrum rapidly decreases at the high energy. The other is the annihilation of Michel positrons in flight with electrons in the materials such as target, positron drift chamber, etc. Contributions from both processes were comparable in MEG. About 55% of background γ-rays in the analysis region ($E_\gamma > 48\,\mathrm{MeV}$) came from the RMDs, and the others came from the annihilation in flight.

The effective branching ratio of the accidental background was the limiting factor in MEG. Since the number of the accidental background events depends on the detector resolution as follows[*1] [3]:

$$N_{\mathrm{BG}} \propto R_\mu^2 \times \Delta E_\gamma^2 \times \Delta E_e \times \Delta t_{e\gamma} \times \Delta\Theta_{e\gamma}^2, \tag{1.1}$$

and the MEG II experiment tries to reduce it by improving the detector resolutions.

Branching ratio sensitivity

The branching ratio sensitivity of MEG is determined by a combination of two terms. One is the single event sensitivity which is an inverse of the accumulated number of muon decays k. The other is the contribution from the background events, which is inversely proportional to the square root of k.

In the final result of MEG, the branching ratio sensitivity was 4.2×10^{-13}, while the single event sensitivity was 0.58×10^{-13}. Therefore, the branching ratio sensitivity was limitted by the number of the accidental background events. Fig. 1.6 shows the sensitivities of MEG as a function of the statistics used for each analysis. An improvement in the sensitivity by an increased

---

[*1] This assumes that the accidental background γ-rays only come from the RMDs.
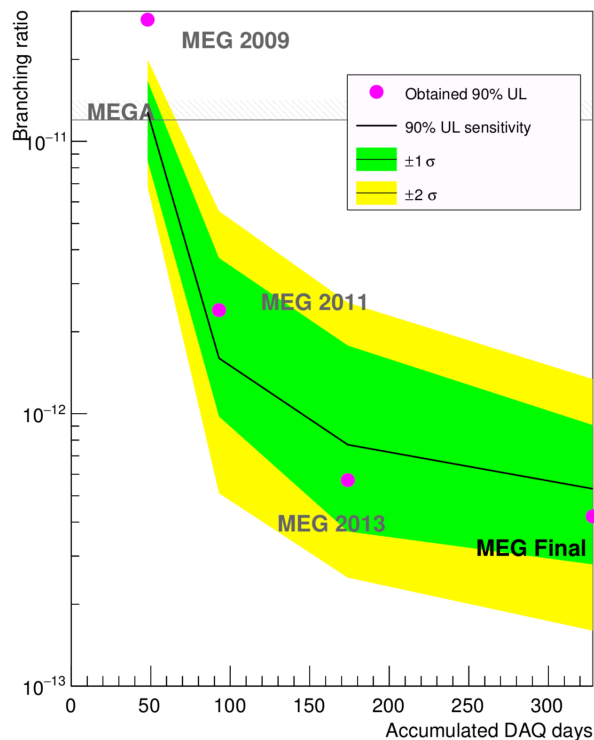
Figure 1.6 Branching ratio sensitivities (black line) and upper limits (purple markers) of MEG results as a function of the statistics used in each analysis [9].

statistics was getting smaller since the contribution from the backgrounds only improves by a square root of the statistics.

1.3 Concept of MEG II experiment

In order to improve the branching ratio sensitivity by one order of magnitude, an upgrade of the MEG experiment, MEG II experiment, is planned. There are two keys to achieve the sensitivity improvement.

One is an upgrade of all detectors to improve the resolutions and to reduce the accidental background events. As is discussed in the previous section, the sensitivity of MEG was limited by the number of the accidental backgrounds. Even if we continue data-taking by using MEG detectors, the sensitivity improves only by a squared root of the DAQ time, and it takes about 100 years to improve it by one order of the magnitude. Therefore, all detectors in MEG are upgraded or renewed in MEG II aiming to improve the resolutions by a factor of 2 and to reduce the accidental background events as shown in Equation 1.1.

The other key is an increase of the accumulated statistics. The muon beam rate in MEG was limited to 3×10^7 mainly due to discharges on the positron drift chamber and an unacceptable background level for the MEG detectors. This issue will be fixed by building a new detector, and the beam rate can be increased to 7×10^7 in MEG II. The detection efficiency of the positron spectrometer is also doubled by the upgrade.

Fig. 1.7 shows the detectors in the MEG II experiment. Positive muons coming from a beam line are stopped on a target placed at the center of the detectors. Positrons from the muon decays are measured by a spectrometer (Section 1.5) which consists of a constant bending radius (COBRA) magnet, a cylindrical drift chamber, and a positron timing counter. A liquid xenon γ-ray detector (Section 1.6) is used for a measurement of γ-rays from the muon decays. A new detector called radiative decay counter (Section 1.7) is installed to measure low energy positrons from the RMDs for an active background tagging. A data acquisition (DAQ) system (Section 1.8) to measure signals from the detectors is also upgraded for MEG II.

A global coordinate system (x, y, z) is defined as follows. The origin is defined at the center of the COBRA magnet where the muon stopping target is located. The z-axis is set parallel with the muon beam, and the y-axis is set vertical upward. The x-axis is set horizontal, so that (x, y, z) forms a right-handed system. A cylindrical coordinate system (r, θ, ϕ) is also defined as, $r := \sqrt{x^2 + y^2}$, $\theta := \tan^{-1}(z/r)$, $\phi := \tan^{-1}(y/x)$.

The search of the $\mu \to e\gamma$ is performed with a set of observables $(E_\gamma, E_e, t_{e\gamma}, \phi_{e\gamma}, \theta_{e\gamma}, E_{rdc}^{ds}, t_{rdc}^{ds})$. Positron tracks are measured by the spectrometer to reconstruct its energy E_e, direction, and decay vertex on the target. The γ-ray direction is reconstructed from the hit position in the γ-ray detector and the decay vertex, and is utilized to calculate the opening angles $(\phi_{e\gamma}, \theta_{e\gamma})$ of the positron and the γ-ray. The energy of the γ-ray E_γ is measured by the γ-ray detector. Time difference of the positron and the γ-ray $t_{e\gamma}$ is calculated from the timing measured by the positron timing counter, and the γ-ray detector. Their propagation times from the decay vertex to the detectors are calculated and corrected from their reconstructed track lengths. Measured positron energy and timing at the radiative decay counter $(E_{rdc}^{ds}, t_{rdc}^{ds})$ are also used in the MEG II analysis.

1.4   Beam and target

The MEG II experiment will be carried out at the πE5 beam line at PSI (Fig. 1.8), where the world's most intense continuous muon beam is available. The ring cyclotron at PSI can supply a 590 MeV proton beam of 2.2–2.4 mA. It is injected into a pion production target (target E) made of 4 cm-thick graphite. The muon beam is generated by collecting muons from the pion decays at the surface of the target E. This is called surface muon beam. Since the frequency of the cyclotron (50.7 MHz) is higher than the pion lifetime (26 ns), the extracted muon beam can be regarded as a continuous beam. The small momentum of the surface muons (28 MeV/c) with a good momentum-byte of about 7% (FWHM) enables us to stop the muons by a thin target E.

A Wien-filter (often called "Separator") is installed in the πE5 beam line to separate positron contamination in the muon beam, which is derived from the Michel decay of the muon and the π^0 decay in the target.

A superconducting beam transport solenoid (BTS) is installed to connect the πE5 beam line to the MEG II detectors. It applies a 0.36 T magnetic field to focus the beam. A degrader made of 300 μm thick Mylar is placed at the center of the BTS to adjust the muon momentum.
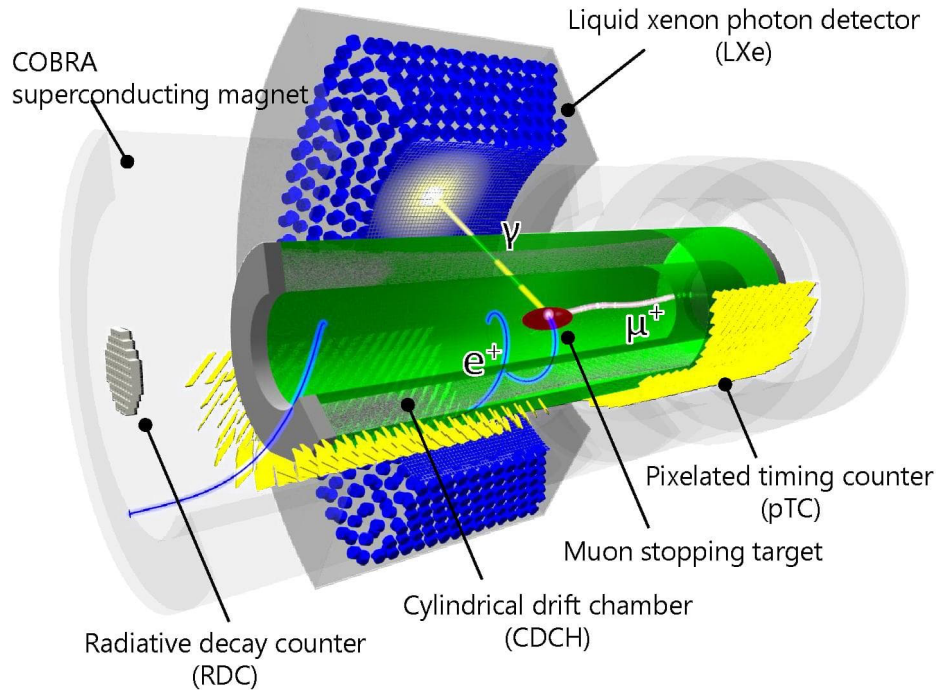
Figure 1.7 Detectors in the MEG II experiment [7]
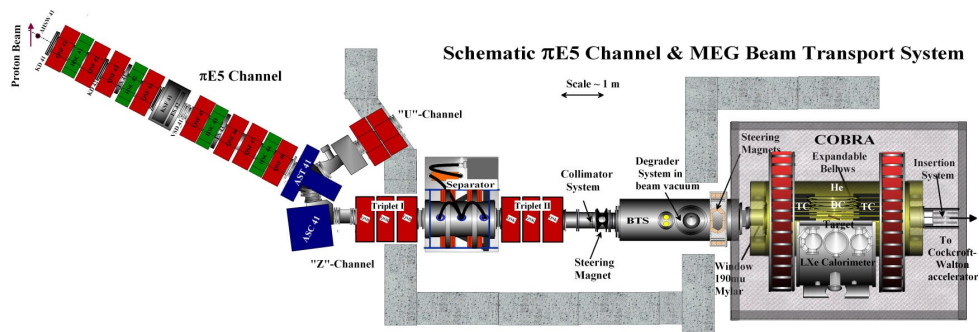
Figure 1.8 Schematic view of the πE5 beam line and the MEG (II) experimental area [7].

The muon beam is injected into the muon stopping target placed at the center of the MEG II detectors. This target has to be thin enough to avoid a multiple scattering and an annihilation of the emitted positrons. In the pilot run for MEG II, a $174\,\mu$m-thick plastic scintillating film (Fig. 1.9) was used as a target. It was placed 15° slanted from the beam axis to achieve a longer effective thickness for the muon beam and a shorter thickness for the positron. The scintillation light from the target can be used to measure the intensity and profile of the beam with a CCD camera.

In the MEG experiment, a distortion of the target during the data-taking was found, which introduced a systematic uncertainty in the reconstructed positron direction. This was the source of the largest systematic uncertainty in MEG. To monitor the stability of the target, optical markings are printed on the target for MEG II, and are monitored by CCD cameras [10].

Figure 1.9   Muon stopping target for MEG II (width:270 mm, height:66 mm) [7].
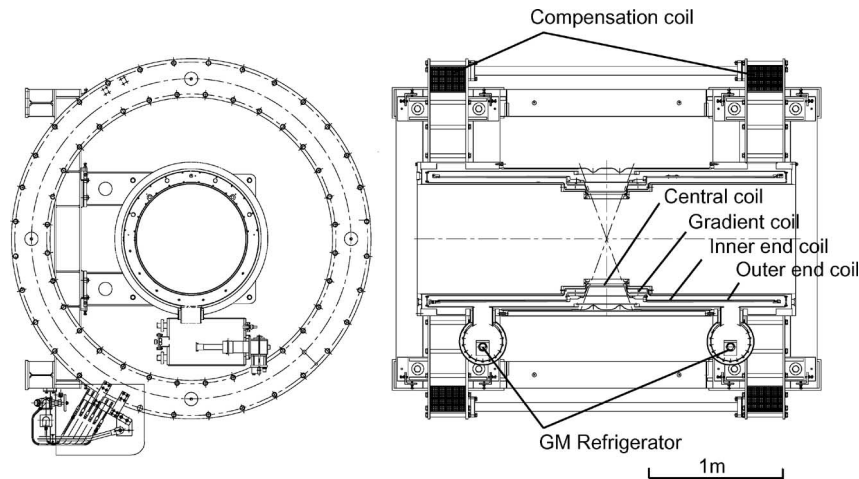
Figure 1.10   Schematic view of the COBRA magnet [11].

1.5   Positron spectrometer

The positron spectrometer in MEG II consists of the COBRA magnet, the cylindrical drift chamber, and the positron timing counter.

COBRA magnet

COBRA is a superconducting magnet specially designed for MEG, and is reused in MEG II (Fig. 1.10) [11]. Its gradient magnetic field (1.27 T at $z = 0$) is designed to have the same bending radius for the monochromatic positrons emitted from the target independent of the emission angles. It also sweeps low energy positrons quicker from the magnet than a simple solenoid. These features enable us to measure only the high energy positrons, which we are interested in. The COBRA magnet is also deigned to allow the signal γ-rays to penetrate it. It has a thin window at the acceptance region of the γ-ray ($|\cos\theta| < 0.35$), whose radiation thickness is $0.197X_0$. It has two compensation coils to suppress the magnetic field at the LXe detector for the PMT operation.

Cylindrical drift chamber

A new single volume wire drift chamber (green one in Fig.1.7) is built for the positron tracking in MEG II. It has a cylindrical shape whose inner radius is 17 cm, outer radius is 29 cm, and length is 191 cm. It is designed to have a high transparency to avoid multiple scatterings of the positrons. A low mass gas mixture of He : C_4H_{10} = 90 : 10 is used. The total radiation length
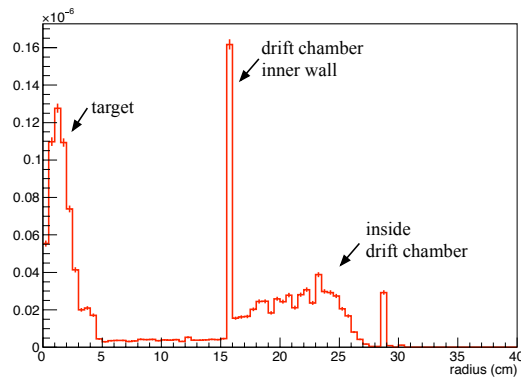
Figure 1.11   Simulated position (radius) distribution where the background γ-rays ($E_\gamma >$ 48 MeV) are generated from the Michel positrons. The y-axis is normalized to the probability per one muon decay on the target.

is $1.58 \times 10^{-3} X_0$, while it was $2.0 \times 10^{-3} X_0$ in MEG.

The low material budget can reduce the accidental background γ-rays from the annihilation in flight. Fig. 1.11 shows the position distribution where the background γ-rays are generated from the Michel positrons. The major contribution comes from the target, and the positron drift chamber. The number of the accidental background γ-rays above 48 MeV from the annihilation in flight per one muon decay on the target is reduced to $1.35(1) \times 10^{-6}$ from 2.3×10^{-6} in MEG.

The drift chamber consists of nine drift cell layers as shown in Fig. 1.12(a)[*2]. Each drift cell is composed of a $20 \, \mu$m gold plated tungsten sense wire surrounded by $40/50 \, \mu$m silver plated aluminum field wires. The size of the drift cell ranges from 6.6 mm (inner layers) to 9.0 mm (outer layers). A stereo wire configuration is adopted, in which wire planes are slanted at alternating signs stereo angles of $6.0°$–$8.5°$. This allows us to reconstruct z position of the positron track. The sense wire signals are read out from both sides, so that additional information on z can be reconstructed from a charge division, and from a propagation time difference.

The positron detection efficiency in MEG was limited to 30% by a service material of the drift chamber on the positron track (Fig. 1.12(b)). They are removed in MEG II, and a 70% detection efficiency is expected.

Positron timing counter

The positron timing counter is renewed for MEG II. For the positron timing measurement in MEG, 30 BC404 scintillator bars ($80 \times 4 \times 4 \, \text{cm}^3$) read out by fine mesh photomultiplier tubes (PMTs) were used. Though its intrinsic resolution was 40 ps, actual timing resolution in MEG was 70 ps. This is mainly due to a variation of the optical photon path length from its large size, and a degradation of the PMT performance in the magnetic field.

To cope with these issues, a new highly segmented positron timing counter has been developed

---

[*2] This figure is for the original design where ten layers were planned. The outer most layer was omitted in the real detector.
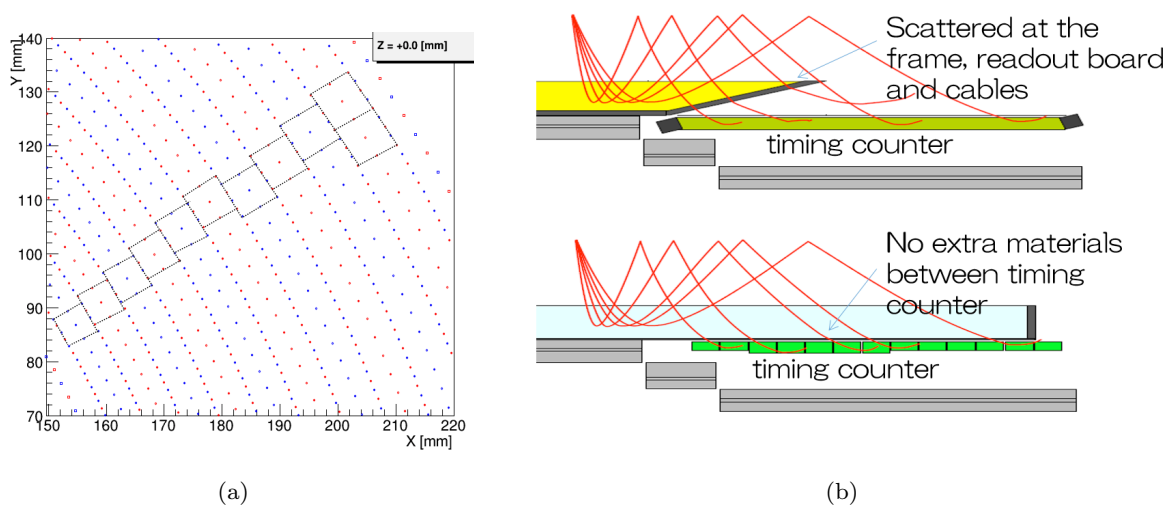
Figure 1.12   (a) Drift cells configuration at the center of the drift chamber [7]. (b) A cross section of the positron spectrometer for MEG (top), and MEG II (bottom) [12]. Detection efficiency of the positrons is improved by removing service materials on the positron track.

for MEG II. The counter is composed of an upstream sector and a downstream sector. Fig. 1.13 shows a design of the downstream one. It consists of 256 small plastic scintillator tiles. Each tile is $120 \times 40/50 \times 5\,\mathrm{mm}^3$ BC422 scintillator coupled to six silicon photo-multipliers (SiPM) from AdvanSiD (ASD-NUV3S-P High-Gain(MEG)) at each end (Fig. 1.14). The tile is wrapped by an enhanced specular reflector (ESR) from 3M to enhance the light collection. The six SiPMs on each side are connected in series and read out by a PCB. An optical fiber is inserted to distribute a synchronous laser signals for the time alignment between tiles.

Thanks to the thin scintillator tile, signal positron can penetrate multiple tiles. Fig. 1.15(a) shows the expected number of hit counters N_{hit} for a signal positron. On average, nine counters are hit. Positron timing is reconstructed from a combination of the hit counters. The combined resolution will be $\sigma_t^{\mathrm{single}}/\sqrt{N_{\mathrm{hit}}}$, where $\sigma_t^{\mathrm{single}}$ is the timing resolution of a counter, which includes the intrinsic resolution of a counter, the error in time alignment over the counters, and the electronics jitter. This segmentation scheme also benefits the operation in high pileup environment, and can supply additional information of the positron track. Fig. 1.15(b) shows the timing resolution measured for Michel positrons in the pilot run. Improvement in the resolution proportional to $1/\sqrt{N_{\mathrm{hit}}}$ is observed, and $31\,\mathrm{ps}$ timing resolution is achieved at $N_{\mathrm{hit}} = 9$.

Expected performance of spectrometer

Combined performance of the spectrometr is simulated by MC. The expected performance is summarized in the Table 1.1.
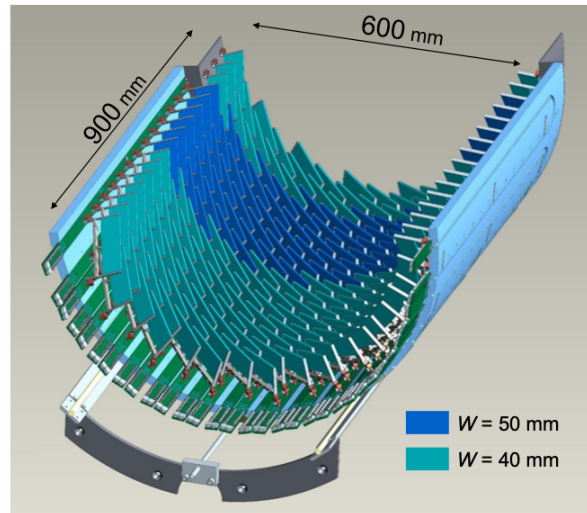
Figure 1.13   Design of a module of the positron timing counter [7].
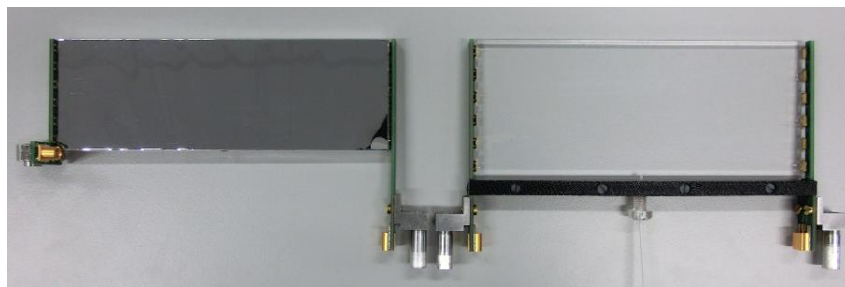
Figure 1.14   A scintillator tile used for positron timing counter. (left) 40 mm height tile with reflector wrapping, (right) 50 mm height tile before wrapping [7].

(a)

(b)
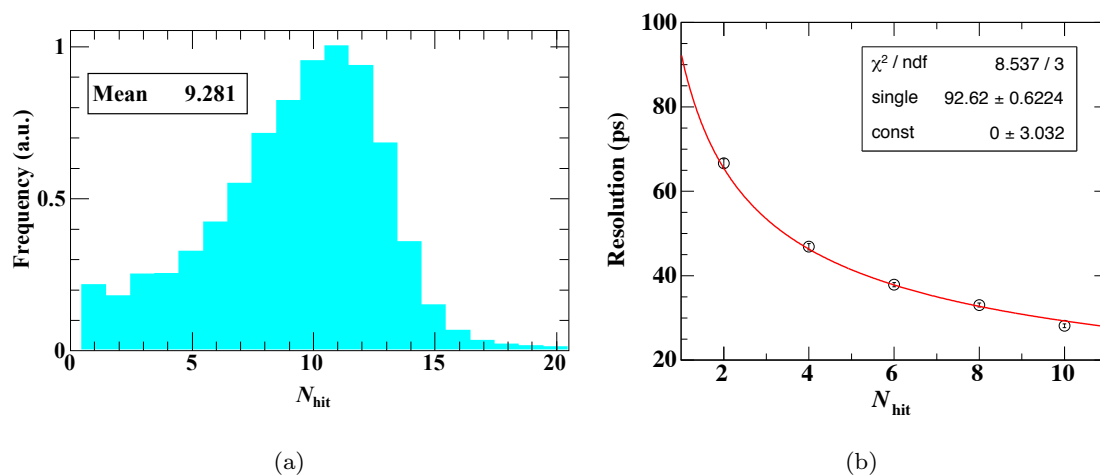
Figure 1.15   (a) Expected number of hit counters for a signal positron from the simulation [7]. (b) The total timing resolution measured in the pilot run 2016 [7]. The red curve shows the best fit by a function of $\sigma_{\mathrm{single}}/\sqrt{N_{hit}} \oplus \sigma_{\mathrm{const}}$.

Table 1.1   Positron detector performance [7].

	MEG (measured)	MEG II (simulated)
E_e resolution (keV)	380	130
θ_e resolution (mrad)	9.4	5.3
ϕ_e resolution (mrad)	8.7	3.7
t_e resolution (ps)	107	37
vertex resolution (z_e/y_e, mm)	2.4/1.2	1.6/0.7
efficiency (%)	30	70

1.6   LXe γ-ray detector

In order to measure the γ-ray from $\mu \to e\gamma$ decay with a good resolution and efficiency, a liquid xenon (LXe) detector was used in the MEG experiment. This detector has been upgraded to MEG II to improve its performance. A review of the MEG LXe detector is given in Section 1.6.1 and 1.6.2, and a concept of the upgrade is given in Section 1.6.3.

1.6.1   LXe as a scintillator

In the LXe γ-ray detector, LXe is used as a scintillator. Table 1.2 summarizes its properties. The LXe is suitable for the γ-ray detector in MEG (II) experiment in several aspects. The high stopping power of the LXe thanks to its large atomic number and high density makes it possible to construct a rather compact detector with a reasonable detection efficiency. Its sufficient light yield enables us to achieve a good detector resolution. The fast decay time of the scintillation is suitable for an operation in a high pileup environment. Since it is liquid, it is easier to achieve a uniform response than a crystal scintillation detector.

Table 1.2   Properties of the LXe

Item	Value
Atomic Number	54
Density	$2.953\,\mathrm{g/cm^3}$ [13]
Radiation length	$2.872\,\mathrm{cm}$ [13]
Moliere radius	$5.224\,\mathrm{cm}$
Scintillation Wavelength (mean)	$174.8 \pm 0.1(\mathrm{stat.}) \pm 0.1(\mathrm{syst.})\,\mathrm{nm}$ [14]
Scintillation Wavelength (FWHM)	$10.2 \pm 0.2(\mathrm{stat.}) \pm 0.2(\mathrm{syst.})\,\mathrm{nm}$ [14]
Decay time (fast)	$4.2\,\mathrm{ns}$ [15]
Decay time (slow)	$22\,\mathrm{ns}$ [15]
Decay time (recombination)	$45\,\mathrm{ns}$ [15]
W-value for electron	$21.6\,\mathrm{eV}$ [16]
W-value for alpha	$17.9\,\mathrm{eV}$ [16], $19.6\,\mathrm{eV}$ [17]
Refractive index (for $\lambda = 175\,\mathrm{nm}$)	1.65

When a particle deposits its energy in the LXe, scintillation light is generated by two processes [18][19]. The first one is from the excited xenon atom Xe^*.

$$\mathrm{Xe}^* + \mathrm{Xe} + \mathrm{Xe} \to \mathrm{Xe}_2^* + \mathrm{Xe}$$
$$\mathrm{Xe}_2^* \to 2\mathrm{Xe} + h\nu$$
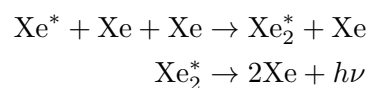
The second process is the recombination of the ionized xenon Xe^+.

$$Xe^+ + Xe \rightarrow Xe_2^+$$
$$Xe_2^+ + e^- \rightarrow Xe^{**} + Xe$$
$$Xe^{**} \rightarrow Xe^* + heat$$
$$Xe^* + Xe + Xe \rightarrow Xe_2^* + Xe$$
$$Xe_2^* \rightarrow 2Xe + h\nu$$
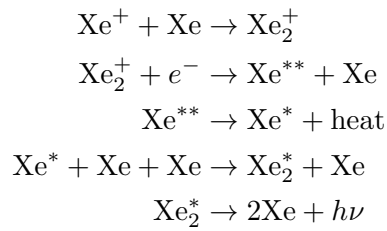
In both processes, scintillation light centered at $\lambda = 174.8\,\mathrm{nm}$ is emitted from $Xe_2^* \rightarrow 2Xe + h\nu$.

Fig. 1.16(a) shows the scintillation decay time for different particles. For the alpha particles, the recombination occurs very fast, and the decay time constant is determined by the lifetime of Xe_2^* [20]. Two time components of $4.2\,\mathrm{ns}$ and $22\,\mathrm{ns}$ are observed, which correspond to a singlet state and a triplet state, respectively. For the electrons or the γ-rays whose energy deposit densities are lower than the alpha particles, the decay time constant is determined by that of the recombination and becomes $45\,\mathrm{ns}$. This different decay time can be utilized for a particle identification.

There are three technical difficulties in the usage of the LXe. Firstly, its allowed region of temperature is limited as shown in Fig. 1.16(b). Since our detector is operated at about $1.2\,\mathrm{atm}$, the liquid phase is only in the range of about $10\,\mathrm{K}$. Secondly, its scintillation light is in the vacuum ultraviolet (VUV) region, and photosensors used for this detector have to be VUV-sensitive. Finally, impurities in the LXe have to be removed because an oxygen or a water contamination can easily absorb scintillation light, and a nitrogen contamination can quench the xenon scintillation by the following process:

$$Xe_2^* + N_2 \rightarrow 2Xe + N_2.$$
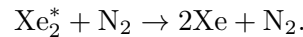
1.6.2   LXe detector in MEG

Fig. 1.17 shows the LXe detector used in MEG. LXe of $900\,\ell$ is surrounded by 846 PMTs placed on the detector wall to detect the scintillation light. The energy, the hit position, and the hit timing of the incident γ-ray are reconstructed from the observed scintillation light. This detector is designed to subtend 10.8% of the solid angle from the muon stopping target. The thickness of the LXe is $38.5\,\mathrm{cm}$ ($= 13.8X_0$) to fully contain the electromagnetic shower of the $52.8\,\mathrm{MeV}$ γ-ray from the signal decay. The detector wall consists of six faces (called inner, outer, upstream, downstream, top, and bottom face). The upstream and the downstream faces are called lateral face, and four faces except for the inner and the outer faces are called side face.

A dedicated local coordinate system is defined on this C-shape cryostat as shown in Fig. 1.18. The horizontal and vertical coordinates on the inner face are defined as u and v, respectively,
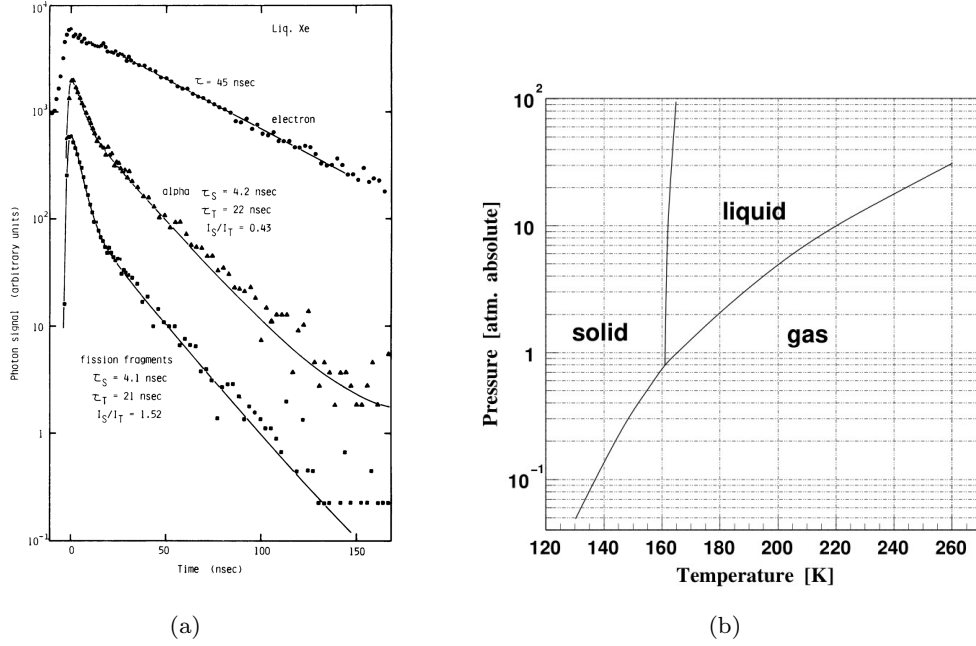
Figure 1.16   (a) LXe scintillation decay time for each particle [15]. (b) Phase diagram of xenon.

and the depth from the inner face is defined as w[*3]:

$$u = z$$
$$v = \tan\left(-y/x\right) \times R_{in}$$
$$w = \sqrt{x^2 + y^2} - R_{in}.$$

The R_{in} is the radial distance from the beam axis at the photosensor surface placed on the inner face, which is $R_{in} = 67.85\,\text{cm}$ for MEG, and $R_{in} = 64.84\,\text{cm}$ for MEG II. The active volume of this detector, where   -ray hits are analyzed, is defined as follows:

$$|u| < 23.9\,\text{cm}$$
$$|v| < 67.9\,\text{cm}$$
$$0 < w < 38.5\,\text{cm}.$$

The detector cryostat consists of an inner vessel and an outer vessel (Fig. 1.17(a)). The outer vessel is evacuated to thermally insulate the inner vessel filled with the LXe. Super insulation layers are installed between these vessels to suppress the heat inflow through the thermal radiation. Since the γ-ray goes into the LXe through an entrance window, the window has to be as thin as possible to achieve a better efficiency. The γ entrance face of the inner vessel is composed of a honeycomb-structure aluminum window and a carbon fiber plate. Its radiation thickness is only $0.081X_0$.

For the LXe detector in MEG, a new PMT with metal channel dynodes shown in Fig. 1.19(a) was developed in collaboration with Hamamatsu Photonics K.K (HPK). It is equipped with a quartz window to transmit the VUV light, and Bialkali (K-Cs-Sb) is used as a VUV sensitive

---

[*3] This equation is true if the LXe detector is placed at the designed position.
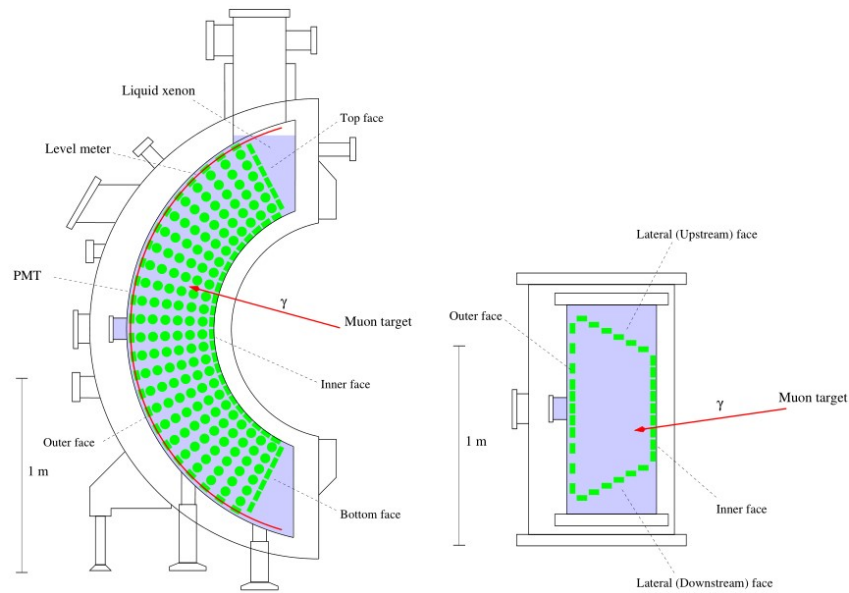
(a)
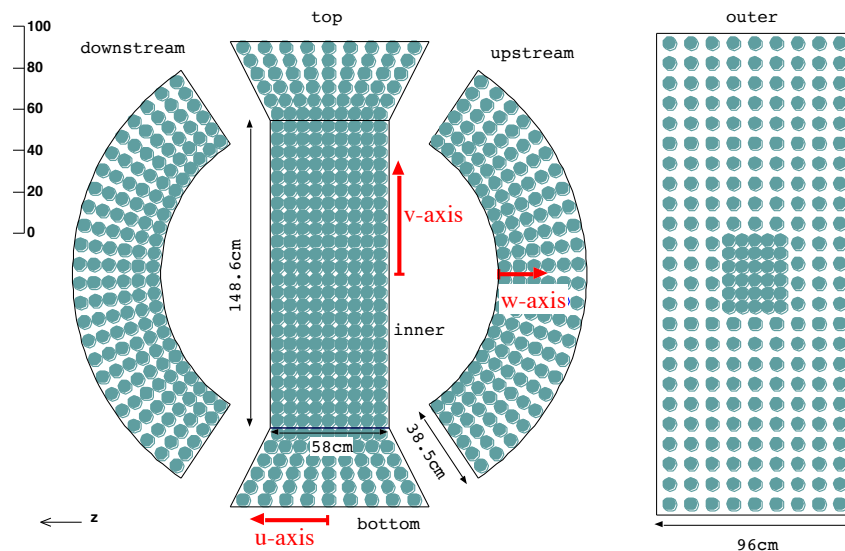
(b)

Figure 1.17   (a) Overview of the LXe γ-ray detector in MEG [21]. (b) Layout of the PMT in the LXe detector for MEG [21].

photo-cathode. Zener diodes are put in the last two amplification stages as shown in Fig. 1.19(b), in order to stabilize the gain under a high background condition.

In the MEG data-taking, high voltage applied to each PMT was adjusted to have the same gain (about 1.7×10^6) at the beginning of each year. Fig. 1.20(a) shows the time evolution of the gain averaged over all PMTs in 2013. A gradual decrease of the PMT gain was observed during the data-taking, probably due to the degradation of the dynode material by the induced current. The quantum efficiency of each PMT was measured from the calibration source inside the detector. It was measured to be about 22% as shown in Fig. 1.20(b).

The performance of the MEG LXe detector was limited by the granularity and the uniformity
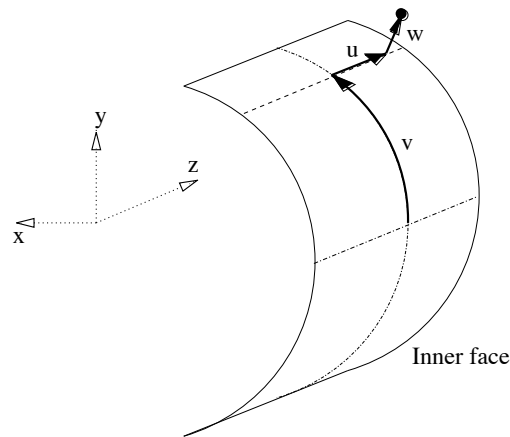
Figure 1.18   Dedicated coordinate on the LXe detector

(a)   (b)
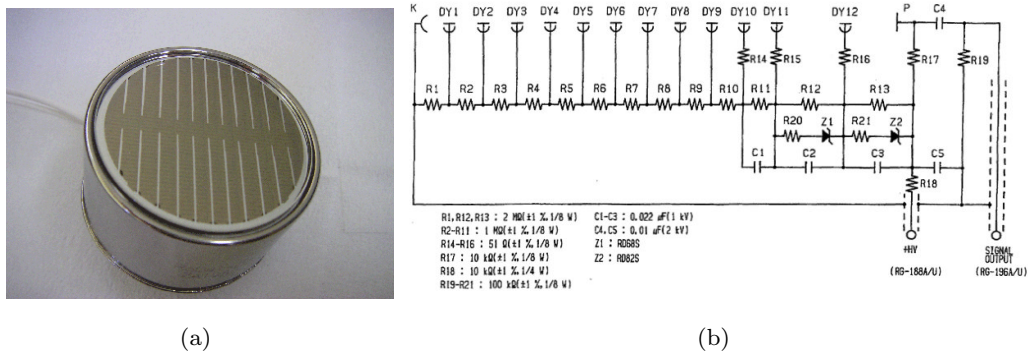
Figure 1.19   (a) VUV-sensitive PMT for MEG experiment (Hammatsu R9869) [21]. (b) Circuit of the PMT [21].

(a)   (b)
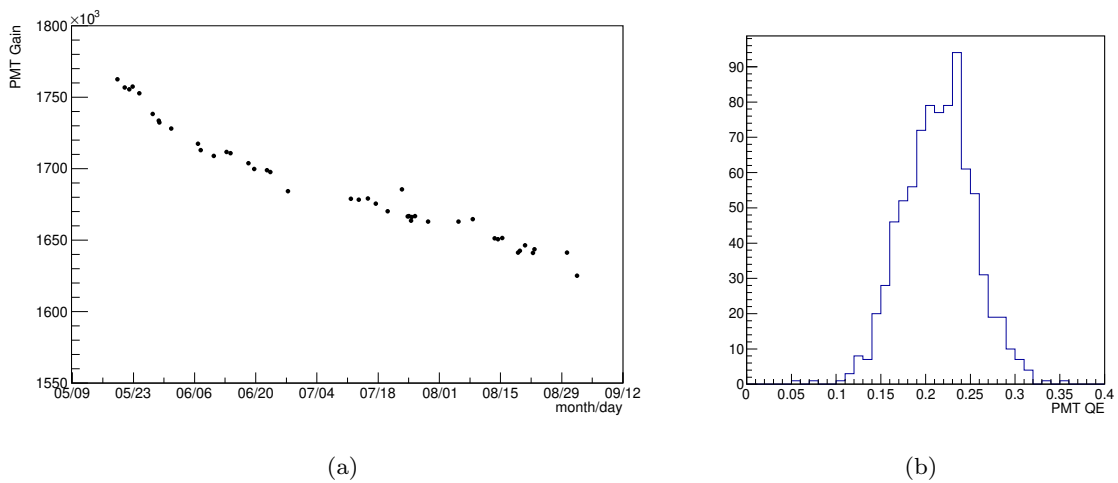
Figure 1.20   (a) History of the gain averaged over all PMTs in the run 2013. (b) Quantum efficiency of the PMTs measured in MEG (2013).
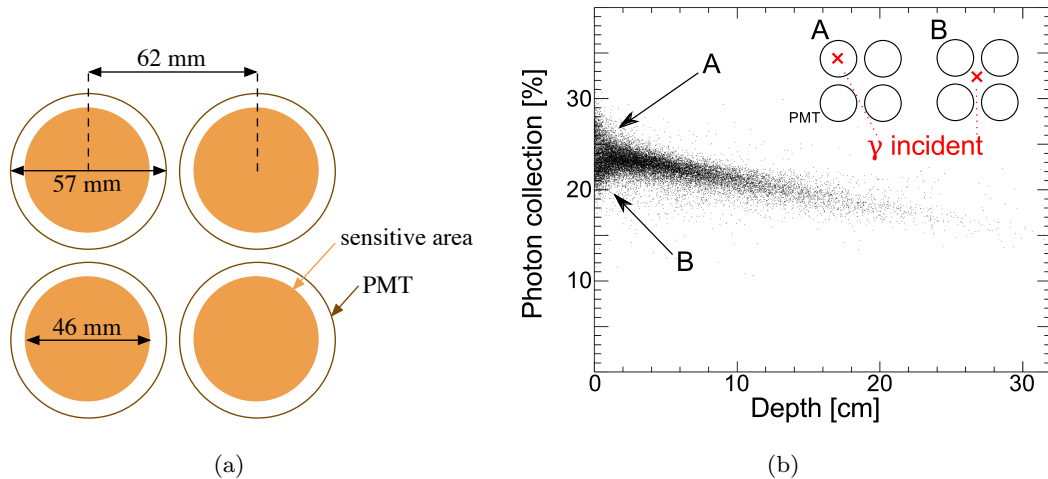
Figure 1.21   (a) Layout of the PMTs on the inner face in MEG. (b) Simulated photon collection efficiency as a function of the photon conversion depth in MEG [7].
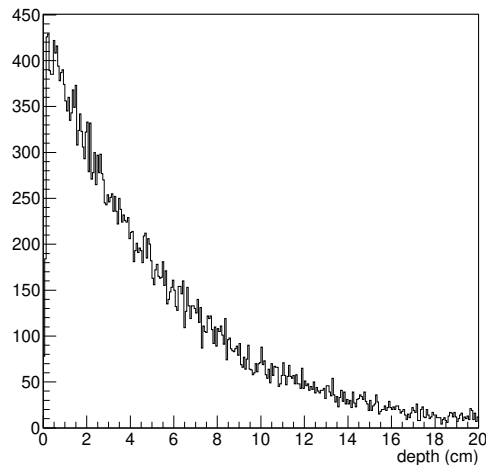
Figure 1.22   Simulated distribution of the conversion depth for the signal γ-rays [7].

of the scintillation readout. Even though the PMTs were placed with minimum spacing on the inner face, there was still a large insensitive area between the PMTs as shown in Fig. 1.21(a). This insensitive area leads to a non-uniformity of the total detected number of photons, from which the γ-ray energy is reconstructed. Fig. 1.21(b) shows a photon collection efficiency of each event. The collection efficiency becomes lower for the events where the γ-ray interacts in front of the insensitive area, and the event-by-event fluctuation becomes larger for shallow event (typically $w < 2\,\mathrm{cm}$). This results in a worse energy resolution for the shallow events. Since roughly one third of the signal γ-ray converts in the region of $w < 2\,\mathrm{cm}$ as shown in Fig. 1.22, this limited the performance of the LXe detector in MEG. The position resolution was also limited by this insensitive area for the shallow events.

1.6.3   LXe detector in MEG II

1.6.3.1   Upgrade concept

For the MEG II experiment, an upgrade of the LXe detector is planned to improve the performance as shown in Fig. 1.23 [7][22]. The major upgrade is a replacement of the 216 PMTs on the inner face with 4092 multi-pixel photon counters (MPPC). Thanks to the smaller size and the square shape of the MPPC, the inner face can be covered much more uniformly by the sensitive area than MEG. This leads to a better position and energy resolution of the shallow event.

The MPPC is a silicon photosensor developed by HPK, and it is a kind of the SiPM. As is in the normal silicon photosensor, the MPPC is operated by applying a reverse bias voltage to the p-n junction. By applying the voltage above the breakdown voltage, a photoelectron generated by an incident photon causes an avalanche in the depletion layer. A MPPC chip consists of many pixels connected in parallel as shown in Fig. 1.24. A quenching resistor is connected in series to each pixel such that avalanche is stopped by the voltage drop of generated charge. By this mechanism, a single photoelectron always induces the same amount of charge defined by the capacitance of the pixel and the bias voltage. Sum of the induced charge in all pixels is measured as a signal, and the number of the arriving photoelectrons can be measured from it.

Compared to the PMT, the MPPC has advantages as follows:

- photoelectron counting capability,
- insensitive to the magnetic field,
- smaller size,
- operated at lower voltage ($\sim 50\,\mathrm{V}$) with lower power consumption.

On the other hand, it has several drawbacks as follows:

- Higher dark signal rate: signal caused by thermal excitation even without external photons.
- Correlated noise: single photon may fire multiple pixels (crosstalk and afterpulse).
- Saturation: when the number of fired pixels is as large as the total number of pixels, measured number of photoelectrons gets deviated from the true number of photoelectrons.
- Larger temperature coefficient.

These drawbacks of the MPPC are measured in test setups, and the effects on our detector will be discussed in Section 2.1.3.

The PMTs on the outer face and the side faces are reused from MEG.

As shown in Fig. 1.25, a layout of the lateral PMTs is modified for MEG II. The horizontal width of the entrance face is extended by 10% to enlarge a fiducial volume of the LXe to suppress the energy leakage. The geometrical acceptance for the γ-ray is not extended since it is limited by the size of the thin entrance windows of the COBRA and the LXe detector. In MEG, entrance face of each lateral PMT is not on the holder surface plane (Fig. 1.25). This is modified in
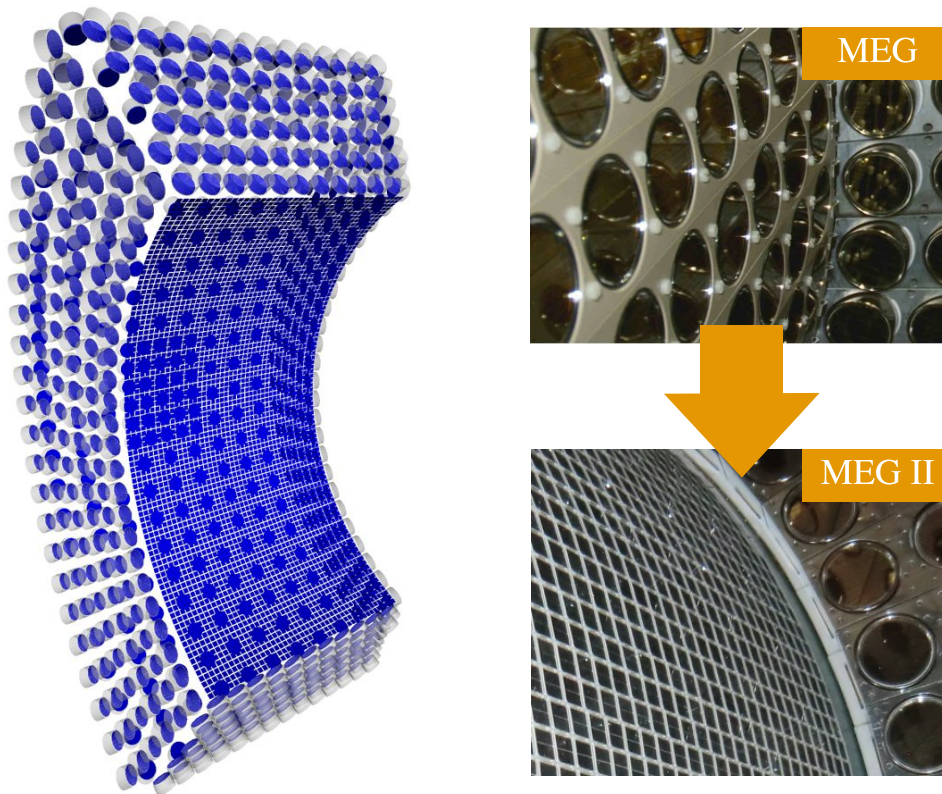
Figure 1.23   LXe γ-ray detector in MEG II.
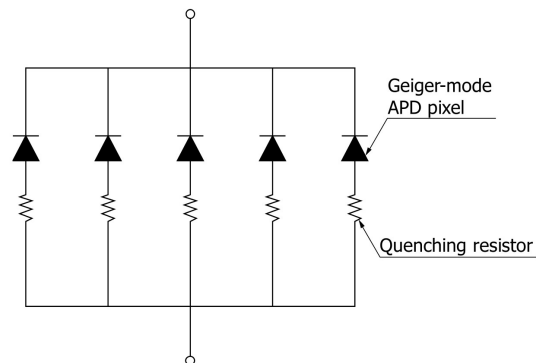
Figure 1.24   Conceptual illustration of the MPPC [23].

MEG II to be on the holder surface in order to minimize the effect of the shower fluctuation for the events near the lateral wall.

A layout of the top and the bottom PMTs is also modified as presented in Fig. 1.26. A staggered layout is adopted and more PMTs than MEG are placed with minimum spacing to have more uniform readout of the scintillation light near the top or the bottom face.

1.6.3.2   Expected performance

Table 1.3 gives the expected performance of the MEG II LXe detector. The position resolution will be improved especially for shallow events ($w < 4\,\mathrm{cm}$) thanks to the better granularity of the
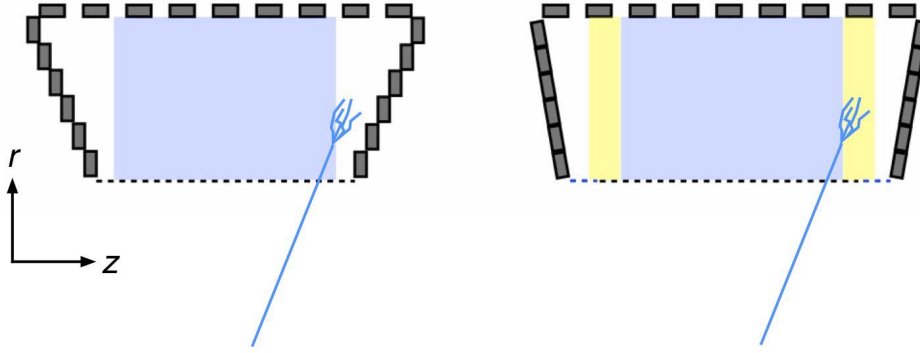
Figure 1.25   Upgrade of lateral PMT layout from MEG (left) to MEG II (right) [7].

(a)   (b)
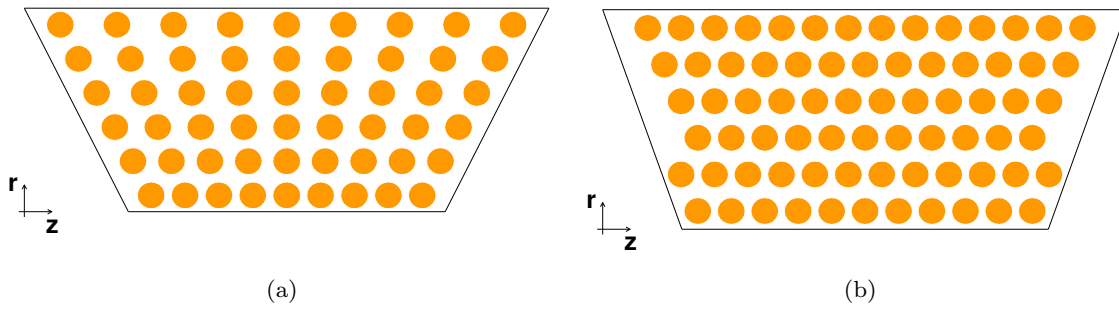
Figure 1.26   PMT layout in the top and the bottom face (a) in MEG and (b) MEG II.

scintillation readout realized by the MPPCs as shown in Fig. 1.27. This is useful since roughly half of the the signal γ-rays are converted in this region (Fig. 1.22). The detection efficiency is defined as a ratio of the number of the signal γ-rays which deposit energy above 48 MeV in the LXe to that of whose initial momentums are in the geometrical acceptance of the LXe detector. Thanks to the reduced thickness of the MPPC than the PMT, an improvement from 63% to 69% is expected.

Table 1.3   LXe detector performance

	MEG (measured)	MEG II (simulated)
position resolution $(u/v/w)$(mm)	5/5/6	2.6/2.2/5
energy resolution (%)($w < 2\,\mathrm{cm}/w > 2\,\mathrm{cm}$)	2.4/1.8	0.6/0.5 [*]
timing resolution (ps)	62	50
efficiency (%)	63	69

[*] refer to main text for detail

Thanks to the better uniformity realized by the MPPCs, the energy resolution will get improved especially for the shallow events ($w < 2\,\mathrm{cm}$). Though there might be a local non-uniformity of the resolution for the shallow events in MEG which was integrated in the physics analysis, this kind of non-uniformity should also be fixed in MEG II. Simulated energy resolution becomes 0.5–0.6% independent of the conversion depth. However, this simulated resolution
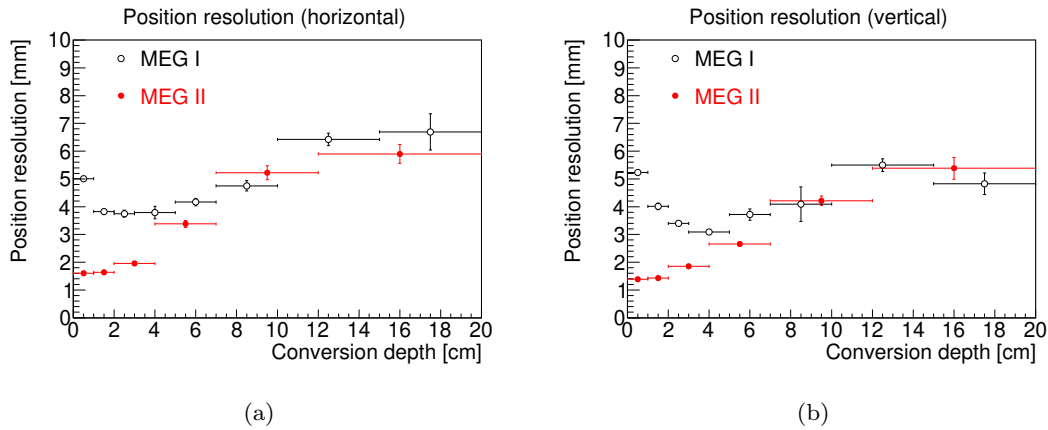
Figure 1.27   Simulated hit position resolution as a function of conversion depth. (a) horizontal direction, (b) vertical direction.

may not be reliable. In the MEG LXe detector, the measured energy resolution for the deep events was 1.8%, while 1.0% was expected in the simulation. The reason for this discrepancy of 1.5% $(= 1.8\%(meas.) \ominus 1.0\%(MC))$ has not been understood yet, and thus this contribution can remain in MEG II. Therefore, the expected energy resolution of MEG II is 0.5–1.6%.

1.7   Radiative decay counter

A radiative decay counter (RDC) is newly introduced for MEG II. As mentioned in Section 1.2, some of the accidental background events are caused by the γ-rays coming from the RMDs. The RDC identifies these events by detecting a positron from the RMD. Fig. 1.28(a) shows its concept. Since the positrons from the RMDs emitting a high energy γ-ray tend to be low energy (typically a few MeV), they are swiped out along the beam axis by the COBRA magnet. The RDC is placed at the downstream of the beam line to detect them. About half of the RMD positrons are emitted to the downstream side, and 42% of the positrons from the RMDs $(E_\gamma > 48\,\mathrm{MeV})$ can be detected by the RDC[*4].

The RDC consists of a timing counter and a calorimeter as shown in Fig. 1.28(b). Twelve plastic scintillators (BC418) are used for the timing counter, whose signals are read out by the MPPCs (S13360-3050PE). The timing resolution is estimated to be 90 ps by using a ^{90}Sr source. Fig. 1.29(a) shows the expected time difference between the LXe detector and the RDC. Accidental background events from the RMD γ-rays have a peak in the time distribution, while a uniform distribution is expected for the signal $\mu \to e\gamma$ events due to the accidental Michel positron hits on the RDC. The achieved timing resolution is sufficient to distinguish the RMD events from the accidental events in this distribution.

The positron energy is measured by the RDC calorimeter made of LYSO crystals placed behind the RDC timing counter (Fig. 1.28(b)). Fig. 1.29(b) shows the expected energy spectrum on the

---

[*4] A study of another counter to detect RMD positron placed at the upstream side (upstream RDC) is also ongoing. It is more difficult than the (downstream) RDC since the muon beam penetrates it.

(a)   (b)
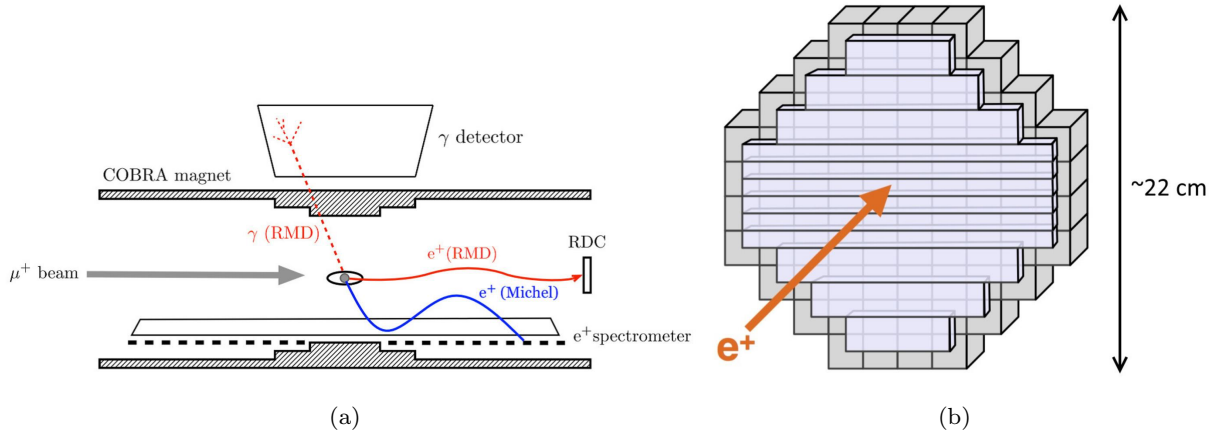
Figure 1.28   (a) Concept of the RDC [7]. (b) Design of the RDC. It consists of a timing counter (plastic scintillators) and a calorimeter (LYSO crystals) [7].

(a)   (b)
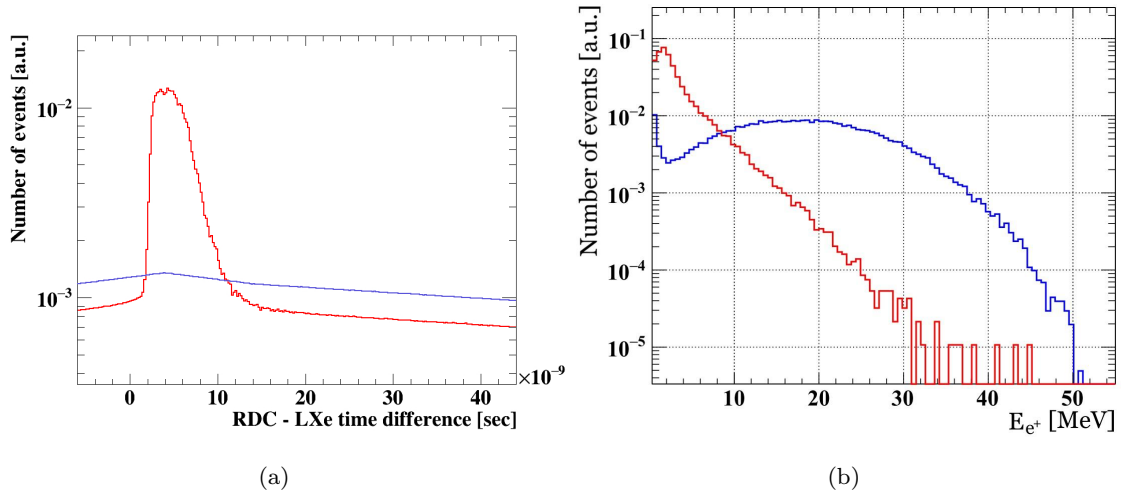
Figure 1.29   (a) Expected time difference between the LXe detector and the RDC. Accidental backgrounds from the RMD γ-rays (red) have a peak, while the signal events (blue) are uniformly distributed. The uniform components in both distribution is due to the accidental pileups of the Michel positrons on the RDC. Note that some events are not shown in this plot, since they have no RMD hit and pileup hit on the RDC [7]. (b) Expected energy spectrum of the RDC [7]. (Blue) The Michel positrons. (Red) The RMD positrons emitting a γ-ray above 48 MeV.

RDC. Typical energy of Michel positrons is higher than that of the RMD events emitting a high energy γ-ray. The calorimeter consists of 76 blocks of $2 \times 2 \times 2\,\mathrm{cm}^3$ LYSO crystals each of which couples to an MPPC (S12572-025). The intrinsic radioactivity of the LYSO is used to calibrate the response of each LYSO crystal and MPPC. The energy resolution is measured to be 6% for 1 MeV γ-ray by using a ^{60}Co source. This is sufficient to distinguish the RMD positrons from the Michel positrons.

1.8   Data acquisition system

The DAQ system is also upgraded for MEG II. In MEG, detector signals were actively split for a trigger system and a waveform digitizer. Waveforms of all detectors were recorded at the $O(\mathrm{GHz})$ sampling speed, and utilized in the offline analysis such that we can achieve a good detector resolution and deal with the high pileup environment. Due to the increased number of readout channels in MEG II by a factor of three, a simple extension of the MEG's system is impossible in the limited space in the experimental area. Therefore, an integrated DAQ system called WaveDREAM is being developed. Fig. 1.30 shows an overview of the WaveDREAM system. Signals from each detector are digitized by the WaveDREAM boards (WDB) whose trigger is generated on the trigger concentrator boards (TCB), and transferred to the online computer through a Gigabit ethernet from the data concentrator boards (DCB). The whole DAQ system is controlled by the MIDAS DAQ system [24].

WaveDREAM boards

The signals from each detector are connected to the WDB (Fig. 1.31), on which several functionalities are implemented. Input waveforms are digitized by DRS4 (Domino Ring Sampling [25]) chips. Fig. 1.32 shows a mechanism of the DRS chip. The amplitudes of the waveforms are stored on the 1024 capacitors called "DRS cells" as a charge by a logic wave propagating through the inverter domino chain. The sampling is stopped when the trigger is fired, and the stored charge is read out by an external ADC in the order of the DRS cells by a shift resistor.

Two stage amplifiers and a programable attenuator are implemented on the analog frontend of the WDB, so that we can apply an appropriate size of amplification for each purpose. For example, in the LXe detector, the maximal amplifier gain (about 100) is used to measure the single photoelectron signals of the MPPCs, while no or smaller amplification is used to measure $O(10^4)$ photoelectrons signals from the signal energy γ-ray.

The bias voltages for the SiPMs and the MPPCs can be supplied from the Cockcroft-Walton voltage multiplier on the WDB. The applied voltage for each channel can be tuned via a 5 V DAC to deal with the individual difference of the operating voltage.

To achieve a good timing resolution, a synchronization between channels is important. For this purpose, a distributed reference clock is digitized on each DRS chip. The precision of the timing alignment is measured to be about 20 ps [12][26], after the timing alignment by the reference clock.

One WDB can measure the waveforms from sixteen channels, and about 530 WDBs will be used to read out about 9000 channels in MEG II.

Trigger

The trigger logic of MEG II is based on an online reconstruction of the observables in the $\mu \to e\gamma$ search on the FPGA [27]. Since the signals from the drift chamber cannot be used for the trigger generation due to its slow response, those from the LXe detector and the positron
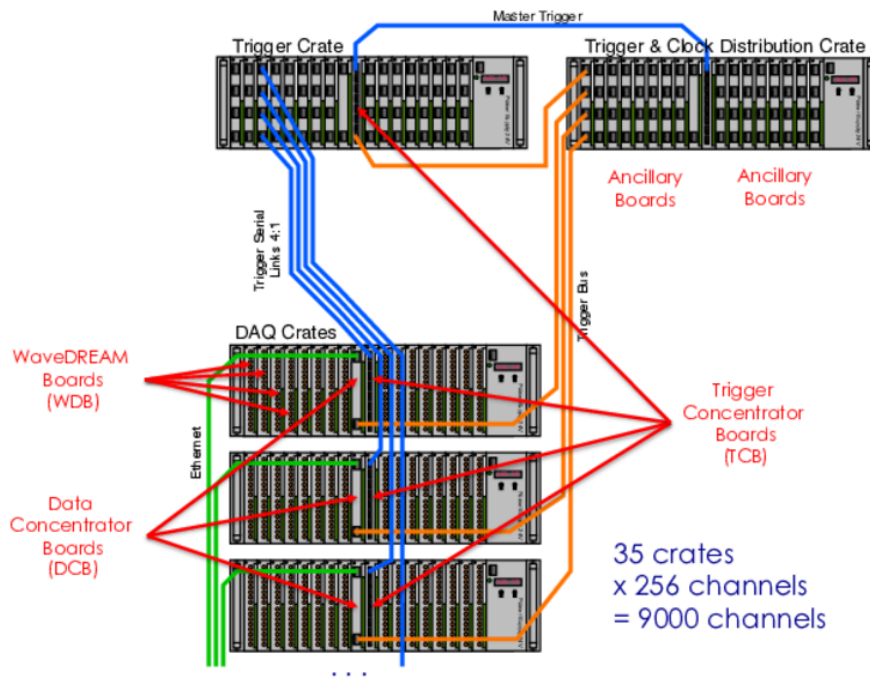
(a)

(b)

Figure 1.30   (a) Concept of the WaveDREAM system. (b) A prototype WaveDREAM crate.
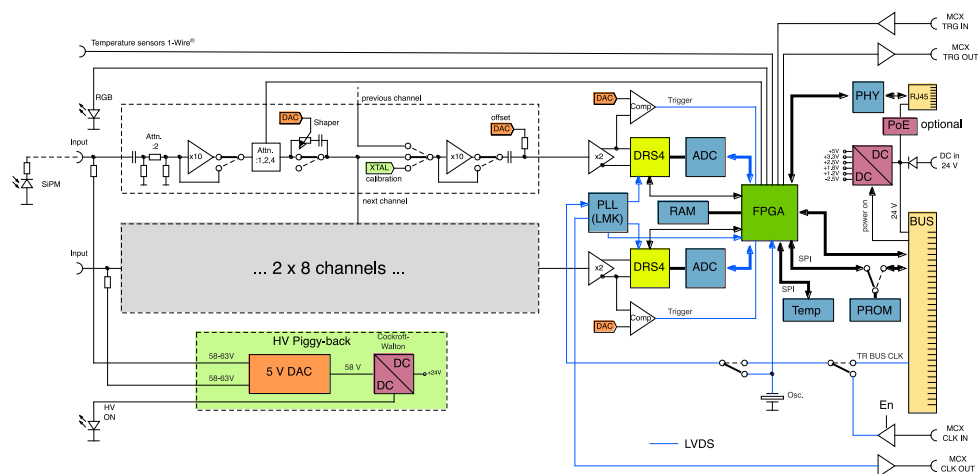
Figure 1.31   Schematic of WDB [7]
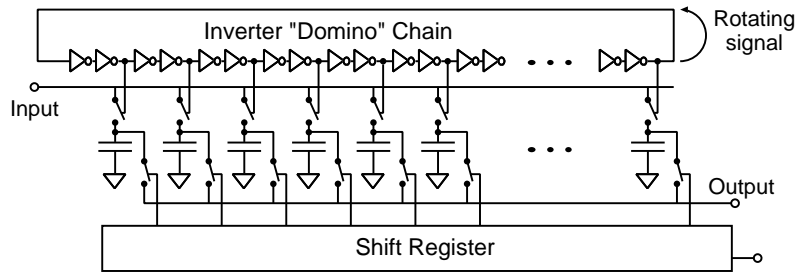
Figure 1.32   Mechanism of DRS.

timing counter are used for it.

The γ-ray energy is reconstructed from a sum of the waveforms of the LXe detector. While the DRS is sampling, the ADC is used for a digitization of the input waveforms at a 80 MHz sampling frequency. The sum of these digitized waveforms is calculated on the FPGA, whose peak amplitude corresponds to the online reconstructed energy. In the calculation of the sum waveform, each waveform can be multiplied by a given weight to compensate an individual difference of the photosensor performances such as the gain and the PDE. A difference of the waveform shape between the MPPCs and the PMTs is also corrected by this weight. Events with an amplitude exceeding a given threshold are triggered to select the events with a signal-like energy γ-ray. A veto threshold can also be set to reject high energy background events caused by the cosmic rays which typically have more than 120 MeV energy deposit in the LXe detector.

The timings of the γ-ray and the positron are reconstructed by using a comparator on the WDBs connected to the signal of each channel.

An event selection on the opening angle is also possible thanks to the detector segmentation in MEG II (MPPC readout in the LXe detector, and scintillator tiles in the positron timing counter). A correlation between the timing counter hit and the peak position on the inner face of the LXe detector allows us an angular constraint on the decay kinematics.

By combining these criteria, a trigger rate ≈ 10 Hz is expected for the physics data-taking at the MEG II beam intensity.

Data size

Obtained data is stored in the 1.2 PB data storage to be analyzed on an offline computing cluster. In order to store all the MEG II data in the storage, the data size of each event should be below about 3 MB assuming a trigger rate of 10 Hz [*5]. Because the data size of each event will be about 7.7 MB[*6] if we simply store the obtained waveforms with bzip compression, a data size reduction by a factor of a few is needed. For this purpose, data reduction algorithms are being studied for each detector waveform to eliminate the information unnecessary or unimportant in the reconstruction. For example, for the LXe detector which occupies more than half of the

---

[*5] Total size becomes 930 TB after three years data-taking in this case.

[*6] Estimated by scaling a measurement in the run 2019 with a limitted number of readout channels (Chapter 3). The data size was 1.0 MB/event with 1088 channels readout.
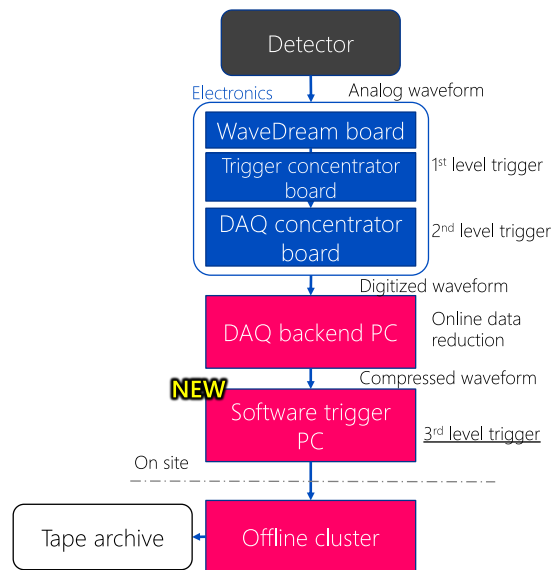
Figure 1.33   A schematic of the online DAQ system including the software trigger [28].

readout channels and the data size before the reduction, algorithms summarized in Appendix A are planned.

Another planned solution to reduce the data size is an introduction of a software trigger (Fig. 1.33). By running a fast event reconstruction on a dedicated computer which is more sophisticated than the trigger generation by the FPGA, better resolutions of the observables than the online resolution should be achievable. A positron track information may also be utilized. With the software trigger, a more stringent event selection can be applied, and the number of stored events is expected to be reduced.

1.9   Branching ratio sensitivity expected at design stage

The branching ratio sensitivity of MEG II was calculated by assuming the expected resolutions of the upgraded detectors at the design stage [7][22]. The result is shown in Fig. 1.34.

Since there was an uncertainty on the performance improvement in each detector, the sensitivity in an optimistic scenario, and a pessimistic scenario were also calculated. Ambiguity of the sensitivity was estimated to be 30%. It is notable that the sensitivity of the nominal scenario shown in Fig. 1.34 adopted an intermediate energy resolution (1.0%) of the LXe detector, where a half of the unknown contribution is assumed.
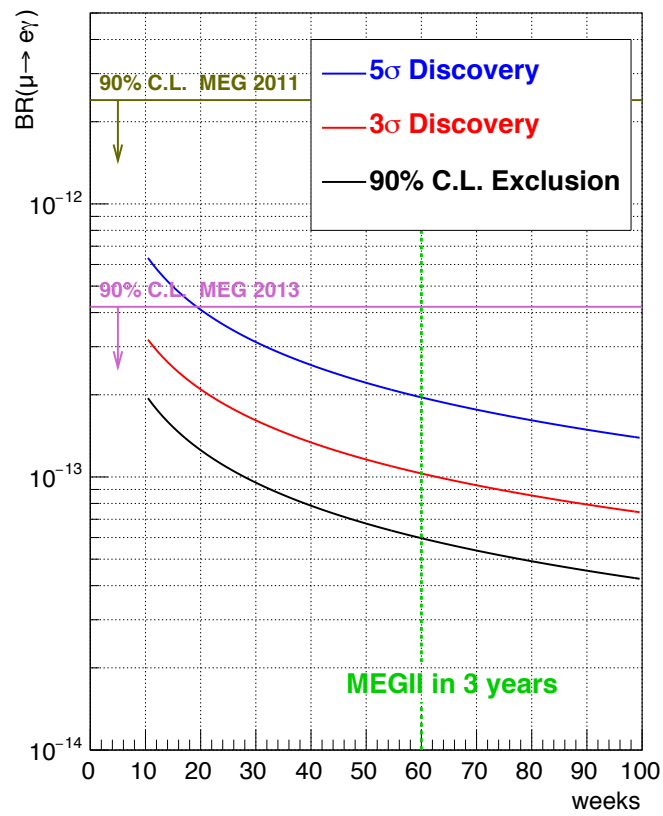
Figure 1.34 Expected branching ratio sensitivity of MEG II experiment at the design stage as a function of the DAQ time [7].

Chapter 2

Development of LXe Detector

Based on the design shown in Section 1.6, the LXe detector has been upgraded to improve its performance to achieve the physics goal of the MEG II experiment. This chapter describes the development of the LXe detector. Section 2.1 describes a concept and a performance of a new MPPC developed for this detector. Section 2.2, and 2.3 explains a quality control of the photosensors. Support structures and the signal readout chain for the photosensors are shown in Section 2.4. Section 2.6 describes the alignment of the MPPCs, which is required for a good position resolution of γ-ray. Other subsystems of the detector operation such as a slow control system and calibration sources are also summarized in this chapter.

2.1 VUV-sensitive MPPC

2.1.1 Concept of VUV-MPPC

There are three major requirements for the MPPCs used in the MEG II LXe detector. First, it has to be sensitive to the xenon scintillation light in the VUV range ($\lambda = 175\,\mathrm{nm}$). Since standard MPPCs do not have a sensitivity to the VUV light, a new MPPC has to be developed. Second, in order to cover the whole inner face by the MPPCs with a reasonable number of readout channels, the sensitive area per channel has to be as large as $12 \times 12\,\mathrm{mm}^2$. Typical commercial MPPCs can read out $3 \times 3\,\mathrm{mm}^2$ per channel at most, and are not suitable for our use. Third, it has to be operational inside the $165\,\mathrm{K}$ LXe.

A new MPPC which satisfies these requirements has been developed in collaboration with HPK (Fig. 2.1, S10943-4372, also called VUV3).

In the standard MPPC, there is a protection layer of epoxy resin at the sensor surface. This layer is removed in our MPPC since it absorbs VUV photons before entering the sensitive region. To improve the VUV sensitivity, optical matching between the liquid xenon and the sensor surface is optimized, and the contact layer before the active layer is thinned down. The dopant concentration in the contact layer is also adjusted to have an non-zero electric field. Instead of the removed protection layer, a VUV-transparent quartz window is mounted on the MPPC package. The LXe can go into the gap between the window and the MPPC chips when the MPPC is immersed in the LXe. Since the refractive index of the quartz is 1.60 and is
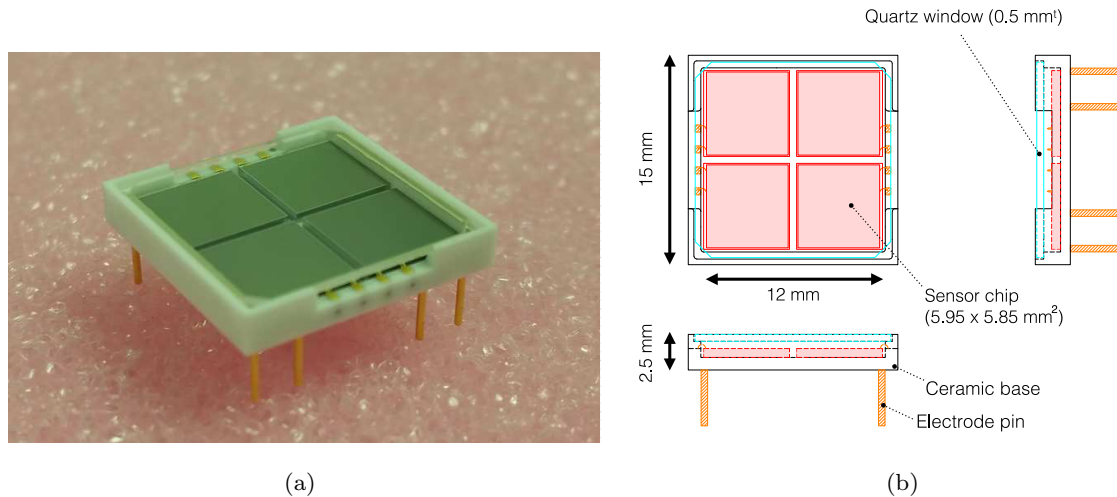
Figure 2.1 VUV sensitive MPPC developed for MEG II (Hamamatsu S10943-4372) [29]

sufficiently close to that of the LXe (1.65), a loss of the VUV photon by the reflection on the quartz window is negligible in the LXe.

The detection mechanism of a VUV photon is different from that of the visible light. In the detection of the visible light in an MPPC, a photon generates an electron-hole pair in the active layer, which directly triggers an avalanche. Since the attenuation length in silicon for the VUV light is only 5 nm, and is still shorter than the thickness of the contact layer, a VUV photon is detected in the way that a part of the charge carriers generated in the contact layer drifts to the active layer, and triggers an avalanche.

There are two possible issues to have a large sensitive area on the MPPC. One is the dark signal whose rate is proportional to the size of the MPPC. This is, however, not a problem in our case because the dark signal caused by a thermal excitation is largely suppressed at the LXe temperature. The other is a longer decay time caused by the larger capacitance of the larger sensitive area. To reduce the capacitance, our MPPC package is designed to have four independent $6 \times 6\,\mathrm{mm}^2$ chips, which can be connected in series when it is read out.

The pixel pitch of this MPPC is $50\,\mu\mathrm{m}$. The number of pixels per channel is 5.57×10^4. This is sufficient for our use in terms of the saturation of the MPPC because the largest signal on one MPPC is expected to be about 1×10^4 photoelectrons for the 52.8 MeV signal γ-ray.

2.1.2 Apparatus for test measurements

The performance of the VUV-MPPC was measured in test setups to confirm its sufficient performance. This section shows two kinds of setups used for these measurements.

Small chamber

The first setup is a 2 ℓ LXe setup used for the measurement of a small number of MPPC samples (up to eight). A pulse tube refrigerator (Iwatani PDC08) was used for the xenon
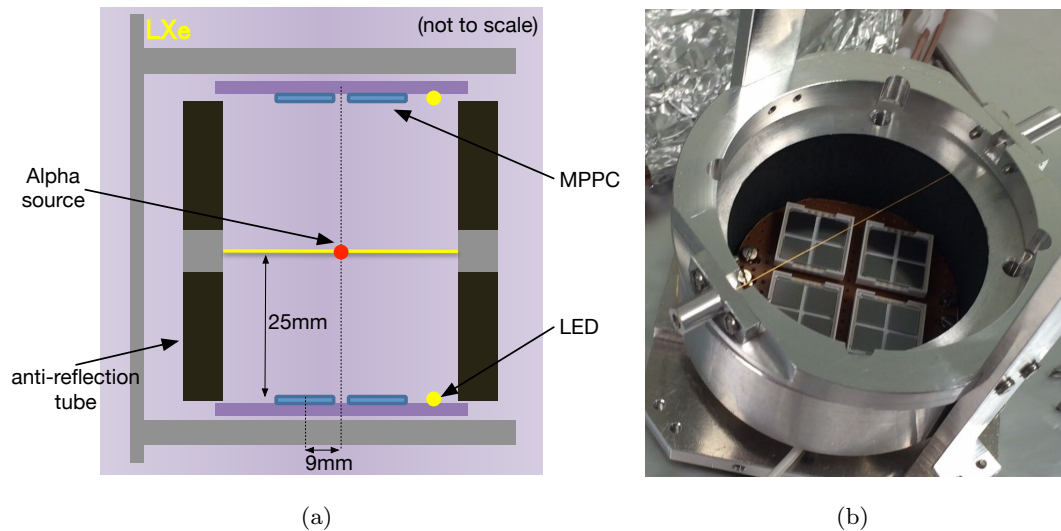
Figure 2.2   Small chamber setup

liquefaction. A heater was attached on the refrigerator to regulate the cooling power based on the xenon pressure or temperature.

Fig. 2.2 shows the core part of this setup. The MPPCs were placed on a circuit board on which the signals from four chips on an MPPC package are connected in series. A few blue LEDs were installed to measure single photoelectron signals from them. An alpha source (^{241}Am) placed on a tungsten wire was installed for the PDE measurement. Thanks to the short path length ($40\,\mu$m) of an alpha particle in the LXe, this source can be used as a point source of the xenon scintillation light. Due to the energy loss in the protection material around the source, the energy of the emitted alpha particle becomes smaller than the original energy of $5.5\,$MeV. Its energy was measured to be $4.8\,$MeV on average with a spread of 4% by a silicon surface barrier detector. In order to suppress the reflection of the scintillation light at the cryostat wall, the whole setup was placed inside a tube with anti-reflection coating (Acktar black [30]).

The signals from the MPPCs are transmitted to the outside of the cryostat through coaxial cables and a feedthrough. The signals are amplified by an amplifier developed by PSI shown in Fig. 2.3, and are recorded by a DRS evaluation board. A pi-pad attenuator is implemented on this amplifier, whose strength can be adjusted by replacing the resistance in order to keep the size of the output signals in the dynamic range of the DRS and the amplifier.

Large chamber

Another setup called "large chamber" was used for a mass test of about 600 VUV-MPPCs of a prototype version (called VUV2 [31]). The major difference between the prototype model and the final model is that an optical trench around every MPPC pixel to suppress the optical crosstalk [23] is not implemented on the prototype version. The main purpose of this test is to check the performance of many MPPCs inside the LXe before starting the mass production of the final model. Another purpose is to test a signal transmission scheme in the LXe detector.

Fig. 2.4 shows a support structure used for this test, which was immersed in the LXe. Twenty
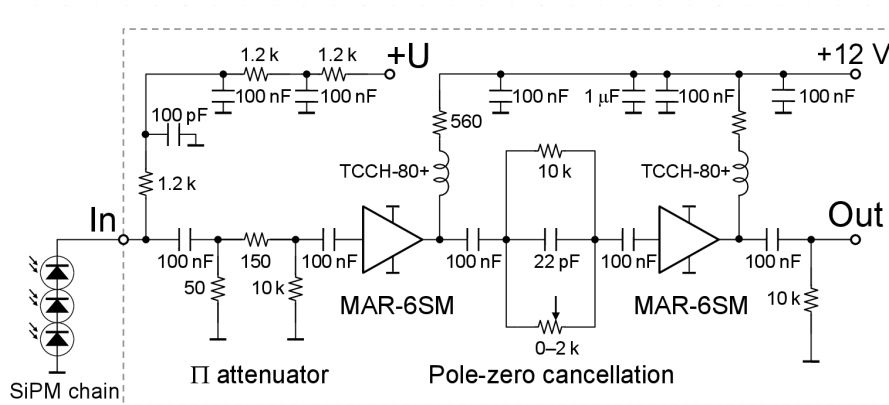
Figure 2.3   Amplifier developed by PSI.

(a)   (b)
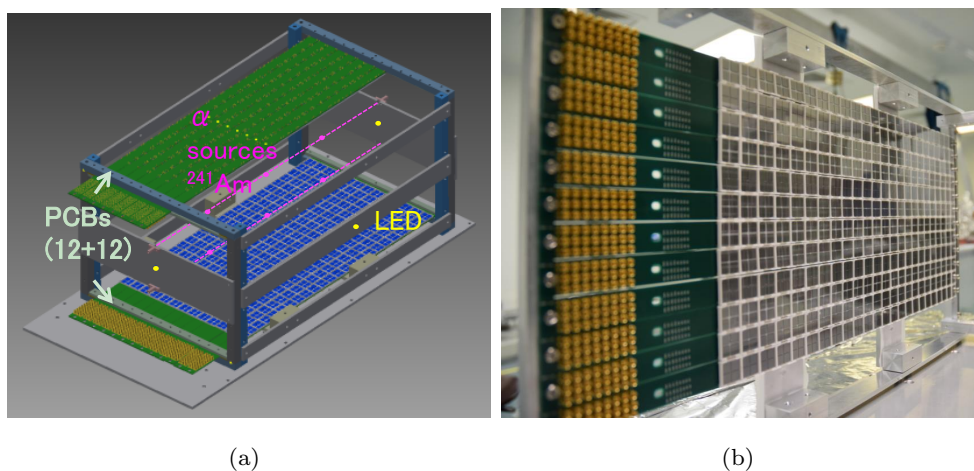
Figure 2.4   Support frame in large chamber test. About 600 MPPCs are arranged.
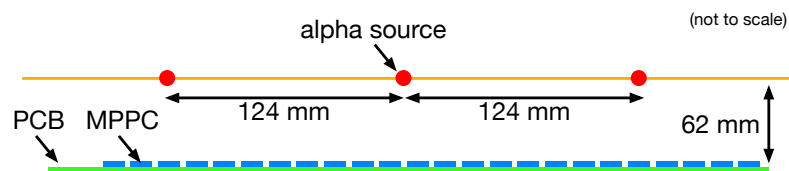
Figure 2.5   The position of the alpha sources and the MPPCs in the large chamber test.

four MPPCs were placed on a PCB, and twenty four PCBs were fixed on the support structure. LEDs and alpha sources were installed to measure the MPPC characteristics.

This setup was also used to study the angular dependence of the PDE. Fig. 2.5 shows the position of the alpha sources. The PDEs at different incident angles can be measured from many kinds of geometrical combinations of the alpha sources and the MPPCs.

2.1.3   Measured performance of VUV-MPPC

Gain and single photoelectron signal

Fig. 2.6 shows two-photoelectrons waveforms obtained from a weak LED light. As is discussed in Section 2.1.1, our MPPC package consists of four independent chips which can be connected in series to reduce the decay time of the MPPC signal. The decay time of the MPPC signal by a series connection is found to be shorter than that by a parallel connection.

The gain of the MPPC is estimated by integrating the MPPC waveform in a time window of 150 ns. A charge distribution shown in Fig. 2.7(a) is obtained, where photoelectron peaks are clearly resolved. The gain is measured from the difference between the single photoelectron peak and the pedestal. Fig. 2.7(b) shows the measured gain with series connection as a function of the applied voltage, and a linear correlation is obtained as expected.

Correlated noise

In the MPPC, a primary avalanche can trigger another avalanche [23]. This phenomena is called correlated noise. One source of the correlated noise is an afterpulse. An avalanching carrier trapped by a impurity energy level is released after short delays and generates another avalanche. Another source is a prompt optical crosstalk, where a photon produced by an avalanche generates electron-hole pairs in a neighboring pixel. The probabilities of these correlated noises are estimated from the weak intensity LED data. If there is no correlated noise, the detected number of photoelectrons from a LED follows a Poisson distribution $P_\lambda(x)$, where λ is the Poisson mean. Since the number of zero photoelectron events is not affected by the correlated noise, λ
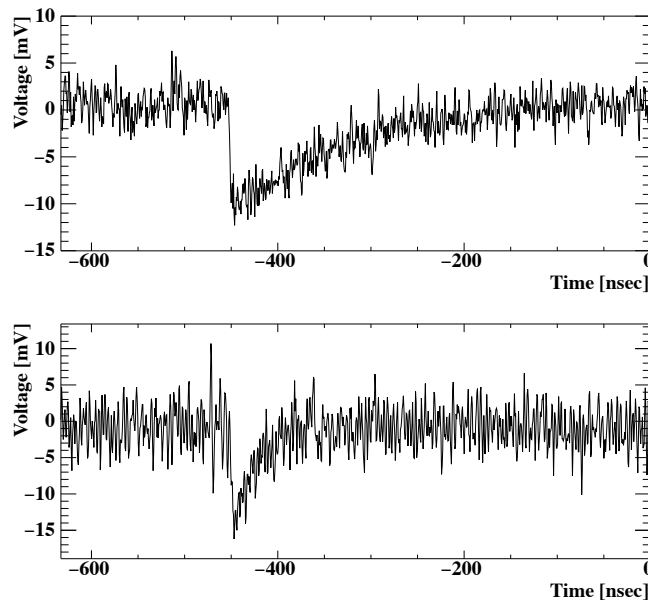

Figure 2.6   Typical two-photoelectrons waveform of our MPPC (primary single photoelectron signal from LED with a optical crosstalk), connected in parallel (top), and connected in series (bottom) [29].

can be obtained from the relation of

$$(\text{A fraction of 0 photoelectron events}) = P_\lambda(0) = e^{-\lambda}.$$

The probability of the correlated noise p is derived from the measured fraction of the single photoelectron events, which reflects the effect of the correlated noise as follows:

$$(\text{A fraction of 1 photoelectron events}) = P_\lambda(1) \times (1 - p).$$

Another variable which represents the size of the correlated noise is an averaged amplification size of signals, called the excess charge factor (ECF). This is calculated as $ECF := \mu/\lambda$, where μ is a mean of the detected number of photoelectrons.

Fig. 2.8(a) shows the correlated noise probability estimated from a charge distribution of a short integration range (30 ns). This should represent prompt effects like optical crosstalk. The correlated noise probability with a longer integration range (150 ns) is shown in Fig. 2.8(b), where the probability in the short range is subtracted. This should represent the delayed contribution such as afterpulse. Thanks to the suppression technique implemented on the final model of MPPC, the correlated noise probability is only up to 30%, and operation at higher over voltages up to 7 V becomes possible.

Dark count rate

The dark count rate at the LXe temperature is measured by counting events above the single photoelectron charge without external light. Scintillation events caused by environmental radioactivity are subtracted by identifying them from the coincident signals on the several MPPCs. Since some of the scintillation events observed only on one MPPC may still be left, the measured rate is an upper limit of the dark count rate. Fig. 2.9(a) shows that the rate is measured to be only $5\,\text{Hz/mm}^2$, which is sufficiently small for our use.

(a)   (b)
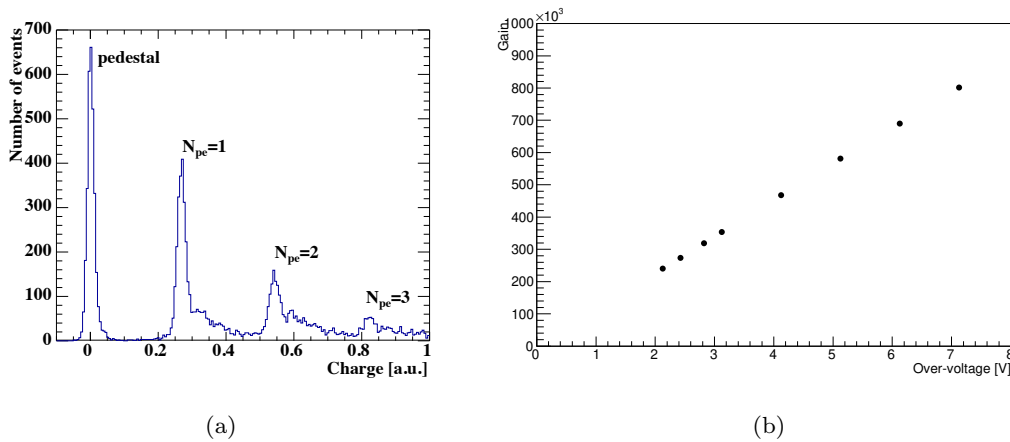
Figure 2.7   (a) Charge distribution of LED [29]. (b) Gain of MPPC as a function of over voltage (series connection). Gain of amplifier is corrected.
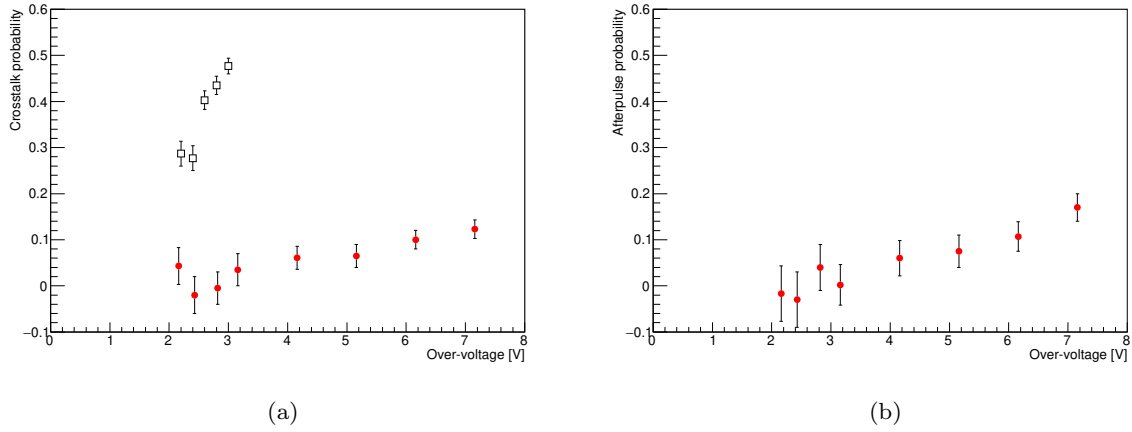
Figure 2.8   Measured correlated noise probability of final version MPPC as a function of over voltage [29]. (a) crosstalk (b) afterpulse. Black data series in (a) is for the prototype version without crosstalk suppression technology.

PDE for LXe scintillation light

The photon detection efficiency (PDE) for the LXe scintillation light is measured by using an alpha source, which can be regarded as a point source of the xenon scintillation light by the energy deposition of $E_\alpha = 4.8\,\text{MeV}$. The PDE is calculated as a ratio of the detected number of photoelectrons N_phe to the arriving number of photons N_pho. The N_phe is obtained from a mean of the measured charge Q of alpha events, and the N_pho is calculated by a solid angle Ω from the alpha source subtended by each MPPC, and the W-value of the LXe $W = 19.6\,\text{eV}$ (Table 1.2). The amount of indirect light is estimated in the simulation, and included as a correction factor r. The systematic uncertainty of the measured PDE is mainly coming from about 10% uncertainty of the W-value (Table 1.2).

$$PDE := \frac{N_\text{phe}}{N_\text{pho}},$$
$$N_\text{phe} = \frac{Q}{Gain \times ECF},$$
$$N_\text{pho} = \frac{E_\alpha}{W} \times \frac{\Omega}{4\pi} \times r.$$

Fig. 2.9(b) shows the measured PDE, a sufficient PDE above 15% is confirmed.

Energy resolution

The energy resolution, namely the precision of the number of photoelectrons measurement, is checked. In the ideal case, the energy resolution just follows a statistical fluctuation. The excess noise factor (ENF) is a parameter which stands for a degradation of the resolution from this ideal case defined as:

$$ENF := \sigma_\text{meas}^2 / \sigma_\text{ideal}^2,$$

where σ_meas is the measured resolution, and σ_ideal is the ideal resolution. Since the energy reconstruction of the LXe detector is based on the total number of detected photoelectrons, its
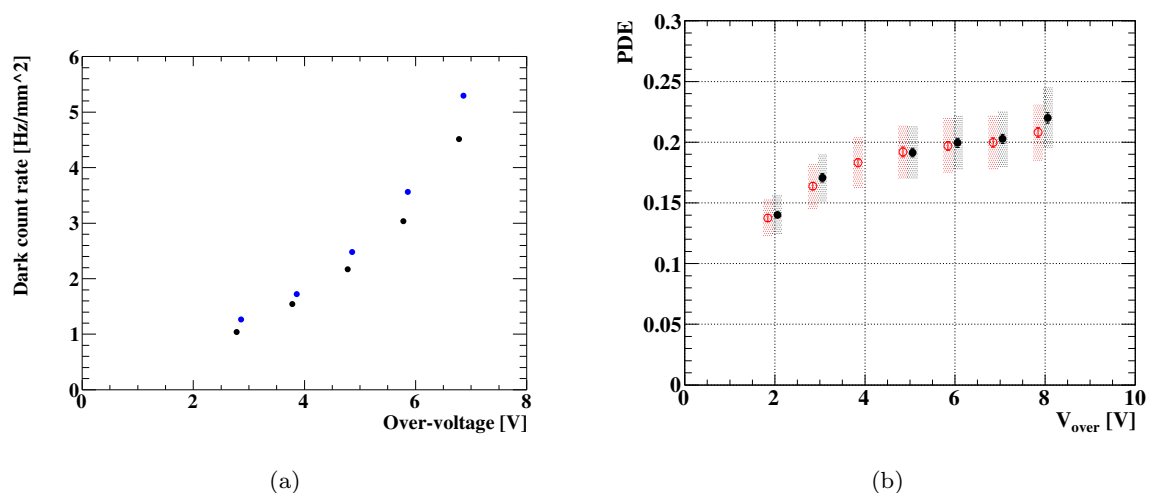
Figure 2.9   (a) Dark count rate per $1\,\mathrm{mm}^2$ at LXe temperature. Different colors correspond to different MPPCs [29]. (b) PDE for xenon scintillation light as a function of the over voltage. The PDEs for two MPPCs are shown [29].

energy resolution can deteriorated if the ENF is too large. The statistical fluctuation of the MPPC signals for the 52.8 MeV γ-ray is expected to be only 0.2%. Therefore, the contribution to the energy resolution from the ENF of the MPPCs is small enough to achieve the 1% of energy resolution if the ENF is smaller than 10.

The correlated noise is one process which can contribute to the ENF. Since the correlated noise is a stochastic process, it will add some fluctuation to the measured charge. In a model of the correlated noise often used, distribution of the number of the photoelectrons becomes a generalized Poisson distribution [32]. In this model, the ENF caused by the correlated noise becomes $1 + p + 3p^2/2 + O(p^3)$, where p is the correlated noise probability. The ENF does not become as large as 10 under the normal operation condition.

In order to check other unexpected contributions to the ENF, the resolution for the visible light was measured from the relative spread of the charge distribution from LED light. This measurement was performed at different LED intensities. The MPPC was operated at the over voltage of 1.5 V to suppress the effect of the correlated noise.

Fig. 2.10(a) shows the measured resolution as a function of the total detected number of photoelectrons N_{phe}. It is confirmed that the resolution goes down to 1% according to the statistical relation that the resolution is inversely proportional to the square root of N_{phe}. The smaller ENF observed at larger photoelectrons is probably due to an underestimation of the number of photoelectrons by the saturation of the MPPC. The ENF for the visible light is measured to be 1.4–1.7 including the contribution from the ECF.

The resolution for VUV light is also measured to study a wavelength dependence. Due to a higher energy of the VUV photons than the visible light, a single VUV photon may generate multiple photoelectrons. This process is reported for a VUV-PMT [33], and can also occur at VUV-MPPC. If a single photon generates multiple photoelectrons, a real bottleneck of the

(a)   (b)
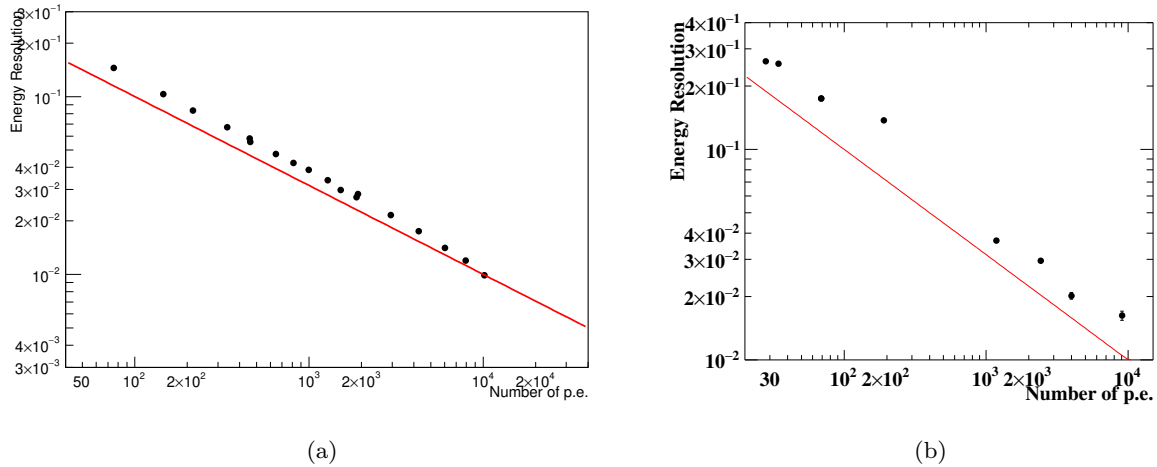
Figure 2.10   Relative energy resolution for xenon scintillation light as a function of total number of photoelectron [29]. (a) For visible light. (b) For VUV light. Red line shows the statistical fluctuation of $1/\sqrt{N_{\mathrm{phe}}}$.

statistical fluctuation can become smaller, and the statistical fluctuation can be larger than the expectation from the apparent photoelectron statistics.

The energy resolution for the VUV light cannot be directly evaluated from a spread of the charge in alpha events due to the 4% spread of the alpha energy. Instead, an even-odd analysis is adopted. The same alpha events are measured by MPPCs A and B, and the spread of $N_{\mathrm{pheA}} - N_{\mathrm{pheB}}$ is measured as an energy resolution at a photoelectron statistics of $N_{\mathrm{pheA}} + N_{\mathrm{pheB}}$. With this method, a contribution from the event-by-event fluctuation of the alpha energy can be cancelled out, while a stochastic process on each MPPC remains. This measurement was performed at over voltage of $1.5\,\mathrm{V}$, which is the same as the measurement for the visible light. Several geometrical setups were used to change the distance from the alpha source to the MPPCs. Fig. 2.10(b) shows the resolution as a function of the number of photoelectrons. Similar to the visible light, the resolution of VUV light also follows the statistical relation. A rather larger ENF than the visible light may indicate the effect mentioned above.

Mass test of prototype MPPCs

The basic characteristics of the 600 prototype MPPCs were measured in the large chamber. Except for 24 MPPCs (i.e. 4% of all), normal characteristics are confirmed for all MPPCs. For most of the bad channels, technical issues on the signal readout chain was found and fixed in the final detector.

Angular dependence of PDE

The angular dependence of the PDE for LXe scintillation light was measured in the large chamber test. Fig. 2.11 shows measured PDE as a function of the incident angle. The measured PDE decreases faster than the theoretical expectation of the reflection calculated from the refractive index. The reason for this dependence is not yet identified, but this may be caused by
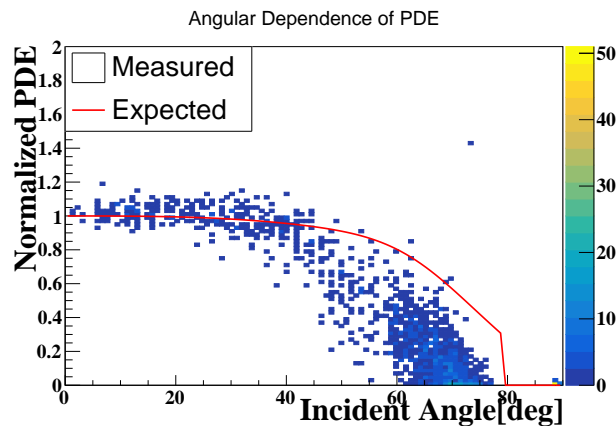
Figure 2.11   VUV PDE measured in the large chamber test as a function of the incident angle from alpha sources to each MPPC. The red line shows expectation from Fresnel reflection at the sensor surface [34].

some insensitive layer which can be effectively thicker for photons with larger incident angles. A crosscheck of this dependence is performed in the LXe detector (Section 6.2), and the effect on the γ-ray reconstruction will be discussed in Section 7.3.

2.2   Test of all VUV-MPPCs

After the development of the VUV-MPPC, a production of 4200 MPPCs including about 100 spares was performed by HPK, and completed by Oct 2016. They were delivered in four batches called lot A, B, C, and D in this thesis.

To identify bad MPPCs, I-V curves of all MPPC chips at over voltage of $-3\,\text{V}$ to $+7\,\text{V}$ were measured at room temperature. In total, the I-V curves of 16800 chips were measured.

Fig. 2.12(a) shows a typical I-V curves of four chips on a normal MPPC. The I-V curves are fitted by a quadratic function smoothly connected to a linear function below the breakdown. The breakdown voltage V_{bd} is estimated from the fitted transition point, and compared to the operation voltage V_{hama} recommended by HPK. It is found that V_{hama} corresponds to the over voltage of $4.9\,\text{V}$ as shown in Fig. 2.12(b). The estimation of the breakdown voltage works correctly for most of the MPPCs except for bad chips mentioned below.

Three types of bad chips are found in this I-V curve measurement. The first one is a "current offset chip" which has significantly large current below the breakdown. Current of the normal chips below the breakdown is typically a few tens of nanoampere. Chips whose current is $100\,\text{nA}$ larger than the other three chips on the same MPPC package are identified as bad chips. The second one is a "strange I-V chip" which has a strange shape of I-V curve. The third one is a "large current chip" whose current is much larger than that measured by HPK. In total, 31 bad chips (0.2% of all chips) were identified in this measurement, and removed from the detector construction.

Some of these bad chips were tested in the LXe. Fig. 2.13 shows the measured gain and PDE. No difference was found between the normal chips and the bad chips. Therefore, they can

(a) (b)
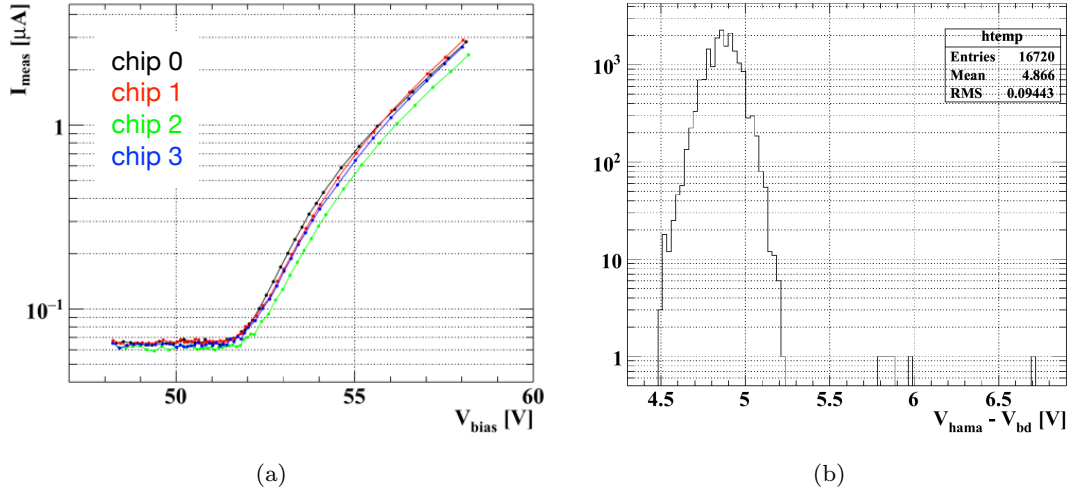
Figure 2.12 (a) Typical I-V curves measured for four chips in an MPPC package. (b) Difference of V_{hama} and V_{bd}.

(a) (b)
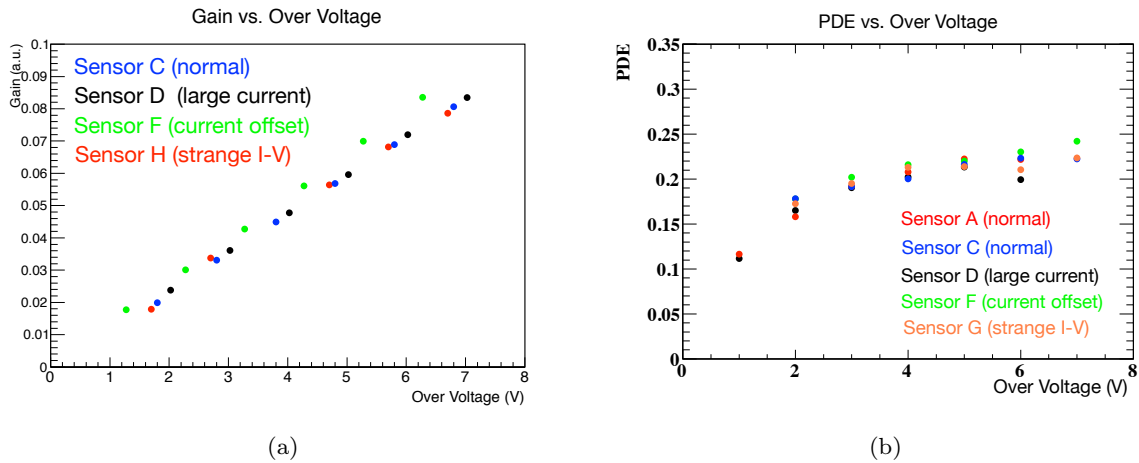
Figure 2.13 Performance of bad MPPCs in the LXe. (a) Gain, (b) PDE.

probably be used in the detector, but are not used because we have sufficient number of normal MPPCs.

The waveform of each MPPC whose four chips are connected in series for the pulsed LED light was also measured. Fig. 2.14 shows the pulse decay time of each MPPC. A production lot dependence probably due to different after pulse probabilities is observed. This lot dependence is also measured in the LXe detector (Section 6.1.1), and is corrected in the reconstruction of the γ-rays.

2.3 Selection of PMTs

In the upgrade of the LXe detector, PMTs on the entrance face is replaced with MPPCs, and the number of PMT is reduced from 846 to 668. These surplus PMTs are utilized to replace problematic PMTs in MEG, such as dead PMTs or PMTs with strange gain evolution during
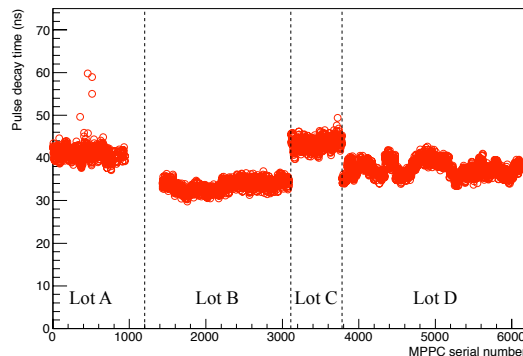
Figure 2.14   Pulse decay time of each MPPC as a function of serial number [29].

the MEG beam time.

The PMTs which cannot keep operating in the whole MEG II experiment are also replaced. As is mentioned in Section 1.6.2, a gradual degradation of the PMT gain was observed in MEG, and the applied high voltage was increased from time to time, in order to keep a reasonable gain ($> 1 \times 10^6$) for detector operation. On the other hand, the applied voltage must be lower than $1400\,\mathrm{V}$ since larger voltage will increase a risk of a high voltage trip at the cables and connectors. This sets a lifetime of PMT. The expected lifetime of each PMT is calculated from the gain degradation speed observed in MEG, assuming that the gain degradation is proportional to the beam intensity. Only the PMTs whose lifetimes are longer than three years are used.

Table 2.1 summarizes types of replaced PMTs. In total, 63 PMTs are replaced.

Table 2.1   List of replaced bad PMTs

Type	number of PMT
Dead	15
Low QE	2
Strange gain evolution	29
Strange QE history	6
Lifetime too short for MEG II	20
Sum (including overlaps)	63

(a)   (b)
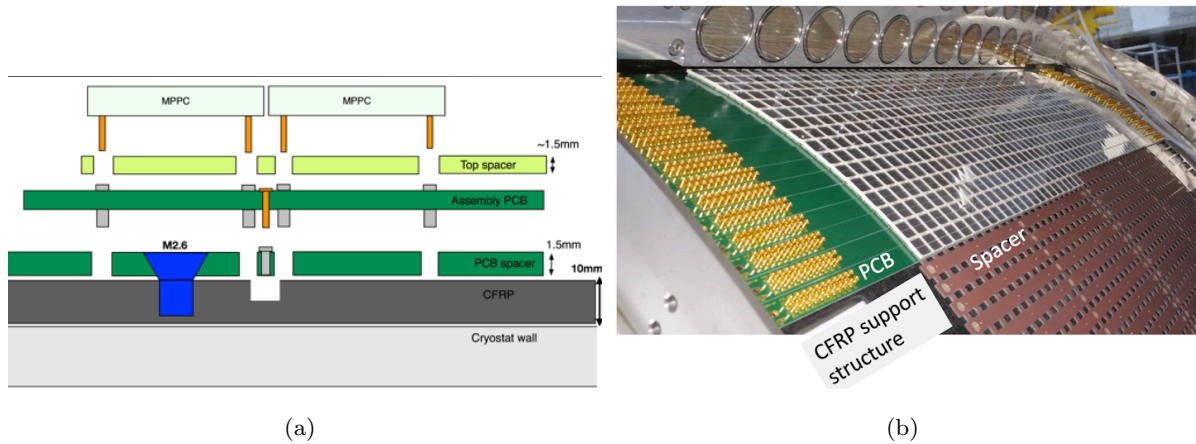
Figure 2.15   MPPC support structure.

2.4   Photosensor installation

MPPC support structure

To install the MPPCs into the detector, a support structure has been prepared which satisfies several requirements:

- The MPPCs have to be aligned within 0.5 mm precision.
- Its material budget has to be minimized since signal γ-ray goes through it.
- It has to be able to be placed inside the LXe, and should not contaminate the LXe.

Fig. 2.15 shows the support structure for MPPC. The MPPCs are aligned on a PCB, which is fixed on a structure made of Carbon Fiber Reinforced Plastic (CFRP). Considering the thermal contraction at LXe temperature, the temperature coefficient of the CFRP is adjusted to be consistent with that of the PCB. This CFRP structure is fixed on the cryostat. A spacer made of FR4 is inserted in the gap between the MPPC and the PCB to prevent the LXe from filling the gap. Since the CFRP is conductive, another spacer is inserted between the PCB and the CFRP.

The material budget of photosensors and the support structure is shown in Fig. 2.16 and Table 2.2. The radiation length is reduced from $0.183X_0$ to $0.029X_0$, leading to an improvement in the γ-ray detection efficiency by a factor of 1.13.

Twenty two MPPCs are placed on the PCB as shown in Fig. 2.17, and two PCBs are placed in a row. In total, 93 rows (i.e. $93 \times 22 \times 2 = 4092$ MPPCs) are installed in the detector. In the detector construction, the MPPCs are mounted on the PCBs in lab, and each PCB is fixed to the CFRP frame which was fixed to the cryostat beforehand.

Signal readout chain

The MPPC signals are read out through this PCB. A coaxial-like structure is implemented in this PCB as shown in Fig. 2.18(a). Each signal layer is shielded by ground layers, and
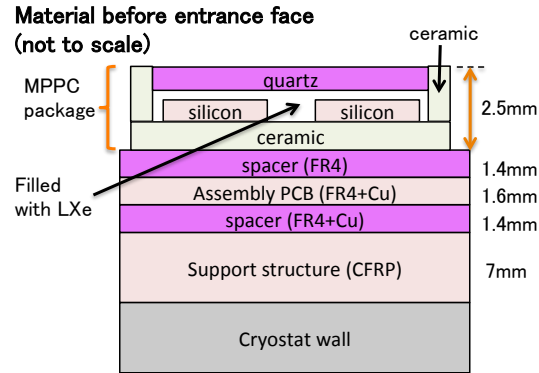
Figure 2.16   Material of the γ entrance window

Table 2.2   Material budget of the γ entrance window of the LXe detector. (left) MEG, (right) MEG II.

	Radiation thickness X_0		Radiation thickness X_0
Outer cryostat wall	0.040	Outer cryostat wall	0.040
Honeycomb (Section 1.6.2)	0.018	Honeycomb (Section 1.6.2)	0.018
Inner cryostat wall	0.023	Inner cryostat wall	0.023
Peek support or PMT	0.183	CFRP frame	0.003
Total	0.264	PCB & Spacer	0.006
		MPPC	0.020
		Total	0.110
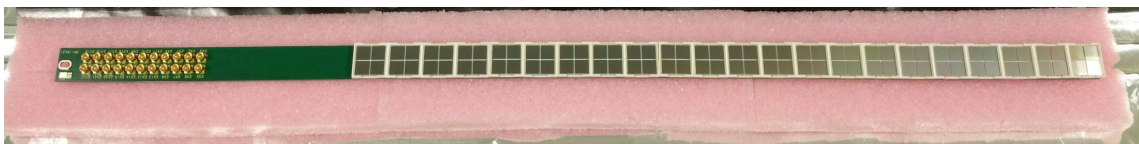
Figure 2.17   PCB used to align the MPPCs.

the characteristic impedance is adjusted to $50\,\Omega$ to avoid a reflection at the interface. The signal transmission line of each channel is designed to have the same length and thus the same propagation time.

The four MPPC chips on each sensor are connected in series by a circuit implemented on the PCB shown in Fig. 2.18(b). Fig. 2.19 shows the schematic of the circuit. In this so-called "hybrid connection", the four chips are connected in series, but with a decoupling capacitor in between, in order to connect signals in series with applying bias voltage in parallel. This method has an advantage that the needed high voltage becomes smaller than that with a simple series connection. This removes a possibility of sparks between adjacent MPPC chips placed with a spacing of $0.5\,\mathrm{mm}$ since a common voltage is applied on each MPPC chip.

Fig. 2.20(a) shows a concept of the signal transmission of this detector. The signals from the

<div align="center">(a)   (b)</div>
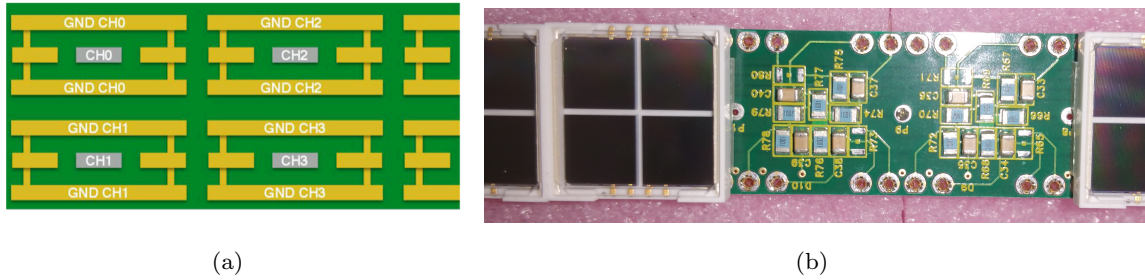
Figure 2.18   (a) Cross section of the PCB [7]. A coaxial like structure is implemented. (b) Circuit implemented on PCB to connect MPPC chips in series.
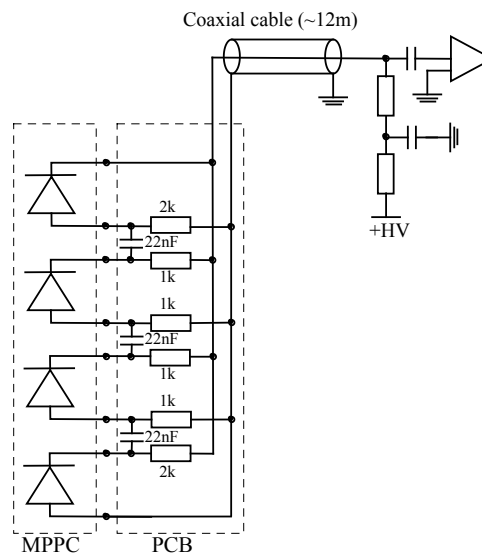
Figure 2.19   Hybrid connection [29].

PCB are transmitted by coaxial cables from the cable connectors implemented on the edge. The signals are transmitted to outside the cryostat through a custom PCB-based feedthrough shown in Fig. 2.20(b). This feedthrough is made of a DN160CF flange, and six PCBs are glued on it. The coaxial cables are directly soldered on the PCBs at the both sides. The coaxial structure (Fig. 2.18(a)) is also implemented on this PCB. Each flange accommodates 432 signal channels, and twelve feedthroughs are installed on the chimney of the detector. The cable length from the photosensor to the feedthrough is different depending on the sensor position in the detector as shown in Fig. 2.21, to deal with the limited volume of the inner vessel of the cryostat. A patch panel is installed on the detector where we can select the channels to be connected to the readout electronics. After the patch panel, sixteen cables that goes to a WDB are bundled. Fig. 2.22 shows the grouping scheme. This unit is also used for the online reconstruction for the trigger generation (Section 1.8). For example, a γ-ray direction and timing are reconstructed from the group of the sixteen MPPCs which has the largest signal amplitude. For this purpose, channels read out by the same WDB are designed to have the same cable length.

(a)   (b)

Figure 2.20   (a) Concept of signal transmission. (b) Feedthrough for the photosensor signal cables.
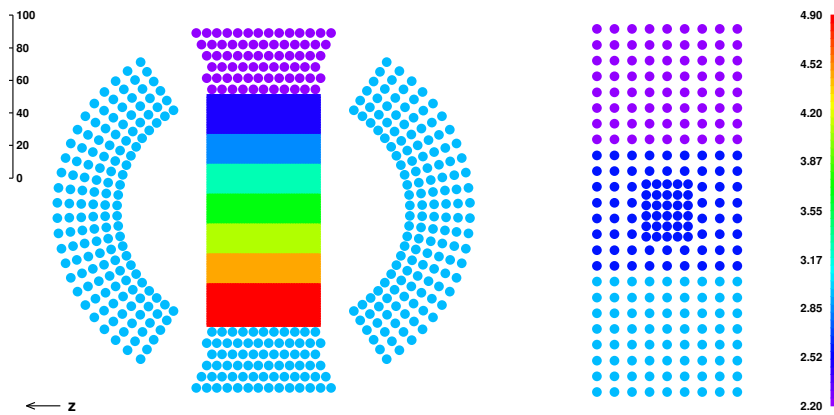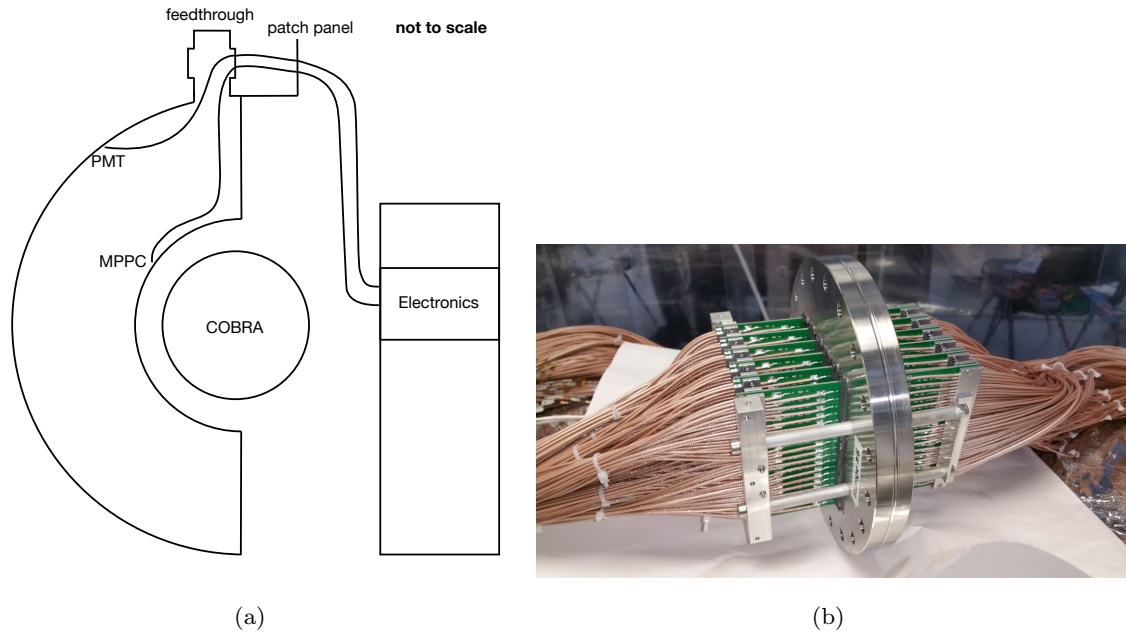
Figure 2.21   Map of signal cable length inside detector.
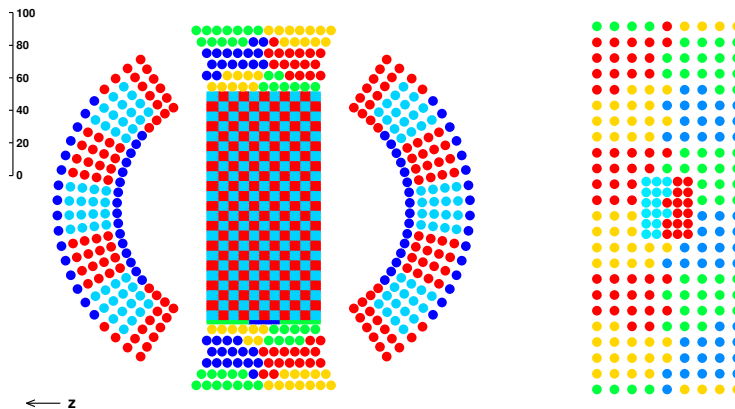
Figure 2.22   Assignment of photosensors to the WDBs. Each group of connected sixteen channels with the same color is read out by the same WDB.
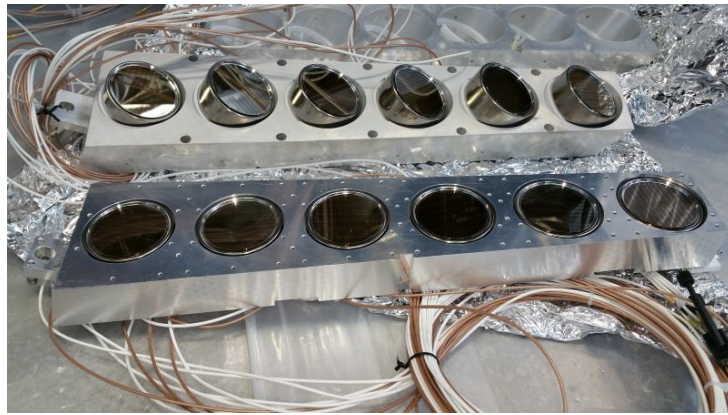
Figure 2.23   Lateral PMT holder (top) in MEG, and (bottom) in MEG II.
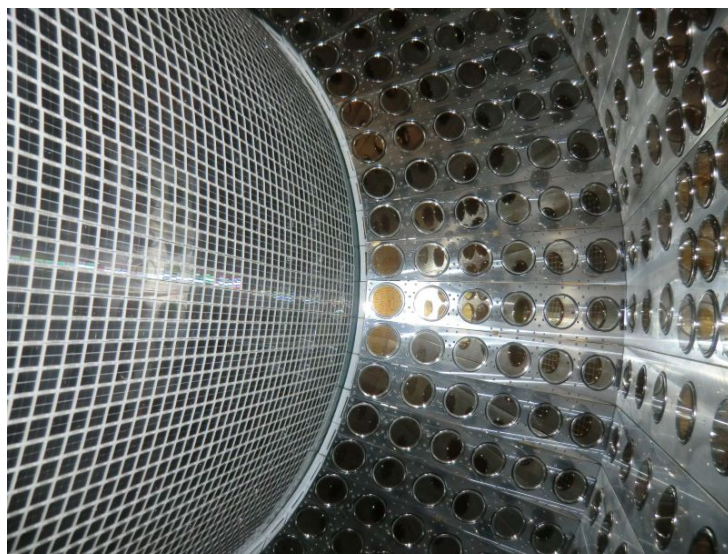
Figure 2.24   Inside of the constructed LXe detector. View from the upstream face.

PMT support structure

Support structures for the PMTs on the lateral face are modified from MEG as explained in Section 1.6.3. On the lateral PMT holder in MEG, PMT's entrance face is not on the holder surface plane. On the MEG II holder, it is designed to be on the holder surface as shown in Fig. 2.23. To cope with the reduced thickness and radius of the inner face, position of lateral PMTs are shifted shallower in radial direction from MEG, to achieve a uniform scintilation readout for the shallow events. A piece of Teflon is attached at the inner edge of these holders to fill the gap between the entrance face and to keep the scintillation light inside the detector wall.

Fig. 2.24 shows the constructed detector.

2.5   Calibration sources

Table 2.3 shows the calibration sources prepared for the MEG II LXe detector. Many of them are updated from MEG to calibrate the MPPCs and to measure the improved detector resolutions.

Table 2.3   Calibration tools of the LXe detector for MEG II experiment. (from [7]. Updated by the author)

Process		Energy
Charge exchange by pion beam	$\pi^- p \to \pi^0 n$	$55, 83\,\mathrm{MeV}$ photons
	$\pi^0 \to \gamma\gamma$	
Proton accelerator	$^7\mathrm{Li}(p,\gamma)^8\mathrm{Be}$	$14.8, 17.6\,\mathrm{MeV}$ photons
	$^{11}\mathrm{B}(p,\gamma)^{12}\mathrm{C}$	$4.4, 11.6, 16.1\,\mathrm{MeV}$ photons
Neutron generator	$^{58}\mathrm{Ni}(n,\gamma)^{59}\mathrm{Ni}$	$9\,\mathrm{MeV}$ photons
Radioactive source	$^{241}\mathrm{Am}(\alpha,\gamma)^{237}\mathrm{Np}$	$5.5\,\mathrm{MeV}$ αs
Radioactive source	$^9\mathrm{Be}(\alpha_{241\mathrm{Am}},n)^{12}\mathrm{C}^\star$	$4.4\,\mathrm{MeV}$ photons
	$^{12}\mathrm{C}^\star(\gamma)^{12}\mathrm{C}$	
LED		blue-UV region

LED

Blue LEDs are installed for the photosensor calibration. Fig. 2.25 shows a location of the LED installed in the detector. LEDs on the lateral face (Toyoda Gosei E1L49–3B1A–02. [35]) are reused from MEG, and used for a gain calibration of the PMTs (Fig. 2.26(a)). LEDs (Kingbright KA-3021QBS-D. $\lambda = 460\,\mathrm{nm}$ [36]) on the outer face are newly installed for MEG II to illuminate the MPPCs with a uniform light distribution (Fig. 2.26(b)). These LEDs are covered by a Teflon sheet to diffuse the light. Another purpose of this Teflon cover is to attenuate the light intensity and to operate LEDs at higher voltage, so that we can suppress an instability of the light intensity from the lower applied voltage. LEDs are flashed by a pulse signal. A LED pulser is reused from MEG for the reused LEDs, and a function generator is used for newly introduced LEDs. These are controlled by a slow control system integrated to the DAQ system (Section 1.8).

Alpha source

Alpha sources are installed as point sources of the xenon scintillation light for a photosensor calibration. It is based on the same technology as the one used in MEG [37]. Five $100\,\mu\mathrm{m}$ tungsten wires are stretched between the upstream and the downstream faces. On each wire five alpha sources ($^{241}\mathrm{Am}$) are crimped at $12.4\,\mathrm{cm}$ intervals (Fig. 2.27). Since the activity of each alpha source is $200\,\mathrm{Bq}$ at most, these sources do not affect the γ-ray data-taking near the signal energy. The installed positions are shown in Fig. 2.28.
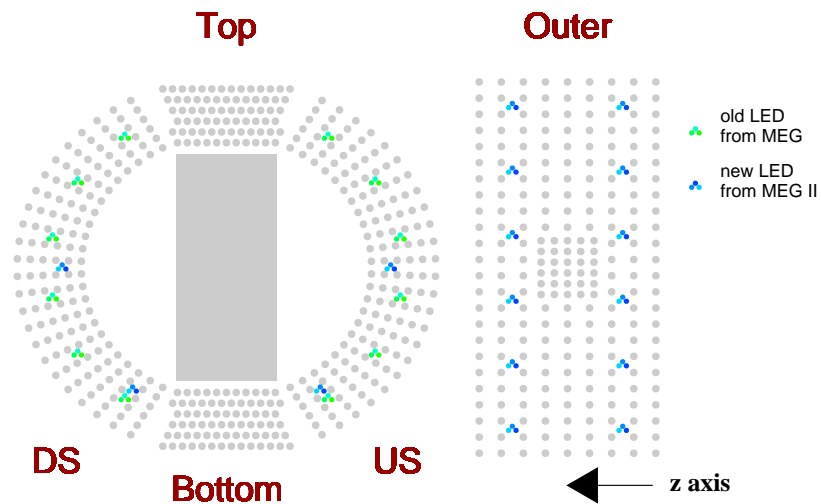
Figure 2.25   Installed position of the LEDs [34]

(a)   (b)

Figure 2.26   LEDs for photosensor calibration [34]. (a) LEDs on the lateral face. (b) LEDs on the outer face.

Figure 2.27   Alpha source crimped on a wire

17.6 MeV γ excited by proton beam

A dedicated 1 MeV Cockcroft-Walton (CW) proton accelerator is placed at the downstream side of the $\pi E5$ beam line (Fig. 2.29). Accelerated protons are injected into the crystal disk made of $Li_2B_4O_7$ placed on the center of COBRA [38]. Gamma-rays both from the lithium excitation $^7Li(p,\gamma)^8Be$ at $E_p = 440$ keV, and the boron excitation $^{11}B(p,\gamma)^{12}C$ at $E_p = 163$ keV can be utilized.

In this thesis, 17.6 MeV γ from lithium excitation (often called CW-Li) is mainly used, due to its large cross section. Its energy spread is only 12 keV, and it is also good for energy resolution
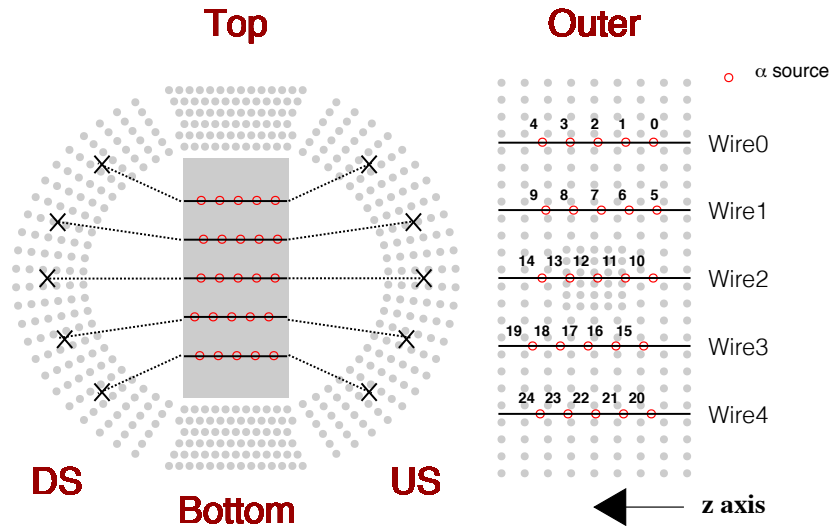
Figure 2.28   Installed position of the alpha sources [34]
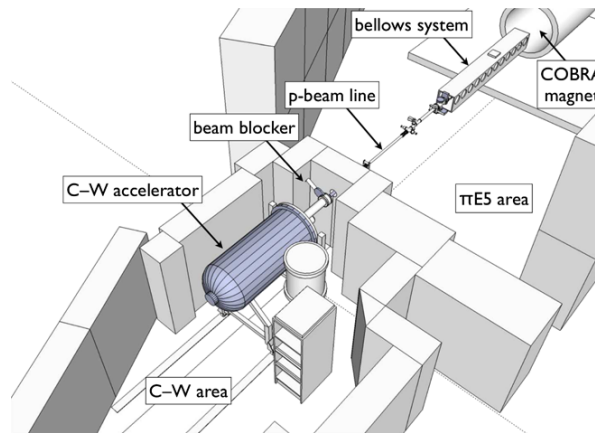
Figure 2.29   CW proton accelerator at the downstream side of the $\pi E5$ beam line [39].

measurement. Another peak of CW-Li at 14.8 MeV is not used due to the large decay width and the overlap with a lower energy tail of the 17.6 MeV peak.

Coincident γ-rays of 11.7 MeV and 4.4 MeV emitted from the boron excitation can be utilized for timing alignment of the LXe detector and the positron timing counter in the future.

55 MeV γ from CEX

Another important calibration source is quasi-monochromatic γ-rays from the charge exchange (CEX) reaction of the π^- captured in a hydrogen target (Fig. 2.30). A negative pion beam is injected into the liquid hydrogen target, and two coincident γ-rays are emitted from $\pi^- p \rightarrow \pi^0 n, \pi^0 \rightarrow \gamma\gamma$. Since the energies of two γ-rays are correlated with their opening angle, nearly monochromatic γ-rays of 55 and 83 MeV can be obtained by selecting two γ-rays emitted back-to-back. If the events with opening angle above $175°$ are selected, the energy spread becomes only 0.2%, which is sufficient to measure the energy resolution of 1%. One of the γ-rays is measured by a reference counter composed of a timing counter and a calorimeter, and the other
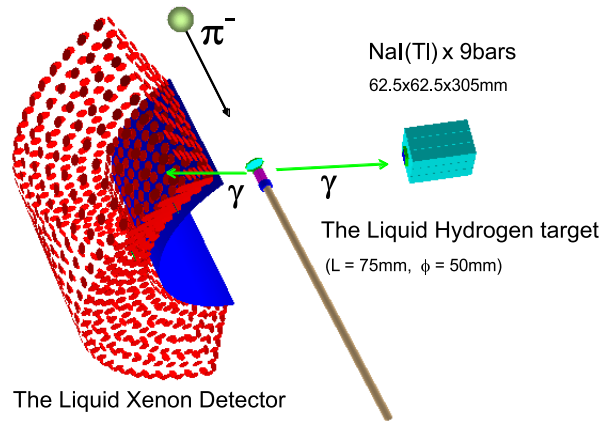
Figure 2.30   Overview of the CEX measurement [43]. The reference counter of NaI was upgraded to that of BGO during the MEG experiment.

is used for detector calibration. The calorimeter consists of 4×4 BGO crystals ($46 \times 46 \times 200\,\text{mm}^3$ each). The size of each crystal is small enough to select γ-rays emitted back-to-back.

The timing resolution of the LXe detector can also be measured with the CEX events by using the reference timing counter which consists of plastic scintillators placed behind a lead converter. The plastic scintillator counter used as the time reference is upgraded to cope with the improved timing resolution in MEG II. In MEG, signals from the scintillator were read out by the PMTs, and its timing resolution was 81 ps. For MEG II, a plastic scintillator read out by SiPMs is adopted [40][41], which is based on the technology developed for the MEG II positron timing counter [42]. Two scintillator plates (EJ-230, $80 \times 175 \times 5\,\text{mm}^3$) read out by 16 MPPCs (S13360-3050PE) on each side are placed in front of the BGO crystals. The timing resolution of this counter is measured to be 49 ps.

2.6   Alignment of MPPCs

In order to achieve a hit position resolution of 2 mm, positions of the installed MPPCs have to be measured at a precision of 0.5 mm. For this purpose, two independent measurements were performed.

Measurement by laser scanner

The surfaces of all the installed MPPCs were surveyed by a three-dimensional laser scanner (FARO Edge ScanArm) during the detector construction (Fig. 2.31(a)). An example of surveyed MPPC surface is shown in Fig. 2.31(b). The gap between four chips on each MPPC package is fitted to reconstruct the position and the normal vector of each MPPC. Due to the limited space of the cryostat between inner and outer faces, and the available reach of the scanner arm, sufficient data quality like in Fig. 2.31(b) was achieved only for a part of the MPPCs. Positions of about 10% of MPPCs are reconstructed, and the others are interpolated by the reconstructed ones.

(a)   (b)
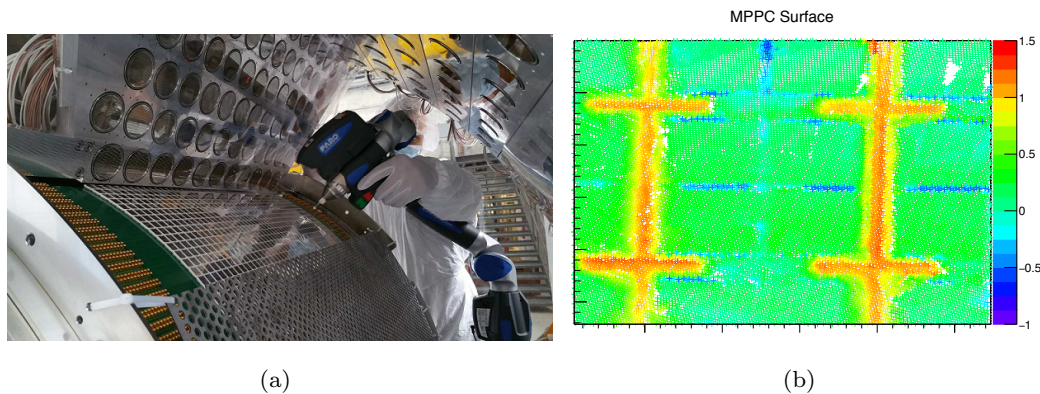
Figure 2.31   (a) MPPC position measurement by a laser scanner [44]. (b) Example of measured MPPC surface by laser scanner [34]. Color shows the coordinate of perpendicular direction. The red region corresponds to the ceramic package of each MPPC, and the blue region corresponds to the gap between four chips on a package (Fig. 2.1).

Measurement by collimated γ-rays

Since the position of MPPCs are affected by the thermal contraction at the LXe temperature, a complementary measurement was performed after the start of the detector operation. Gamma-rays of $120\,\mathrm{keV}$ from ^{57}Co were injected into the detector, which interact with the LXe within $3\,\mathrm{mm}$. A compact source with a brass collimator was used for the generation of the γ-ray beam (Fig. 2.32(a)). The beam size on the MPPC surface is $1.5 \times 40\,\mathrm{mm}^2$. To scan the inner face of the LXe detector, the position and the direction of the γ-ray beam can be changed by motion stages for the z and ϕ direction. Its movement is monitored by an optical laser attached on the stage projected at a quadrant photodiode, and a bubble level [44]. The accuracy of the beam alignment is $30\,\mu\mathrm{m}$ in z, and $80\,\mu\mathrm{m}$ in ϕ.

Fig. 2.32(b) shows the event rate on an MPPC as a function of beam position. Since the scintillation light is localized thanks to a short attenuation length of low energy γ-ray in LXe, an excess of the event rate is observed when it hits above the MPPC, and the MPPC position can be reconstructed.

Combined analysis

A three-dimensional position of each MPPC in the LXe is obtained by combining these two measurements. The laser scanner measurement can give us a three-dimensional position of MPPCs at room temperature, while it is affected by the thermal contraction. The measurement by the γ-ray gives us the MPPC positions at LXe temperature, while only the two-dimensional (u-v) position can be reconstructed.

The reconstructed position in γ-ray measurement is fitted by the measured position by the laser scanner $\vec{x}_{\mathrm{laser}}$ with a transformation (Euler rotation: $R(\alpha, \beta, \gamma)$, offset: $\vec{c}_{\mathrm{offset}}$) and a thermal contraction a defined as follows:

$$\vec{x'}_{\mathrm{laser}} = (1 - a)R(\alpha, \beta, \gamma)\vec{x}_{\mathrm{laser}} + \vec{c}_{\mathrm{offset}}.$$
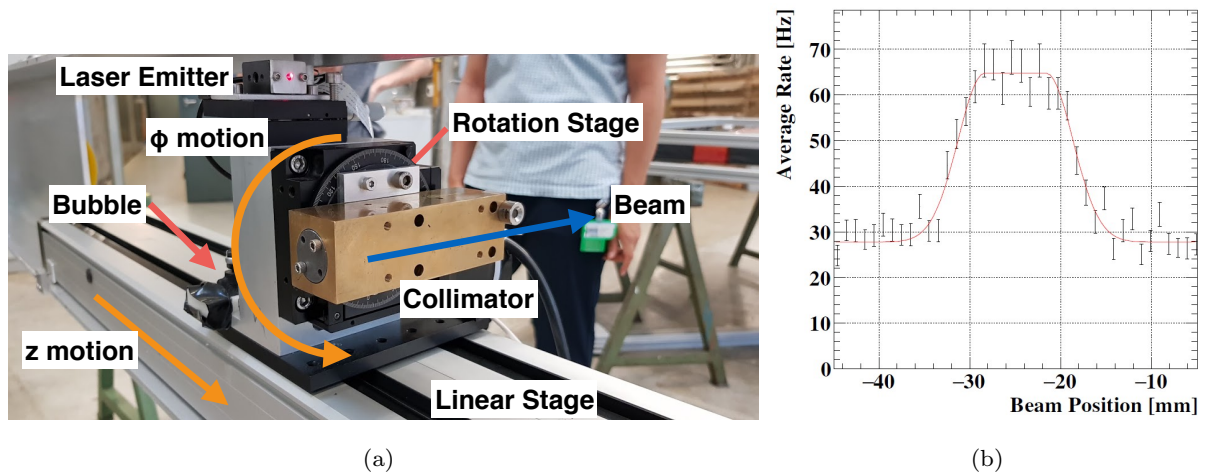
Figure 2.32   (a) The collimated γ-ray source used for MPPC alignment [34]. (b) The γ-ray event rate of an MPPC as a function of z position of the beam [44].

The fitted thermal contraction rate is found to be consistent with that of the detector material (16 ppm/K). The fitted laser positions and the γ-ray positions are in agreement within an accuracy of 300 μm, which fulfills the requirement of 500 μm.

2.7   Xenon control system

To operate the LXe detector safely and stably, the pressure and the temperature of the liquid xenon have to be well controlled. For this purpose, the xenon control system is upgraded from MEG[*1]. It consists of the detector cryostat, refrigerators, storage tanks, and purifiers. A 200 W pulse-tube refrigerator [45] placed at the top of the detector is reused from MEG. A new 400 W Gifford-McMahon (GM) refrigerator [46] is introduced in MEG II, which is placed on an independent platform to avoid a possible noise. This is to compensate the heat income from the increased number of cables. A 1000 ℓ Dewar (often called "1000 ℓ storage tank") with a pulse-tube refrigerator is used to safely store the LXe when the detector is not operated. Since it is thermally-insulated and is tolerate up to 6 bar, it can store the LXe for 100 hours even without a cooling power. The xenon control system is equipped with two purification systems: a purification in the gaseous phase by a metal-heated getter, and that in the liquid phase by a molecular sieves. The gaseous circulation for the gaseous phase purification was continued when the detector is operating. This is also useful to efficiently transfer the cooling power from the GM refrigerator to the detector.

The temperature of the MEG II LXe detector is controlled with a precision of 0.1 K by a PID control of the xenon pressure and temperature. The breakdown voltage of the MPPCs is known to have a temperature coefficient of 55 mV/K [47]. The fluctuation of the breakdown voltage due to the temperature instability of 0.1 K is expected to be only 0.1% if operated at 7 V over

---

[*1] see [21][39] for MEG's system
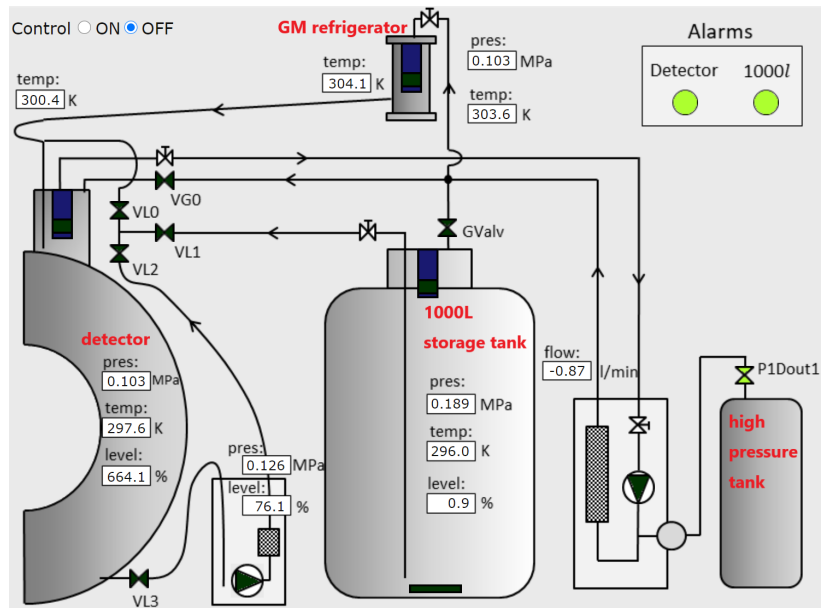
Figure 2.33   Xenon control system in MEG II

voltage. This is sufficiently smaller than the goal of energy resolution of about 1%.

Chapter 3

Pilot run

This chapter summarizes a series of pilot runs performed under the high intensity muon beam to evaluate the performance of the LXe detector.

After the construction of the LXe detector was finished in April 2017, the detector was installed in the MEG experimental area, and the commissioning was started. Fig. 3.1 shows an overview of the commissioning timeline. We had three beam time periods near the end of each year. To be ready for each beam time period, detector operation was started from each summer, and the photosensor calibration and the LXe purification were performed[*1].

3.1 Pilot runs

3.1.1 Pilot run 2017

The purpose of the run 2017 was to try taking some γ-ray data. Similar to the MEG II physics data-taking, a muon beam was stopped on the target located at the center of the MEG II detector, and γ-rays near the signal energy from the Standard Model muon decays were measured. These γ-rays are often called "background γ-rays" since they will be background
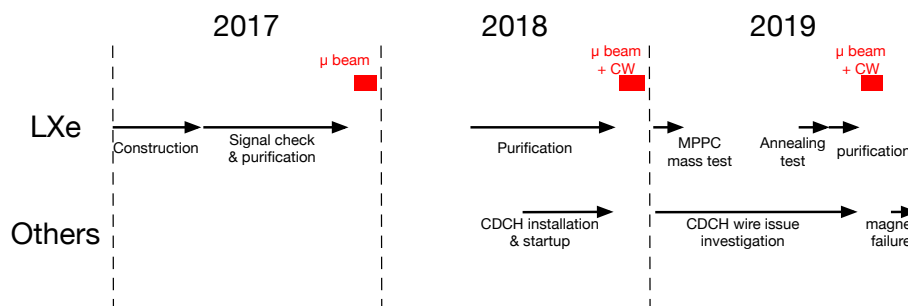
Figure 3.1   Timeline of LXe detector commissioning.

[*1] Since there is an annual power cutoff, and the maintenance of the ground water at PSI at the beginning of January, we cannot keep LXe inside the detector in that period. This is why we cannot keep the detector operating.

events in the search of $\mu \to e\gamma$ decay. The muon beam intensity was adjusted to be lower than MEG II ($3.2 \times 10^7 \, \mu/\text{s}$) to keep the induced current on the RDC in the dynamic range of the readout. This dynamic range has been extended since the run 2018, and thus this limitation is only for 2017 data.

3.1.2   Pilot run 2018

In the pilot run 2018, a series of measurements to evaluate the detector resolution was performed. The 17.6 MeV γ-rays from the CW-Li were measured to estimate the energy resolution. The CW-Li data with placing a lead collimator in front of the detector was also obtained to estimate the position resolution. The background γ-rays were also taken at a reduced beam intensity ($0.7 \times 10^7 \, \mu/\text{s}$) and a MEG II beam intensity ($7 \times 10^7 \, \mu/\text{s}$) for a study on the background γ-ray spectrum and the pileup elimination performance. On the other hand, a data-taking of 55 MeV γ-ray data from the CEX run was cancelled due to the delay of the installation of the drift chamber.

Even though we were able to take data, the 2018 run was not a stable beam time. The major reason was that this beam time was shared by several MEG II detectors, and the beam intensity and DAQ configuration were often switched. Another reason was an instability on the BTS magnet due to an instability of the liquid helium supply from the PSI.

3.1.3   Pilot run 2019

An unexpected degradation of the MPPC sensitivity to the VUV light by a beam radiation was suggested from the run 2018 data, but it was difficult to get a conclusive result due to the instability of the 2018 run. Since this degradation is too rapid and could be a crucial issue for the MEG II experiment, a dedicated data-taking period to confirm this degradation was assigned for the LXe detector in 2019. The detector was operated under the MEG II intensity muon beam, and the photosensor performance was often measured to monitor its degradation.

It is found that the muon beam intensity seems to be 10–20% higher than expected likely due to a problem on the beam blocker during a beam intensity measurement. This will be discussed in Section 9.3.5.

Another purpose of the 2019 run was to measure 55 MeV γ from the CEX reaction. However, it was cancelled again because the BTS magnet was broken by an accident.

3.2   DAQ system

3.2.1   Prototype of WaveDREAM system

As mentioned in Section 1.8, a DAQ system called WaveDREAM is being developed for the MEG II experiment. Since the full DAQ system was not yet available due to the delay of the development, a prototype system of WaveDREAM was used for the data acquisition in those

pilot runs [27].

Compared to the full system, there are two major limitations on the prototype system. The first is the number of readout channels. This prototype system has only 96 WDBs which have to be shared between several detectors for MEG II in the pilot runs. The second is the DAQ rate. The DAQ rate of the current system is limitted by the 1 Gbps ethernet connection used for the data transfer from each WDB to the DAQ computer. The limitation was especially obvious in the run 2017 and 2018. Thanks to an upgrade of the DAQ computer and an improvement in the frontend software, a reasonable DAQ rate was achieved in the 2019 run. This improved the statistical precision of the sensor calibration. Table 3.1 summarizes the number of readout channels and the DAQ rate for each year [*2].

Table 3.1   Number of readout channels, and DAQ rate for each year.

Year	number of MPPC channel	number of PMT channel	Typical DAQ rate (γ-ray data)
2017	704	192	$\sim 3\,\mathrm{Hz}$
2018	640	378	$\sim 3\,\mathrm{Hz}$
2019	640	378	$10 - 25\,\mathrm{Hz}$

Due to the limitted number of readout channels, only a quarter of the detector was read out. Fig. 3.2 shows the channel assignment for run 2017, and 2018/2019. These channel assignments were decided for the following reasons. To reconstruct the γ hit position, the charge distribution on the MPPCs near the γ conversion point has to be measured. The information from these MPPCs is also important for the timing reconstruction, since they have a large signal amplitude. For this purpose, 640 adjacent MPPCs are read out. Only the events hitting the central part of the readout area are selected in the offline analysis to be used for the performance estimation. Additionally, for energy reconstruction based on the total detected number of photons, it is important to read out the PMTs which cover the whole detector in order to achieve a reasonable uniformity of reconstructed energy. This is also useful to identify the pileup γ-rays whose hit position is far from the MPPC readout region, while its tail of the light distribution can still be observed in the readout MPPC[*3]. Therefore, widely distributed PMTs are also read out.

The waveforms of all the readout photosensors are digitized at a given sampling frequency by the DRS4 chips on each WDB. In the DAQ of the pilot runs, the sampling frequency was set to $1.2\,\mathrm{GHz}$, instead of 1.4–$1.6\,\mathrm{GHz}$ planned in the physics data-taking. This is because the trigger latency is about $680\,\mathrm{ns}$ in the prototype system, and $853\,\mathrm{ns}$ ($= 1024\,\mathrm{pnt}/1.2\mathrm{GHz}$) time window is needed to keep waveform inside the window. In the final system, the trigger latency is reduced by replacing the ADC with a shorter conversion latency one [27], and a data-taking at the higher sampling frequency becomes possible.

[*2] In reality, the channel configuration was changed during the pilot run for several times in each year to use the limited readout channels and beam time as efficient as possible. This table shows a major configuration used in this thesis.

[*3] Importance of the PMT information described here was overlooked in the run 2017. This is why the channel assignment was improved from 2017 to 2018/2019 by increasing the number of the PMT channels.

(a)

(b)
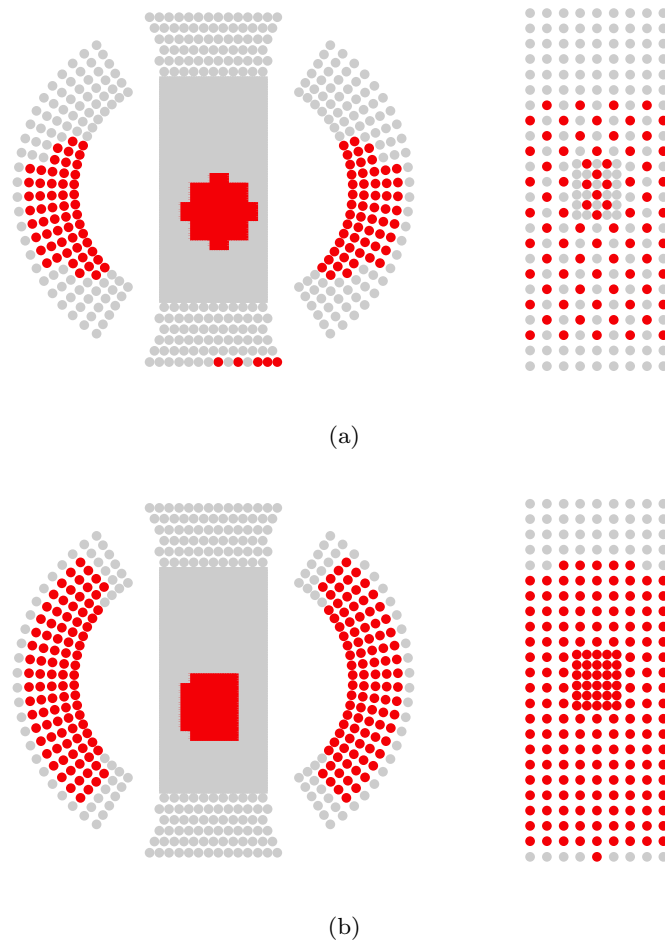
Figure 3.2   Readout channels in (a) 2017 run, (b) 2018/2019 run. Adjacent MPPCs and widely distributed PMTs around it are read out.

In the pilot run, the PMTs were operated at lower gain than MEG to extend its lifetime (Section 5.1.3), and the MPPC PDEs were found to be smaller than expected (Section 6.2.2). In order to keep the signal to noise ratio with these small signal amplitudes, an amplification by 2.5 on the analog frontend of the WDBs was applied, while it was not originally planned.

Fig. 3.3 shows an event display of a typical γ-ray event. The most part of scintillation light is included in the readout region of the detector.

3.2.2   Trigger

In the WaveDREAM system, many kinds of trigger logics are prepared for the physics data-taking and for the detector calibrations. The trigger logics used for this thesis are as follows.

EGamma trigger

In the data-taking of background γ and CW-Li γ, a self trigger called "EGamma trigger" was used, which is based on the online reconstructed γ energy. As explained in Section 1.8, the online γ-ray energy is reconstructed from a weighted sum of the photosensor waveforms,
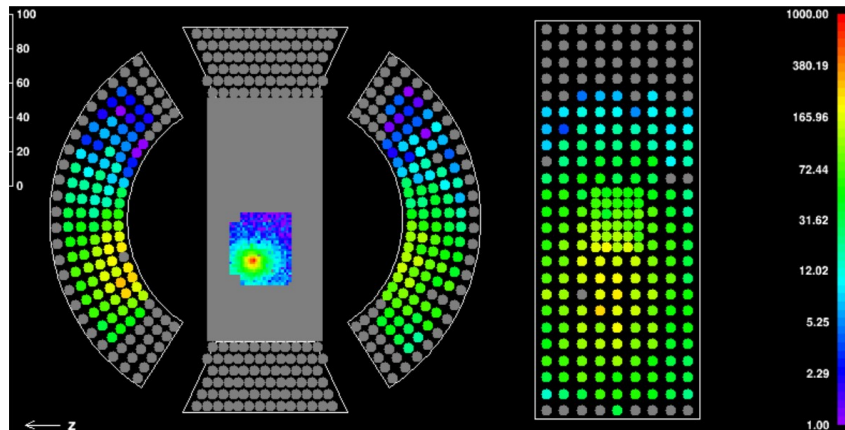
Figure 3.3   Typical background γ-ray event in the pilot run.

and the trigger is fired when the amplitude of the sum waveform exceeds a given threshold. In the pilot runs, the different weights for the MPPCs and the PMTs were adopted, which were estimated from the calibrated photosensor performances and validated by the 17.6 MeV peak from the CW-Li.

Due to the limited readout area, the purity of this trigger was typically only 10 %. This is because γ-ray hitting the outside of the MPPC readout area can also be triggered due to signals from widely distributed PMTs. In addition, some of the cosmic ray events cannot be vetoed, since only a part of its energy deposit is read out.

In the prototype system, the online energy resolution was limited by a noise coming from the DRS[*4] [27]. It is measured to be about 4% for 52.8 MeV γ-rays, while it is expected to be 1–2% in the design. An additional filter for noise reduction will be implemented in the final DAQ system to solve this issue. In the data-taking of the pilot runs, the energy threshold was set rather lower (42 MeV) in order not to miss interested events typically above 48 MeV, though the fraction of these interested events gets smaller.

Alpha trigger

A dedicated trigger is implemented to take α events from the calibration source (Section 2.5). This trigger is based on the sum of the sensor waveforms like the EGamma trigger, but only the PMTs around each α source wire shown in Fig. 3.4 are included in the sum to have a better signal to noise ratio. A particle identification based on the waveform shape, namely charge-height ratio, is also implemented to remove a contamination from the γ-ray and cosmic ray as shown in Fig. 3.5.

LED trigger

Several kinds of LEDs are installed in the LXe detector, and used for the sensor calibration (Section 2.5). Events from these LEDs are taken by a LED trigger generated from the pulse

---

[*4] This was confirmed by checking the noise level with the DRS digitization turned off.
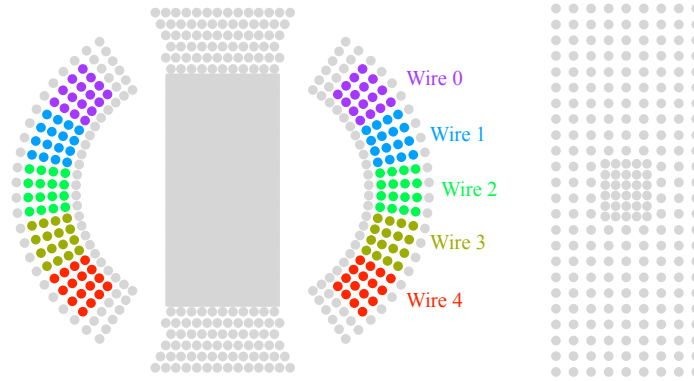
Figure 3.4   PMTs used for the alpha trigger. 32 PMTs around each wire are used for the alpha trigger.
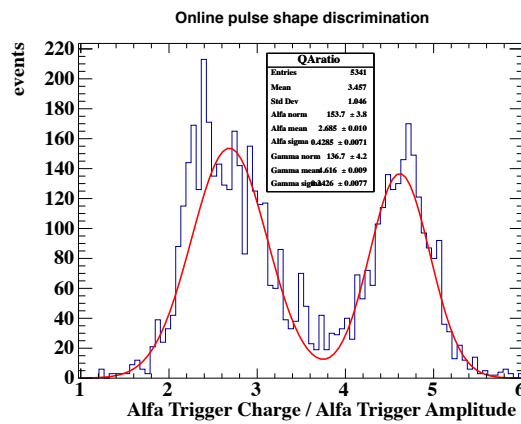
Figure 3.5   Pulse shape discrimination in the alpha trigger. A peak at the lower side corresponds the alphas, and the other corresponds to the γ-rays and the cosmic rays [27].

coincident with LEDs.

Random trigger

Data of random trigger are useful to monitor the performance of electronics like noise level and event-by-event fluctuation of the baseline.

Chapter 4

Detector simulation

In addition to the data obtained in the pilot runs, a simulation of the detector is another tool to understand the performance of the LXe detector. It is used not only for an estimation of the expected detector resolutions, but also for a confirmation whether the detector works as expected. For example, measured background γ-ray spectrum is compared with a simulated spectrum including the pileup effect to check their consistency. It is also used to understand how much the photosensor performance is important to achieve the designed resolutions.

For these purposes, simulation software of the LXe detector is developed to estimate its expected response. It consists of several programs as shown in Fig. 4.1. The software called "gem4" based on the Geant4 (version 10.4 [48][49]) generates an event, and simulates interactions of particles in the detector. The software called "bartender" simulates sensor responses. The output of the bartender is a set of waveform of each sensor with the same format as the real data, so that it can be analyzed by the same reconstruction algorithm implemented in the software called "analyzer". The bartender and the analyzer are based on the ROME framework [50].
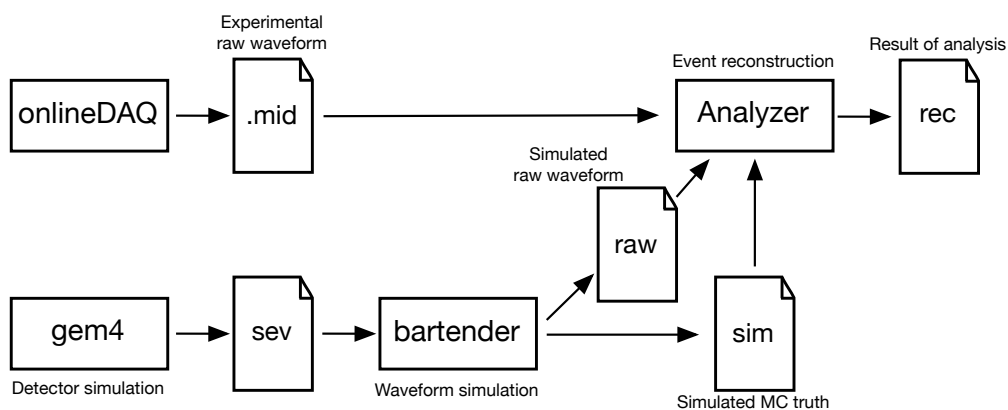
Figure 4.1   MEG II simulation software framework.
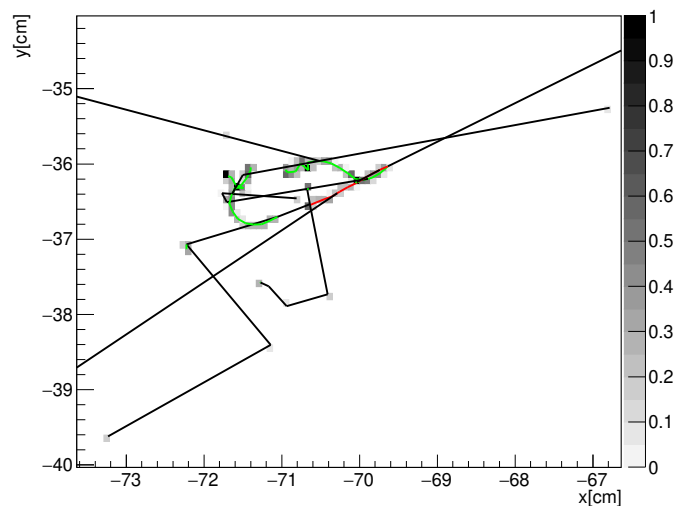
Figure 4.2   Simulation of electromagnetic shower. Particle tracks are shown as line (black: γ, red: e^+, green: e^-). Original γ-ray is coming from the right. Energy deposit on each point is overlaid. The scale of the gray bar is in the unit of MeV.

4.1   Event generation

In the gem4 software, an event generation and simulation of particle interactions are carried out based on the Monte Carlo simulation of Geant4. Users can select a type of the generated event for each purpose. Event types of signal γ, calibration sources, and Standard Model muon decay are used in this thesis which are summarized in Table 4.1. All the MEG II detectors and components are implemented in the gem4, and physics interactions of generated particles with materials and sensors are simulated in the framework of the Geant4.

Table 4.1   List of event types in gem4

ID	Description	Generated particle(s)
21	Signal γ	52.8 MeV γ from the signal decay on the target
12	Michel decay of μ	e^+ from the Michel decay on the target
22	Radiative decay of μ	e^+ and γ from the RMD on the target
30	Muon beam	μ^+ injecting into MEG detectors
63	Alpha	5.5 MeV α from ^{241}Am inside LXe detector
64	CW-Li	17.6 MeV γ from the target

In the simulation of the LXe detector, electromagnetic showers produced by the incident particles are simulated as shown in Fig. 4.2. Based on the energy deposit inside the LXe, scintillation photons are generated at each energy deposit point of the electromagnetic shower with a given scintillation time constant. The number of generated scintillation photons is calculated from the energy deposit divided by the W-value of LXe. A Poisson fluctuation is added to the number of photons assuming a maximal fluctuation on it. Propagations of scintillation photons are
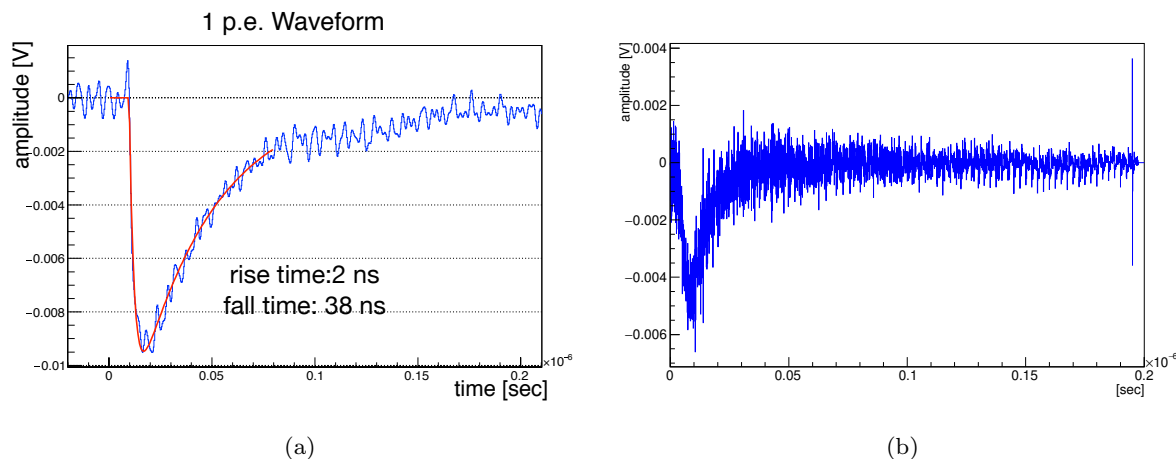
Figure 4.3   The waveform template used as the single photoelectron response in the wave-form simulation. (a) MPPC, (b) PMT.

simulated where a reflection on the detector material, an attenuation by the impurities, and a Rayleigh scattering in the LXe are included. If an scintillation photon enters into a sensitive volume of a photosensor, the timing, the fired MPPC pixel (i.e. hit position in MPPC), and the incident angle of the photon are recorded. The LXe properties used in this simulation are summarized in Table 1.2. A "gaseous xenon mode" can also be selected, in which the W-value, the scintillation time constant, the density, and the refractive index of xenon are different from the LXe mode.

4.2   Waveform simulation

The bartender software simulates photosensor waveforms from the gem4 output. It can also mix different events such that pileups can be simulated.

In the waveform simulation, the single photoelectron response of each photosensor is summed up with the time distribution of the arriving photons simulated in the gem4. Fig. 4.3 shows the single photoelectron response derived from the data. For the MPPCs, it is obtained from the single photoelectron events in the weak LED data. For the PMTs, it is obtained by deconvoluting γ-ray waveforms by an exponential function of the scintillation time constant since the single photoelectron peak cannot be resolved in the charge distribution.

The MPPC characteristics are also simulated in the bartender. In the simulation of the crosstalk, each fired pixel in an MPPC can fire another adjacent pixel with a given probability. It can also trigger another hit on the same pixel with a given probability and time constant to simulate the afterpulse. To simulate the saturation, when more than one photons hit the same pixel, waveform from the second photon is reduced as a function of the elapsed time from the first photon.

In the nominal configuration, the angular dependence of the MPPC PDE is based on that of the reflection at the sensor surface, which is calculated from a complex refractive index in gem4.
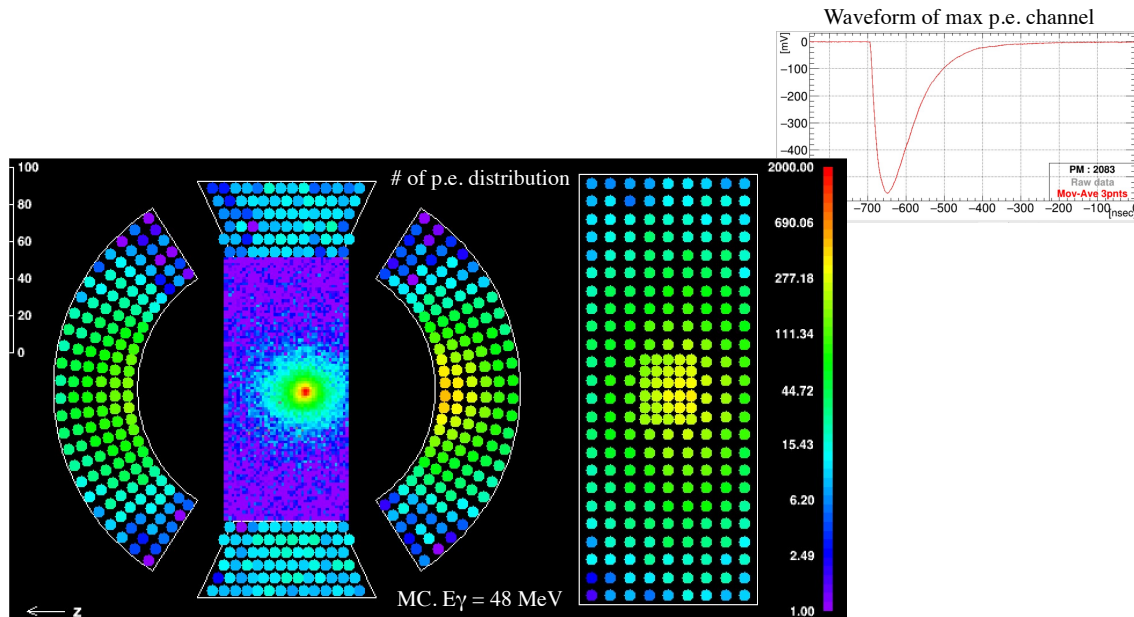
Figure 4.4   An example of a simulated event.

Additional angular dependence observed for our MPPC (Section 2.1.3) can also be included from the recorded incident angle of the arriving photons, if needed.

After these simulations, an electronics response is also applied. Two independent methods are prepared to include a noise contribution. The first method adds a white noise of a given standard deviation, and the second method adds the measured random trigger waveform. The simulated waveform is digitized by the sampling frequency of $1.2\,\mathrm{GHz}$, and the waveform outside the dynamic range of the DRS chip (from -950 to $+50\,\mathrm{mV}$) are cut, as is done in the real electronics.

Fig. 4.4 shows a display of a simulated event.

4.3   Background γ-ray

The simulations can be performed in a reasonable time for most of the event types, except for the background γ-ray from the muon beam. In this section, a dedicated operation for this background γ simulation is described.

Background γ events from the muon beam are the events mainly taken in the pilot runs from 2017 to 2019, and its simulation is needed to evaluate the detector performance. In principle, it can be simulated by accumulating γ-ray events by generating many muon decays. However, due to a very small probability of having a high energy γ from a muon decay, the computation time for the tracking of the muons and the Michel positrons becomes a bottleneck[*1]. The probability of having a γ-ray above $48\,\mathrm{MeV}$ in the readout of 2019 run is $O(10^{-7})$, and thus $O(10^{11})$ events

---

[*1] This kind of "full simulation" of background γ was not actually performed in MEG.

have to be simulated to get comparable statistics with real data. To reduce the computation time, following operations were carried out.

Background γ-ray events are classified into three groups by their sources as follows[*2], and events of each group are simulated separately.

- AIF : γ-ray originating from a Michel muon decay stopped on the target. High energy γ mainly comes from the annihilation in flight of the Michel positrons.

- RMD : γ-ray from a radiative muon decay stopped on the target.

- DIF : γ-ray from a muon decay in flight (i.e. not on the target).

Since we are only interested in the high energy γ above $20\,\mathrm{MeV}$, simulations of particles below $20\,\mathrm{MeV}$ is skipped. The phase spaces of the muon decay for the AIF and the RMD are restricted to $P_e > 20\,\mathrm{MeV}$ and $E_\gamma > 20\,\mathrm{MeV}$ respectively. In the AIF simulation, positrons which reach more than $16\,\mathrm{cm}$ away from the center of the COBRA along beam-axis are killed because they are found not to produce the high energy γ-rays arriving at the LXe detector. With these reductions, events roughly corresponding to one day of data-taking in the 2019 run were simulated by using 200 physical cores of the recent CPUs for 50 days.

[*2] Definition of RMD event is having photon above $500\,\mathrm{keV}$. Soft photons below this threshold are ignored, and defined as a Michel decay without radiative photon.

Chapter 5

PMT performance

For a stable detector operation and good resolutions, it is important to calibrate and monitor photosensor performances correctly. The number of photons N_{pho}, and the number of photoelectrons N_{phe} on each photosensor are calculated from the observed charge of each waveform q as follows:

$$
\begin{aligned}
q &= Gain \times N_{\mathrm{phe}} \times e \\
&= Gain \times CE \times QE(VUV) \times N_{\mathrm{pho}} \times e \\
&= R(VUV) \times N_{\mathrm{pho}} \times e,
\end{aligned}
$$

where a response to a VUV light $R(VUV)$ is defined as $R(VUV) := Gain \times CE \times QE(VUV)$. The QE (quantum efficiency) is a probability of the photon conversion on the photocathode of the PMT, and the CE (collection efficiency) is the probability where the converted photoelectrons can reach the first dynode. Similarly, for the observed charge q of visible light, a response to the visible light $R(vis)$ is defined as follows:

$$
\begin{aligned}
R(vis) &:= Gain \times CE \times QE(vis) \\
q &= R(vis) \times N_{\mathrm{pho}} \times e.
\end{aligned}
$$

Since the N_{pho} and N_{phe} are used in the reconstruction of the γ-rays, an individual difference of each photosensor response has to be measured correctly.

From the viewpoint of the detector operation, it is also good for all the MPPCs and PMTs to have a similar response. Each PMT has a large individual difference on its gain, and the PMT high voltage has to be adjusted to have a uniform gain distribution.

In addition, the sensor response has a time variation because of a gain degradation by the beam usage, a slow recovery of the degradation, a gain dependence on the beam intensity, a light yield of the LXe affected by impurity, an external magnetic field, and a fluctuation of the LXe temperature. If we fail to monitor these effects correctly, it will lead to a fluctuation of the energy scale, which becomes a systematic uncertainty in the search of $\mu \to e\gamma$. Even though the energy scale will be monitored once per week by the 17.6 MeV monochromatic γ-rays from the CW-Li during the physics data-taking, it is still important to monitor and understand the daily variation of the photosensor performances.
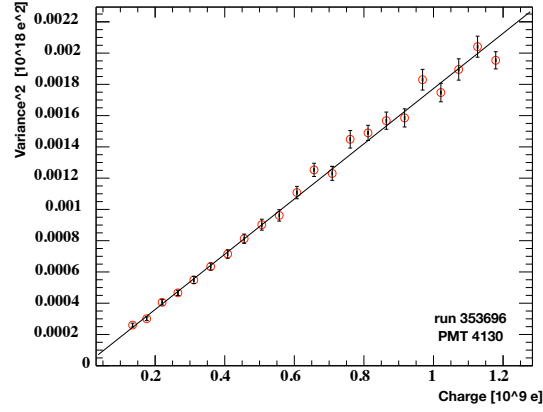
Figure 5.1 Charge variance squared σ_q^2 as a function of charge mean $\langle q \rangle$ in LED data of a PMT. Different points correspond to different LED intensities.

5.1 Resoponse to visible light

5.1.1 Measurement of visible light response

The PMT response to visible light $R(vis)$ was measured by using pulsed blue LED light (Section 2.5).

The PMT gain was measured from a relation of the mean and the spread of the LED charge distribution on the assumption that the LED light follows a Poisson distribution[*1]. An observed charge q from the LED is denoted as $q = e \times Gain \times N_{\mathrm{phe}} + noise$, where $noise$ is a noise contribution whose mean is calibrated to be zero beforehand, while it still has some event-by-event fluctuation. The relation between the mean and the spread of the LED charge is written as,

$$\langle q \rangle = e \times Gain \times \langle N_{\mathrm{phe}} \rangle$$
$$\sigma_q^2 = (e \times Gain)^2 \times \sigma_{Nphe}^2 + \sigma_{\mathrm{noise}}^2$$
$$= (e \times Gain)^2 \times \langle N_{\mathrm{phe}} \rangle + \sigma_{\mathrm{noise}}^2$$
$$= Gain \times \langle q \rangle \times e + \sigma_{\mathrm{noise}}^2.$$

Fig. 5.1 shows measured σ_q^2 as a function of $\langle q \rangle$ for a PMT at different LED intensities. The gain is estimated from the slope of this plot, and the contribution of σ_{noise} is extracted as a constant term[*2]. Typically the noise contribution σ_{noise} is about 1×10^1 photoelectron.

Independent of this gain estimation, a relative change of the $R(vis)$ can be monitored by a time variation of the LED charge since the light intensity of our LEDs is known to be sufficiently

---

[*1] Our VUV PMT is known to have a large position dependence of the gain on the photocathode. Therefore, single photoelectron peak cannot be separated from pedestal.

[*2] In reality, in the LED data taken during a beam usage, an effect from the accidental pileup γ is not negligible. If the charge contribution of the pileups is a Gaussian, it is included in the constant σ_{noise}, and dose not affect the gain calibration. However, the pileup γ-ray spectrum has longer tail for the higher energy, and its contribution is not a Gaussian. To solve this, pileup charge distribution is measured during the beam usage by the random trigger beforehand, and is used for a subtraction of the pileup effect.
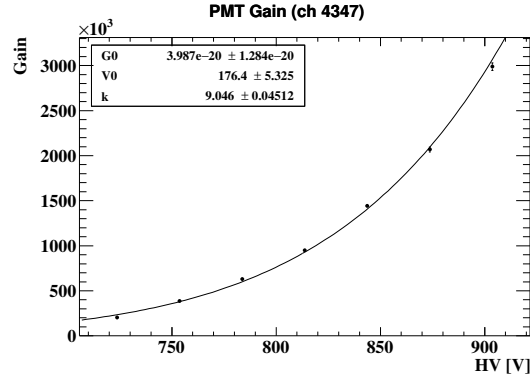
Figure 5.2   The gain of a PMT as a function of the high voltage fitted by a function: $Gain = G_0 \times (V - V_0)^k$ [51].
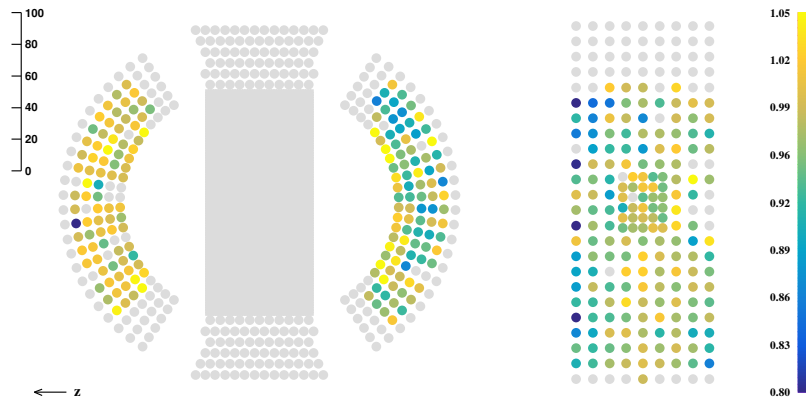
Figure 5.3   Effect of the magnets on the PMT Gain. "Gain when magnets on" / "Gain when magnets off".

stable. This variation includes effects of CE and QE for visible light. Thus, we can measure a relative time variation of $CE \times QE(vis)$ by comparing the variation of the LED charge and that of the PMT gain.

5.1.2   Gain and CE

Fig. 5.2 shows a voltage dependence of a PMT gain. This dependence can be modeled by a equation of $Gain = G_0 \times (V - V_0)^k$, where k is a parameter proportional to the number of dynode stages, and V_0 is an voltage offset mainly by the two Zener dynodes (Section 1.6.2). The voltage dependence of the gain was measured for all PMTs, and applied high voltages were adjusted to have a common gain.

The gain and CE of the PMTs are affected by an activity of the COBRA magnet even though its magnetic field is suppressed at the LXe calorimeter location by the compensation coils. They are also affected by an activity of the BTS. Fig. 5.3 and 5.4 show the ratio of the gain and the CE of each PMT with those magnets on and off. These effects have some z dependence, due to the fact that BTS is located on the upstream side.
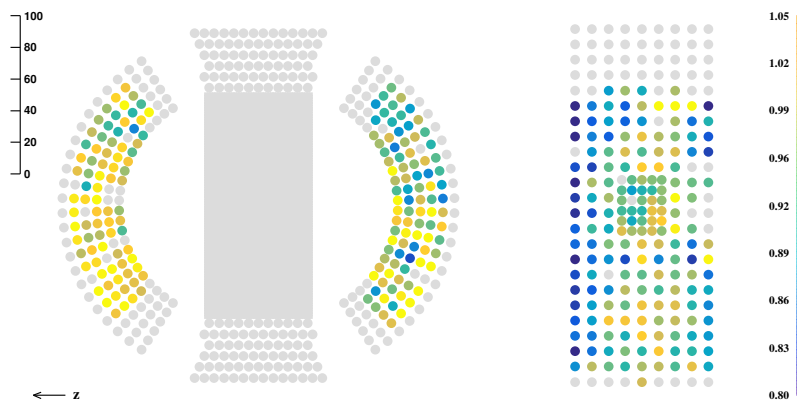
Figure 5.4   Effect of the magnets on the PMT CE. "CE when magnets on" / "CE when magnets off".

5.1.3   Gain degradation by muon beam

The gain of our PMT is known to be decreased by a beam usage in the physics data-taking (Section 1.6.2). To compensate the gain degradation, the applied high voltage will be increased. If the degradation is too fast, the demand voltage may become too high, and we may not be able to operate the PMTs in the whole MEG II experiment. As explained in Section 2.3, the lifetime of each PMT was calculated from the observed degradation speed in MEG assuming that the degradation speed is proportional to the beam intensity. Only the PMTs which can be operated for three years data-taking were installed in the MEG II LXe detector.

To crosscheck the expected lifetime of the PMTs, we measured the gain degradation speed at the MEG II beam environment in the pilot runs. The PMT gains were adjusted to the nominal value (Gain $= 1.6 \times 10^6$, same as MEG) before the beam usage, and the degradation was monitored. The red markers in Fig. 5.5(a) show the history of the averaged PMT gain in 2019 run whose high voltages are kept during the beam time. The degradation speed shown in Fig. 5.5(b) is calculated from its derivative. It is gradually decreasing and not yet saturated. Even after six days of operation, the degradation speed is still 1% per day, which is much faster than the 0.35% per day expected from MEG.

Even though a further irradiation may reduce the degradation speed in the future, this was not able to be confirmed in the limited beam time. To test another possible solution, some of the PMTs were operated at the reduced voltage (Gain $= 0.8 \times 10^6$, half of the nominal value) in the latter half of the beam time. Because the PMT gain degradation is expected to be due to the deterioration of the surface of the last stage dynode, its speed should be suppressed by reducing induced current on the dynode. Black data markers in Fig. 5.5(a) and 5.5(b) show the result of these PMTs, and a smaller degradation speed is confirmed.

In order to check whether PMTs can be operated throughout the physics run, an expected demand voltage of each PMT after the physics run is simulated. As the best estimation from the data so far, the degradation speed measured after the six days of operation is assumed. As shown in Fig. 5.6, there is a large individual difference on the gain degradation speed, and this
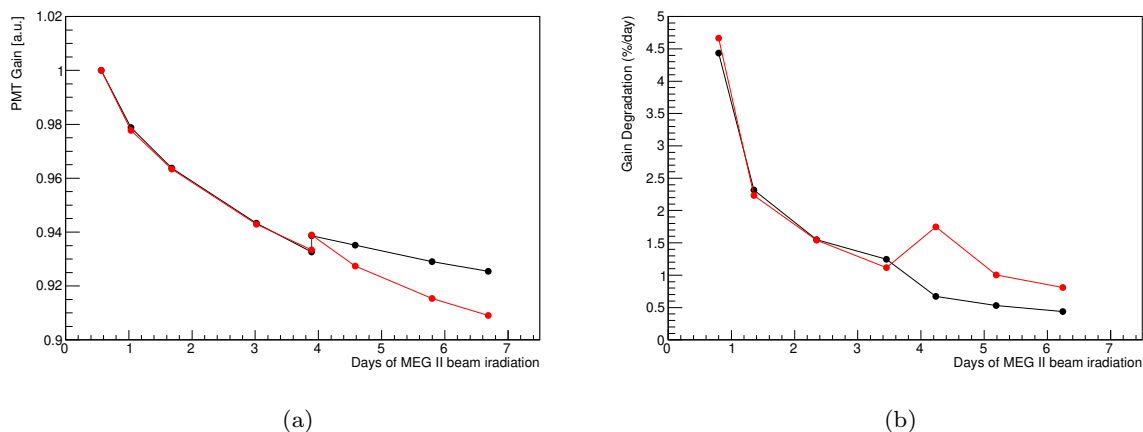
Figure 5.5   (a) History of the PMT gain in the 2019 run, and (b) the gain degradation speed estimated from the derivative of (a). Each color shows the result for each group of the PMTs. For the PMTs of red markers, the high voltage was kept during the measurement. For the PMTs of black markers, it was reduced after 4 days of operation to halve the gain.
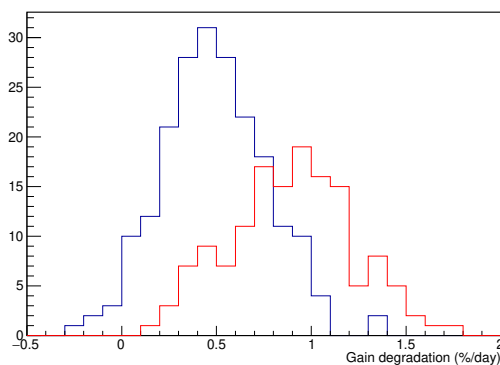
Figure 5.6   Gain degradation speed of each PMT per day in 2019 run after the six days of operation. Operated at gain 1.6×10^6 (red), and at gain 0.8×10^6 (blue).

is included in the simulation. The high voltage currently applied, and the voltage dependence of the gain of each PMT are also included based on the measurement.

The simulated high voltage of each PMT is shown in Fig. 5.7. The operation at the gain of 1.6×10^6 is possible for the three years physics data-taking, while the five years data-taking may not be a realistic since the demand voltages of one third of the PMTs will exceed the limit of $1400\,\mathrm{V}$. The operation at the gain of 0.8×10^6 looks promising even for five years data-taking, since only 5% of the PMTs will exceed this limit.

In the case of the operation at the reduced gain, the signal to noise ratio can get worse. To solve it, an additional signal amplification is applied on the frontend of the readout electronics. Since the dominant noise component comes from the electronics after the amplifiers, the signal to noise ratio can be kept event if we operate the PMTs at the reduced gain. The noise contribution to the energy resolution at the reduced gain is measured to be only 0.4% in the run 2019, and thus does not become a limiting factor to achieve the 1.0% energy resolution.
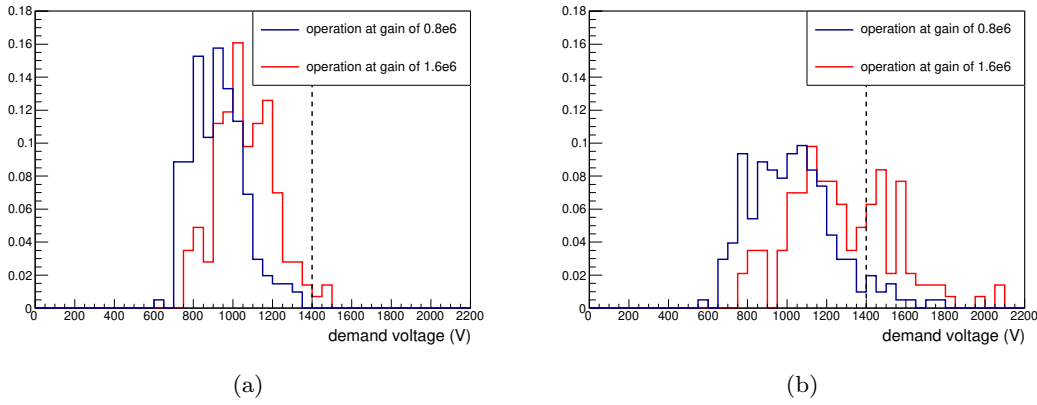
Figure 5.7   Expected demand high voltage for PMT assuming operation at gain of 0.8×10^6 (blue), and 1.6×10^6 (red). (a) After three years operation. (b) After five years operation.

Another concern is a reduction of the CE, which may lead to a larger statistical fluctuation of the number of photoelectrons. The reduction of the CE is measured to be only 5% by comparing that of the gain and the fixed intensity LED charge. Since the photoelectron statistics is not a major contribution to the resolution in this detector, this reduction does not affect the detector resolution.

Additionally, the transit time spread (TTS) of the PMTs may also become larger. This should not be a problem since the timing resolution of the LXe detector is not limited by the TTS. The timing resolution of the LXe detector is measured by operating the PMTs at the reduced gain, and the result will be shown in the Chapter 8.

5.2   Resoponse to VUV light

5.2.1   Measurement of VUV light response

The PMT response to the xenon scintillation light $R(VUV)$ is estimated by using a scintillation light from the calibration alpha sources (Section 2.5). It is measured from the observed charge q, which can be written as follows:

$$q = Gain \times CE \times QE(VUV) \times N_{\mathrm{pho}} \times e.$$

The number of arriving photons from the alpha source N_{pho} can be estimated from the simulation. By introducing a parameter LY, which explains a different level of the light yield for each year, it can be written as

$$N_{\mathrm{pho}} = N_{\mathrm{pho}}^{\mathrm{mc}} \times LY,$$

where $N_{\mathrm{pho}}^{\mathrm{mc}}$ is an expected number of photons calculated in the MC simulation assuming the best condition achieved in MEG. The direct observable of this measurement is $CE \times QE(VUV) \times LY$, which can be calculated as follows:

$$CE \times QE(VUV) \times LY = q/Gain/N_{\mathrm{pho}}^{\mathrm{mc}}.$$

In the offline analysis of data to estimate charge q, a series of event selections is applied. Events from the cosmic-ray or the environmental radiation are rejected by a particle identification based on the waveform shape of the PMTs. The vertex of each alpha event is reconstructed from the charge weighted mean of the sensor position, and the reconstructed position is utilized to identify an alpha source out of 25 sources installed in the detector. More details on the event selections are given in [34].

5.2.2   QE and light yield

Fig. 5.8(a) shows a history of the xenon light yield during the preparation period of 2017. In 2017, the purification of xenon was conducted both on gaseous circulation and liquid circulation. A gradual improvement in the light yield was observed, while we could not reach the maximum light yield achieved in MEG. It shows some degradation once the liquid purification is stopped, and there should be some source of contamination inside the cryostat or the purification system. Though the purification was continued also in 2018 and 2019 to improve the situation, the light yield does not reach the ideal value, due to a time constraint from the schedule and a much slower improvement by the purification than that in MEG.

Fig. 5.8(b) shows the measured $CE \times QE(VUV) \times LY$ of each PMT compared to that in MEG. On the assumption that the average of the PMT QE is not changed from that in MEG, the achieved light yield for each year's beam time LY is extracted from the slope of this correlation. The estimated LY are summarized in Table 5.1.

(a)   (b)
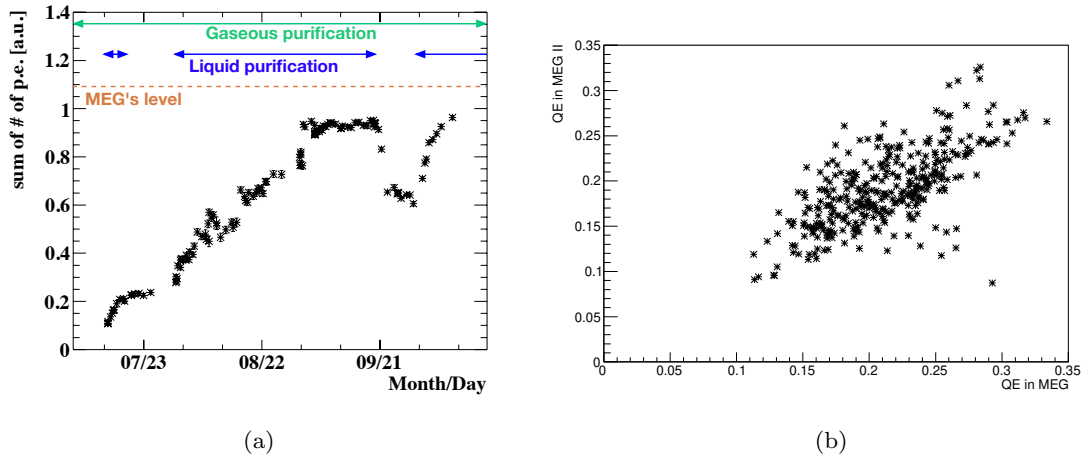
Figure 5.8   (a) History of the sum of the detected number of photoelectrons on the all read out PMTs in the preparation period of 2017.   (b) Measured $CE \times QE(VUV) \times LY$ of each PMT. Result in MEG II (2019) is shown as a function of that in MEG (2013).

Table 5.1   Light yield LY relative to the best condition achieved in MEG, during the beam time of each year.

Year	2017	2018	2019
LY	89%	78%	86%

Chapter 6

MPPC performance

The MPPC response was calibrated and monitored by using LEDs and alpha sources with similar methods for the PMTs shown in Section 6.1, and 6.2.1.

Surprisingly, a gradual decrease of the PDE for the xenon scintillation light was observed in the run 2018, which suggests some radiation damage to our MPPC. The absolute value of the PDE was measured to be lower than the design value, and this also supports the hypothesis of the radiation damage. Therefore, we conducted a precise PDE measurement in 2019 by controlling systematic uncertainties, and concluded that the VUV PDE degraded during the beam usage. The results of these measurement are given in Section 6.2.2.

Further investigations of this degradation were performed. It is found that an annealing of the MPPC can recover this degradation. This is important since the observed degradation is so fast that we may not be able to operate our detector for the whole MEG II experiment without any recovery. These results are summarized in Section 6.3.

6.1 Resoponse to visible light

6.1.1 Gain and ECF

The gain of each MPPC was measured by a single photoelectron peak from a weak LED light. Several LEDs installed in the cryostat were used to achieve a uniform light distribution. Since the peak amplitude of the single photoelectron signal is roughly only $0.1\,\mathrm{mV}$, the signal was amplified by a factor of 100 on the frontend of the readout electronics. To suppress the coherent noises picked up on the $10\,\mathrm{m}$ cable between the cryostat and the electronics, an "even-odd" procedure was adopted. In this procedure, bias voltages are applied only to the even channels, and the coherent noises are subtracted in offline based on the waveform of the adjacent odd channel, and vice versa. Fig. 6.1 shows a typical charge distribution, where photoelectron peaks are clearly resolved. The zero photoelectron peak and the single photoelectron peak in the charge distribution were fitted by a sum of two Gaussians to evaluate the gain of each MPPC.

All the MPPCs were operated at the over voltage of about $7\,\mathrm{V}$. The operation voltage V_{op} for each MPPC was calculated from a voltage provided for each MPPC by HPK called V_{Hama}
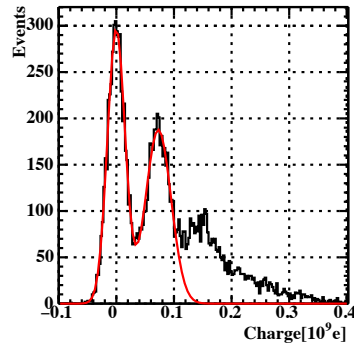
Figure 6.1   Single photoelectron charge distribution of an MPPC obtained by the even-odd procedure.

as follows:

$$V_{\mathrm{op}} = V_{\mathrm{Hama}} - 4.9\,\mathrm{V} + 6.8\,\mathrm{V} - c \times (298\,\mathrm{K} - 165\,\mathrm{K}).$$

Here we used the fact that V_{Hama} corresponds to the over voltage of 4.9 V (from the test at room temperature shown in Section 2.2). The last term is a temperature correction, where $c = 55\,\mathrm{mV/K}$ is the temperature coefficient of the breakdown voltage of the MPPCs [47].

Fig. 6.2(a) shows the measured MPPC gains. The power of the amplification on each electronics channel is measured independently and corrected in this plot. Sufficiently uniform gain distribution is obtained by applying V_{op} based on HPK's information, while a slight production lot dependence is observed.

The excess charge factor (ECF) of the MPPCs was also measured by using the weak LED light on the assumption that LED light follows a Poisson distribution. The detail of this method is described in Section 2.1.3. Fig. 6.2(b) shows the measured ECF. Even though a large production lot dependence is observed, this is still acceptable as long as we can measure it correctly. Over voltage of 7 V is adopted in this thesis to improve the S/N ratio to resolve the single photoelectron peak as much as possible. The rather large ECF and its lot dependence are drawbacks of the rather higher over voltage, and operation at smaller over voltage may be an option in the future.

6.1.2   History of visible light response in the beam time

Similarly to the PMT, the visible light response was monitored by the observed charge from the fixed intensity LED light. This method cannot give us an absolute size and an individual difference of gain and ECF, but can give us a history of the relative response with much better precision than the single photoelectron measurement. Fig. 6.3 shows the history of the visible light response during the run 2019. It shows a slight degradation of 1% probably correlated with the beam activity. A similar but much more prominent degradation is observed for the VUV response, which will be discussed in the next section.

(a)   (b)
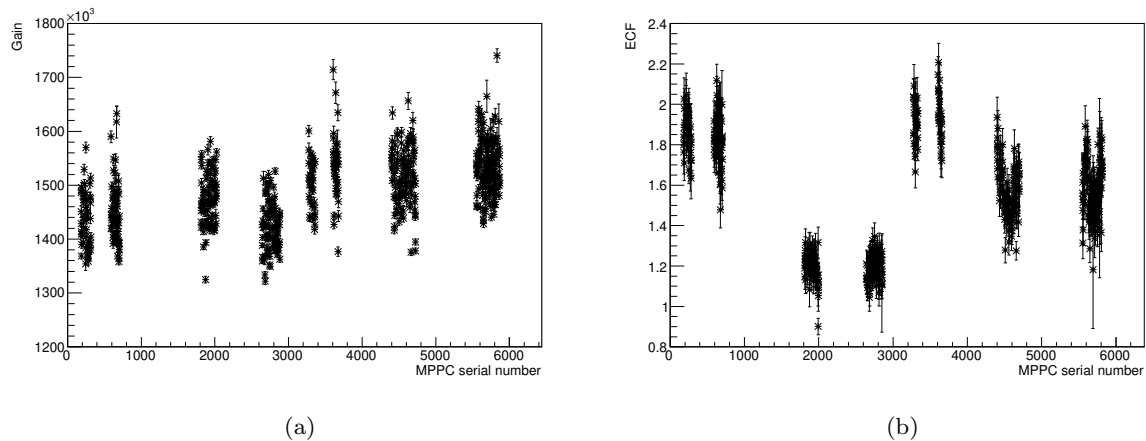
Figure 6.2   MPPC characteristics as a function of its serial number at the over voltage 7 V. (a) Gain, (b) ECF.
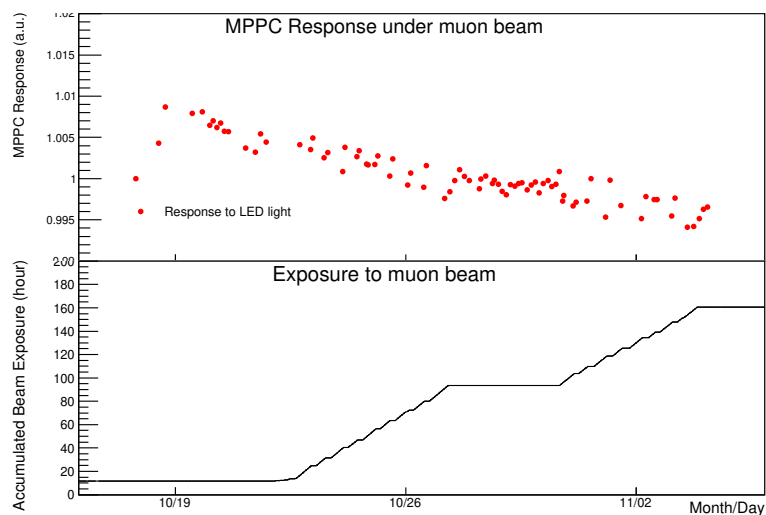
Figure 6.3   History of the visible light response ($\lambda = 470$ nm from blue LED) of the MPPCs during the run 2019. An average of all MPPCs is shown. Lower half is the accumulated muon beam usage.

6.2   Resoponse to VUV light

6.2.1   MPPC VUV PDE

Similar to the PMT described in Section 5.2, a response to the VUV light $R(VUV) = Gain \times PDE(VUV) \times LY$ of each MPPC was measured from the alpha calibration sources.

Fig. 6.4(a) shows the VUV PDEs measured at the beginning of the run 2019, where the light yield LY is taken from Table 5.1. The average of the PDE is 7%, while 18–22% is obtained in the measurement at the lab (Section 2.1.3). The possible reason for this inconsistency will be discussed in the next subsection.

The angular dependence of the PDE was measured to crosscheck the unexpected angular

(a)

(b)
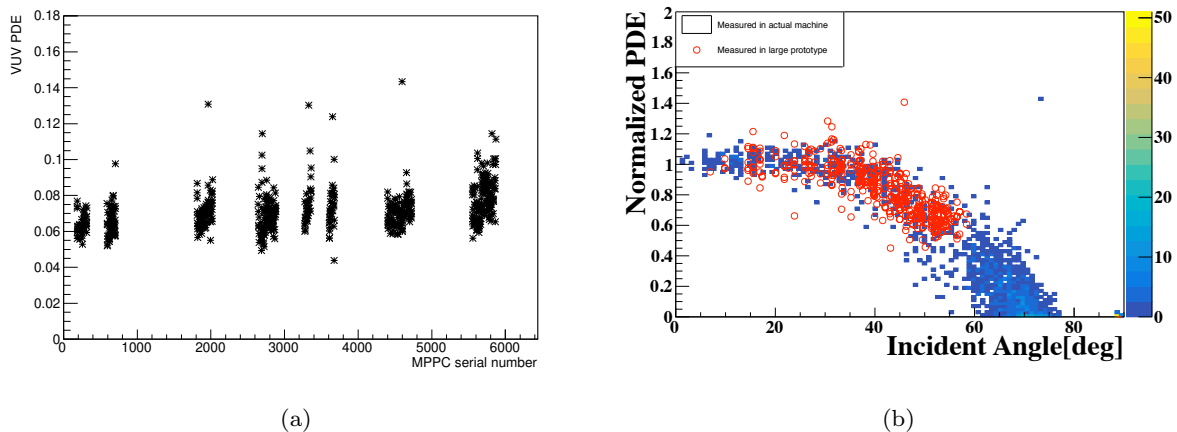
Figure 6.4   (a) PDE of VUV MPPC as a function of serial number at over voltage 7 V. Smaller LXe light yield (88 % of ideal case in 2019) is corrected. (b) MPPC VUV PDE as a function of the incident angle [34]. The individual difference of PDE of each MPPC is corrected by using the data point of the smallest incident angle.

dependence observed in the prototype test (Section 2.1.3). The PDEs of each MPPC were measured by using many alpha sources located at different positions, and Fig. 6.4(b) shows the VUV PDE as a function of the incident angle from each alpha source to each MPPC. A consistent result with the prototype test is observed. The effect of this dependence on the detector performance will be discussed in Section 7.3.

6.2.2   Degradation of MPPC VUV PDE by radiation damage

During the run 2019, the MPPC response to the VUV light was monitored with the alpha sources. Fig. 6.5 shows a history of the VUV-response averaged over all the MPPCs. The VUV response is found to be decreased by 11%, and its degradation is correlated with the beam activity. This degradation can be caused by a degradation of the gain, the ECF, the VUV PDE, or the xenon light yield. However, the MPPC response to the visible light decreased only by 1% in this period (Fig. 6.5), and thus the gain and the ECF should not be a cause of this degradation. A slight degradation was found also on the VUV response of the PMTs as shown in Fig. 6.6. This can be due to a degradation of the PMT VUV QE or the xenon light yield. However, its size is only 4% and cannot explain the observed degradation of the MPPC VUV response, even if it is totally due to the degradation of the xenon light yield.

Based on these observations, it is concluded that the degradation of the MPPC VUV response is mainly caused by that of the MPPC VUV PDE. Since the degradation is correlated with the beam usage, this should be a radiation damage while it is totally unexpected. The degradation speed is $9 \pm 2\%$ in the 160 hours MEG II beam usage, where the possible instability of the light yield is included as a systematic uncertainty estimated from the PMT response to the VUV light.

To investigate and crosscheck this degradation, several variables are checked and they are
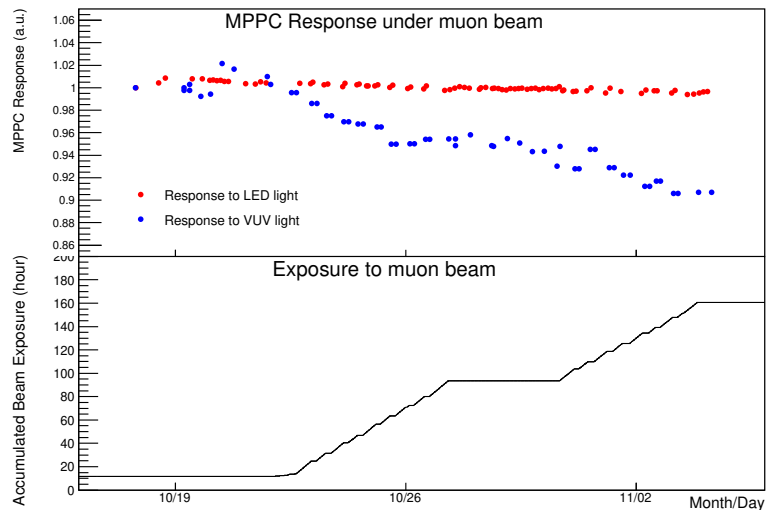
Figure 6.5   History of the VUV response of the MPPCs to the alpha source during run 2019 (blue). The average over all MPPCs is shown. The response to the visible light is also shown for comparison (red, same as Fig. 6.3). Lower half shows the accumulated beam usage. A much larger degradation correlated with the beam usage is observed for the VUV light than the visible light.
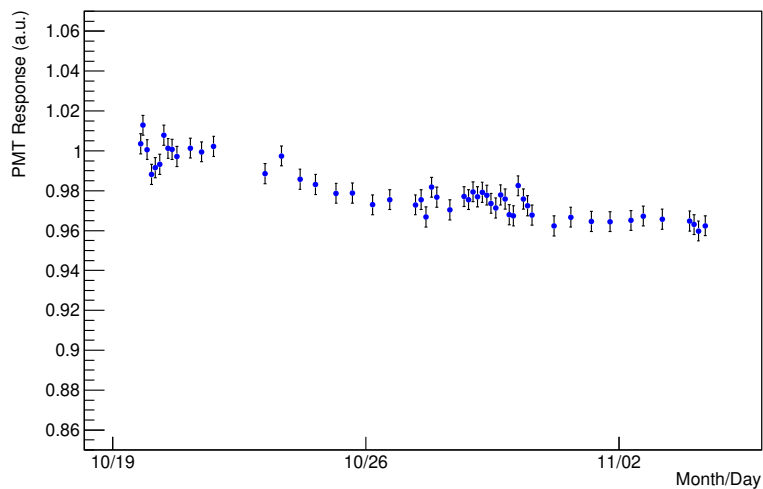
Figure 6.6   History of the $CE \times QE(VUV) \times LY$, namely the VUV response except for the gain degradation, of each PMT in the run 2019. The average over all PMTs is shown.

described in the following subsections.

PDE from 2017 to 2019

Fig. 6.7 shows the measured PDE from 2017 to 2019 as a function of the accumulated muon beam usage. A gradual decrease of the MPPC PDE is confirmed.

It is also notable that the degradation speed in run 2019 is slower than that in 2017 and 2018. This implies that the degradation is slowing down, but further irradiation is needed in the future
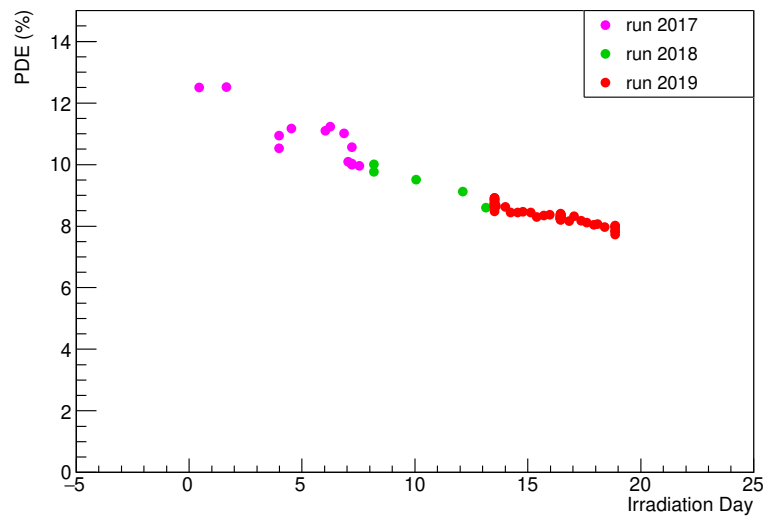
Figure 6.7   Averaged VUV PDE of the MPPCs estimated from the alpha sources from 2017 to 2019. The x-axis shows the accumulated irradiation days with the MEG II beam intensity. A period with a reduced intensity muon beam is normalized to the MEG II beam intensity. The different level of the xenon light yield in each year is corrected based on the Table 5.1.

to understand a full history of the PDE degradation.

VUV charge from γ-rays

In addition to the alpha events, the background γ-rays mainly from the RMDs were continuously measured during the beam time. This can be used as another source of VUV light. Due to the deterioration of the PDE, the MPPC charge distribution from the RMD γ-ray is shifted smaller as shown in Fig. 6.8(a). Here, only the events with PMT energy above 36 MeV is selected to eliminate the effect of the online energy threshold. The size of the shift is calculated from the mean of the charge distribution. Fig. 6.8(b) shows a relative history of the MPPC VUV response estimated from the observed shift. A degradation by 9% is observed and this is consistent with the observation with the alpha source.

Fig. 6.9(a) shows the averaged waveform shapes for the monochromatic γ-rays from the CW-Li measured before and after the irradiation. This degradation does not affect the waveform shapes, and only the signal amplitude deteriorates.

MPPC Current

An induced current on each MPPC from the background γ-rays was also monitored, and its history is shown in Fig. 6.9(b). Even though the current measurement seems to have some instability, about 10% degradation, which is consistent with the PDE measurement, is observed only for the VUV light. The current measurement is independent of the charge measurement

(a)   (b)
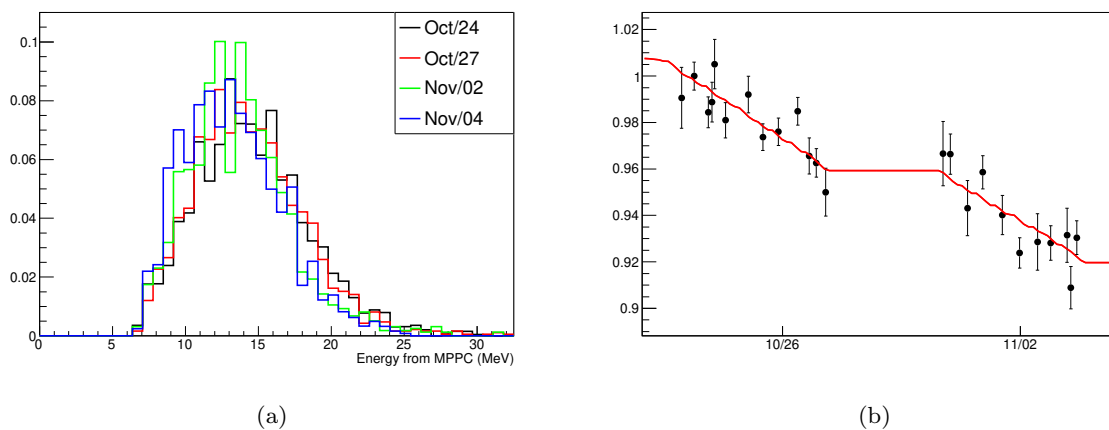
Figure 6.8   (a) Reconstructed γ energy only from the MPPC assuming a constant PDE
in this period (i.e. sum of the MPPC charge). (b) History of the PDE which can explain
the observed shift. The red line is a fitted function assuming a degradation of 0.059(4)%
/hour.

(a)   (b)
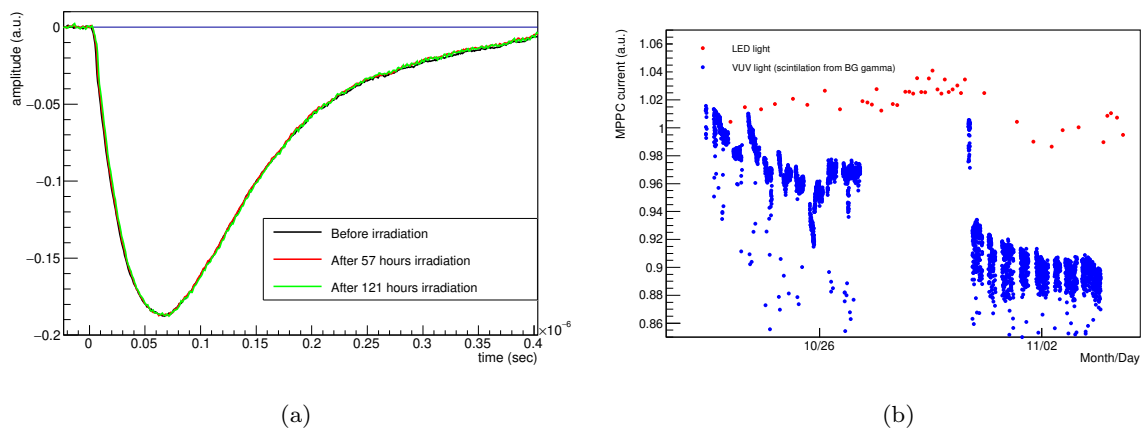
Figure 6.9   (a) Averaged MPPC waveforms of γ events before and after the irradiation.
The peak amplitude is normalized to compare its shape. (b) The MPPC current during
a run 2019 (blue). An average of all MPPCs except for bad channels is shown. Current
induced by a fixed intensity blue LED is also given for comparison (red).

using the digitized waveforms, so this result rejects a possibility of an instability issue of the
readout electronics only apparent on the VUV signals.

PDE of all MPPCs

The results mentioned above use the data during the beam time with a limited number of
readout channels. Additionally, at the end of the run 2018, PDEs of all the MPPCs were
measured by subdividing 4092 MPPCs into 12 groups and changing the readout channels from
one group to another. Fig. 6.10 shows a map of the measured PDEs. The PDEs of the MPPCs
located at the edge of the detector along horizontal axis (z-axis) are found to be larger than the
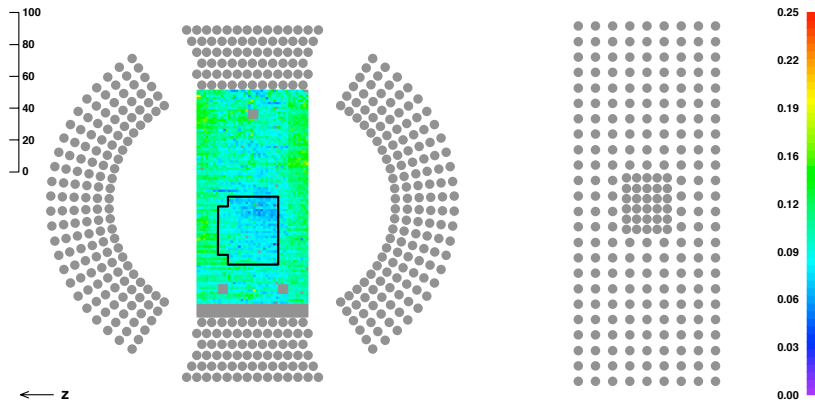
Figure 6.10   VUV PDE measured after the run 2018. MPPCs used in the run 2018 is indicated by a region surrounded by the black line. PDEs of most of the gray MPPCs were not measured just due to a technical reason, and not dead channels.

others. This is likely due to a position dependence of the irradiation fluence. For example, if we assume that this radiation damage is caused by the VUV scintillation light, the dominant contribution is the scintillation of the γ-rays coming from the muon decays on the target. Since the LXe detector and the COBRA magnet are designed to have a reduced material budget only in the acceptance region, such kind of irradiation is expected to be smaller outside the acceptance like large $|z|$ region. Fig. 6.11(a) shows the simulated irradiation fluence of the VUV scintillation light. An anti-correlation of the measured PDE and the expected fluence is observed. It must be noted that the same discussion is also applicable to the γ-ray irradiation dose.

During the beam irradiation, the bias voltage was applied only to the MPPCs inside the readout area, and no voltage was applied to the others. Fig. 6.11(b) shows a comparison of the PDEs with "voltage on" MPPCs and "voltage off" MPPCs. Only the MPPCs located at $|z| < 15\,\mathrm{cm}$ are selected, where a uniform irradiation level is expected. Since the original PDE should be 18–22%, the degradation process also occurs without applying bias voltage. The PDE of "voltage off" MPPCs is a little higher than that of "voltage on". It is still not clear that this is due to an effect of the bias voltage on the PDE degradation or just due to a unknown systematics in this measurement like v dependence of the PDE measurement.

6.3   Investigation of VUV PDE degradation

6.3.1   Possible cause of PDE degradation

Two types of radiation damage are known for the MPPC and SiPM: a bulk damage and a surface damage [52].

In the bulk damage, an atom in the silicon bulk is displaced by a non ionizing energy loss (NIEL) by high energy particles. This results in a formation of a defect, which introduces an additional energy level between the band gap of the silicon. Typical phenomena of the bulk damage are a larger leakage current and dark count rate, which are caused by the increased

(a)   (b)
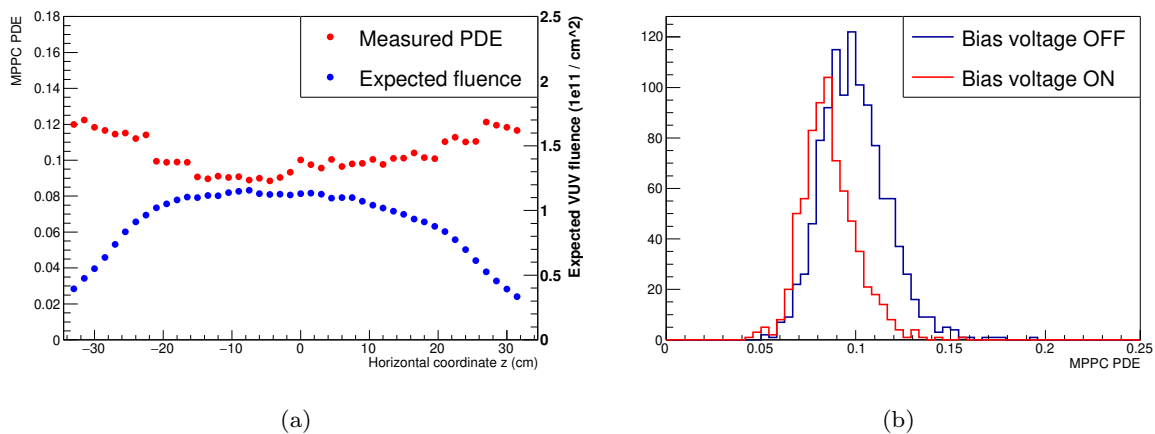
Figure 6.11   (a) The z dependence of the measured MPPC PDE and that of the expected
fluence of the VUV photons from the simulation. (b) Comparison of the PDE just after
the run 2018 between the MPPCs irradiated with bias voltage and those without voltage.
Only the MPPCs located at $|z| < 15\,\mathrm{cm}$ are shown.

probability of the thermal excitation of electron-hole pairs due to the new energy level. These are
reported by many studies typically above $1 \times 10^8 \,/\mathrm{cm}^2$ (1 MeV neutron equivalent) [53][54][55].
Some studies also report a decrease of the signal size, namely a product of the PDE, the gain,
and the ECF, at $5 \times 10^{13} \,/\mathrm{cm}^2$ (1 MeV neutron equivalent) [55]. A possible explanation of this
is an increased pixel occupancy by the increased dark signals. If a photon hits a pixel which is
not fully recovered from the previous discharges, the effective gain can be smaller.

The other damage on SiPMs is the surface damage by an ionizing energy loss (IEL) by elec-
tromagnetic particles such as X-rays and electrons. By the energy deposit above the band gap,
electron-hole pairs are generated in the high resistivity passivation layer (e.g. SiO_2). Some of
the holes are captured by deep traps in the passivation layer or the interface traps between
silicon layer, while most of the electrons leave it by a relatively high mobility and low trapping
probability. This leads to an accumulation of the stationary charges. A large increase of the
dark current is reported above 200 Gy [56], which is very likely due to the accumulated and
stationary charges at the surface generated by the breakup of SiO_2 molecules [57].

Fig. 6.12 shows the radiation environment of the LXe detector. When the muon beam is
used, γ-rays mainly from the RMDs on the target hit the detector through the MPPCs on the
entrance face. The xenon scintillation light ($7.1(\mathrm{mean}) \pm 0.1(\mathrm{FWHM})\,\mathrm{eV}$) from these γ-rays hit
the MPPCs. Neutrons from the accelerator also hit the detector in the MEG II experimental
area.

Table 6.1 shows the expected irradiation dose in the run 2019. The neutron fluence is estimated
to be less than $2.9 \times 10^6 \,/\mathrm{cm}^2$ (1 MeV neutron equivalent) from the measurement at the MEG II
experimental area [22]. This is much smaller than the level where the NIEL damage is reported.
The gamma-ray dose is estimated to be 0.01 Gy by the simulation [22], and should not be a
problem. The VUV fluence is measured to be $4.6 \times 10^{10} \,/\mathrm{mm}^2$ from the induced current on the

MPPC in the run 2019. It is also estimated to be 5.8×10^{10} /mm^2 from the simulation, and agrees with a 30% accuracy. A radiation damage on SiPMs by the VUV irradiation was not reported. Therefore, the degradation of the VUV PDE by a radiation damage was unexpected.

One hypothesis to explain the observed PDE degradation is a surface damage by the VUV photon irradiation. In the surface damage, the accumulated oxide charges near the interface between the silicon layer and the passivation layer can distort the electric field around it. Due to the special detection mechanism of the VUV photons (Section 2.1.1), the collection efficiency for the VUV light can be affected by the distortion, while that for the visible light is hardly affected. It has to be pointed out that the energy of the xenon scintillation light (7.1 eV) is smaller than the band gap of passivation layer (8.9 eV), if it is made of SiO$_2$. The mechanism of carrier generation in the SiO$_2$ has not been understood in this case, but may be related to an intermidiate energy level in SiO$_2$ by a defect or a photoemission of the holes from the silicon valence band to the SiO$_2$ valence band, known for other silicon devices [58][59].

Some studies report that a thermal annealing can recover the radiation damage on the SiPMs [53][54]. In the thermal annealing, SiPM is kept at a high temperature, so that the accumulated charges are de-trapped by the thermal excitation. We tried it with our damaged MPPCs, and the results will be given in the next subsection.

Table 6.1   Expected irradiation fluence in run 2019 (i.e. 160 hours MEG II beam)

| irradiation source	dose/fluence
γ	0.01 Gy
VUV photon	4.6–5.8 $\times 10^{10}$ /mm^2
neutron	2.9×10^6 n/cm^2
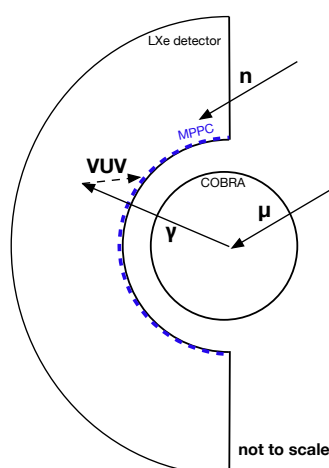
Figure 6.12   Radiation environment of the LXe detector.

6.3.2   Annealing

As is discussed in the previous subsection, annealing may cure this radiation damage. We tested it for a small number of MPPCs in the LXe detector after the run 2018. We used an intense LED light to heat up the MPPCs by the Joule heating of the induced current flowing through the quench resistors. In order to perform this test, the liquid xenon was transferred to the storage tank, and the detector was filled with gaseous xenon at room temperature. Annealing was tested at the several levels of induced current and the duration for the six MPPCs as is shown in Table 6.2. The temperature of the MPPC chips under these conditions were not directly measured, but it is expected to be about 70°C from a lab test performed under the same condition.

Table 6.2   Tested annealing conditions.

MPPC ID	current	duration
2802	17–19 mA	23 hours
2712	19 mA	23 hours
2672	19–20 mA	23 hours
2789	19–24 mA	38 hours
2700	20–24 mA	38 hours
2658	21–24 mA	38 hours

The PDEs of the annealed MPPCs were measured before starting the beam usage in 2019. A significant recovery of the PDE from $\sim 8\%$ to $\sim 17\%$ was observed. The ratios of PDEs after the annealing to those before the annealing are presented in Fig. 6.13(a). A significant recovery of PDE is observed for the annealed MPPCs, and its size is correlated with the annealing strength. The response to the visible light is also found to be recovered by the annealing as shown in Fig. 6.13(b). Similar to the PDE degradation, the recovery for the visible light is much smaller than that for the VUV light.

One concern was that the recovered PDE by the annealing might rapidly decrease by a small amount of irradiation. Fig. 6.14 shows the PDE degradation during the run 2019 of the annealed MPPCs compared with the non-annealed MPPCs. Its degradation speed is found to be the same or a little slower than the non-annealed MPPCs.

6.3.3   PDE degradation at room temperature

A series of irradiation tests was performed in lab to crosscheck the degradation observed in the LXe detector. All these irradiations were performed at room temperature.

6.3.3.1   VUV photon irradiation

A VUV-MPPC was irradiated with the intense VUV light from a xenon lamp (Hamamatsu L9456-03 [60]) to study the effect of the VUV light on the VUV sensitivity. Fig. 6.15(a) shows

(a)   (b)
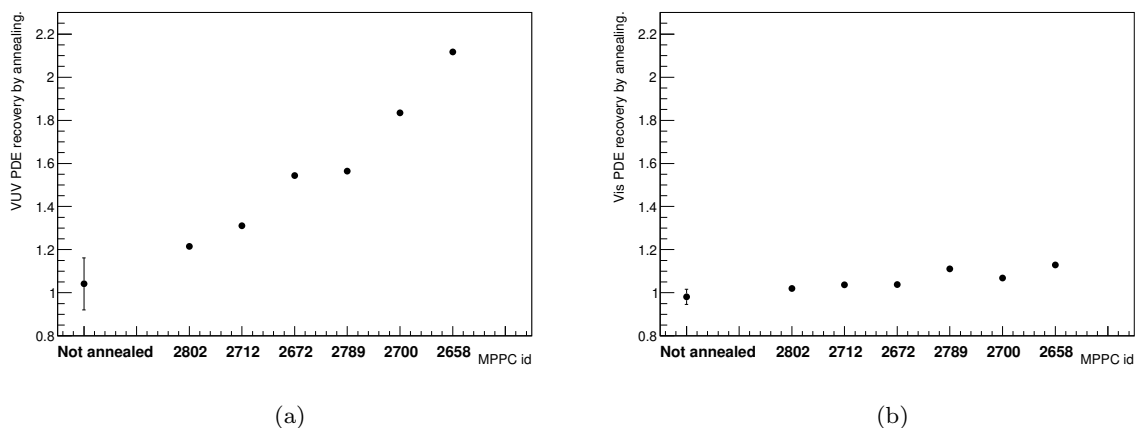
Figure 6.13   Recovery rate of the PDE of the annealed MPPCs (a) for VUV light, (b) for
blue LED light. Non-annealed MPPCs are also shown for comparison. The MPPC ids
in the x-axis are in an ascending order of the annealing strength (Table 6.2). The error
bar of the non-annealed MPPCs shows the 1σ spread of the PDE ratio distribution of the
non-annealed MPPCs.
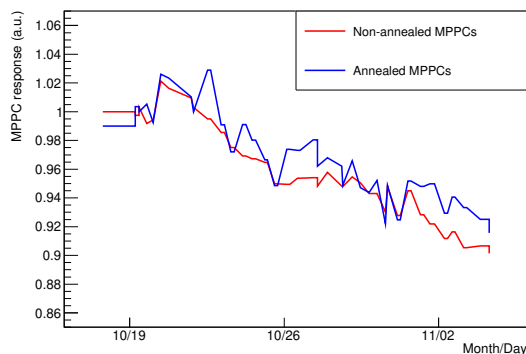
Figure 6.14   History of the VUV PDE in the run 2019 of the annealed MPPCs. Relative
shift is shown.

schematic of the setup. Light ranges from VUV to blue are emitted from the xenon lamp as
shown in the spectral intensity (Fig. 6.15(b)). The xenon lamp was placed 5 cm away from the
surface of the MPPC without any filters.

   The VUV component of the irradiated light was measured to estimate irradiation flux in this
test. Two bandpass filters (ACTON FB180–B–.5D and Edmund optics #33–026, Fig. 6.16)
were placed to select VUV light peaked at 190 nm. Measurement was performed at a larger dis-
tance beforehand and the results were extrapolated to that in the measuring point to avoid
a saturation of the MPPC. The irradiation flux of the VUV light is estimated to be 5×10^{13} photons/mm^2/hour.

   In order to monitor the VUV response, the charge from another xenon lamp (Hamamatsu
L9455-13 [60]) placed 35 cm away from the MPPC was measured periodically during the irradi-
ation. The two bandpass filters and one ND filter were placed to monitor the response to the
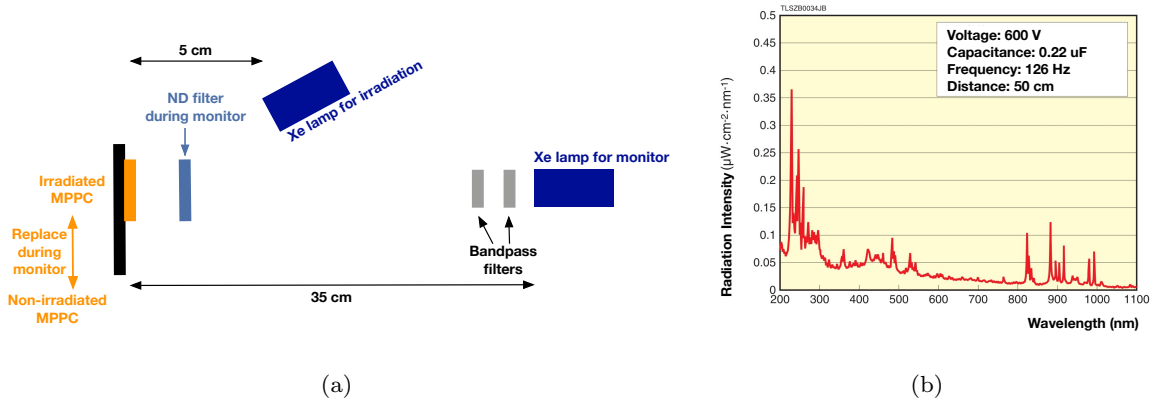
Figure 6.15   (a) Setup of VUV photon irradiation. (b) Spectral radiation intensity of the Xe lamp (from [60], translated by the author). This lamp can emit VUV light down to $\lambda = 185\,\mathrm{nm}$.
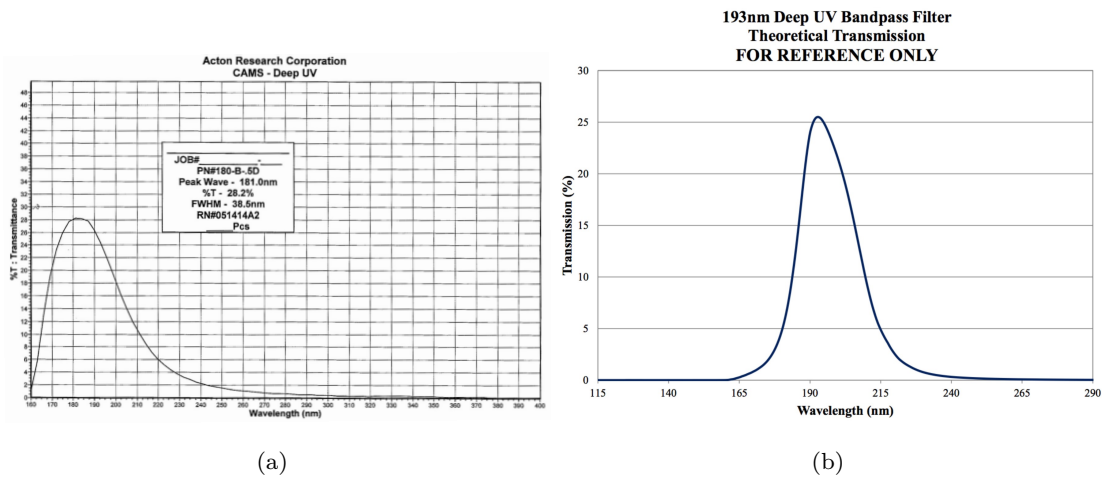
Figure 6.16   Spectrum of the bandpass filters.

VUV light peaked at 190 nm and to suppress the signal to avoid saturation.

A VUV response of another MPPC without irradiation was also monitored for the comparison. These measurements were carried out in a thermal chamber kept at 25°C.

Fig. 6.17(a) shows VUV charge history for the irradiated and the non-irradiated MPPCs. A degradation of the VUV response is observed only for the irradiated MPPC. The observed degradation is 65% in total after 3×10^{16} /mm^2 VUV photons irradiation. It is 9% after 1×10^{15} /mm^2 irradiation. Since the degradation in the LXe detector is 9% at the expected fluence of 4.6×10^{10} /mm^2 VUV photon, this is much slower than the observation in the detector by a factor of $O(10^4)$. It is notable that the degradation of PDE is saturated when it reaches 35% of the original value.

The annealing of the irradiated MPPC was also tried. The irradiated MPPC was kept at 70°C for 24 hours. With this annealing, VUV charge is increased from 35% to 105% of that before any irradiation. Thus, the degradation is fully recovered. It is also notable that a jump of VUV response was observed when we suspended the irradiation for twelve days (at 400 hours

(a)

(b)
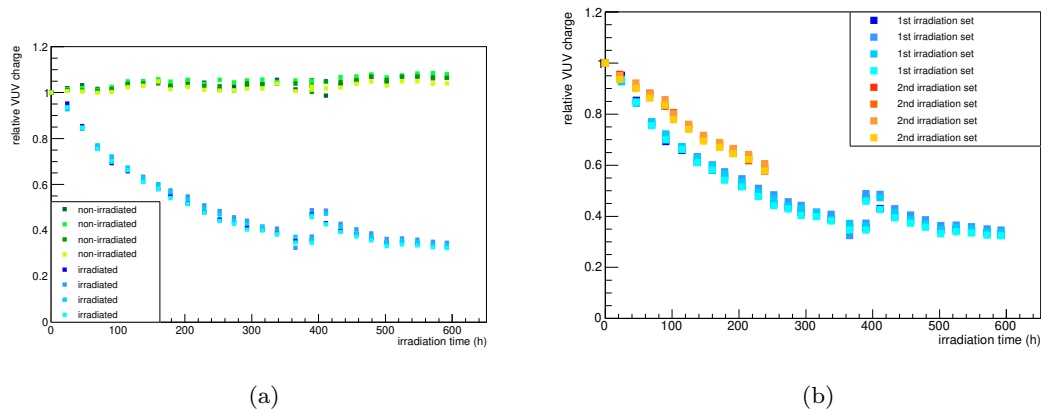
Figure 6.17   (a) Response to VUV light from a fixed intensity Xenon lamp. Different data series with similar colors show four chips on the same MPPC package. (b) VUV response in the second irradiation after one cycle of annealing.

of irradiation of Fig. 6.17(a)), which can be due to a slow annealing at 25°C.

Another irradiation is performed for the annealed MPPC. The degradation is slower than the first irradiation as shown in Fig. 6.17(b).

6.3.3.2   Gamma irradiation

Several MPPCs are irradiated with γ-rays from a ^{60}Co source ($E_\gamma = 1.17, 1.33$ MeV). The irradiation was carried at the Takasaki Advanced Radiation Research Institute in 2015. The total irradiation dose of each MPPC is 1–4×10^3 Gy [61], which is much higher than the expectation of 0.6 Gy in the whole MEG II experiment.

We measured the VUV PDEs in 2019 using the small test setup (Section 2.1.2). Fig. 6.18(a) shows the result[*1]. Three irradiated MPPCs show consistent PDE with a non-irradiated MPPC. The other one irradiated MPPC shows inconsistent PDE with others, which may be due to some systematics or mistake in the measurement. In any case, no significant damage was observed even at the much higher irradiation fluence, and the PDE degradation observed at the LXe detector was not reproduced by this γ irradiation. It must be, however, noted that the irradiated MPPCs were kept at room temperature for four years after the irradiation and a possibility of the recovery by an annealing at room temperature cannot be excluded.

6.3.3.3   Neutron irradiation

An irradiation damage with neutrons is also tested. The irradiation was performed at the Tandem electrostatic accelerator at Kobe University in 2015. Deuterons are accelerated to 3 MeV and neutron from $^9\text{Be} + \text{d} \rightarrow {}^{10}\text{B} + \text{n}$ was used for irradiation. The total fluence of each MPPC, which was measured by a ELMA diode, ranges from 5×10^9–2×10^{12} n/cm^2 (1 MeV neutron equivalent), depending on the irradiation time and the geometrical distance from the

---

[*1] Though the I-V curve of the MPPC was checked just after the irradiation as reported in [61], VUV PDE was not measured at that time since its degradation was not expected.
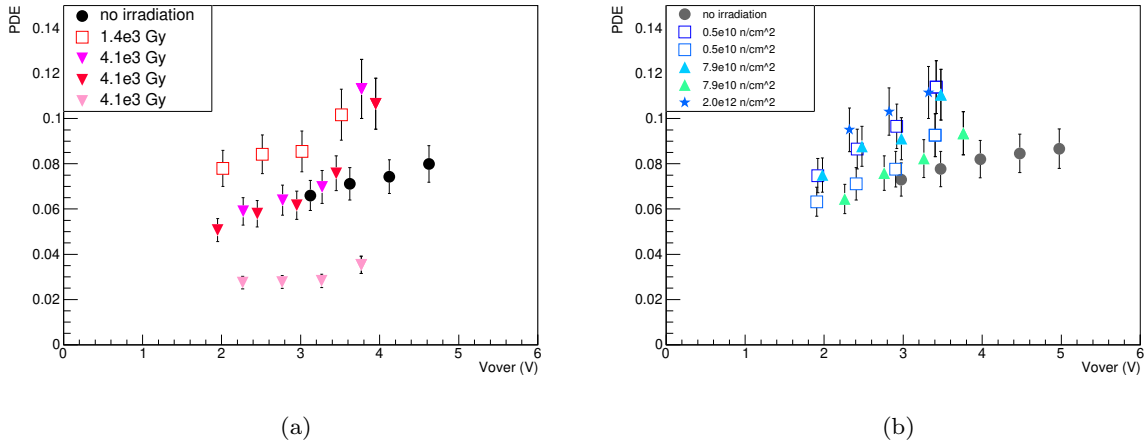
Figure 6.18   VUV PDE of the irradiated MPPCs as a function of the over voltage in (a) gamma irradiation test, and (b) neutron irradiation test. Different colors show different MPPCs. Black markers in (a) and gray markers in (b) are the MPPCs without any irradiation, and the others are the MPPCs with different dose levels.

target [61].

The VUV PDE measured in the small test setup in 2019 is shown in Fig. 6.18(b). No effect of irradiation is observed.

6.3.4   Discussion

Possible cause of PDE degradation

The degradation of the VUV response is observed by the VUV irradiation at room temperature, while its speed is much slower than that at LXe temperature. This suggests that the radiation damage in the detector is caused by a surface damage by the VUV irradiation, and its physics process is enhanced by a factor of $O(10^4)$ at the LXe temperature. Another possible reason of this inconsistency is a wavelength dependence of the damage. Since the light only above 185 nm is guaranteed in the specification of the xenon lamp [60], the wavelength of the irradiated light can be different from the xenon scintillation light peaked at 175 nm. This may affect the speed of the charge accumulation in the passivation layer. The MPPC response to the 190 nm was monitored by using the bandpass filters, and this can also be different from that to the xenon scintillation light, due to a wavelength dependence of the attenuation length in silicon.

In contrast, PDE degradation was not observed by the irradiation of γ-ray and neutrons. It is notable that the degradation observed in the detector could still be explained by these irradiations, if we assume even larger enhancement at LXe temperature ($> O(10^5)$ for γ, $> O(10^6)$ for neutron) is needed.

In any case, temperature dependence of these processes needs to be studied for a further understanding. Therefore, an irradiation test at low temperature is planned.
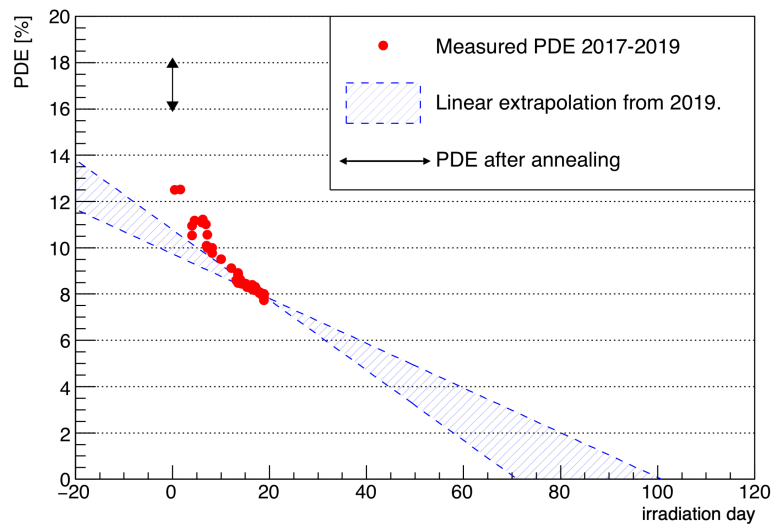
Figure 6.19 Measured PDE history (same as Fig. 6.7) and its extrapolation. The x-axis is the usage time of the MEG II beam. Blue band shows a linear extrapolation of the $9 \pm 2\%$ degradation observed in the run 2019.

Original PDE without irradiation damage

The original PDE of the MPPCs without any radiation damage is not yet fully understood. The PDE of 18–22% was expected from the measurement in the lab test (Section 2.1.3), but it was measured to be 12% just before the beam usage in 2017. The PDE after the annealing in the detector is measured to be 17%, which is slightly lower than the PDE in lab. On the other hand, a full recovery of the PDE by the annealing was observed for the VUV irradiated MPPC at room temperature.

There are several possibilities which may explain these differences, but we cannot reach the conclusion on this point.

- The lower PDE just before the run 2017 may be due to some damage accumulated during the installation to the detector or a beam tuning conducted at the upstream of the πE5 beam line before the run 2017.
- The annealing performed in the detector may still not get saturated. The annealing in the lab test was performed at higher temperature than that performed in the LXe detector.

Detector operation with PDE degradation

From the viewpoint of the detector operation, it is important for the MPPCs to have a sufficient PDE for a sufficient resolution during the data-taking. Fig. 6.19 shows the history of the measured PDE and its extrapolation to the future. It is notable that an extrapolation of the PDE with a good precision is rather difficult since the degradation speed seems gradually slowing down. Thus, only the most optimistic case and the most pessimistic case are discussed.

In the most optimistic scenario, the PDE degradation will get saturated at about 6%, as is

observed in the VUV irradiation at room temperature (Section 6.3.3.1). In the VUV irradiation test, the PDE was saturated at 35% of the original value, namely, PDE of 18–22%, which corresponds to the PDE of 6%. The gradual decrease of the degradation speed also supports this possibility.

In the most pessimistic scenario, the PDE will continue decreasing linearly, and become zero after 70–100 days operation in MEG II beam. The original MEG II DAQ plan assumes a continuous 120 days of data-taking per year, which is not possible in this scenario.

It is notable that the x-axis of Fig. 6.19 is calculated in a conservative way, and the maximal days of continuous operation in the pessimistic scenario may be biased for the following reasons. Firstly, the beam intensity in the run 2019 seems to be about 10–20% higher than the MEG II beam intensity (Section 3.1.3), but this excess is not reflected. Secondly, the smaller LXe light yield of each year (roughly 85%) is corrected in the calculation of x-axis assuming that the VUV photons are the cause of this damage. This leads to an overestimation of the degradation speed if the γ-rays are the cause of this damage. Thirdly, this scenario assumes that the PDE starts from 12% as observed in the run 2017. It implicitly assumes that the PDE is reduced from 17% after the annealing to 12% with little amount of irradiation. These assumption are adopted to be conservative since the PDE without damage is not yet fully understood, though it obviously contradicts the observed PDE history for the annealed MPPCs (Fig. 6.14).

If the degradation does not get saturated at a reasonable PDE, it is needed to anneal all the MPPCs in each year. This can be performed in the annual accelerator shutdown period from January to May. From the experience of the annealing in the detector, the annealing of one MPPC can be finished in two days. If we perform the annealing of 200 MPPCs in parallel [*2], it will take 40 days to anneal all the MPPCs, and can be completed in the shutdown period.

The effect of the PDE degradation on the MEG II branching ratio sensitivity in these scenarios will be discussed in detail in Chapter 11, combined with the expected detector resolutions at the reduced PDE of the MPPCs.

[*2] For this purpose, a voltage supply which can supply sufficient power for 200 channel is needed, and it is already ordered.

Chapter 7

Position resolution

Good resolutions of the LXe detector are important to reduce the accidental background events as shown in Equation 1.1 and to achieve the goal of the MEG II experiment. The resolutions were measured from the data in the pilot run. From this chapter, each measured resolution will be presented.

7.1   Position reconstruction

The hit position of the γ-ray $\vec{x}$ is reconstructed from the light distribution on the MPPCs. The detected number of photons of each MPPC N_{pho} is fitted by a function proportional to the solid angle Ω from the γ hit position subtended by each MPPC. The fit is performed by a minimization of the χ^2 defined as

$$\chi^2 := \sum_{\mathrm{MPPC}} \left(\frac{N_{\mathrm{pho}} - C \times \Omega(\vec{x})}{\sigma(N_{\mathrm{pho}})} \right)^2 .$$

C is a normalization of the light distribution and a nuisance parameter in the fitting. The uncertainty of the N_{pho} of each channel $\sigma(N_{\mathrm{pho}})$ is calculated from the statistical fluctuation of the number of photoelectrons as,

$$\sigma(N_{\mathrm{pho}}) := N_{\mathrm{pho}}/\sqrt{N_{\mathrm{phe}}}.$$

This fit function assumes that all the scintillation light comes from a point, but in reality it is emitted from each point of the electromagnetic shower. Therefore, the fitted position does not correspond to the true hit position, and is biased to the shower development direction. To reduce this bias, the MPPCs used in the position fitting are limited to those around the hit position.

Additionally, a series of corrections is applied. The first type of correction is called "global correction". The direction of the shower development tends to be similar to that of the incident γ-ray. Events with larger $|u|$ tends to be reconstructed larger as is shown in Fig. 7.1. This dependence is corrected as a function of the u. Another correction called "shower correction" is also applied. Even for the events hitting the same position, the shower direction can fluctuate event-by-event. The position fit is performed for several sizes of the fit regions, and the shower

(a) (b)
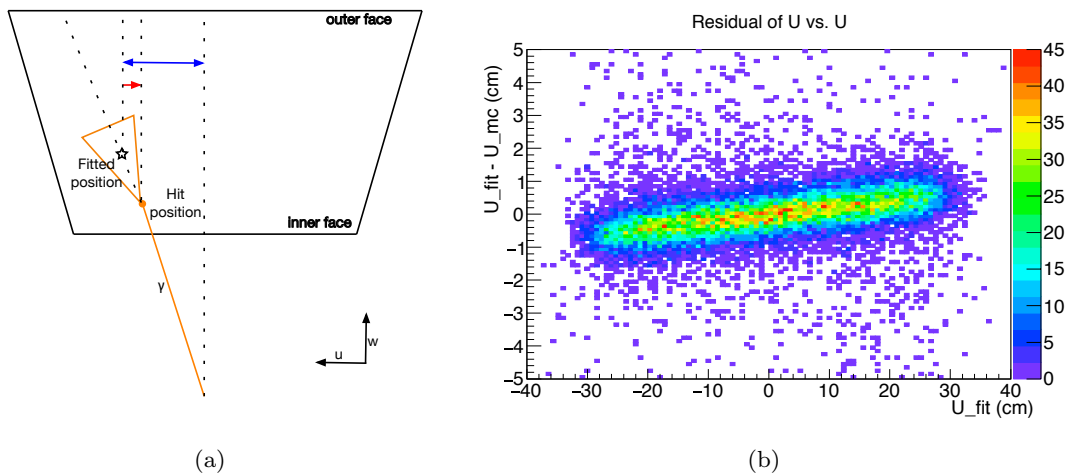
Figure 7.1 (a) Schematic of the global correction. A bias in the reconstruction (red arrow) is corrected by the γ hit position (blue arrow). (b) Correlation between red arrow vs. blue arrow in (a) (in MC).

(a) (b)
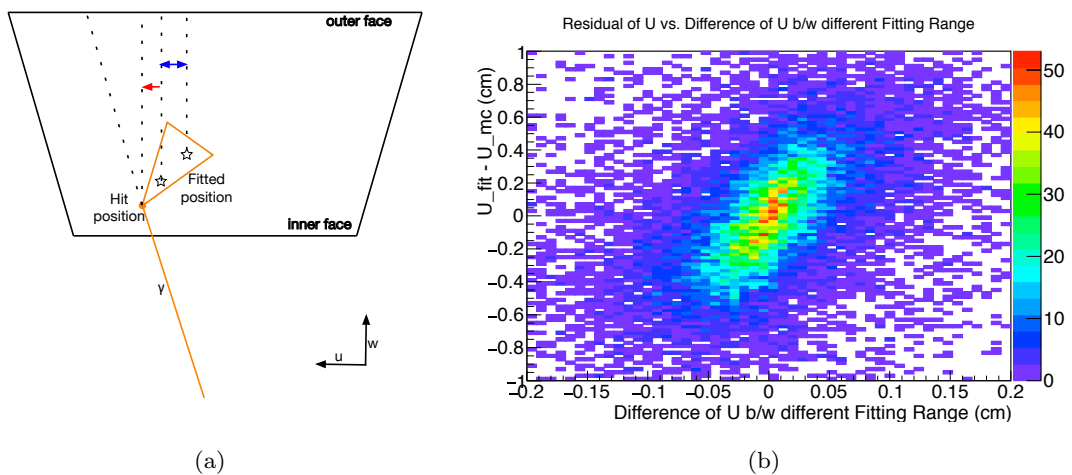
Figure 7.2 (a) Schematic of the shower correction. A bias in the reconstruction (red arrow) is corrected by the difference of the position using different size of the fit regions (blue arrow). (b) Correlation between red arrow vs. blue arrow in (a) (in MC).

direction is reconstructed from the fact that the bias by the shower direction is clearer for wider fit region (Fig. 7.2). The reconstructed direction is utilized to correct the event-by-event fluctuation of the bias.

7.2 Measurement with lead collimator

Thanks to the improved granularity realized by the MPPCs, a better position resolution is expected for the shallow events. To verify this improvement, γ-ray data were taken by placing a collimator in front of the detector as shown in Fig. 7.3(a), so that the resolution can be
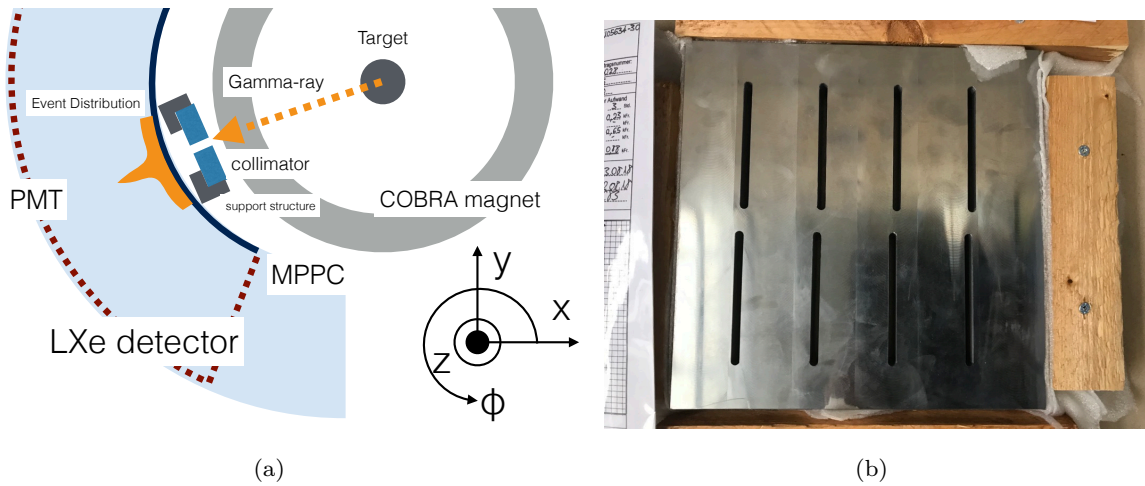
Figure 7.3   (a) Principle of position resolution measurement [34].   (b) Lead collimator $(240 \times 240 \times 25 \, \text{mm}^3)$ with slits of $5 \, \text{mm}$ width used for the resolution measurement. [34].

evaluated from the width of the reconstructed position distribution of the slits. Fig. 7.3(b) shows a collimator used in this measurement. It is a $25 \, \text{mm}$-thick lead on which several slits of $5 \, \text{mm}$ width are implemented with a $50 \, \text{mm}$ spacing. The collimator can be rotated in $90°$ to measure the resolutions of both horizontal and vertical directions. In the pilot runs, the vertical resolution was mainly measured, and horizontal resolution was also measured for a cross check.

In this measurement, a spread of the generation vertex of the γ-rays has to be sufficiently small. As shown in Fig. 7.4, a spread of the γ generation vertex leads to a smearing of the reconstructed edge in the position distribution and an overestimation of the resolution. Since the ratio of the distance between the target and the collimator to that between the collimator and the LXe detector is about $5 : 1$, the size of the smearing is about 20% of the spread of the generation vertex. From this point of view, the γ-rays from the RMDs are not suitable for this measurement because the spot size of the muon beam on the stopping target is $1.2 \, \text{cm}$ for vertical direction, and $4 \, \text{cm}$ for horizontal direction, and the size of the smearing is comparable or larger than the a few millimeter resolution to be measured. Instead, the γ-rays of $17.6 \, \text{MeV}$ from the CW-Li were used for this measurement. The spot size of the proton beam for the lithium excitation is measured to be $0.6 \, \text{mm}$ for vertical direction, and $0.8 \, \text{mm}$ for horizontal direction. Thus, the size of the smearing are less than $0.2 \, \text{mm}$ for both directions, and are negligible. Even though the energy of the CW-Li γ-ray is lower than the signal γ-ray, almost the same position resolution as the signal energy should be obtained because the resolution is not dominated by the statistical fluctuation and does not depend on the γ-ray energy so much.

Fig. 7.5(a) shows a distribution of the reconstructed hit position. An excess of the event rate corresponding to each slit is successfully observed. The peak of each slit is fitted by a simulated hit position distribution smeared by a Gaussian as shown in Fig. 7.5(b), and the sigma of the Gaussian is regarded as the position resolution.

Fig. 7.6 shows the estimated resolution as a function of the reconstructed conversion depth for horizontal direction and vertical direction, respectively. Improvements of the resolutions from
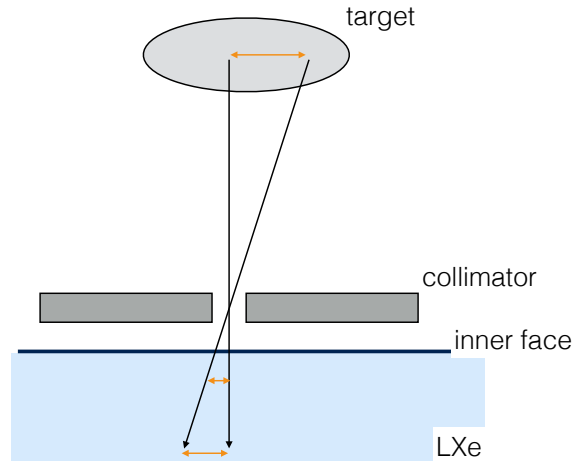
Figure 7.4   Smearing of the reconstructed edge due to the spread of the γ generation vertex [34].
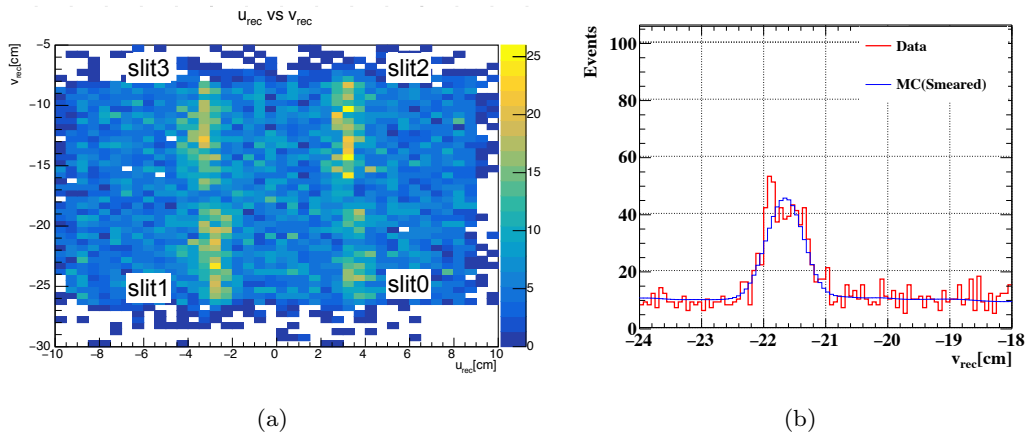
Figure 7.5   (a) Hit position distribution of the γ-rays in the collimator run on the uv plane. (b) Projected position distribution of a slit fitted by the simualted distribution to evaluate the resolution.

those in MEG are confirmed for the shallow events.

The resolution is measured to be slightly worse than expected for the deep events (Fig. 7.6). This kind of degradation only for deep events can be qualitatively due to a statistical fluctuation of the number of photoelectron distribution or a contribution of the noise, but it has not yet been understood quantitatively. Fig. 7.7 shows the measured degradation of the position resolution. Because many of the signal γ-rays hit in the shallow region, the degradation of the position resolution for the deep events does not affect the MEG II branching ratio sensitivity so much. A qualitative discussion of this effect on the sensitivity will be given in Section 11.2.

7.3   Effect of PDE angular dependence

As mentioned in Section 2.1.3 and 6.2, an angular dependence of the MPPC PDE which cannot be explained by that of the Fresnel reflection was found. The PDE for the larger incident angle decreases faster than expected. The light distribution on the MPPCs becomes sharper with this
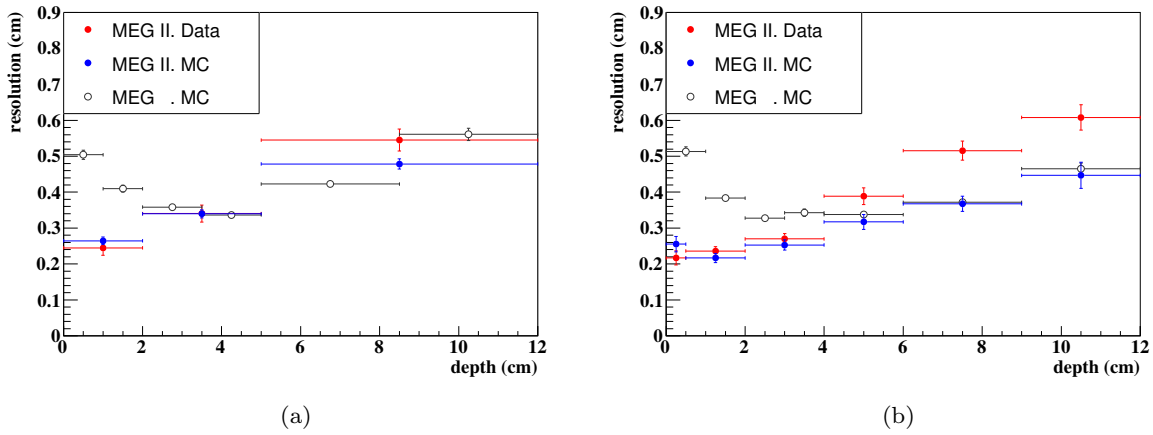
Figure 7.6   Position resolution for 17.6 MeV γ-ray as a function of the conversion depth for (a) horizontal u-direction, and (b) vertical v-direction. The resolutions in MEG are also shown for comparison.
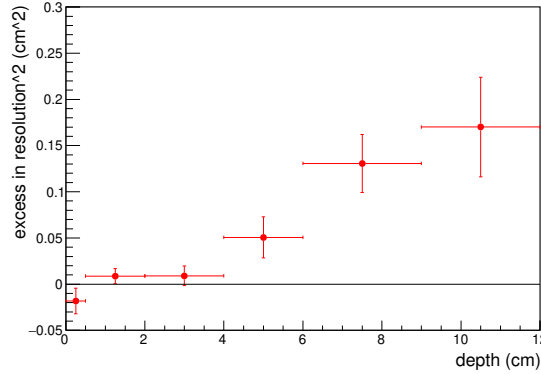

Figure 7.7   Degradation of the vertical position resolution ($\sigma_{\mathrm{meas.}}^2 - \sigma_{\mathrm{exp.}}^2$) as a function of the conversion depth.

dependence, and the conversion depth reconstructed from its width is biased to be shallower.

This bias can be corrected if we know the angular dependence of the PDE correctly. Since the dependence measured in the large chamber and that in the LXe detector are found to be consistent with each other, we can use them for the correction. Nonetheless, an uncertainty of this angular dependence may have to be included as a systematics in the physics analysis.

Here we discuss the effect on the physics analysis in the most pessimistic case, assuming that this unexpected dependence is fully included as systematics. Fig. 7.8 shows the bias in the reconstructed depth when the angular dependence is fully ignored in the reconstruction. The relative size of this bias is constant at the leading order because the shape of the light distribution on the inner face and its change by the angular dependence are independent of the depth, in the assumption that the scintillation light comes from a point light source. The conversion depth is reconstructed to be about 10% shallower in this case.

The bias in the conversion depth leads to that in the reconstructed propagation time of the γ-ray from the decay vertex to the hit position, and that in the reconstructed opening angle
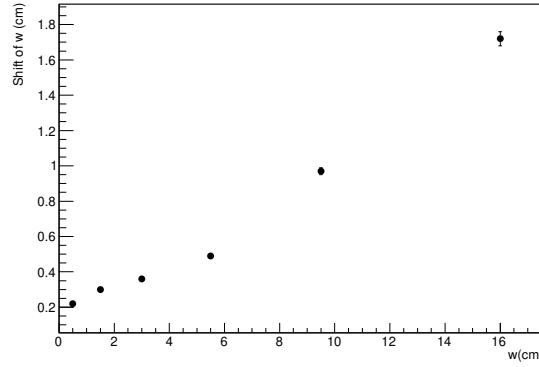
Figure 7.8   Expected bias in the reconstructed conversion depth if we fully ignore the angular dependence of PDE (MC).

(a)   (b)
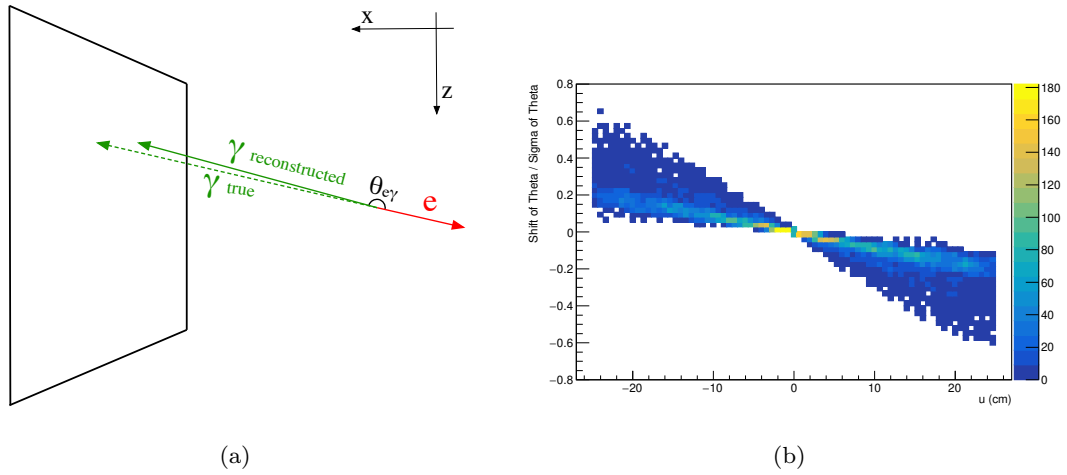
Figure 7.9   (a) Reconstruction of opening angle with a bias in depth. (b) Expected shift of $\theta_{e\gamma}$ for the signal events divided by resolution of $\theta_{e\gamma}$ as a function of z (MC).

of the positron and the γ-ray. The bias in the propagation time is not an issue since it can be measured and corrected by using the CEX data and the RMD events in the energy-sideband of the physics data. On the other hand, the bias in the opening angle cannot be measured. In the search of $\mu \to e\gamma$, the opening angle of the positron and the γ-ray $\theta_{e\gamma}$ is used to distinguish the signal event from background events. For the signal event $\theta_{e\gamma}$ should be back-to-back, while it is randomly distributed for the accidental background. As shown in Fig. 7.9(a), the bias in the reconstructed depth leads to a misestimation of the γ emission direction for large $|z|$ and w, and the reconstructed opening angle of the signal event is deviated from back-to-back. Fig. 7.9(b) shows the shift of $\theta_{e\gamma}$ for the signal events. Even if we ignore the dependence on z and w of this shift, the $\theta_{e\gamma}$ resolution will relatively increase only by 1.2%. The degradation of the branching ratio sensitivity will be only about 0.6%, and thus the uncertainty of the angular dependence will not be crucial for the physics analysis. The degradataion can be even smaller by taking the z and w dependence of the shift into account.

Chapter 8

Timing resolution

8.1 Timing reconstruction

In the LXe detector of MEG, the hit timing of a γ-ray was reconstructed from a weighted average of the timing of each PMT's waveform. The same algorithm is used in MEG II with modifications to match with MPPC signals. The timing of a γ-ray at the hit position t_γ is reconstructed from a minimization of the χ^2 defined as follows:

$$\chi^2 := \sum_{\mathrm{pm}} \chi^2_{\mathrm{pm}},$$

$$\chi^2_{\mathrm{pm}} := \frac{(t_{\mathrm{pm}} - t_{\mathrm{corr}} - t_\gamma)^2}{\sigma^2},$$

$$t_{\mathrm{corr}} := t_{\mathrm{prop}} + t_{\mathrm{walk}} + t_{\mathrm{offset}}.$$

Here, t_{pm} is the timing of each photosensor's waveform, where pm stands for both the MPPCs and the PMTs. t_{prop} is the propagation time from the reconstructed γ hit position to each photosensor, t_{walk} is the time walk effect, t_{offset} is the time offset of each channel due to the individual difference of the cable length and electronics, and σ is the precision of the timing information of this channel. These parameters are estimated beforehand, including its dependence on the number of photoelectrons. The γ-ray timing at the $\mu \to e\gamma$ decay vertex, which is used for the MEG II analysis, is calculated by subtracting γ-ray propagation time from the reconstructed decay vertex to the reconstructed γ hit position. To eliminate the pileup effect, timing information of the photosensors whose chi-square χ^2_{pm} is above a threshold of 10 are removed from the reconstruction.

Even though the timing information of all photosensors can contribute to the timing resolution, only a part of them has a sufficient signal amplitude to have a non-negligible timing resolution. Typically, contributions from channels below 100 photoelectrons are negligible. The timing resolution achievable with the limited channel readout in the 2019 run is good enough to evaluate the resolution achievable with the full channel readout, if the γ-ray events hitting the central region of the readout area are selected.
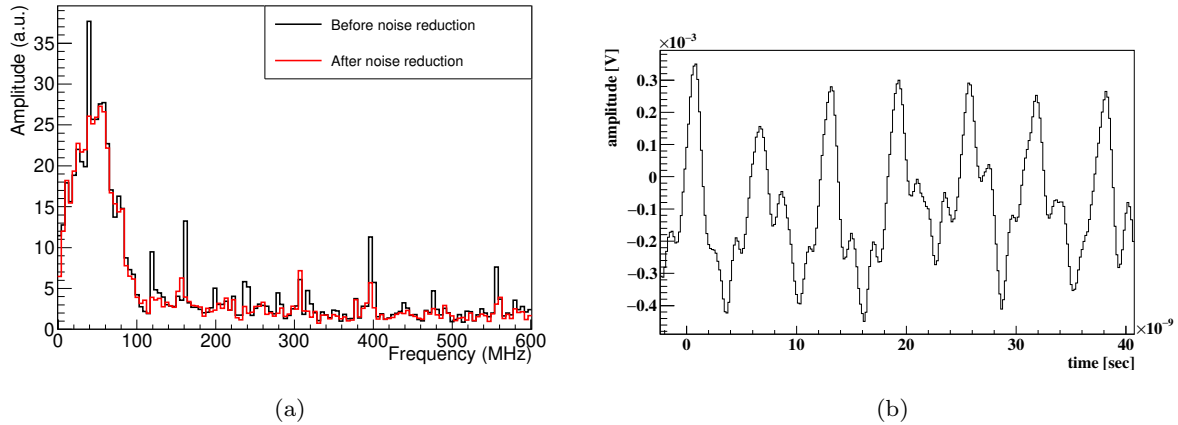
Figure 8.1   (a) Frequency spectrum of a summed waveform of all MPPC channels in a random trigger event. Calculated by a Fourier transformation. (b) A typical waveform template of the noise synchronous to the system clock.

8.2   Waveform analysis

Noise reduction

Since the timing extraction from a sensor waveform is sensitive to high frequency noises, it is useful to reduce the noise as much as possible. As is described in Section 1.8, a dedicated DAQ system is being developed for MEG II, and several new functionalities are integrated on one readout board in that system. As a drawback of this integration, high frequency noise level is increased from MEG.

To improve this situation, noise reduction algorithm have been implemented in the offline analysis. Since the development of DAQ was ongoing, and the noise situation was different for each year, different algorithms were applied. A reduction algorithm used for 2019 data is given as an example. Fig. 8.1(a) shows a frequency spectrum of a random trigger waveform. Peaks at $40, 120, 160, 240$, etc. MHz are clearly seen, and they are coming from the readout electronics whose system clock is 80 MHz. Since these components should be synchronized to the phase of the system clock, they can be reduced if the phase of the system clock to the obtained waveform is known. Since this phase fluctuates event-by-event, one channel on each DRS chip is assigned to measure the sine-wave generated by the system clock and to extract its phase. A template of the synchronous noise to the system clock (Fig. 8.1(b)) is generated for each channel by taking an average of the waveforms in $O(1000)$ random trigger events. The noise in each event is reduced by subtracting this template.

The noise spectrum after the subtraction is shown in Fig. 8.1(a). The peaks from the system clock are removed. Table 8.1 summarizes the noise level. The size of the reduction is the most obvious in 2017 data because part of the noise reduction is implemented in the hardware from 2018 based on the successful reduction of this thesis. Even after the reduction, the noise level is still worse than $0.35\,\mathrm{mV}$ observed in MEG.

To further reduce the noise, a digital low-pass filter (moving average filter of adjacent three

Table 8.1   Noise level of each channel. Average of all the readout channels is shown. The noise level is defined as a standard deviation of the random trigger waveform by the 1.2 GHz sampling.

| Year	noise level (without reduction)	noise level (with reduction)
2017	1.7 mV	0.8 mV
2018-19	0.8 mV	0.7 mV
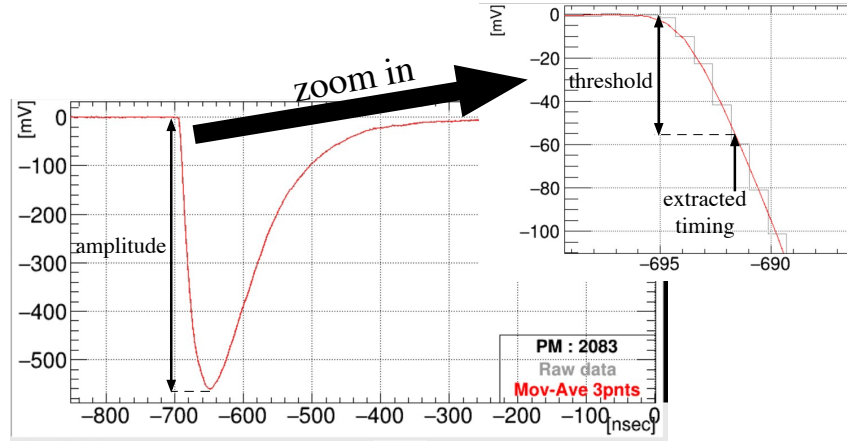
Figure 8.2   Timing extraction from the waveform. The threshold is defined as "amplitude $\times$ r + baseline".

points, a cutoff frequency of 177 MHz) is also applied for the MPPC waveforms. The application of the digital lowpass filter is a trade-off between a reduction of the high frequency noise and a smearing of the sensor waveforms. The strength of this filter is decided to get the best timing resolution.

Timing extraction

The timing from each waveform is extracted by using the constant fraction method in the offline analysis shown in Fig. 8.2. In this method, a threshold is defined to be proportional to the signal amplitude as "amplitude $\times r$ + baseline". The timing of each waveform is obtained from the crossing point of this threshold. This method has an advantage that the time walk is suppressed. The timing resolution is dependent on the constant fraction r, and the fraction is optimized to get the best resolution as discussed in the next section.

8.3   Single channel performance

Calculation of calibration parameters

Since the γ-ray hit timing t_γ is reconstructed from a combination of all channels information, its resolution is much better than the resolution of each channel. Thus the timing resolution of each channel σ can be estimated from the spread of the distribution of $t_{\rm pm} - t_{\rm prop} - t_\gamma$, if the t_γ is known. The time walk $t_{\rm walk}$ can also be estimated from the mean of the distribution.
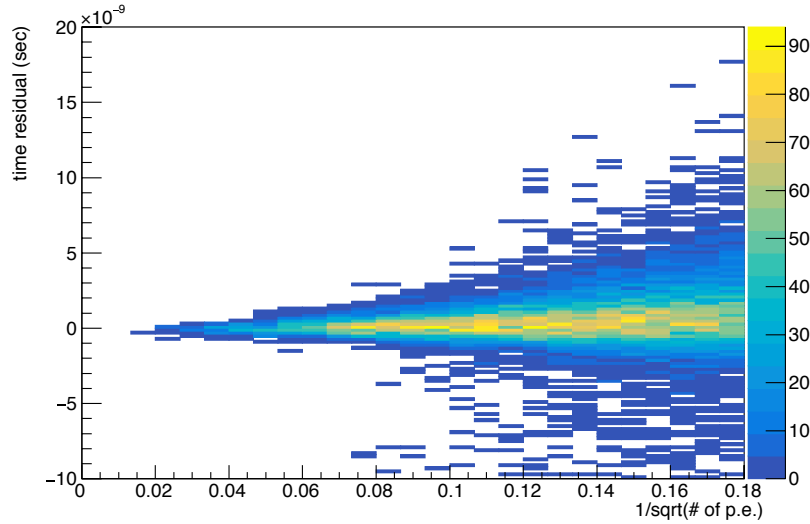
Figure 8.3 $t_{\mathrm{pm}} - t_{\mathrm{prop}} - t_\gamma$ as a function of the number of photoelectron (MPPC LotA, 5% threshold). 116 channels × 1000 events are overlaid.


| (a) | (b) |
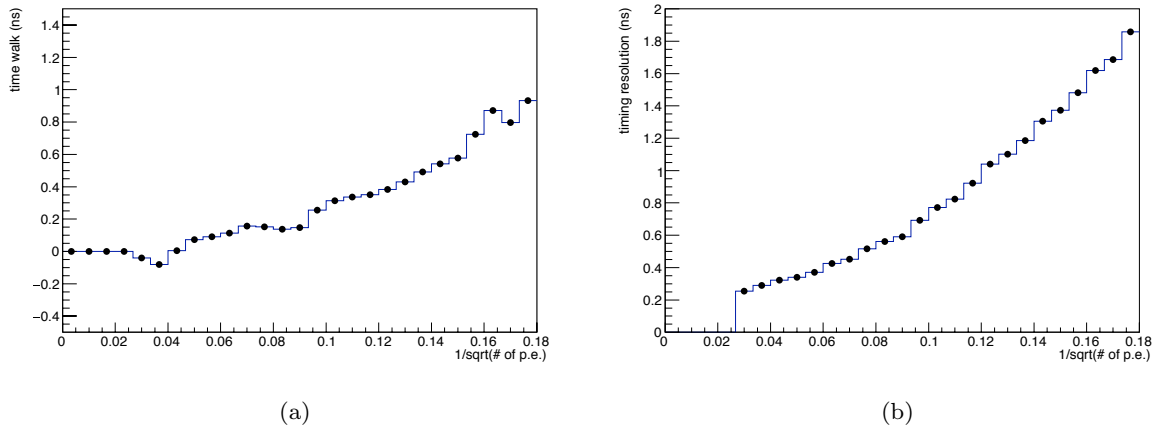
Figure 8.4   Measured (a) time walk t_{walk}, and (b) timing resolution σ of an MPPC as a function of $1/\sqrt{\text{number of p.e.}}$.

The σ and t_{walk} are estimated from the background γ events above $47\,\mathrm{MeV}$ in the 2019 run, by reconstructing t_γ from the obtained parameters iteratively. Fig. 8.3 shows $t_{\mathrm{pm}} - t_{\mathrm{prop}} - t_\gamma$ as a function of the number of photoelectrons, where t_{prop} is calculated from the distance from the reconstructed hit position to each photosensors divided by the effective velocity of light in the LXe ($11.5\,\mathrm{cm/ns}$). Fig. 8.4(a) and Fig. 8.4(b) show the mean and the standard deviation of the slice along y-axis of Fig. 8.3, which are interpreted as t_{walk} and σ respectively. For the MPPCs, these parameters are calculated for each production lot since they can have a different waveform shape due to the different afterpulse probabilities. The outer PMTs and the side PMTs are treated separately, since their resolutions are found to be different. The mean of $t_{\mathrm{pm}} - t_{\mathrm{prop}} - t_\gamma$ on the limit of infinite number of photoelectrons has a channel-by-channel difference, and this is interpreted as a time offset of each channel t_{offset}.
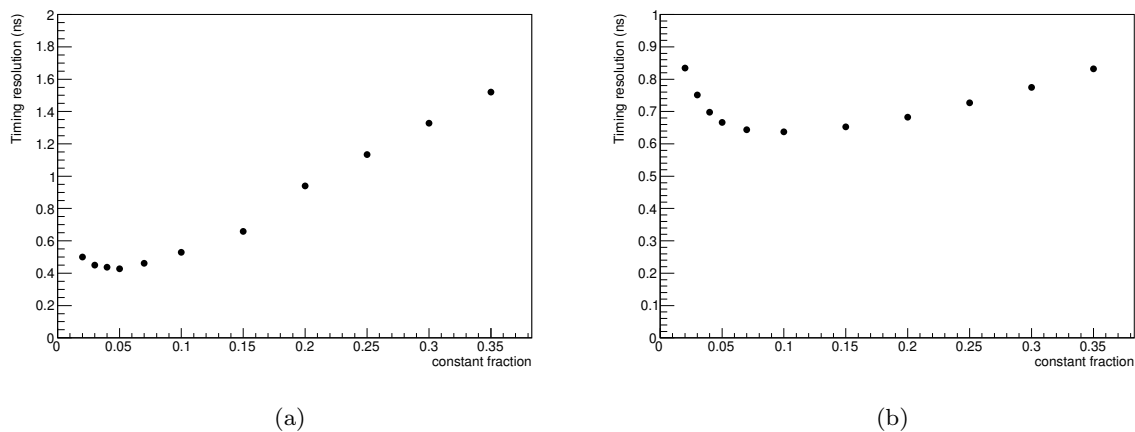
Figure 8.5   The timing resolution σ of a sensor, as a function of the constant fraction r used in timing extraction. Resolution of 200 photoelectron signals is shown. (a) MPPC Lot A, (b) Side PMT.

Timing resolution of each channel

Fig. 8.5 shows the timing resolution of an MPPC and a PMT as a function of the constant fraction r. Lower thresholds gives us better resolutions thanks to the smaller statistical fluctuation for the first arriving photon timing. Due to the effects of the noise and the transit time spread which become dominant at the lower threshold, there is an optimal threshold which gives best timing resolution. Further details on the dependence on the threshold are given in Appendix B. From these plots, the constant fractions are set to 5% for MPPC, and 10% for PMT. Because this dependence on the fraction was not considered in MEG and MEG II design and the fraction was set to 30% in their studies, the optimized threshold leads to a better t_γ resolution and hence a better MEG II branching ratio sensitivity.

Time offset of each channel

Fig. 8.6(a) shows the t_{offset} distribution obtained for the PMT and the MPPC channels. The distribution of the measured time offset of the PMTs is wider than that of the MPPCs. This is likely due to the individual difference of the cable length, since the PMT signal cables are reused from MEG and the treatment at both ends are modified for MEG II. The time offsets of the MPPCs are shown in Fig. 8.6(b), and some dependence on the readout electronics channel is observed.

The time offset of each MPPC channel is also estimated by another independent method [40]. The MPPCs are illuminated by an intense LED light, and the time offset is extracted from the time difference of each channel's waveform. Dependences on the incident angle and the distance from each LED to each MPPC, and an effect of the time walk are corrected. Fig. 8.7 shows a comparison of the time offsets estimated from the two methods, and a clear correlation is observed.

(a)   (b)
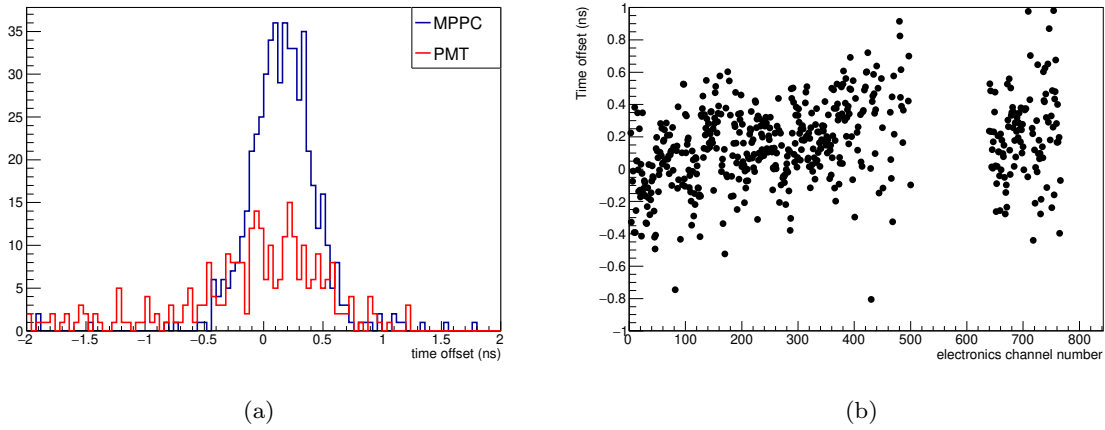
Figure 8.6   (a) Measured time offset of each channel. (b) Time offset of the MPPCs as a function of the electronics channel number.
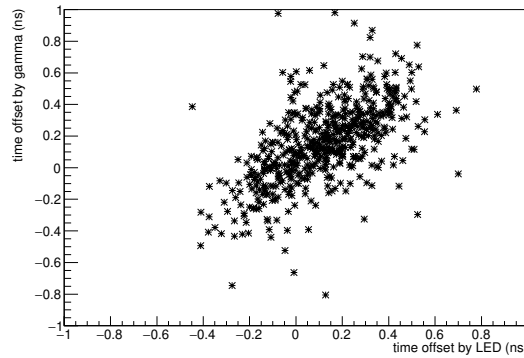

Figure 8.7   Time offset estimated from gamma (in this thesis) vs. time offset estimated from LED (in [40])

8.4   Detector performance

There are three variables which describe the detector timing resolution. One is the absolute timing resolution which is a spread of the difference between the reconstructed timing and its true value. This is the resolution directly related to the analysis of the $\mu \to e\gamma$ search. In the MEG LXe detector, the absolute resolution was directly measured in the CEX run. In a CEX event, two coincident γ-rays are emitted. The timing of one γ-ray measured by plastic scintillators was used as a time reference. However, the data-taking of the CEX has not yet been performed for MEG II (Section 3.1), and its direct measurement is still not possible. In this thesis, instead of the direct measurement, the absolute resolution is estimated from the simulation which is validated by the other two resolutions measured with data.

The second resolution is the intrinsic timing resolution estimated from an even-odd analysis. In the even-odd analysis, photosensors are subdivided into two groups (e.g. sensors with even channel numbers, and odd channel numbers), and the timing reconstruction is performed independently for both groups. The intrinsic resolution is estimated from the difference of the

(a)   (b)
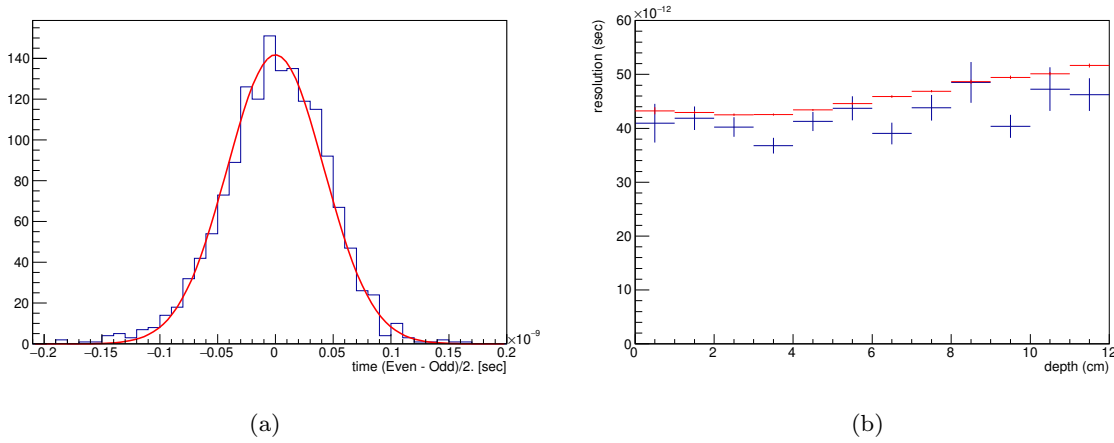
Figure 8.8   (a) Distribution of $t_\gamma(\text{even})/2 - t_\gamma(\text{odd})/2$ of the background γ-ray data. In-
trinsic timing resolution is estimated to be $40(1)\,\text{ps}$ from this plot. (b) Intrinsic resolution
(blue) and combined resolution of all photosensors (red) as a function of the conversion
depth of γ.

reconstructed timings. This intrinsic resolution is a part of the absolute resolution. For example,
a precision of the propagation time decided by the hit position resolution is included only in
the absolute resolution. An effect from a coherent noise is also included only in the absolute
resolution.

The third one is the combined precision σ_total of all photosensors, defined as follows:

$$1/\sigma_\text{total}^2 := 1/\sigma_\text{MPPC}^2 + 1/\sigma_\text{PMT}^2 \tag{8.1}$$

$$1/\sigma_\text{MPPC}^2 := \sum_\text{MPPC} 1/\sigma^2 \tag{8.2}$$

$$1/\sigma_\text{PMT}^2 := \sum_\text{PMT} 1/\sigma^2, \tag{8.3}$$

where σ is the timing resolution of each channel estimated by the method mentioned above.
This combined precision should be consistent with the intrinsic resolution.

The intrinsic resolution and the combined precision are estimated from the background γ
events above $47\,\text{MeV}$ in the 2019 run. Fig. 8.8(a) shows the distribution of the difference
between γ timing reconstructed from the even channels and that from the odd channels. Intrinsic
resolution of $40(1)\,\text{ps}$ is achieved. The intrinsic resolution with MEG's threshold ($r = 30\%$) in
this data set is estimated to be $56(2)\,\text{ps}$. Thus 30% improvement is achieved by the threshold
optimization. As shown in Fig. 8.8(b), the combined precision is found to be consistent with
the intrinsic resolution including its dependence on the conversion depth.

These results are compared with the simulation. To correctly introduce the real noise situation
into the simulation including its coherence between channels, the measured random trigger
waveforms are added to the simulated waveforms. The estimation of the calibration parameters
and the reconstruction of the timing are applied to the simulated waveforms in the same way
as data. Table 8.2 compares obtained detector resolutions with different conditions. MC and
data are consistent with each other with a few picosecond precision. Absolute timing resolution

is estimated to be 53 ps by this simulation, which is better than the 62 ps resolution achieved in MEG.

Table 8.2   Comparison of the detector timing resolution between MC and data.

Variable	MC	data
Combined precision (MPPC only)	71 ps	71 ps
Combined precision (PMT only)	57 ps	55 ps
Combined precision (MPPC and PMT)	44 ps	43 ps
Intrinsic resolution (MPPC and PMT)	43 ps	40 ps

Chapter 9

Energy resolution

In this chapter, the performance of the energy measurement by the LXe detector is discussed. In terms of the upgrade from MEG, there are two aspects to be checked in MEG II.

One is a conversion depth dependence of the energy resolution. In MEG, due to the non-uniformity of the scintillation readout, the energy resolution for the shallow events was worse than that for the deep events. This depth dependence is expected to disappear, and the resolution for the shallow events is expected to improve, thanks to the improved uniformity realized by the MPPCs as explained in Section 1.6.3.2.

The second one is a consistency with the simualted energy resolution. The measured energy resolution was worse than expected in MEG, and there was an unknown contribution in the resolution as large as 1.5% (Section 1.6.3.2). The reason of this unknown contribution has not been understood yet, and it can also remain in MEG II. Since the energy resolution in MEG II expected from the simulation is only about 0.7%, this unknown contribution can become a dominant contribution. In an optimistic scenario, this contribution is related to the behavior of the PMTs, and gets smaller in MEG II. In a pessimistic scenario, this contribution is due to some intrinsic property of the LXe or that of our LXe detector, and remains unchanged.

In the Section 9.1, the energy reconstruction algorithm, which is common both in MEG and MEG II, is summarized. A study on the unknown contribution obseerved in MEG is given in Section 9.2. The measured energy resolution in MEG II from the pilot runs is shown in Section 9.3.

9.1 Energy reconstruction

The energy of the γ-ray E_γ is reconstructed from the weighted sum of the detected number of photons on each photosensor.

$$E_\gamma = C \times \sum_{\mathrm{pm}} N_{\mathrm{pho,i}} \times w_i$$

$$N_{\mathrm{pho,i}} = Q_i/Gain_i/ECF_i/QE_i \tag{9.1}$$

The number of photons $N_{\mathrm{pho,i}}$ on each sensor is calculated from the integrated charge Q_i of each sensor waveform. This is a sum with a set of weights w_i defined for each sensor to achieve

uniform response in the whole detector. This weight is calculated from the size of the insensitive area around each sensor divided by the size of its sensitive area. A factor C is used to convert the sum of the number of photons to the energy. In MEG, this is calculated from the monochromatic γ-ray sources of different energies. In the analysis of the MEG II pilot runs, it is defined from the 17.6 MeV peak in the CW-Li data, which is the only available monochromatic data for the present. An offset of the reconstructed energy is monitored independently from the random trigger data.

A hit position dependence of the reconstructed energy is evaluated from the monochromatic γ-ray data, and is used for a further correction of the non-uniformity. This is to correct possible errors in the calibrated photosensor responses, and to correct a position dependent photon collection efficiency especially in the partial readout of the detector in the pilot runs. A correction by the solid angle from the hit position subtended by the PMTs applied in MEG is no longer adopted in MEG II.

It is often useful to define the energy reconstructed from a part of the photosensors. For example, "energy from MPPC" stands for the energy reconstructed from a weighted sum of the MPPC signals. Energies from the MPPCs, the PMTs, the even channels, the odd channels, etc. are used in this chapter.

9.2   Unknown contribution in MEG

As is mentioned in the previous section, the unknown contribution observed in MEG can be crucial in the energy resolution in MEG II. However, its cause has been poorly discussed in the previous studies, and we review it in this section.

Fig. 9.1(a) shows the measured energy resolution in MEG as a function of the energy. The resolution follows a combination of a constant term and a $1/\sqrt{E_\gamma}$ term. However, the energy dependent term in data is larger than that in MC by a factor of about 2.5 ($= \sqrt{108/17}$). This discrepancy of the energy dependent term is 1.3% for the signal γ-ray, and will explain the most of the observed 1.5% unknown contribution.

The simplest hypothesis to explain the discrepancy proportional to the $1/\sqrt{E_\gamma}$ is to assume a larger statistical fluctuation of the detected number of photoelectrons on the PMTs. In the ideal case, energy resolution of this detector is not affected by the statistical fluctuation. By using the PMTs with a 22% QE, the total detected number of photoelectrons becomes about 3.9×10^4 for the 52.8 MeV γ-ray, and the statistical contribution in the energy resolution is expected to be $\sqrt{14/E_\gamma(\mathrm{MeV})}\%$. Thus, most of the energy dependence in the simulated resolution is due to this statistical fluctuation effect. There are two possibilities which can enlarge this statistical contribution in data. The first is that the ENF of the PMTs is as large as 6.4. As is discussed in Section 2.1.3, a double photoelectron emission from a single VUV photon is reported for some of the VUV-PMT, which can increase the ENF of the PMTs. The second is the smaller QE of the PMT. If the real QE of the PMTs is 3.5%, while it is measured to be 22%, statistical contribution can become larger by a factor of 2.5. It is notable that this assumption is not

consistent with independent QE measurements by HPK.

In this thesis, these hypotheses are tested by directly evaluating the statistical contribution from the PMTs by an even-odd analysis. The energies of the γ-ray from the even channels and the odd channels are reconstructed independently, and the resolution is estimated from an event-by-event fluctuation of their difference. In the case of the large ENF or the low QE of the PMTs, its statistical effect surely appears in the even-odd resolution because it is an independent stochastic process on each PMTs. Since other fluctuations can also contribute to the even-odd resolution, the even-odd resolution gives us an upper limit on the statistical fluctuation. For example, if the hit position of the γ-ray is too close to the PMTs, detected number of photons on an even channel and that on an odd channel can be different. This difference fluctuates depending on the hit position and shower direction, and contributes to the even-odd resolution.

Fig. 9.1(b) shows the measured difference of the energy from even channels and odd channels for CW-Li γ-ray. Here the PMTs located on the outer face or the third–sixth columns of the lateral faces, and the events hitting rather deep region $3 < w < 4$ cm are used, to suppress the other contribution by rejecting PMTs near the γ hit position. The even-odd resolution is measured to be 1.46% at the statistics of 1.06×10^4 photoelectrons. The enhancement of the statistical contribution from the PMTs is estimated to be 1.50 ($= 1.46\% \times \sqrt{1.06 \times 10^4}$) at most. This is too small to explain the observed degradation by a factor of 2.5.

As a consequence of this observation, it turns out that the unknown contribution is not due to a stochastic process on each PMT. Another possibility like unexpected non-uniformity of the readout by an incident angle dependence of the PMT QE also seems not the case, since its effect should be independent of the γ-ray energy at the leading order. Therefore, the PMT behavior is not favored as a source of the unknown contribution, and replacing the PMTs to the MPPCs does probably not help its reduction.

9.3   Energy measurement performance in MEG II

9.3.1   Expected energy resolution in pilot run

In the pilot runs, only a quarter of the photosensors was read out due to the limited number of channels, and the energy of γ-ray was reconstructed from the sum of their signals. To ensure that the most of the signals are contained in the readout region, following event selections are applied for the energy resolution study. Events hitting the central area of the MPPC readout region shown in Fig. 9.2 ($|u| < 9$ cm and $|v + 17| < 9$ cm) are selected. Events hitting very deep region ($w > 12$ cm) are rejected, since their scintillation light distributes wider than the MPPC readout area. Cosmic-ray events are also rejected by applying a selection of "$E_\gamma(\mathrm{MPPC}) > E_\gamma(\mathrm{PMT})/6$". This selection works since the cosmic-rays do not enter the LXe detector from the inner face and a fraction of the observed charge on the MPPCs becomes smaller than that for the γ-rays.

Fig. 9.3 shows the simulated energy spectrum for the monochromatic signal γ-rays. Here, the

(a)   (b)
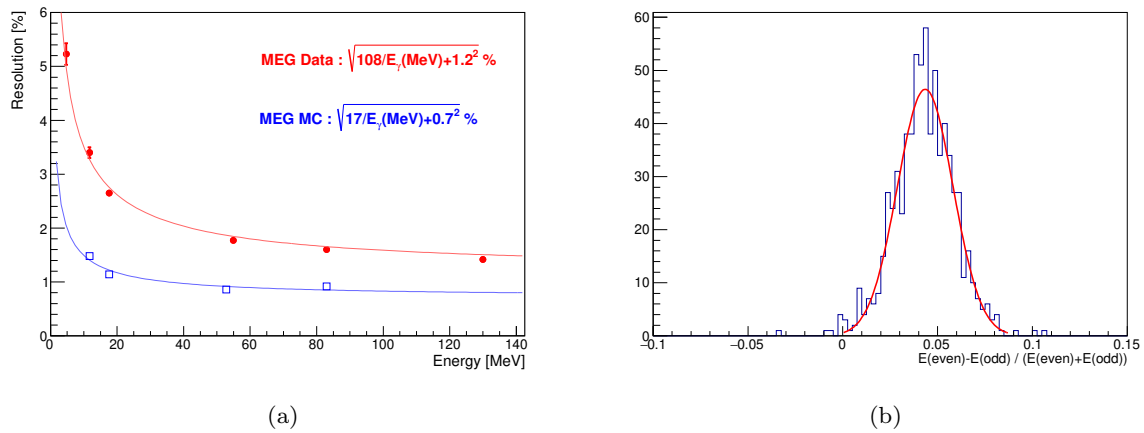
Figure 9.1   (a) Energy resolution in MEG as a function of the γ-ray energy. The resolution for deep events ($w > 2\,\mathrm{cm}$) is shown where the unknown contribution is more obvious. The measured resolution (red) is taken from [43]. The expected resolution from MC (blue) is added by the author. (b) Difference of reconstructed energies for even channel and odd channel in the CW-Li data in MEG, $(E_\gamma(\mathrm{even}) - E_\gamma(\mathrm{odd}))/(E_\gamma(\mathrm{even}) + E_\gamma(\mathrm{odd}))$. Events hitting in a local region "$|u| < 10\,\mathrm{cm}$ & $|v| < 10\,\mathrm{cm}$ & $3 < w < 4\,\mathrm{cm}$" are selected. Due to the limitation of the granularity of the readout, the electromagnetic shower looks differently from the even channels and the odd channels, and the peak position is slightly deviated from zero.
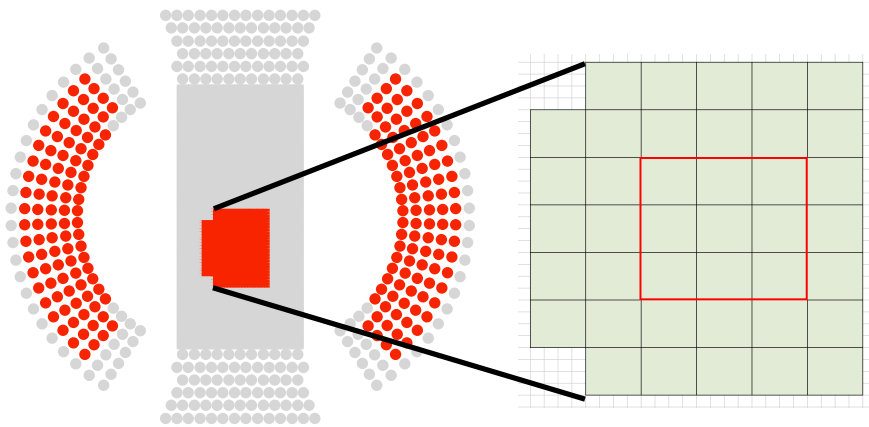

Figure 9.2   Analysis area in run 2019. Green shows MPPC readout area, and red box ($18(u) \times 18(v)\,\mathrm{cm}^2$) shows the area used for the energy resolution estimation. Each green box in the right figure corresponds to a group of 4×4 MPPCs.

measured photosensor performance is simualted including the lower PMT gain and the lower MPPC PDE. The energy resolution is defined from the spread of the upper side of this spectrum as shown in Table 9.1. The same energy resolution is achievable with the limited channel readout by applying the event selection. The low energy tail of this spectrum is caused by the energy escape from the electromagnetic shower and the energy loss before reaching the detector, and is also not affected by the readout channels.

(a)

(b)
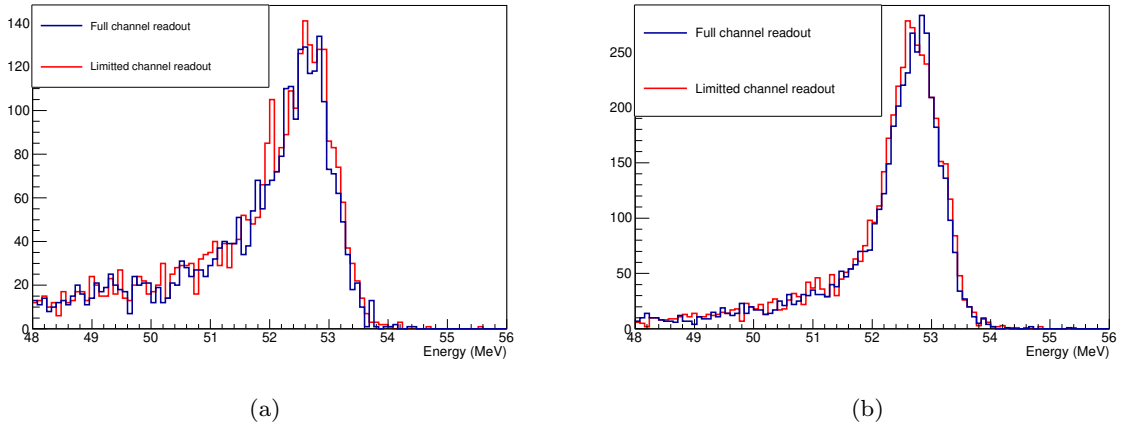
Figure 9.3 Reconstructed energy spectrum in the simulation for signal 52.8 MeV γ-ray after the event selection described in the main text. (a) Shallow event ($w < 2\,\mathrm{cm}$), (b) deep event ($w > 2\,\mathrm{cm}$).

Table 9.1 Expected energy resolution in MEG II for the signal 52.8 MeV γ-ray

	Full channel readout	Limited channel readout
$w < 2\,\mathrm{cm}$	0.72(1)%	0.73(1)%
$w > 2\,\mathrm{cm}$	0.70(1)%	0.76(1)%

9.3.2 Energy offset

In the pilot run, a fluctuation of the reconstructed energy offset was found. The offset fluctuation was monitored by the random trigger. Fig. 9.4(a) shows the averaged random trigger waveforms of a channel measured at different temperatures of the readout electronics. A slope of the waveforms correlated with a temperature can be seen. This is probably due to a temperature dependence of a leakage current of the DRS cells. As is described in Section 1.8, in the WaveDREAM system a waveform is stored in the DRS cells when the trigger is fired and the charge in each cell is read out in the order of time. Some part of the stored charges can be lost due to the leakage current from the cells depending on the elapsed time before the readout, and this leads to a slope of the waveforms. The leakage current is known to be dependent on the temperature of the electronics which is affected by the temperature of the detector hut. The heat generation at the amplifiers implemented on the WDBs, which can be turned on and off for each purpose, is another source of the temperature fluctuation.

To correct this offset, the temperature of each DRS chips was read out during the data-taking. A template of the slope like Fig. 9.4(a) was generated at each temperature for each channel, and is used for the correction. Fig. 9.4(b) shows the energy offset history in the run 2018. The fluctuation in the peak-to-peak is reduced from 0.9 MeV to 0.1 MeV by this correction, and a sufficient stability for the search of $\mu \to e\gamma$ is achieved[*1]. Additionally, an air-conditioning

---

[*1] Long term stability of the γ-ray energy was measured to be 0.2% in MEG. It was included as a systematics in the analysis, and its effect on the branching ratio sensitivity was negligible.

(a)

(b)
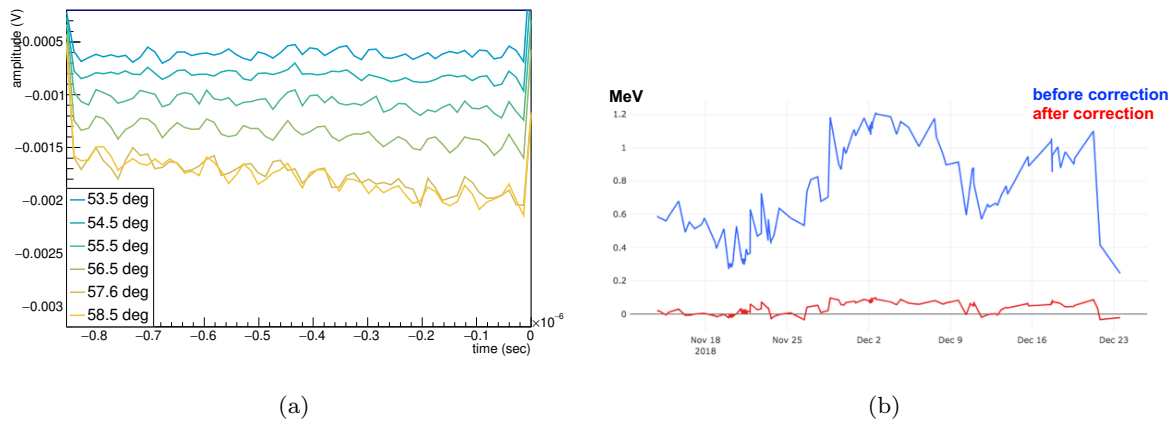
Figure 9.4   (a) Averaged random trigger waveforms of a channel at different temperature of electronics. Declining slope is observed at higher temperature due to larger leakage current. (b) History of energy offset in run 2018 calculated from the random trigger waveforms of all read out channels.


(a)

(b)
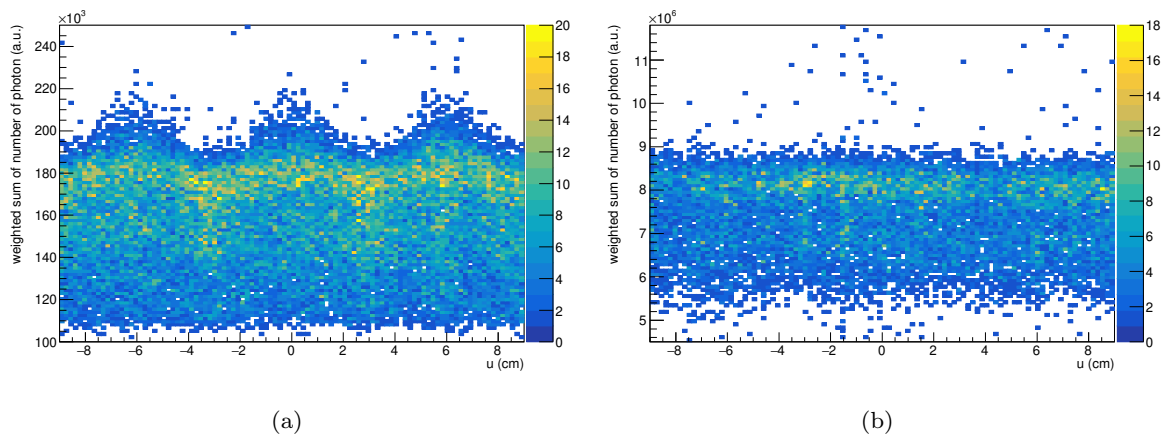
Figure 9.5   Reconstructed γ-ray energy as a function of the γ-ray hit position for shallow events ($w < 1.5\,\text{cm}$). The same scale of the y-axis is used for both plots. Measured spectrum of 17.6 MeV γ-ray from CW-Li is shown. The energy before correcting the hit position dependence is shown. (a) MEG, (b) MEG II.

system was introduced in the detector hut from 2019. This improved the daily temperature fluctuation from about 2 K in the run 2018 to about 0.6 K in the run 2019 (peak-to-peak).

9.3.3   Uniformity of the readout

In MEG, there was a periodical bias on the reconstructed energy for the shallow events correlated with the PMTs placed with 6.2 cm spacing. This bias is expected to be reduced in MEG II thanks to the uniformity of the readout realized by the MPPCs. Fig. 9.5 compares a position dependence of the reconstructed energy measured in MEG and MEG II. An improvement in the uniformity is observed in MEG II.
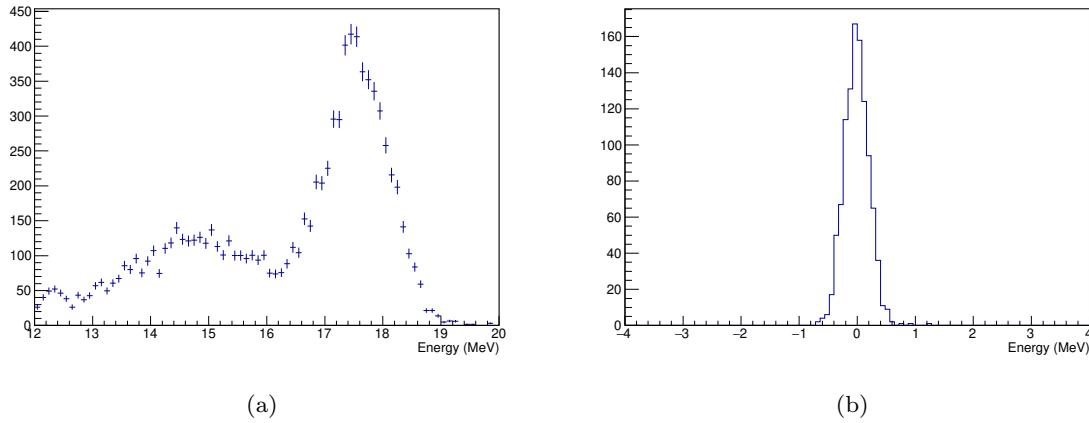
Figure 9.6   (a) Reconstructed energy spectrum of the CW-Li. (b) Reconstructed energy of the random trigger waveform. This is calculated from a random trigger run, and the effect of the offset fluctuation (Section 9.3.2) is negligible in one run.

9.3.4   Energy resolution at low energy ($17.6\,\mathrm{MeV}$ γ-ray)

The energy resolution for the $17.6\,\mathrm{MeV}$ γ-ray was measured by using the CW-Li (Section 2.5). This measurement is useful to know the unknown contribution which is more obvious for the low energy γ-rays, though it does not directly give us the resolution for the signal energy γ-ray. Fig. 9.6(a) shows the reconstructed energy distribution after the non-uniformity correction. The energy resolution is estimated to be $3.1(1)\%$ from the $17.6\,\mathrm{MeV}$ peak. This is much worse than the 1.0% resolution expected from the MC.

A part of the difference between the MC and the data is due to a noise from the readout electronics. Fig. 9.6(b) shows the reconstructed energy distribution of the random trigger waveform, and its spread is $0.21\,\mathrm{MeV}$. This corresponds to 1.2% of the CW-Li energy. Thus, the intrinsic energy resolution of the LXe detector should be $2.8(1)\%$. This is consistent with the 2.8% resolution achieved in MEG for the deep events ($w > 2\,\mathrm{cm}$). The unknown contribution seems still existing in MEG II.

Fig. 9.7 shows the conversion depth dependence of the fitted spread of the $17.6\,\mathrm{MeV}$ peak. The spread of the peak is affected by an energy escape from the electromagnetic shower because the escape peak at $17.1\,\mathrm{MeV}$ is smeared by the energy resolution of about $0.5\,\mathrm{MeV}$. The energy escape can happen more often for the shallow events, and the fitted spread becomes larger for those events, even if the energy resolution is independent of the conversion depth. Fig. 9.7 also shows the expected spread of the $17.6\,\mathrm{MeV}$ peak assuming an additional unknown term of 2.6% independent of the depth. The observed depth dependence can be explained by a constant energy resolution.

Possible causes of the worse energy resolution are examined, and the results are summarized below.
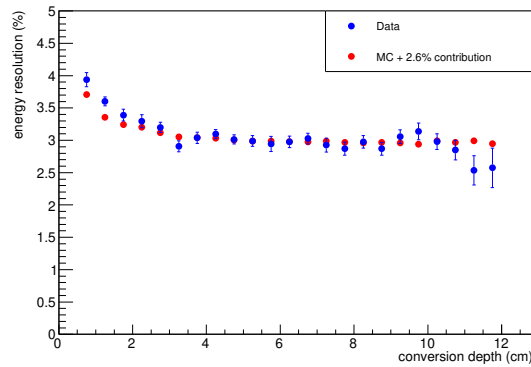
Figure 9.7　Fitted sigma for the 17.6 MeV peak of CW-Li. Observed depth dependence is consistent with an expectation from the simulation.


(a)　　　　　　　　　　　　　　　　　　　(b)
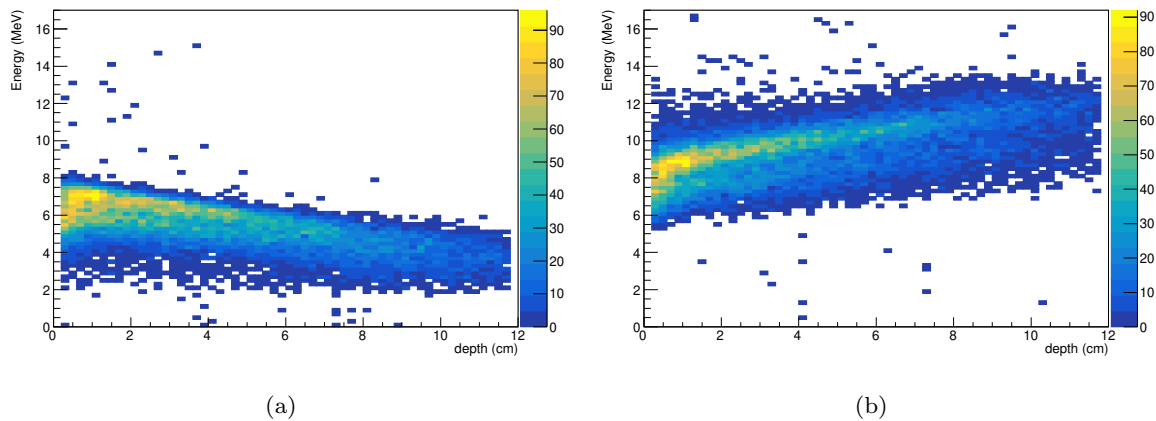
Figure 9.8　Measured energy of CW-Li as a function of the conversion depth, (a) only from MPPC signals, (b) only from PMT signals.

MPPC and PMT

The reconstructed energy only from the MPPCs and the PMTs are compared between the MC and the data. If we decompose the γ-ray energy for the CW-Li into the MPPC energy and the PMT energy, each of them have a conversion depth dependence as shown in Fig. 9.8. Fig. 9.9 shows their reconstructed energy spectra after correcting the dependence on the conversion depth. The spread of the upper side of the measured spectrum is larger than MC for both energies. Therefore, the degradation of the resolution does not seem to depend on the photosensor type.

Stability

An instability of the signal gain can lead to a worse resolution. Fig. 9.10 shows the fitted CW-Li peak as a function of the time. No significant fluctuation is observed, and cannot be a reason of the worse resolution.

(a)   (b)
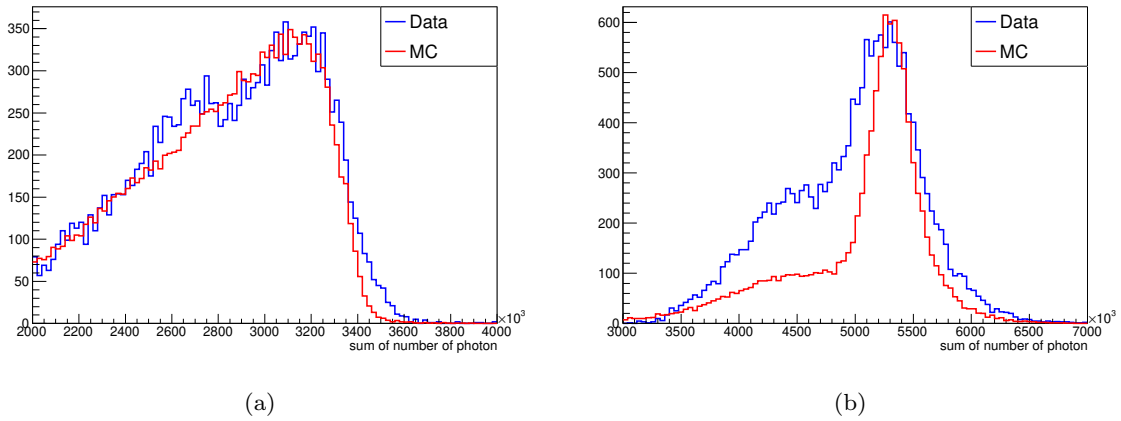
Figure 9.9   The energy spectrum of CW-Li, (a) only from MPPC signals, (b) only from PMT signals. The excess of the both measured spectra in the lower energy region are just because the event rate of 14.7 MeV peak is not correctly simulated.
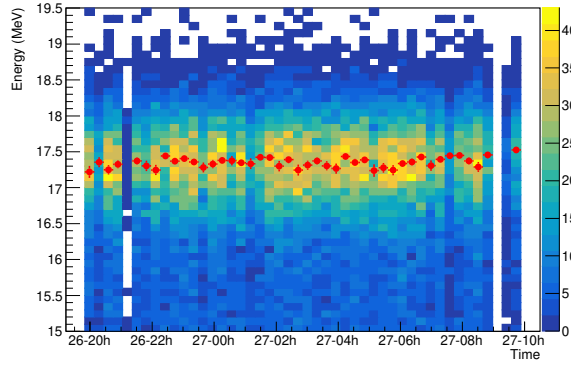

Figure 9.10   Reconstructed energy of the CW-Li as a function of time. Red markers show the fitted peak.

9.3.5   Energy resolution at signal energy ($52.8\,\mathrm{MeV}$ γ-ray)

The energy resolution for the signal energy γ-ray is evaluated. The background γ-rays which mainly come from the RMDs on the target are used, instead of the quasi-monochromatic 55 MeV γ-ray from the CEX used in MEG.

The measured spectrum of the background γ-ray in the run 2019 is fitted by an expected spectrum. The fit is performed by a binned-likelihood method. The likelihood $\mathcal{L}(\boldsymbol{p})$, and its negative log likelihood nll are defined as

$$\mathcal{L}(\boldsymbol{p}) := \prod_{b=0}^{N-1} \frac{f_b(\boldsymbol{p})^{h_b} e^{-f_b(\boldsymbol{p})}}{h_b!},$$

$$nll := -\ln \mathcal{L}(\boldsymbol{p}) = -\sum_{b=0}^{N-1} \{h_b \ln f_b(\boldsymbol{p}) - f_b(\boldsymbol{p})\} + const. \,,$$

where $\{h_b | 0 \leq b < N\}$ is a N-bin histogram of the measured spectrum, and $\{f_b(\boldsymbol{p}) | 0 \leq b < N\}$ is that of the expected spectrum. The expected spectrum is a function of the fit parameters

$\boldsymbol{p} = (Norm, Scale, \sigma)$:

$$f(x|\boldsymbol{p}) = Norm \times \int f_{\mathrm{MC}}(x/Scale + s)e^{-s^2/2\sigma^2}ds + f_{\mathrm{CR}}(x).$$

The simulated energy spectrum f_{MC} is convoluted with an additional resolution σ. An energy scale $Scale$ and an overall rate $Norm$ are also considered as nuisance parameters. A contribution from the energy spectrum without the beam usage f_{CR} is also included based on the spectrum measured without muon beam[*2].

Fig. 9.11 shows the background spectrum measured at the reduced intensity $(0.7 \times 10^7 \, \mu/\mathrm{s})$ and at the MEG II intensity $(7 \times 10^7 \, \mu/\mathrm{s})$, together with the expected spectra. Fig. 9.12 show the excesses of the negative log likelihood from their local minimum. The best estimate of the fitted parameters are

$$Scale = 1.013(3), \ Norm = 1.16, \ \sigma = 1.6(2)\% \quad \text{(for Reduced intensity)},$$
$$Scale = 1.007(1), \ Norm = 1.13, \ \sigma = 1.5(1)\% \quad \text{(for MEG II intensity)}.$$

The larger uncertainty of the reduced intensity data is just due to the limited statistics. The fitted energy scales of the background γ-rays agree with that of the CW-Li γ within 1% precision. The uncertainty in the energy scale will be reduced in the physics data-taking by the CEX measurement whose energy $(55\,\mathrm{MeV})$ is much closer to the signal energy $(52.8\,\mathrm{MeV})$ than the CW-Li $(17.6\,\mathrm{MeV})$. The overall rate of the background γ-rays estimated from the fitting is 10–20% higher than that expected at the MEG II beam intensity. This is likely due to the beam rate higher than the MEG II intensity as mentioned in Section 3.1.3. The energy resolution is estimated to be 1.7(2)% for the reduced intensity, and 1.7(1)% for the MEG II intensity, respectively, from a combination of the fitted σ and the 0.7% energy resolution in the simulation (Section 9.3.1). These resolutions should include the noise contribution, but it is only 0.4% for the signal energy γ-ray (Fig. 9.6(b)) and is negligible. These are consistent with the 1.8% resolution in MEG for the deep events. This implies that the unknown contribution remains in MEG II.

To estimate the depth dependence of the resolution, the events are grouped into three categories $(0 < w < 2\,\mathrm{cm}, \ 2 < w < 5\,\mathrm{cm}, \ \text{and} \ 5 < w < 12\,\mathrm{cm})$, and the spectra are fitted independently. To consider a possible error of energy scale depending on the conversion depth, the nuisance parameters are also fitted independently. The energy spectra of the MEG II intensity are used in order to ensure the sufficient statistics. Fig. 9.13 shows the result. An improvement of the energy resolution for the shallow events is confirmed.

9.3.6   Even-Odd resolution

As is done for MEG data, even-odd energy resolution is estimated also for MEG II. Since the MPPCs and the PMTs can have different ENF, the resolution of the MPPCs and the PMTs are estimated separately. It is estimated both from the CW-Li data and the background γ-ray

---

[*2] It mainly comes from cosmic rays, and neutrons from the accelerator captured by the LXe.
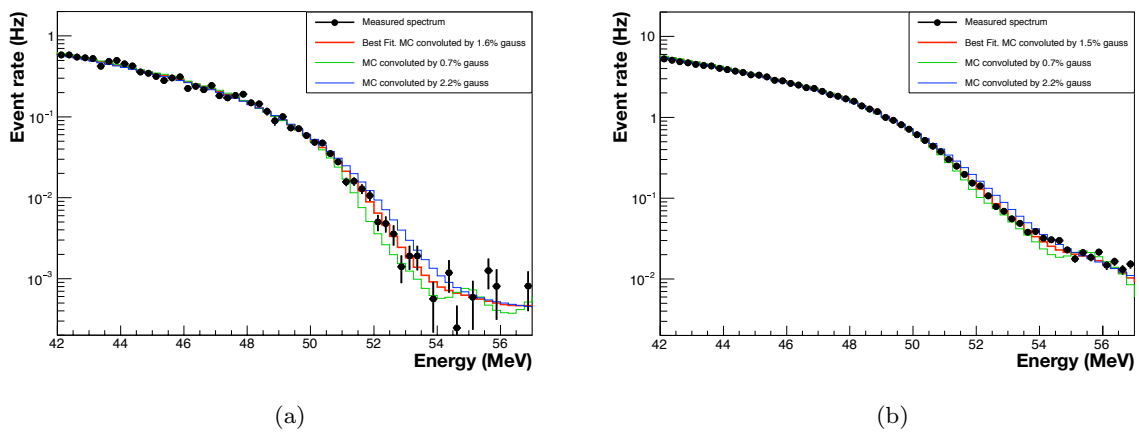
Figure 9.11   Measured energy spectrum of the background γ-ray fitted by the expected spectrum. The expected spectrum at better and worse resolution than best fit are also shown for comparison. (a) At the reduced intensity, (b) at the MEG II intensity.
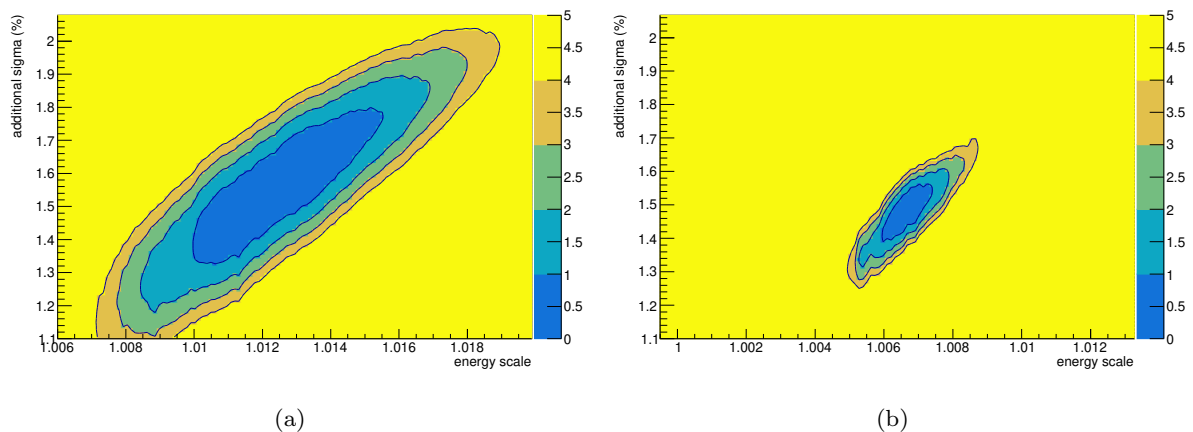

Figure 9.12   Excess of the doubled negative log likelihood ($2 \times nll$) from its local minimum. (a) At the reduced intensity, (b) at the MEG II intensity.
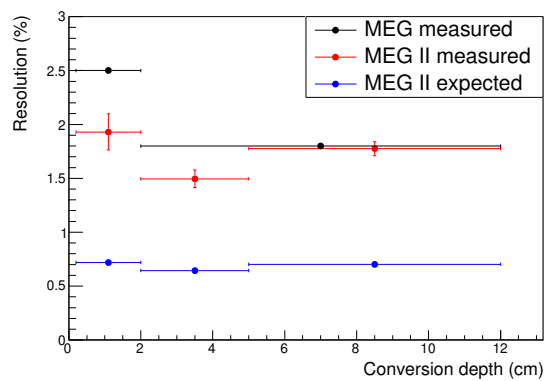

Figure 9.13   Energy resolution as a function of the conversion depth estimated from background γ-rays at MEG II intensity.
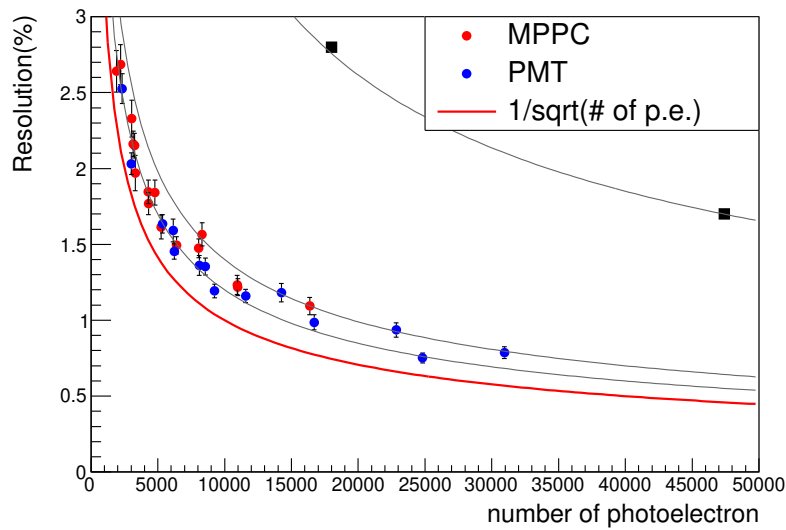
Figure 9.14   Even-odd energy resolution in MEG II as a function of the number of pho-
toelectrons estimated from the partial sums of the CW-Li events and the background γ
events. The measured energy resolutions for CW-Li and background γ-rays are also shown
as black data series for comparison. Three gray lines correspond to the ENF of 1.2^2, 1.4^2,
and 3.7^2, respectively.

data, and events hitting a selected local region are used. In addition to the energy from the
even channels and the odd channels, the energies from many kinds of partial sums are utilized
to estimate the resolution at different photoelectron statistics.

The results are shown in Fig. 9.14, and the ENF is estimated to be as large as 2.0 for both
the MPPCs and the PMTs, which can be due to the stochastic process in the photosensors as
explained in Section 2.1.3. Similar to MEG, this is too small to explain the observed unknown
contribution.

9.4   Summary and discussion

The energy resolution was measured by using the CW-Li γ-rays and the background γ-rays.
Thanks to the better uniformity realized by the MPPCs in MEG II, the energy resolution for the
shallow events has been improved. On the other hand, the energy resolution for the deep events
shown in Fig. 9.15 is not improved from that in MEG. This is probably due to the unknown
contribution also observed in MEG.

Though the cause of the unknown term has not been understood, there are several possibilities
which may result in the unknown contribution. One possibility is a problem of our detector
system such as a convection of the LXe in the cryostat. Another possibility is an event-by-event
fluctuation of the shower development which is not correctly simulated for some reason. Another
possibility is an intrinsic property of the LXe scintillation. A part of the energy deposit in the
LXe can be used for a generation of the charged carriers or an emission of the scintillation light
in the infrared region. The fraction of the energy used for the emission of the scintillation light
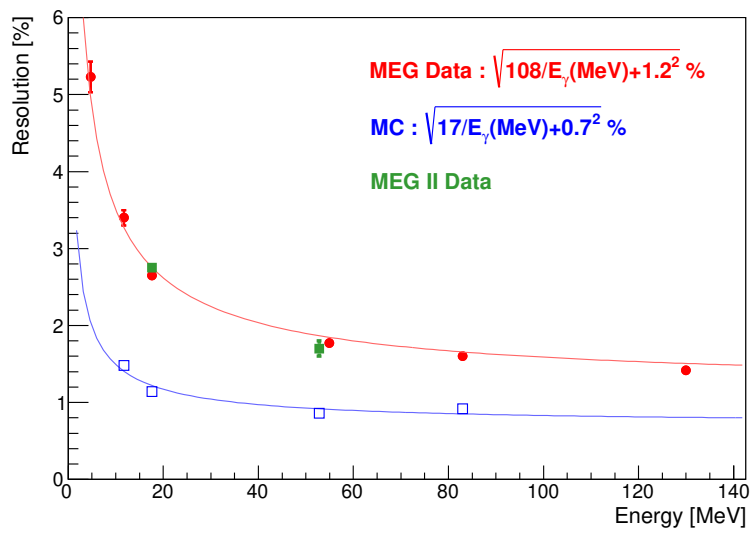
Figure 9.15 Energy resolution of MEG II as a function of the γ-ray energy compared to that of MEG for the deep events ($w > 2\,\mathrm{cm}$). Noise contribution is subtracted to show the intrinsic detector resolution.

in the VUV range may fluctuate event-by-event. These possibilities cannot be investigated in this thesis, and further studies are needed for a better understanding.

Chapter 10

Pileup elimination performance

The LXe detector performances in the previous chapters focus on that without any pileup γ-rays. The position and the timing resolutions will not be affected by pileups because they are reconstructed from the local information only around the hit position. Fig. 10.1 shows the pileup effect on the reconstructed position and timing of the signal γ-rays. The reconstructed timings of some of the signal γ-rays are biased by the pileup γ-rays as shown in the long tail of Fig. 10.1(b). This leads to an analysis inefficiency for the signal events, but it is only 3%, and effect on the branching ratio sensitivity is almost negligible.

On the other hand, the energy is reconstructed from a global sum of the number of photons, and its reconstruction largely deteriorates with pileups. Thus, this chapter focuses on the pileup effect on the reconstructed energy. In the Section 10.1, sources of pileup γ-rays in MEG II are explained. Two complementary methods to identify and eliminate the pileups are described in Section 10.2 and 10.3.


(a)

(b)
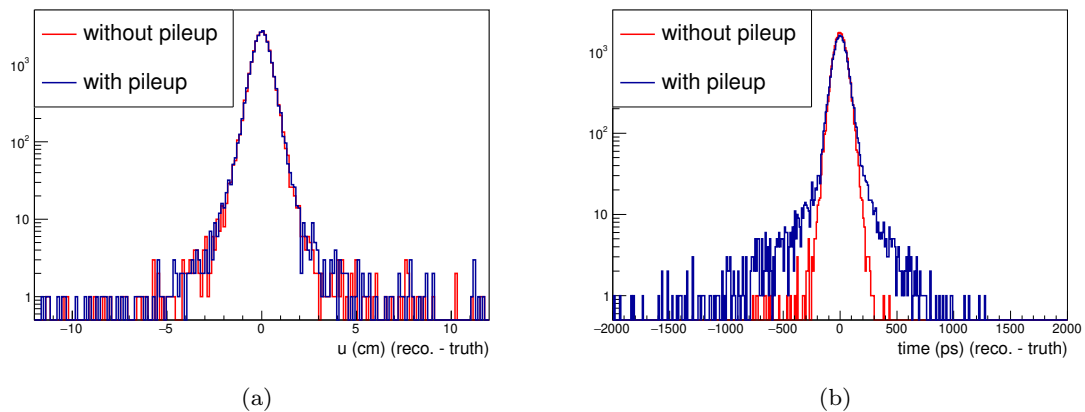
Figure 10.1 Pileup effect on the position and timing reconstruction of the signal γ-rays (MC). The differences between the reconstructed variable and its truth are shown. (a) Hit position (u-direction). (b) Hit timing.
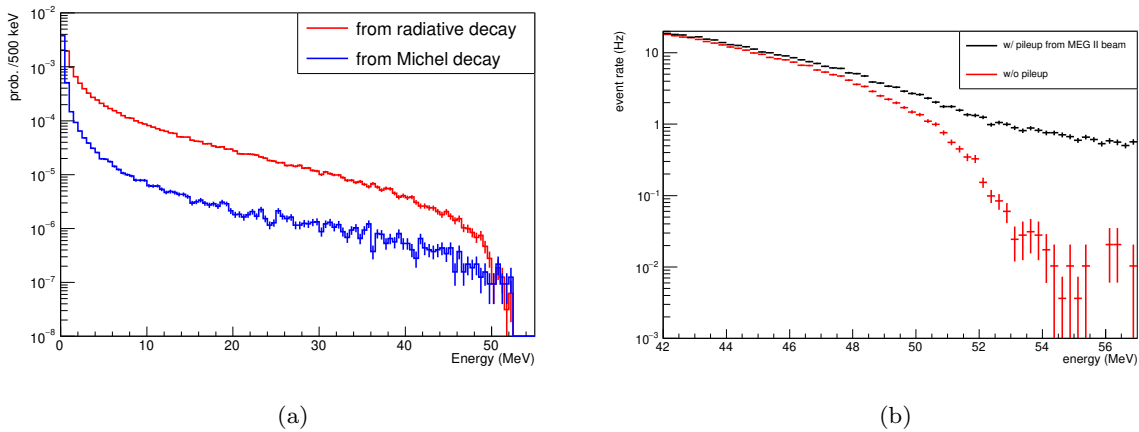
Figure 10.2 (a) Simulated energy deposit from a muon decay on target. The y-axis is normalized to the probability from a single muon decay. (b) Reconstructed energy spectra of background γ in the simulation without applying any pileup elimination analyses assuming (red) no pileups and (black) pileups from the MEG II beam.

10.1 Sources of pileup

10.1.1 Accidental pileup γ from another muon decay

The first type of pileup events is accidental pileup γ-rays from other muon decays. In the MEG II experiment, 7×10^7 muons per second decay on the target. Some of them emit γ-rays in the radiative decay, and they can pile up in the detector. Some of the Michel positrons can also emit γ-rays via interactions with materials. Fig. 10.2(a) shows simulated energy deposit in the LXe detector originating from the muon decays on the target. A single muon decay emits a γ-ray which deposits energy in the LXe with a probability of 1.5%. Thus, one pileup γ comes to the LXe detector in $1\,\mu$s time window on average.

Fig. 10.3 shows a typical pileup γ event. Additional charge caused by the pileups can bias the energy reconstruction, which is based on the global sum of the number of photons. Fig. 10.2(b) shows an simulated energy spectrum of background γ without pileup elimination analyses. Many events are reconstructed at higher energies, and the number of events near the signal energy becomes much larger due to the pileups. This is not acceptable to search for $\mu \to e\gamma$ decay, and some pileup elimination analysis is needed.

10.1.2 Two γ event from annihilation in flight

In addition to the accidental pileups, two coincident γ-rays can come even from a single muon decay. Most of the Michel positrons are swept from the MEG II detectors by the gradient magnetic field of the COBRA, but some of them can annihilate in flight with materials (AIF) and emit two γ-rays which are boosted in the direction of the flight.

The background events with the AIF reconstructed to be signal-like energy can be classified into two groups shown in Fig. 10.4. In the first type, one of the emitted γ-rays comes to the
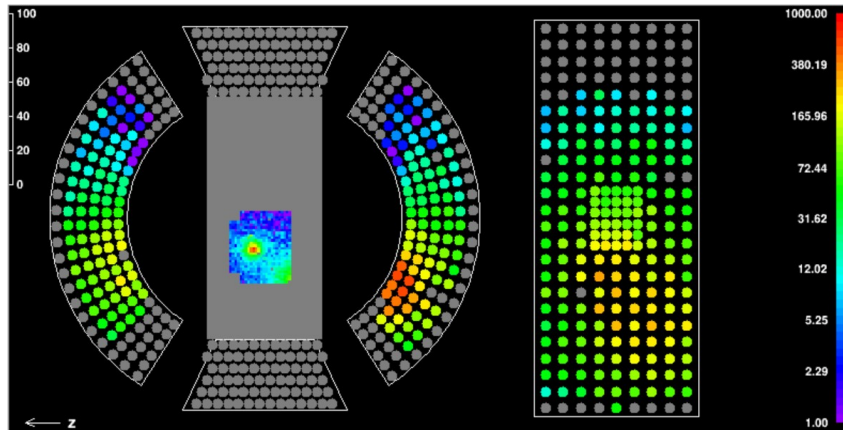
Figure 10.3   Typical event display of a pileup event.

| (a) | (b) |
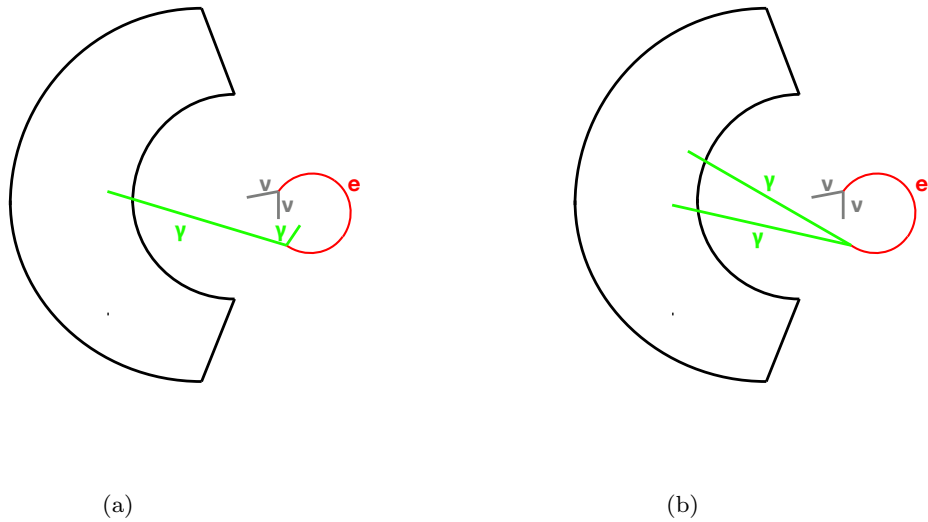
Figure 10.4   Two types of high energy background γ from AIF. (a) AIF 1γ, (b) AIF 2γ.

LXe detector with a large energy up to 52.8 MeV. Since one of the emitted two γ-rays carries most of the positron energy, the other γ-ray is emitted nearly backward, and cannot come to the detector. This type of event is called AIF 1γ event. In the second type, the opening angle of two γ-rays is relatively small, and both γ-rays come to the LXe detector. If the hit positions are too close to identify them as two independent γ-rays, they look like a single high energy γ-ray. This type of event is called AIF 2γ event.

From the full simulation of the background γ (Section 4.3), this AIF 2γ event is found to have a dominant contribution among all types of the backgrounds near the signal energy. Fig. 10.5 shows the energy spectrum of the background γ-ray of each class. The number of the γ-rays from the RMDs rapidly decreases as it goes to higher energy, while that from the AIFs only gradually decreases due to the shape of the Michel positron spectrum (Fig. 1.5(a)). In reality, the large fraction of the AIF 2γ events near the signal energy is smeared by the energy resolution

(a)   (b)
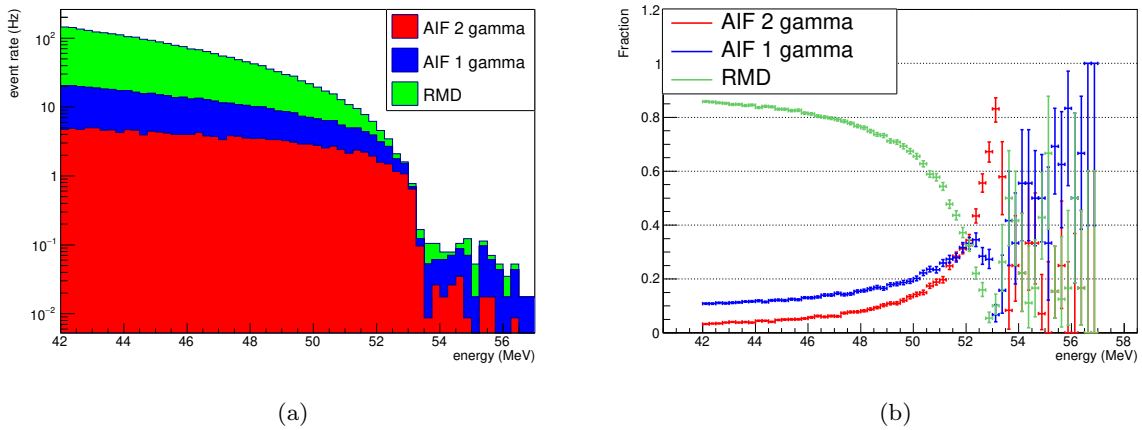
Figure 10.5 (a) Energy spectrum of the background γ. Simulated energy deposit in the LXe is shown. Events above $m_\mu/2$ come from muon decays before stopped on the target. Muon momentum can boost decay products in these events. (b) Fraction of the background γ-rays of each type calculated from (a).
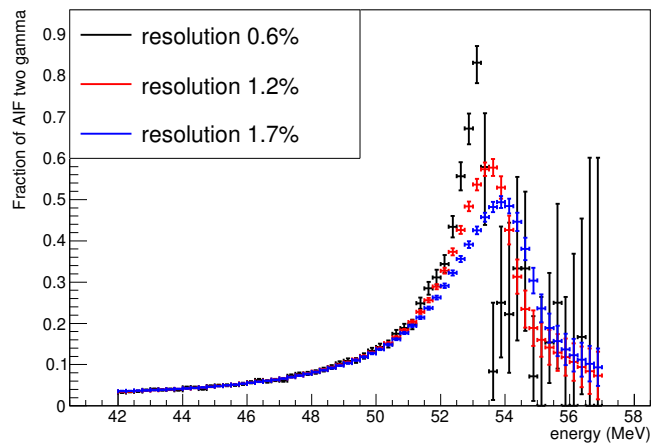
Figure 10.6 Expected fraction of the AIF 2γ events taking the energy resolutions into account (MC).

as shown in Fig. 10.6. Even with the 1.7% energy resolution measured in run 2019, which is worse than expected (Chapter 9), the AIF 2γ events still have 34% contribution near the signal energy[*1] ($51.5 < E_\gamma < 54\,\mathrm{MeV}$). Therefore, an identification of the AIF 2γ events leads to an additional reduction of the background γ and can result in an improvement in the branching ratio sensitivity.

[*1] This region is defined to be $\pm 1.5\sigma$ for a rough and qualitative discussion on the effect of the pileups. Since the MEG II physics analysis adopts a likelihood fitting instead of a cut-counting analysis, a real effect on the branching ratio sensitivity can be different. The qualitative estimation of the effect is given in Chapter 11.

10.2   Pileup elimination by sum waveform

10.2.1   Elimination algorithm

This method tries to eliminate pileup γ-rays from the accidental muon decays. It starts from a calculation of summed waveforms of all MPPCs and PMTs. In the calculation of the sum waveform, the weights and the photosensor performances used in the energy reconstruction (Equation 9.1) are applied, so that the γ-ray energy can be directly reconstructed from the area of the sum waveform. Template waveforms are created from the sum waveform of many γ-ray events as shown in Fig. 10.7, and are used for the peak search in the waveform. The data taken at the reduced intensity is used to eliminate the contamination of the pileup pulses in the template waveform. A relative event-by-event fluctuation in the waveform is also calculated from the standard deviation of Fig. 10.7, as shown in Fig. 10.8. A typical fluctuation is below 1.5% of the peak amplitude in 1σ, except for a time window near the peak. Thus, $2.4\,\mathrm{MeV}$ ($= 52.8\,\mathrm{MeV} \times 1.5\% \times 3$) pileups in the signal events can be identified if we search for a deviation larger than 3σ from the template.

The pileup identification of each event starts from a fitting of the sum waveform by the template assuming no pileup in this event. If a local significant deviation from the template above 3σ is found, another template for the pileup is added in the fit function, and the sum waveform is re-fitted assuming two γ-rays. This step is repeated until the fitting gets converged. The sum waveform is deconvoluted to several pulses by the fit, from which energy of each γ-ray is reconstructed. Fig. 10.9 shows a typical sum waveform with pileups. Excesses of the chi-square value from the template around $-50\,\mathrm{ns}$ and $+150\,\mathrm{ns}$ are solved by adding a pileup γ-ray for each, and the sum waveform is successfully deconvoluted to three γ-rays.

In the current implementation, only the sum waveform of the PMTs is used for a identification of the pileups in the waveform. The MPPC sum waveform is fitted and deconvoluted by assuming the pileup γ-rays found in the PMT. This is to avoid picking up fake peaks due to the larger statistical fluctuation and noise fluctuation when the MPPC PDE will get reduced. The pileup search in the MPPC waveform may be included, once a better understanding on the fluctuation of the MPPC waveform is obtained from the γ-ray data operated at lower PDE in the future.

10.2.2   Performance measurement at run 2019

The performance of this algorithm is tested both in the simulation and in the real data at the MEG II beam intensity. Fig. 10.10 compares the reconstructed spectra of the background γ-ray with and without applying this algorithm. The high energy tails are largely suppressed by this method both in data and MC. The energy spectrum of data after the elimination agrees with MC as shown in Fig. 10.11(a). The number of background events in the "signal region" ($51.5 < E_\gamma < 54\,\mathrm{MeV}$) is $1.4(1)\,\mathrm{Hz}$ in Data, and $1.47(3)\,\mathrm{Hz}$ in MC.

Fig. 10.11(b) shows a simulated energy spectrum after applying this algorithm compared to that without pileup. Some of the pileups are still not identified, and this increases the number

(a)   (b)
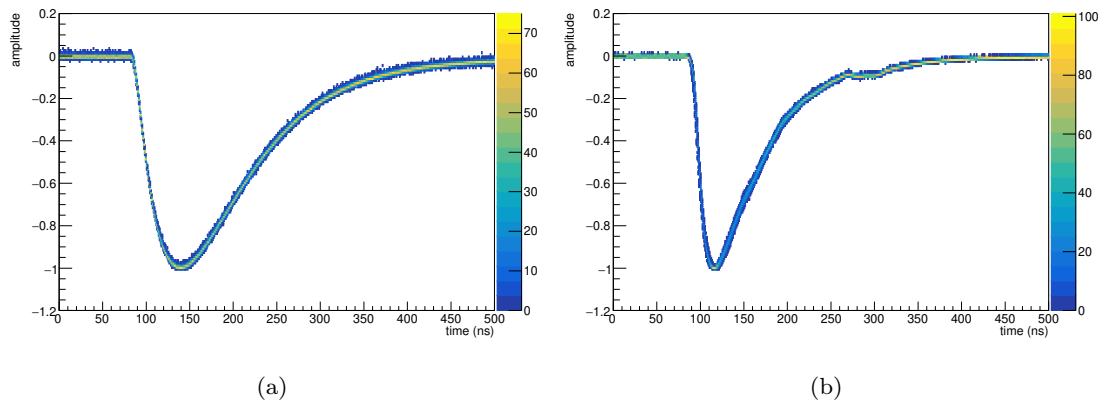
Figure 10.7   Summed waveforms of the (a) MPPCs, (b) PMTs, which are produced by overlaying 1000 events. The peak amplitude and peak timing of each event are normalized and shifted. The second peak in the PMT waveform at 300 ns is due to a reflection.

(a)   (b)
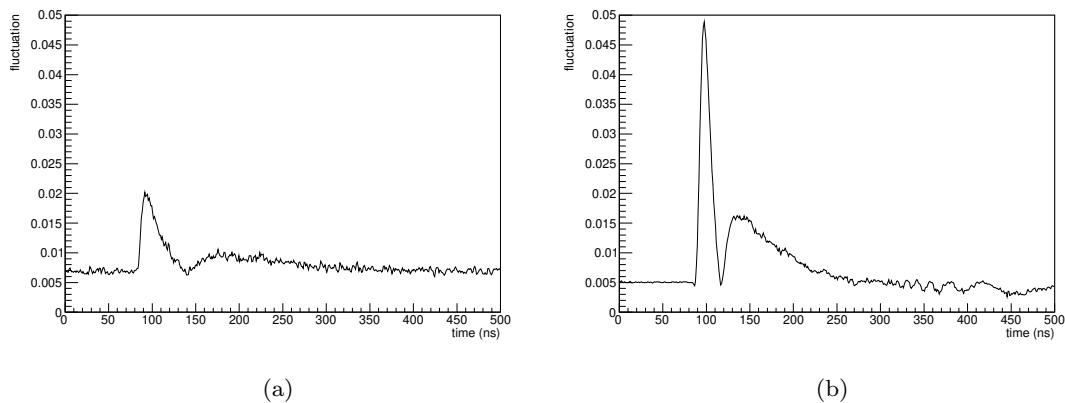
Figure 10.8   Event-by-event fluctuation of the summed waveform (Fig. 10.7) as a function of time. (a) MPPC, (b) PMT. The fluctuation is normalized by the peak amplitude of the sum waveform. The local minimum at 140 ns (MPPC)/120 ns (PMT) are due to the waveform normalization at the peak of the waveform.

(a)   (b)
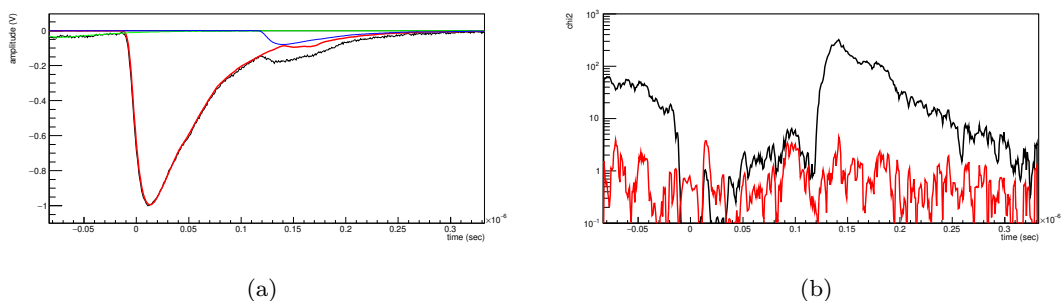
Figure 10.9   Pileup elimination by sum waveform for a typical waveform with pileups. (a) The original PMT sum waveform (black) is deconvoluted to three identified pulses (red, blue, and green). (b) Chi-square of this event assuming (black) signal γ-ray, and (red) three γ-rays.

(a)   (b)
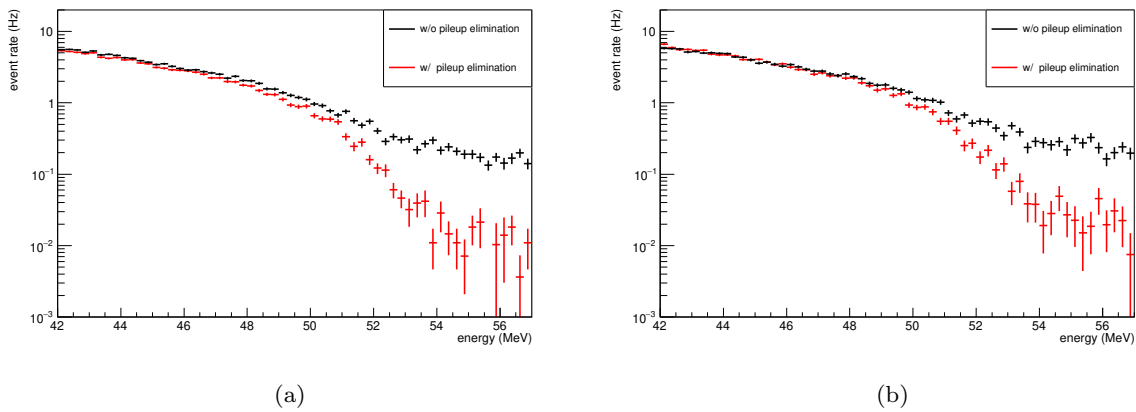
Figure 10.10   Comparison of the energy spectrum of the background γ-ray at the MEG II beam intensity with and without applying pileup elimination by the sum waveform for (a) MC and (b) data. The spectrum of the MC is smeared to match the worse energy resolution in data (Section 9.3.5).


(a)   (b)
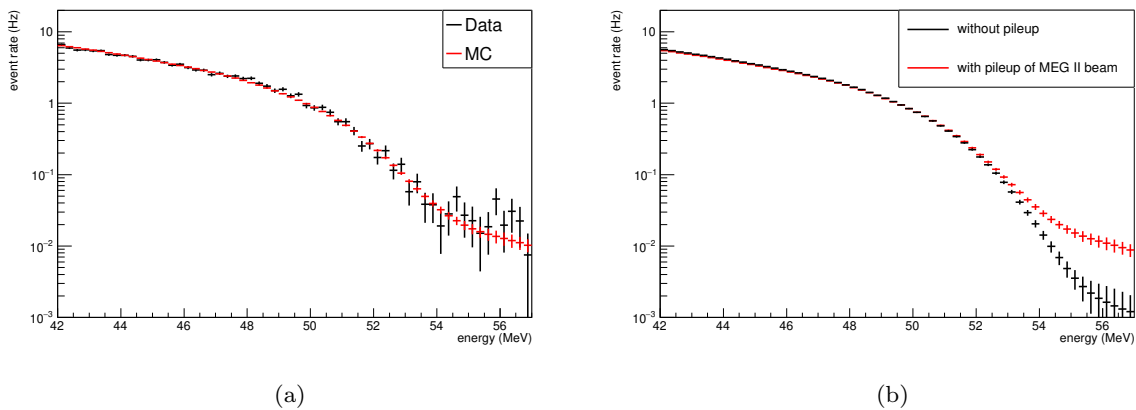
Figure 10.11   (a) Comparison of the background γ spectrum at the MEG II beam intensity between MC (in Fig. 10.10(a)) and data (in Fig. 10.10(b)) with the pileup elimination by the sum waveform. The normalization of the spectrum is also adjusted to match the data at the low energy region. (b) Comparison of the simulated background γ spectra between that assuming no pileup (black), and that assuming pileup from MEG II muon beam (red). The spectra are smeared to match worse energy resolution in data.

of events in the "signal region" by 13%. Most of these events are the pileups which accidently come at the similar timing to the triggered γ, and they are the target of another elimination method in the next section.

In the search of pileup candidates, some of the single γ-ray events can be misidentified as an event with pileups. Energy of these events can be reconstructed to be smaller than the real energy deposit, and this leads to an analysis inefficiency of the signal events. In the simulation, this inefficiency is estimated to be only 0.2%.

To confirm the little inefficiency in the data, a fraction of the events reconstructed as two γ-rays in the background γ data is utilized. These events are composed of the true pileup
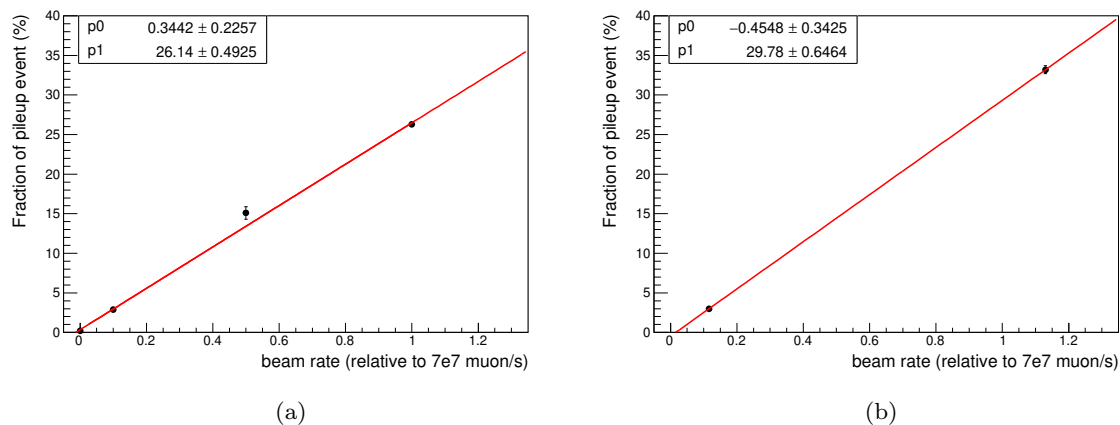
Figure 10.12   Fraction of the background events ($40 < E_\gamma < 42$ MeV) reconstructed as two γ events as a function of the beam rate (a) in MC and (b) in data.

events and the misidentified single γ events, and they are distinguished from the beam rate dependence. Fig. 10.12(a) shows the fraction as a function of the beam rate in the low energy region ($40 < E_\gamma < 42$ MeV[*2]). The beam rate dependence of the fraction is fitted with a linear function except for the data point at $x = 0$ (namely without pileup γ-rays), and the inefficiency to the pure single γ events is estimated to be 0.3(2)% from its y-intercept. This result is consistent with 0.2% inefficiency. The same analysis is applied for measured background γ-rays in the run 2019. As shown in Fig. 10.12(b), the y-intercept is fitted to be $-0.5(3)$%, and the inefficiency is found to be negligible also in the data.

10.3   Pileup rejection by charge distribution

10.3.1   Identification algorithm

This method searches for a local maximum in the charge distribution on the MPPCs to identify the events having more than one peak due to the pileup γ-rays. The peak search algorithm is designed to avoid picking up fake peaks in the charge distribution. Firstly, the granularity of the MPPC readout is re-binned by a factor of two to suppress an event-by-event fluctuation of the charge distribution. Secondly, a low-pass filter is applied by a moving average of 3×3 bins. Thirdly, small peaks whose excess is below a given threshold (typically 200 photon) are ignored in the peak search. Fourthly, each identified peak is fitted by a two-dimensional Gaussian so that we can roughly reconstruct its energy from the integrated volume of the Gaussian[*3]. The identified peaks less than 1 MeV are ignored. Note that peak caused by the triggered γ-ray is also counted as one peak.

Events having more than one peak is discarded from the analysis. In the current implemen-

---

[*2] This is the lowest energy region available in data.

[*3] Currently dependence on the conversion depth is not corrected. This can be improved in the future.
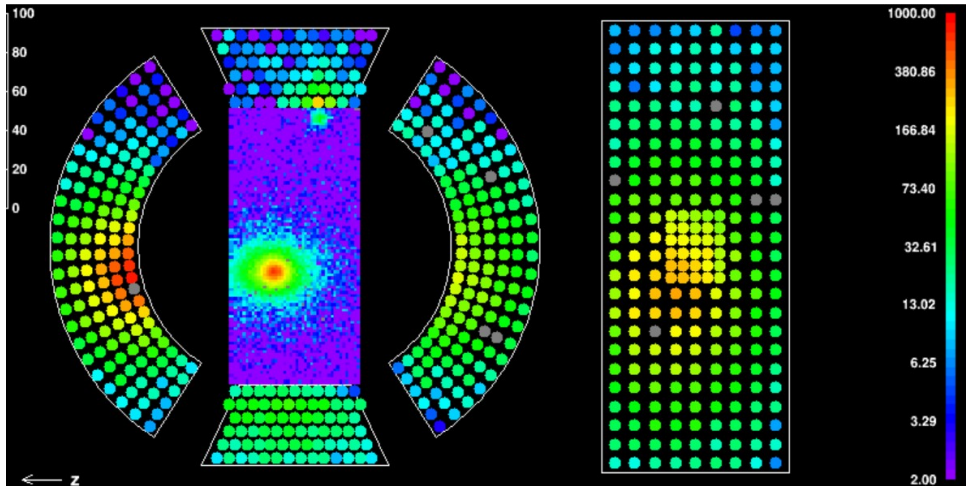
Figure 10.13   Example of two peak event from single γ-ray in MC. In this event, a 50 MeV γ-ray from RMD creates two peaks in the detector.

tation, the algorithm is applied only to the events where no pileup γ-rays are identified in the sum waveform method. In other words, we rely on the sum waveform method for the events whose pileup is identified by both methods. This implementation can be improved in the future to deal with three γ-rays events in which one pileup is identified by the sum waveform method, and the other by this method.

This is a complementary method to the identification by the sum waveform because it is sensitive to the pileup hits coming at the same or similar timing. Since the time window of the charge integration is defined around the timing of the main γ-ray, the pileup hits coming at the same or similar timing tend to have larger charges than the other pileups.

If a signal event is rejected by this analysis, it leads to an inefficiency. There are two sources that causes the second peak in the signal event. One is the accidental pileup γ-ray coincident with the signal event, but its contribution is limited. The inefficiency is estimated to be only 0.3% in the signal MC with pileups. The other inefficiency, which is dominant, is due to the events where a second peak on the charge distribution is created by the signal γ-ray itself. Fig. 10.13 shows an example event of this type, and Fig. 10.14 shows particle tracks in this event. A γ-ray escaped from the main electromagnetic shower is converted in a distant place, and creates a second peak on the inner face.

10.3.2   Expected performance with full channel readout

The expected performance of this algorithm is evaluated by the simulation assuming a full channel readout.

Fig. 10.15 shows the reconstructed energy spectrum of the background γ-ray from the RMD with accidental pileups. The fraction of the background events due to the overlooked pileups in the "signal region" is 13% only with the pileup elimination by sum waveform, and it is improved to 5% also applying this algorithm.
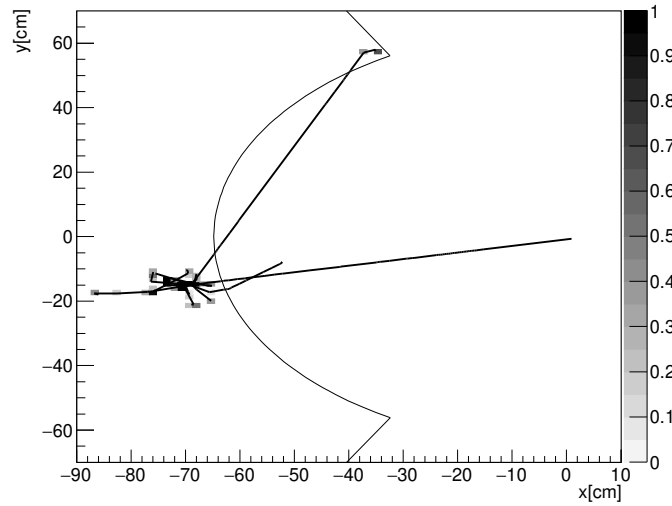
Figure 10.14   Particle track in the simulated event of Fig. 10.13. Each black line shows a track of a γ-ray. A gamma-ray escaped from the shower converted at the top side of the detector. The energy deposit on each point is overlaid. The scale of the gray bar is in the unit of MeV.
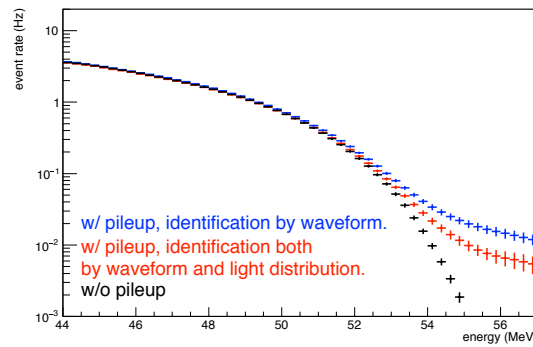

Figure 10.15   Reconstructed energy spectrum of the simulated background γ. The background event only from RMD is shown. (black) no pileup is simulated. (blue) pileup is simualted, and eliminated by sum waveform method. (red) pileup is simulated and eliminated by both the sum waveform and the charge distribution.

Fig. 10.16 shows the expected performance for the AIF 2γ identification. The identification efficiency of the AIF 2γ events eff and analysis inefficiency to the single signal γ events $ineff$ are shown at several peak search thresholds. To have a naive impression on the improvement of the branching ratio sensitivity, the inverse of the significance in the "signal region" is defined as follows, as a figure of merit fom of this analysis.

$$fom := \frac{\sqrt{N_{\mathrm{BG}}}}{N_{\mathrm{sig}}} = \frac{\sqrt{1 - c * eff - (1-c) * ineff}}{1 - ineff}. \tag{10.1}$$

Here, $c = 0.29$ is the fraction of AIF 2γ event in the "signal region" (Fig. 10.6). The branching ratio sensitivity of MEG II will get improved by a factor of this fom, if the statistics is sufficient.

(a)   (b)
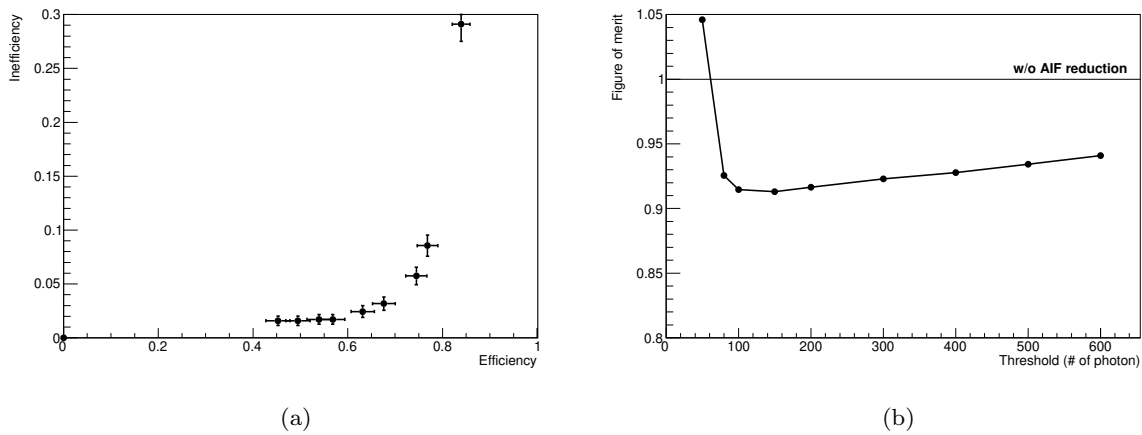
Figure 10.16   (a) Identification efficiency of AIF 2γ event and inefficiency to single γ-ray at various peak search threshold (MC). (b) Figure of merit defined in equation 10.1 as a function of peak search threshold (MC).

(a)   (b)
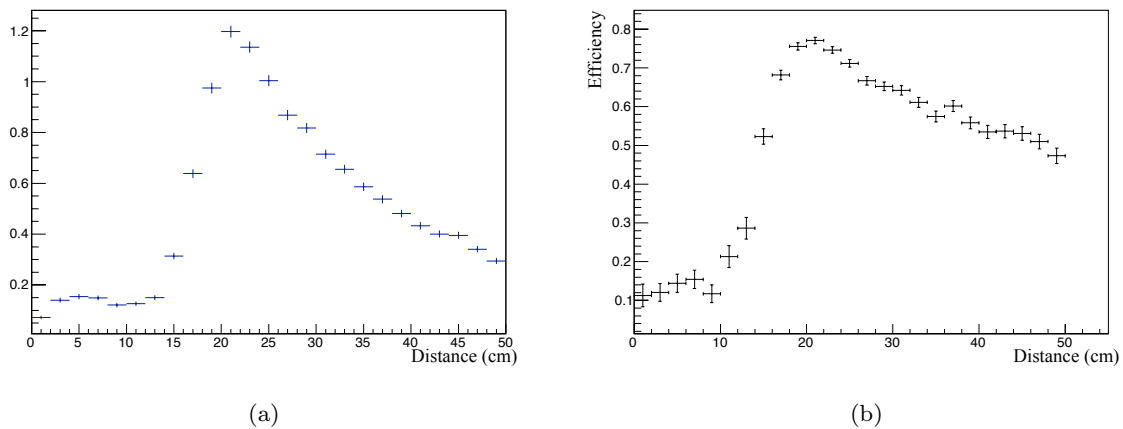
Figure 10.17   (a) Distribution of the distance between two γ-rays from AIF 2γ (MC). (b) Identification efficiency of AIF 2γ event as a function of its distance (MC).

Nominal threshold (200 photon) for the peak search is set near the optimal threshold which minimizes the fom, and a significance improvement by 8% is expected at the $eff = 68\%$, $ineff = 3\%$.

The identification efficiency of AIF 2γ events depends on the distance between two γ-rays. Fig. 10.17 shows a distribution of the distance between two γ-rays, and the identification efficiency as a function of the distance. The typical distance is $20 - 30$ cm, and this algorithm is sensitive to them. The AIF 2γ events closer than 15 cm are difficult to be identified since two peaks are overlapped, but those are very rare. On the other hand, the longer the distance is, the smaller the energy of the second γ-ray tends to be. Therefore, the identification efficiency decreases above 20 cm . Some of the second γ-rays which convert in the deep region of the detector are not identified due to its small observed charge on the inner face. These γ-rays may be identified by also using charge distribution on other faces in the future.
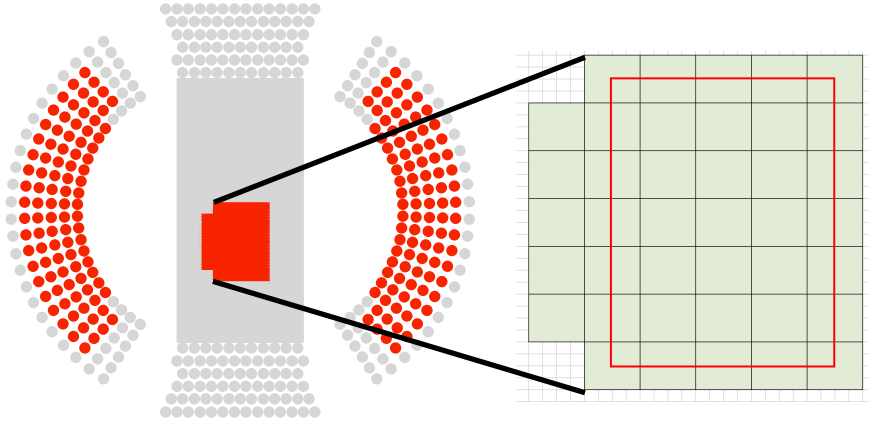
Figure 10.18   Analysis area in run 2019. Green shows MPPC readout area, and red box $(24(u) \times 36(v)\,\mathrm{cm}^2)$ shows area used in this search.

10.3.3   Performance measurement at run 2019

The efficiency and inefficiency of this algorithm were measured in the 2019 run. Due to the limited readout area, the pileup γ-ray which hitting outside the area cannot be identified. Since the distance between AIF 2γ is shorter than that between the accidental γ-rays which are uniformly distributed, most of the identified two γ events in 2019 run come from AIF 2γ.

In the analysis of 2019 data, two γ events where both γ-rays hit the central area shown in Fig. 10.18 are used. This area is defined to have $3\,\mathrm{cm}$ (two MPPCs) margin from the edge of the readout area, in order to veto events whose true hit positions are outside the area. Even though the most of the AIF 2γ events hitting the whole detector cannot be identified with the limited readout area, a reasonable efficiency is expected for the events hitting this region as shown in Table 10.1.

Table 10.1   Identification probability of AIF 2γ in MC

	AIF 2γ in whole detector	AIF 2γ in 2019 area
Peak search in whole detector	78(1)%	80(5)%
Peak search in 2019 area	-	67(4)%

Fig. 10.19(a) shows a fraction of two γ events in the background γ-rays as a function of the energy. The high energy events have a larger fraction of two γ events as expected. The major component of the identified two γ events is not the accidental pileups since the fraction is independent of the beam intensity. This result qualitatively shows that the identification of the AIF 2γ events works correctly.

Fig. 10.19(b) compares the fraction of two γ events at the reduced beam intensity between MC and data. The measured fraction of two γ-ray events in the low energy region ($40 < E_\gamma < 45\,\mathrm{MeV}$) is twice larger than expected. It is confirmed that those identified two γ events in data really have two signal-like peaks on the charge distribution, and not due to a noise or mistakes
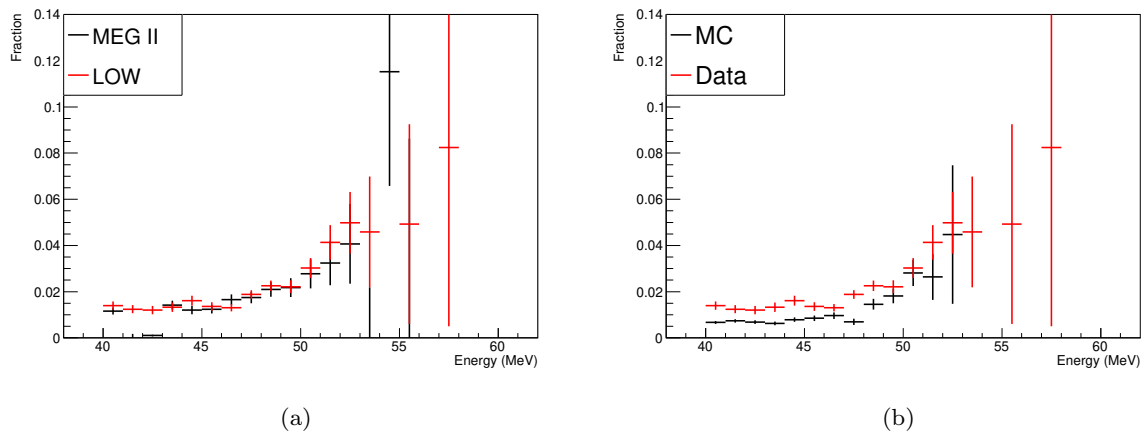
Figure 10.19 Fraction of 2 γ event. (a) Comparison between reduced intensity and MEG II intensity in Data. (b) Comparison between MC and data at reduced beam intensity.

in the analysis. Since this excess is observed in both the reduced intensity data and the MEG II intensity data, it should not be due to the accidental pileups, but due to some two γ events from a single muon decay.

There are two possibilities which explain this inconsistency. One is due to some materials which produce AIF 2γ events but are not implemented in the MC. Since the excess by a factor of two is observed only in the low energy region, the material should not be located in the central part of the beam line, but be located where only the Michel positrons after some energy loss can hit. The other is that the current MC simulation underestimates the probability of having the second peak in the single γ event for some reason. In this case, the inefficiency for signal γ-ray becomes twice larger than expected.

Since the second possibility cannot be rejected, it is difficult to evaluate the inefficiency from 2019 data with a good precision. The inefficiency of this method should be directly measured with reading all the MPPCs in the future.

Chapter 11

Expected branching ratio sensitivity of MEG II

In the design stage of the MEG II experiment shown in Section 1.9, the branching ratio sensitivity was estimated in the expected detector performance from the simulation at that time. In this chapter, the sensitivity is updated based on the measured LXe detector performance summarized in the previous chapters.

The calculation procedure of the MEG II branching ratio sensitivity is summarized in Section 11.1.

In this thesis, many improvements and degradations on the detector performance are discussed. Their effects on the sensitivity are discussed separately in this chapter. In the Section 11.2, the sensitivity achieved by the detector performances measured in the pilot run is discussed. This includes effects from the improved resolutions realized by the MPPCs, and a degradation from the worse energy resolution than expected.

Due to the PDE degradation of the MPPCs, original DAQ plan of MEG II assuming continuous 120 days data-taking may not be possible (Section 6.3.4). Section 11.3 and 11.4 discusses the effect of the PDE degradation including the expected detector resolution with lower MPPC PDE.

A conclusion on the achievable branching ratio sensitivity with the developed LXe detector by a reasonable data-taking time is given in Section 11.6.

11.1 Calculation procedure of branching ratio sensitivity

11.1.1 PDF in likelihood analysis

In the physics search of $\mu \rightarrow e\gamma$ in MEG II, the number of signal events is estimated by a maximal likelihood method. An analysis region where the likelihood fitting is performed is defined as follows: $48 < E_\gamma < 58\,\text{MeV}, 50 < E_e < 56\,\text{MeV}, |t_{e\gamma}| < 0.7\,\text{ns}, |\theta_{e\gamma}| < 50\,\text{mrad}, |\phi_{e\gamma}| < 75\,\text{mrad}$. A time-sideband is defined around the analysis region as $1 < |t_{e\gamma}| < 3\,\text{ns}$, and an energy-sideband is defined as $43 < E_\gamma < 48\,\text{MeV}, 48 < E_e < 53\,\text{MeV}, |\theta_{e\gamma}| < 300\,\text{mrad}, |\phi_{e\gamma}| <$

300 mrad.

The likelihood function is defined from a probability density function (PDF) for signal, RMD, and accidental background events as shown in Equation 11.1.

$$\mathcal{L}(N_{\text{sig}}, N_{\text{RMD}}, N_{\text{BG}}) := \frac{e^{-(N_{\text{sig}}+N_{\text{RMD}}+N_{\text{BG}})}}{N_{\text{obs}}!} e^{-\frac{(N_{\text{RMD}}-\langle N_{\text{RMD}}\rangle)^2}{2\sigma_{\text{RMD}}^2}} e^{-\frac{(N_{\text{BG}}-\langle N_{\text{BG}}\rangle)^2}{2\sigma_{\text{BG}}^2}}$$

$$\times \prod_{i=1}^{N_{\text{obs}}} (N_{\text{sig}}S(\vec{x_i}) + N_{\text{RMD}}R(\vec{x_i}) + N_{\text{BG}}B(\vec{x_i})). \qquad (11.1)$$

Here, N_{obs} is the number of events observed in the analysis region. N_{sig}, N_{RMD}, and N_{BG} are the expected value of the number of signal, RMD, and accidental background events in the analysis region. These are the fitting parameters determined in the maximum likelihood analysis. $\langle N_{\text{RMD}}\rangle$, $\langle N_{\text{BG}}\rangle$, σ_{RMD}, and σ_{BG} are the expected numbers of RMD and accidental background events and their uncertainties estimated from the sidebands. $S(\vec{x_i})$, $R(\vec{x_i})$, and $B(\vec{x_i})$ are the PDFs of signal, RMD, and accidental background events as a function of the observables $\vec{x_i} = (E_\gamma, E_e, t_{e\gamma}, \phi_{e\gamma}, \theta_{e\gamma}, t_{rdc}^{ds}, E_{rdc}^{ds})$ defined in Section 1.3.

These PDFs are calculated from the theoretical expectations and the detector resolutions. For example, the signal PDF $S(\vec{x_i})$ is composed of PDFs of each variable as follows,

$$\begin{aligned} S(E_\gamma, E_e, t_{e\gamma}, \phi_{e\gamma}, \theta_{e\gamma}, t_{rdc}^{ds}, E_{rdc}^{ds}|w_\gamma, \vec{y_i}) = {}& S(t_{e\gamma}) \times S(E_\gamma) \\ & \times S(\phi_{e\gamma}|w_\gamma, \vec{y_i}) \times S(\theta_{e\gamma}|w_\gamma, \vec{y_i}) \\ & \times S(E_e|\vec{y_i}) \\ & \times S(t_{rdc}^{ds}, E_{rdc}^{ds}|E_\gamma), \end{aligned}$$

where w_γ is the conversion depth of a γ-ray, and $\vec{y_i}$ is a set of reconstructed positron variables such as direction, decay vertex, and tracking quality. To estimate the sensitivity, signal PDFs related to the γ-ray are prepared from the measured performance given in the previous chapters. The positron detector performance is assumed to be the same as that in the design summarized in Table 1.1.

The signal PDF of the γ-ray energy $S(E_\gamma)$ is created from the simulated energy distribution for the signal γ-ray. The simulated spectrum is smeared by an additional Gaussian to match the measured energy resolution as shown in Fig. 11.1(a). The signal PDF of the timing $t_{e\gamma}$ is defined as a Gaussian of the $t_{e\gamma}$ resolution. The $t_{e\gamma}$ resolution is a combination of the timing resolutions of the γ-rays and the positrons (Table 1.1). The angular PDFs are the combination of the γ-ray position resolution, the positron vertex resolution, and the positron direction resolution. Conversion depth dependence of the γ position resolution is also included.

Similar to the signal PDF, the background PDF $B(\vec{x_i})$ is also composed of the PDFs of each variable. Fig. 11.1(b) shows the background E_γ PDFs generated from the simulated background spectrum. Pileup events from the MEG II beam are included. It is already confirmed that the generated background spectrum from the simulation agrees with data as shown in Fig. 9.11. The pileup rejection by the charge distribution is not adopted in this thesis since its performance was not confirmed from the data. Thus, only the pileup elimination by the sum waveform is applied.
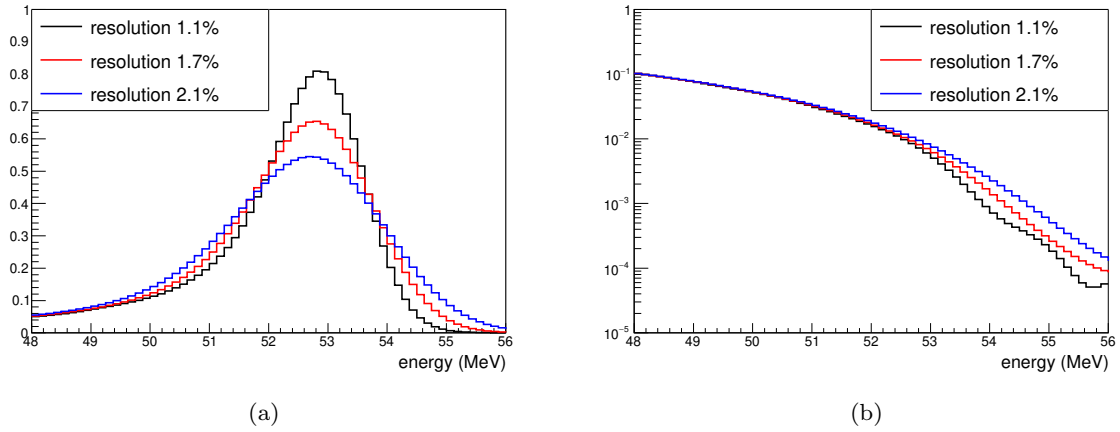
Figure 11.1   Simulated E_γ PDFs assuming several resolutions.   (a) For signal.   (b) For accidental background.

The background PDF of the RDC parameters are updated from the MEG II design. Fraction of the background events identified by the RDC is dependent on the gamma-ray energy as shown in Fig. 10.5(b), and this dependence is newly included in the calculation.

11.1.2   Accumulated number of muon decays

The accumulated number of muon decays is another input parameter needed for the calculation of the branching ratio sensitivity. In the nominal configuration, it is estimated as follows, based on the original DAQ plan of the MEG II experiments.

- beam rate : $7 \times 10^7 \, \mu/\text{s}$
- geometrical acceptance : 10.8%
- positron efficiency : 70%
- γ efficiency : 69%
- trigger and analysis efficiency : 91% (same as the first half of MEG)
- DAQ time : Three years. 20 week data-taking per year with 84% live fraction.

With these parameters, the total number of muon decays called k-factor becomes $k = 1.03 \times 10^{14}$.

11.1.3   Sensitivity calculation from toy experiments

The branching ratio sensitivity of MEG II is calculated by simulating many ($O(10^3$–$10^4)$) toy experiments. In each toy experiment, a set of MEG II observables are simulated from the PDFs assuming a background-only hypothesis. The generated number of the RMD and the accidental background events are calculated from the simulation. Their statistical fluctuations are also taken into account. The best estimate of the number of signals N_{sig} of each toy experiment is calculated by maximizing the likelihood function in Equation 11.1, and the upper limit of N_{sig} at 90% confidence level is calculated by asymptotic formulae in [62].
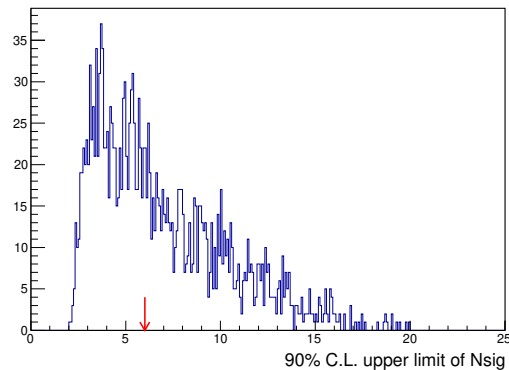
Figure 11.2   The upper limits of the number of signal N_{sig} for 5000 toy experiments assuming nominal detector performance in MEG II, and DAQ time. Red arrow shows the median of this distribution.

Fig. 11.2 shows a distribution of the upper limits of N_{sig} at 90% confidence level. "Branching ratio sensitivity" of the MEG II experiment is obtained from the median of the upper limits divided by the k-factor.

11.2   Sensitivity imporvement by LXe detector

In this section, the achieved improvement on the branching ratio sensitivity is shown for each detector resolution.

Here, the resolutions measured at the MPPC PDE of 8% are used. Note that it does not reflect the effect of further degradation of PDE in the future, which will be discussed in the next sections.

In the comparisons of the branching ratio sensitivity shown below, resolutions other than that being compared are fixed to the measured resolutions in the pilot run, and the nominal data-taking time in the original MEG II DAQ plan is assumed. A sensitivity improvement by the RDC depends on the γ-ray energy resolution because the fraction of the RMD events in the backgrounds near the signal energy depends on it (Section 10.1.2). Thus, the RDC observables are not used in the likelihood analysis in these comparisons to see a pure effect of the γ-ray resolution on the sensitivity.

Position resolution

The position resolution is improved by the better granularity realized by MPPCs in MEG II especially for shallow events. This leads to a 30% improvement of the branching ratio sensitivity as shown in Fig. 11.3(a). On the other hand, in the pilot run, a slight degradation of the resolution for the deep events was observed (Chapter 7). This results in a 4% degradation of the sensitivity, and thus a 26% sensitivity improvement from MEG is achieved in MEG II.

Timing resolution

A better timing resolution than the design is achieved by the analysis optimization (Chapter 8). As shown in Fig. 11.3(b), this leads to an improvement of the branching ratio sensitivity by about 7% from the design. The timing resolution is also better than that in MEG, thanks to the more precise estimation of time of flight by the improved position resolution. The sensitivity improvement from MEG is a few percent.

Energy resolution

As discussed in Chapter 9, the energy resolution is measured to be worse than the expectation from the simulation, probably due to the unknown contribution also observed in MEG. Since the branching ratio sensitivity in the MEG II design assumes only a half of the unknown contribution (Section 1.9), the sensitivity gets worse than the estimation in the design. As shown in Fig. 11.3(c), about 10% degradation of the sensitivity from the design is expected. Even with the same or even worse energy resolution for the deep events than MEG, the better energy resolution for the shallow events improves the sensitivity by about 15% compared to that in MEG.

Pileup

Fig. 11.3(d) shows a comparison of the branching ratio sensitivity with and without the accidental pileups. Since the pileup elimination by the charge distribution is not applied, some of the accidental pileups near the signal energy are still left (Section 10.2.2, Fig. 10.15). This results in a sensitivity degradation by about 10% at MEG II intensity.

Effect of measured resolution uncertainties

Each measured resolution of the LXe detector in the pilot runs has an uncertainty. For example, the energy resolution for the shallow events ($w < 2\,\mathrm{cm}$) have a 0.2% uncertainty from the energy spectrum fitting (Fig. 9.13). The expected branching ratio sensitivity improvement mentioned above uses the best estimate of the resolution, and the result has an uncertainty coming from that of the resolutions. The size of the uncertainty is estimated by calculating a resolution dependence of the sensitivity.

The uncerainty from the 0.2% energy resolution uncertainty for the shallow events is estimated to be 2.6%. The position resolution for the shallow events ($w < 4\,\mathrm{cm}$) have a 0.2 mm fit uncertainty at most (Fig. 7.6(b)). Effect of this is calculated to be a sensitivity uncertainty of less than 0.9%. Effects from other resolution uncertainties, such as the resolutions for the deep events and the timing resolution, are smaller than these and are negligible. The uncertainty of the sensitivity is less than 5% in total if we sum up the effects from the all resolutions.

(a)

(b)

(c)

(d)
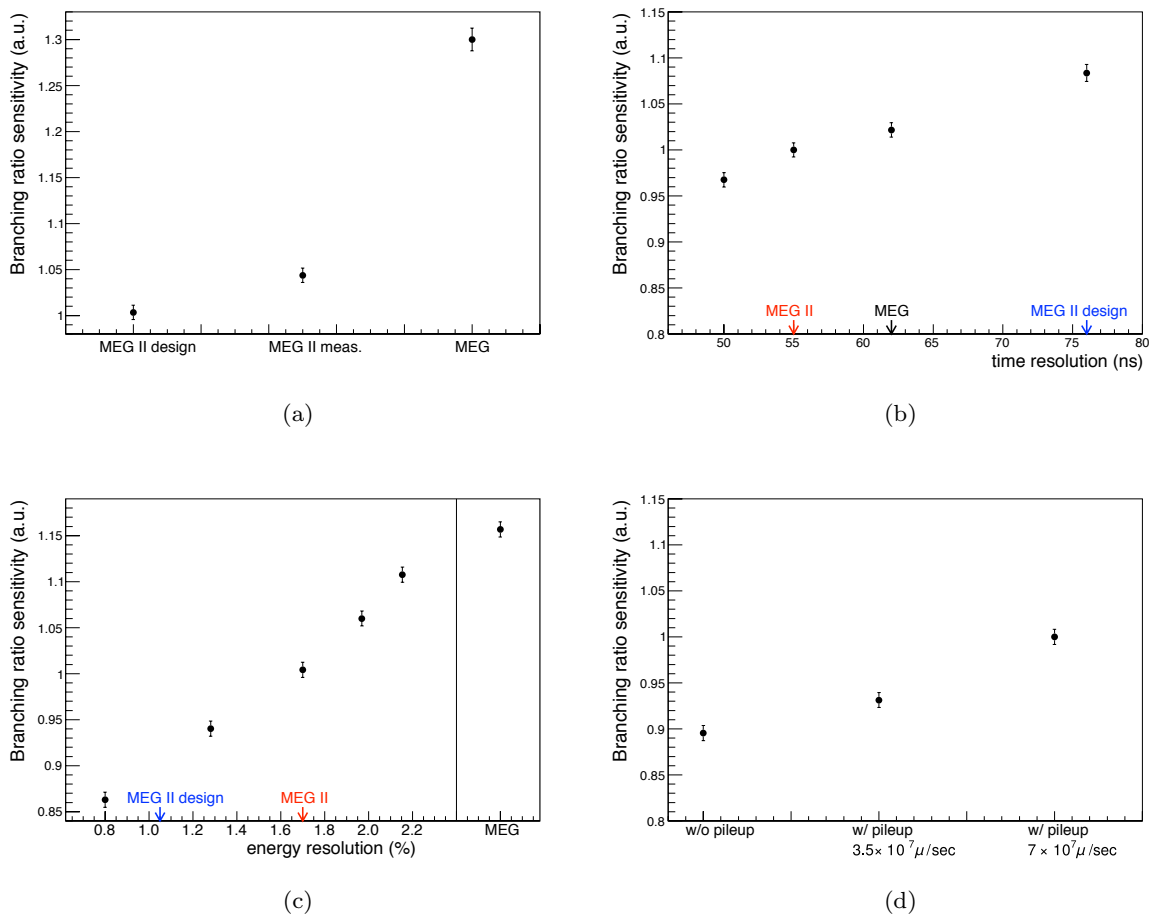
Figure 11.3   Relative size of the branching ratio sensitivity as a function of the LXe detector resolution. A smaller value on the vertical axis corresponds to a better performance of the experiment as defined in Section 11.1.3. (a) Position resolution, (b) timing resolution, (c) energy resolution. Other resolutions are fixed to the resolution measured in the pilot run. The DAQ time in the original MEG II plan is assumed. (d) Effect of the accidental pileups on the sensitivity.

11.3   Effect of PDE degradation: detector performance

As is shown in Section 6.3, a radiation damage to our MPPC was found, which affects the PDE for VUV light. Even though there is still a large uncertainty in the PDE extrapolation to the future, its degradation is too fast to be ignored, and the PDE can become zero after 70 days of detector operation in the worst case.

This degradation will affect the branching ratio sensitivity of MEG II by two processes. The first one is the degradation of the detector resolutions by the decreased PDE. The expected detector resolution at MPPC PDE of 2–22% , and its effect on the sensitivity will be discussed in this section.

The second one is the limitation to the DAQ time. In the most pessimistic scenario, the MEG II DAQ plan which assumes 120 days of continuous data-taking in each year is not possible, and we have to reduce the beam time or the beam rate. This leads to a smaller statistics and a

worse sensitivity. This effect will be discussed in the next section (Section 11.4).

The PDE degradation can affect the detector resolution through two contributions. The first one is the statistical fluctuation by the reduced number of photoelectrons. In the original detector concept, statistical fluctuation does not limit the γ resolutions, but it becomes non-negligible when the PDE becomes very small.

The second contribution is the signal to noise ratio of the MPPC waveforms. As is discussed in Section 8.4 and 9.3, noise from electronics is not negligible in energy and timing reconstructions. This noise contribution will become larger with a lower PDE.

This can be cured by increasing an amplifier gain on the frontend of the electronics, as long as the noise before the amplification is negligible. The gain is easily switchable from the DAQ software. In the original detector design, the amplifier is not used for the physics data-taking to keep the maximum signal amplitude of the MPPCs in the dynamic range of the readout. Since the MPPC signals get smaller with lower PDE, an amplification shown in Table 11.1 can be applied. It is defined to keep the maximum signal amplitude after the amplification, while a further tuning may be possible in the future, including an usage of a smaller operating voltage of the MPPCs.

<div align="center">

Table 11.1   List of assumed amplifier gain

PDE	amplifier gain
$8\% < PDE \leq 22\%$	1
$4\% < PDE \leq 8\%$	2.5
$2\% < PDE \leq 4\%$	5
$0\% < PDE \leq 2\%$	10

</div>

11.3.1   Degradation of position resolution

The hit positions of the γ-rays are reconstructed by fitting charge distribution on the MPPCs. An increased statistical fluctuation due to the reduced PDE can affect the position resolution through the fit uncertainty. Fig. 11.4 shows the position resolution for the signal γ-ray simulated at various MPPC PDEs. A degradation of the resolution is observed mainly for deep events. This is because the fit uncertainty becomes larger for the deep events due to the smaller number of photoelectrons on the inner face, while the contribution from the event-by-event fluctuation depending on the direction of the shower development is dominant for the shallow events.

The noise contribution should not be a problem because no noise issue was found in the resolution measurement by $17.6\,\mathrm{MeV}\gamma$-ray from the CW-Li at the PDE of 7%, whose signal to noise ratio is equivalent to that at the PDE of 2.3% for the signal γ-ray.

Fig. 11.5 shows the effect on the sensitivity by this position resolution degradation, and its
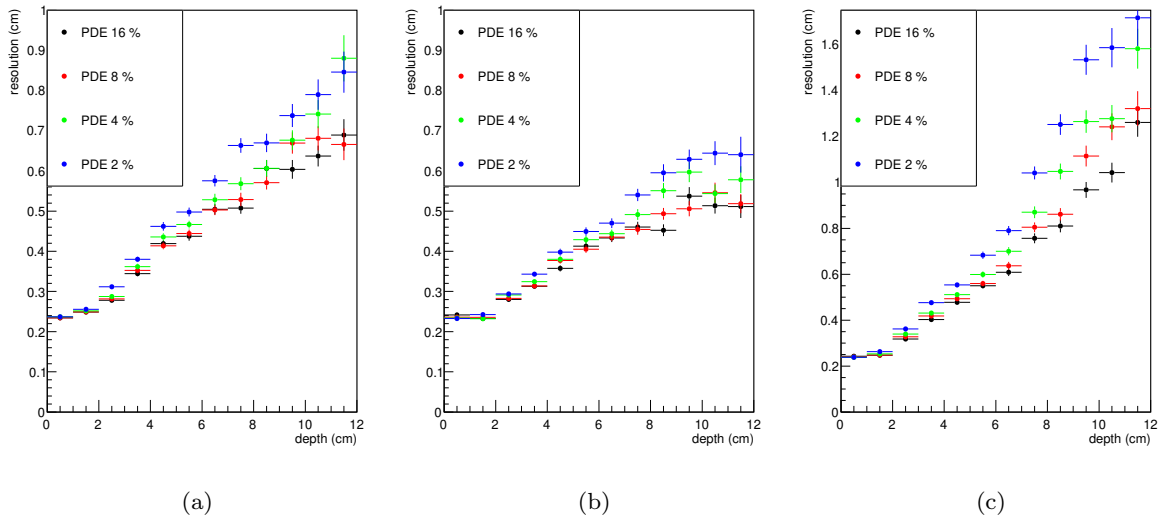
Figure 11.4 Position resolution in the simulation as a function of the conversion depth at various PDE for (a) u, (b) v, and (c) w direction.
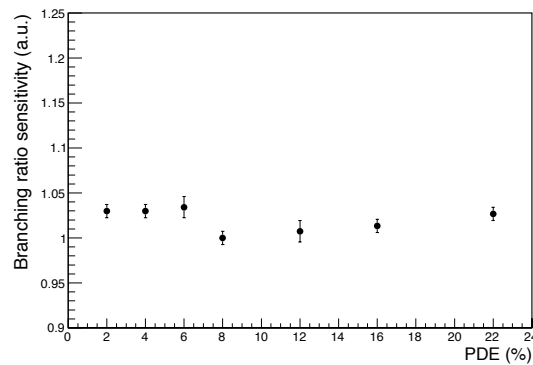

Figure 11.5 Effect on the branching ratio sensitivity from the position resolution degradation at different MPPC PDEs.

effect is found to be less than a few percent. Here, the observed degradation for the deep events is included assuming that the degradation does not decrease even if the resolution improves at the higher photoelectron statistics than the measurement.

11.3.2 Degradation of timing resolution

The hit timing of γ-ray is reconstructed from the timing information of all the channels. The timing resolution of each photosensor can become worse both by the worse S/N ratio, and the larger statistical fluctuation, and this leads to a degradation of the timing resolution.

The degradation of the S/N ratio can be recovered to some extent by using the amplifier. Table 11.2 presents the noise level at each amplifier configuration measured in the run 2019. The increase of the noise level is not proportional to the gain of the amplification, and the relative noise level is improved by the amplification.

Table 11.2   Noise level (RMS of random trigger waveform) at each amplifier gain in the run 2019.

| amplifier gain	1	2.5	5	10
Noise level	0.7 mV	0.8 mV	0.9 mV	1.3 mV

(a)	(b)
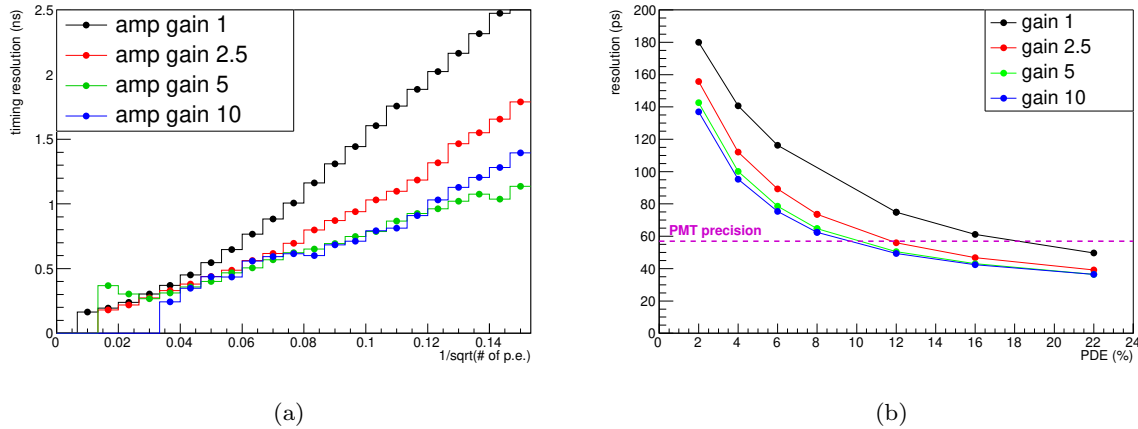
Figure 11.6   (a) Timing resolution of an MPPC channel as a function of the number of photoelectrons (MC). (b) Accumulated timing precision of all the MPPCs as a function of the MPPC PDE (MC).

Fig. 11.6(a) shows the simulated timing resolution of each MPPC channel. The real noise situation in Table 11.2 is directly included in the simulation by simply adding the measured random trigger waveform to the simulated waveform. As can be seen, smaller number of the photoelectrons will lead to a worse resolution, while part of the degradation can be compensated by increasing the amplifier gain. The improvement of the timing resolution is saturated at the amplifier gain of 5–10, and the gain larger than 10 is not useful.

Fig. 11.6(b) shows the accumulated timing precision of all the MPPCs defined in Equation 8.2 calculated from the plot of Fig. 11.6(a). The resolution defined only by the MPPCs will become much worse than that defined by the PMTs when the PDE gets low. Since the detector timing resolution will be determined by the combination of the MPPCs and the PMTs, the detector resolution will be defined only by the PMTs under such condition. It is notable that the accumulated precision of the PMTs is already measured to be consistent with MC (Section 8.4, and Table 8.2).

Fig. 11.7(a) shows simulated absolute and intrinsic timing resolutions. The degradation of the branching ratio sensitivity is shown in Fig. 11.7(b). Its effect is found to be up to 5%.

11.3.3   Degradation of energy resolution

The γ-ray energy is reconstructed from the sum of the photosensor signals, and can be affected both by a statistical fluctuation and a noise on the signals.

The effect of the statistical fluctuation on the energy resolution is not crucial at the nominal PDE. When the PDE is 8%, the total number of photoelectrons observed on the MPPCs is
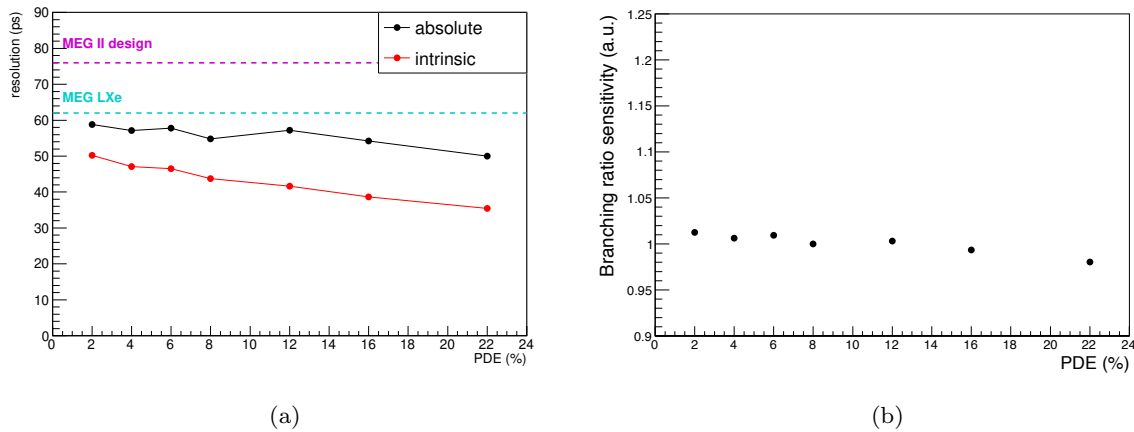
Figure 11.7   (a) Simulated timing resolution as a function of the MPPC PDE. (b) Effect on the branching ratio sensitivity from the timing resolution degradation at the different MPPC PDE. A sensitivity degradation up to 5% is expected at lower MPPC PDE.
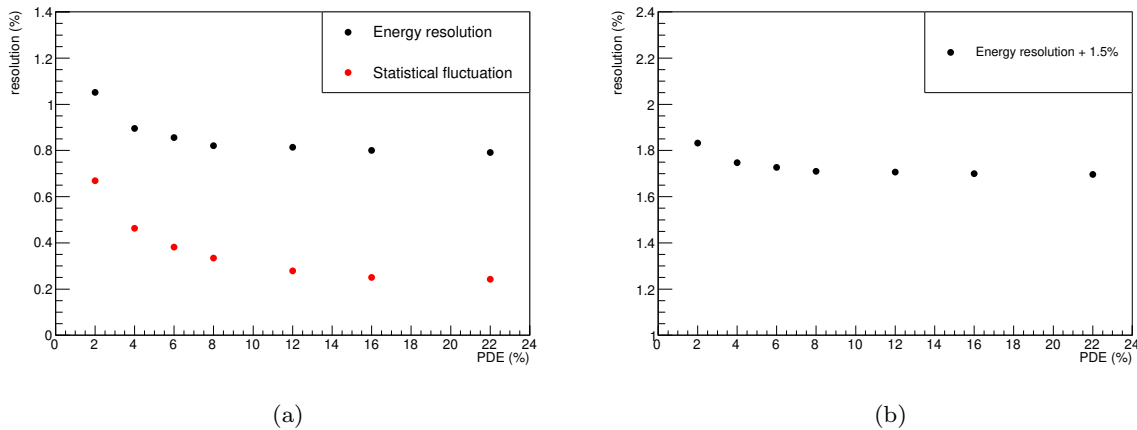

Figure 11.8   Expected energy resolution for the signal γ-ray as a function of the PDE. The ENF of 2.0 is assumed. (a) Expected energy resolution in MC. (b) Expected energy resolution including the unknown contribution of 1.5%.

typically 2×10^4. Since the MPPC signal contributes to one third of the total energy, the statistical fluctuation is only 0.4% $(= 100/\sqrt{2 \times 10^4}/3 \times \sqrt{4}\%)$, even if we take into account ENF of 4.0 (from Section 9.3.6, with some margin). This is negligible compared to the 1.0% energy resolution goal.

This fluctuation becomes larger with lower PDE. Fig. 11.8 shows the simulated energy resolution of the signal γ-ray, and the contribution of statistical fluctuation on it. The energy resolution increases from 0.8% to 1.0% by the lower PDE. This degradation becomes small if we take the unknown contribution of 1.5% observed in the detector into account. It is notable that the statistical fluctuation is directly measured by the even-odd analysis, and the results confirm that the unknown contribution is not related to the statistical fluctuation term.

Fig. 11.9(a) shows the noise contribution evaluated from the random trigger data in run 2019
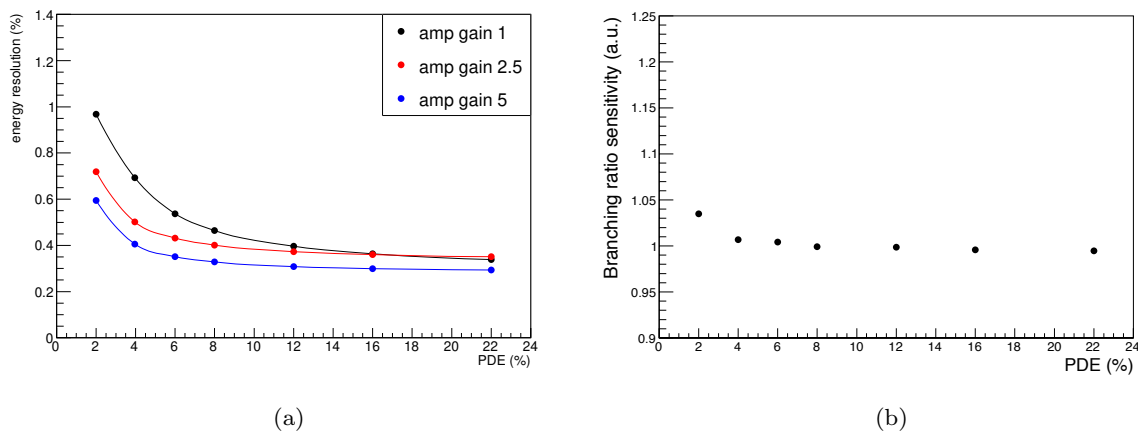
Figure 11.9   (a) Noise contribution in energy resolution. Based on the measurement at each amplification configuration in the run 2019. (b) Effect on the branching ratio sensitivity from the energy resolution degradation at different MPPC PDEs. Assuming the existence of unknown contribution of 1.5%. A slight sensitivity degradation is expected at lower MPPC PDE.

taken at each amplifier configuration. It is still less than 0.6% at 2% of PDE by applying the amplification, and will not be a limiting factor.

Fig. 11.9(b) shows the sensitivity degradation by the energy resolution degradation, where both the statistical fluctuation and the noise contribution are included. A slight degradation by 4% is expected.

11.3.4   Degradation of pileup elimination by sum waveform

The pileup elimination by the sum waveform consists of a pileup identification by the deviation from the template and a waveform fitting with found pileups.

The pileup identification performance is not affected by the lower MPPC PDE since only the PMT sum waveform is used for the pileup identification in the current implementation. The precision of the waveform fitting can be affected by lower PDE. Fig. 11.10 shows the precision of the reconstructed energy A slight degradation of the energy resolution is just due to the statistical fluctuation discussed in the energy resolution section.

11.3.5   Summary of performance degradation

Fig. 11.11 shows the degradation of the sensitivity which combines that of all the resolutions at the low PDE. Degradation by 10% is expected in the case of the 2% PDE compared to the 22% PDE. It is notable that the real effect will be smaller than this, roughly half of this, because the PDE will gradually decrease during the data-taking.
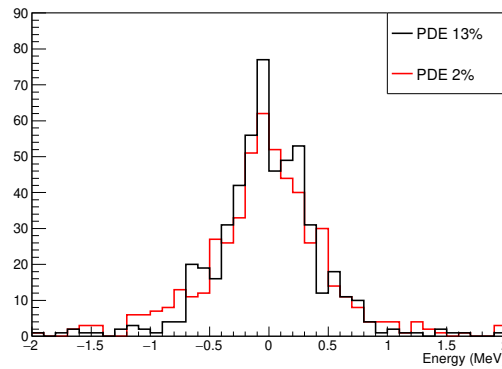
Figure 11.10   Difference between the reconstructed energy by the pileup elimination and the true energy in MC. The simulation including the pileups from the MEG II intensity beam is used.
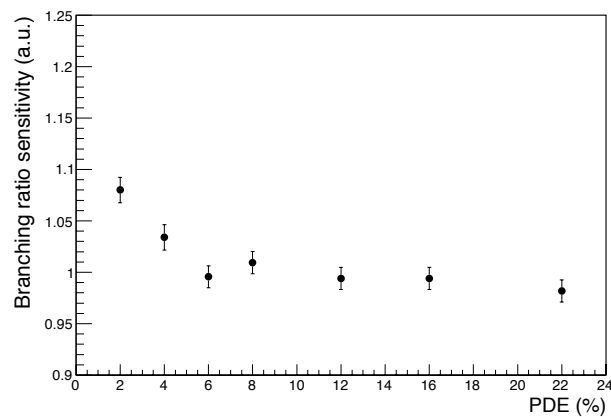

Figure 11.11   MEG II branching ratio sensitivity as a function of MPPC PDE. Effect of all detector resolutions are included. A smaller value on the vertical axis corresponds to a better performance of the experiment as defined in Section 11.1.3.

11.4   Effect of PDE degradation: detector operation

More crucial effect of the PDE degradation than the resolution degradation is a limitation on the maximal operational days without any annealings in the middle. As is shown in Fig. 6.19, it will take only 60–80 days to reach 2% PDE in the MEG II muon beam in the worst case. Even though the annealing of the all MPPCs can be performed during the annual accelerator maintenance period, it is impossible to carry out the planned data-taking for 120 days (84% live fraction in 140 days beam time) in each year. The degradation in Fig. 6.19 may be biased to be faster as discussed in Section 6.3.4, but here we rely on it for a conservative discussion. In this section, three alternative plans of the annual data-taking in Table 11.3 are compared, assuming the PDE degradation in the worst case.

Plan A : 60 days DAQ at MEG II beam intensity

The first plan is just taking data as long as the LXe detector can be operated. The LXe detector can be operated for 60 days, and the accumulated statistics gets reduced by a factor of two.

Plan B : 120 days DAQ at halved beam intensity

The second plan is to reduce the beam intensity by a factor of two so that we can keep our detector operating for 120 days. Since the accidental backgrounds are the dominant backgrounds in the search of $\mu \to e\gamma$, the significance $N_{\mathrm{sig}}/\sqrt{N_{\mathrm{BG}}}$ gets improved than plan A, and the achievable branching ratio sensitivity becomes better than plan A.

Data-taking at the halved beam intensity also improves pileup conditions, and this is another advantage of this plan. The sensitivity degradation by 10% due to the pileup γ-rays shown in Fig. 11.3(d) is expected to be halved.

In addition to that, preliminary studies suggest that a reconstruction performance of the positron track is affected by the pileups. A reduced beam intensity can result in an increased efficiency of the positron. This can also be an advantage of this plan, while it is not taken into account in this thesis since it is not quantified yet.

Plan C : DAQ at MEG II beam intensity + annealing in the middle

The other plan is to anneal all the MPPCs during the beam time. It will take about 40 days to anneal all the MPPCs[*1]. In addition, since the annealing of the MPPCs will be performed at room temperature, detector temperature has to be raised up before the annealing and to be cooled down after the annealing. It takes 1–2 weeks for each temperature control. In total, it will take about 60 days to finish all the annealing processes, and other 80 days can be used for the data-taking. Advantage of this plan is a higher PDE than the plan A and B thanks to the annealing.

Table 11.3   Comparison of the alternative data-taking plans. The number of the signals and the backgrounds is normalized by that in original MEG II plan.

plan	number of signal	number of background	PDE
Plan A	0.5	0.5	2–16%
Plan B	0.5	0.25	2–16%
Plan C	0.57	0.57	5–16%

Branching ratio sensitivity in alternative DAQ plans

Fig. 11.12 shows the expected sensitivities for these scenarios. The gradual degradation of the detector performances by that of the PDE discussed in the previous section is included. The sensitivity improvement by the RDC is also included. The plan B has the best sensitivity

---

[*1] This is the current best estimate, and may include some ambiguity.
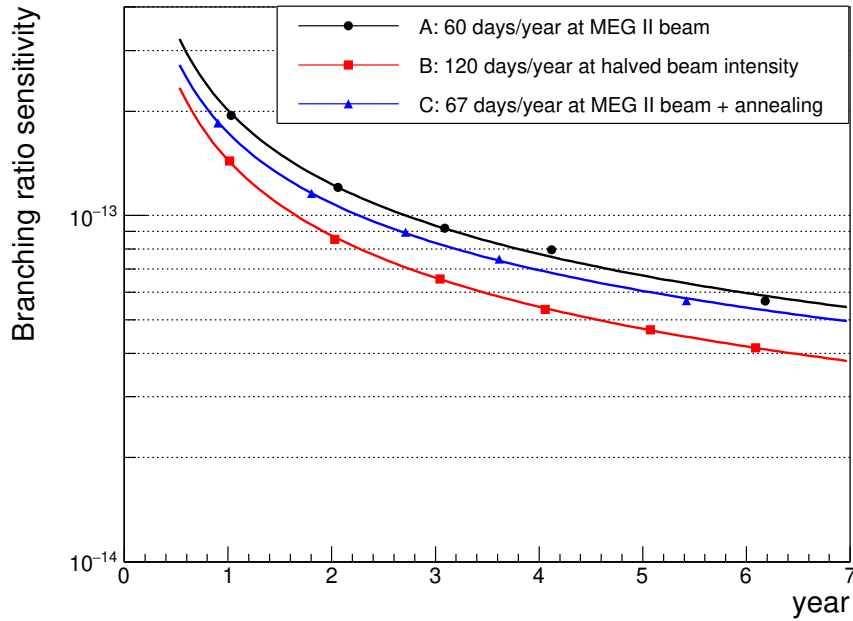
Figure 11.12   Branching ratio sensitivity as a function of time in three DAQ scenario. The PDE degradation in the most pessimistic scenario is assumed.

among these three plans as expected from the best significance, since the MEG II branching ratio sensitivity is dominated by the number of accidental backgrounds not by the single event sensitivity.

Also in the case of the slower PDE degradation, reducing the beam intensity to keep the PDEs above 2% during the whole beam time like the plan B will be the best option because the sensitivity in the plan C is limited by the time needed for annealing. It is notable that a study on the faster and easier annealing procedure is ongoing, in which all the MPPCs are heated at the same time by heating up the cryostat by flowing hot water in a pipe. If the annealing can be performed more shortly, the plan C may outperform the plan B.

11.5   Effect of pileup rejection by charge distribution

As is discussed in the Section 10.3.3, the performance of the pileup rejection by the charge distribution was not able to be validated from the pilot run. Thus, this method is not applied in the sensitivity discussed above. In this section, its effect on the MEG II branching ratio sensitivity is discussed for a future reference assuming the expected performance in the simulation.

This method affects the sensitivity by several aspects. Firstly, it identifies about 60% of the pileup events whose energy is reconstructed near the signal energy (Fig. 10.11(b)). As shown in Fig. 11.13(a), a part of the sensitivity degradation by the pileups is suppressed, and 7% improvement of the sensitivity is expected by this method.

Secondly, this method identifies and rejects about 60% of the AIF 2γ event. Fig. 11.13(b) shows the sensitivity improvement as a function of the reduction power of AIF 2γ events. About

(a)

(b)
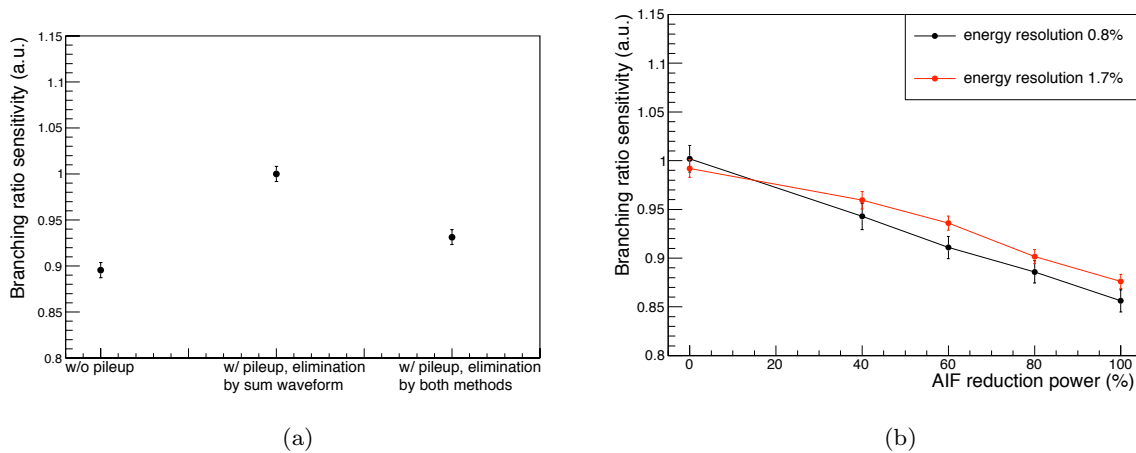
Figure 11.13   (a) Effect of the pileups and the elimination analysis to the branching ratio
sensitivity. A smaller value on the vertical axis corresponds to a better performance of
the experiment. (b) Relative branching ratio sensitivity as a function of the AIF reduction
power, assuming a zero inefficiency. Due to the smearing of the large fraction of the AIF 2γ
events near the signal energy, the performance depends on the energy resolution.

7 % improvement is expected.

Thirdly, some of the signal γ-ray events are rejected by identifying accidental pileup γ-rays
coming at the same time by this method. The inefficiency is estimated to be only 0.3% (Sec-
tion 10.3.1), and the effect to the sensitivity is negligible.

Fourthly, some of the single γ-ray create a second peak on the charge distribution. This
results in another inefficiency of the signal event about 2.4%. The degradation of the sensitivity
is expected to be about 1.6% from a k-factor dependence of the senstivity.

In summary, 12% improvement on the branching ratio sensitivity is expected by this method
if it works as expected in the simulation. Even if the inefficiency is doubled, 10% improvement
is expected.

At lower PDE, the statistical fluctuation becomes larger and a misidentification probability
can become larger. For example, as shown in Fig. 11.14, inefficiency gets larger at lower PDE
especially at 2%. Since its performance was not validated at the PDE of 8%, the expected perfor-
mance at lower PDE may not be reliable. Further study should be done after the inconsistency
is understood by further measurements.

11.6   Branching ratio sensitivity of MEG II experiment

The branching ratio sensitivity of MEG II with the developed LXe detector is calculated.
This calculation includes all the effect discussed in the previous sections, except for the im-
provement by the AIF2γ reduction analysis whose performance has not yet been validated with
the measurement. Table 11.4 and 11.5 show the comparison of the resolution and sensitivity
improvement from MEG.
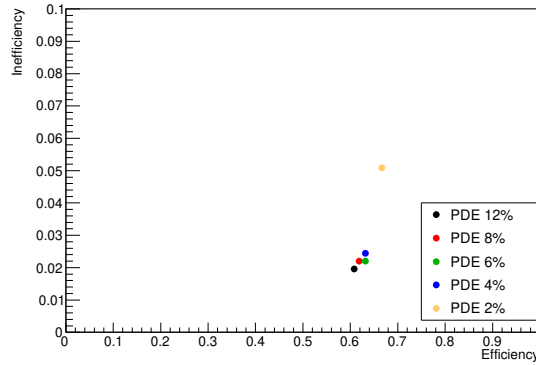
Figure 11.14   Expected inefficney of the signal event and efficiency of the AIF 2γ events at various PDE.

Fig. 11.15 shows the branching ratio sensitivity as a function of the beam time. The sensitivity with three years of data-taking will be 6.0–6.6×10^{-14} depending on the PDE degradation speed in the future. Even in the worst case of the PDE degradation of the MPPCs, the sensitivity is much better than 8.8×10^{-14} achievable with the MEG LXe detector only with the PMTs, and thus an upgrade of the LXe detector is meaningful. Since the ambiguity of the estimated sensitivity comes from that of the PDE degradation speed extrapolated in the future, a further pilot run or a physics run will reduce the ambiguity.

Table 11.4   Summary of the resolution

	MEG	MEG II design	MEG II measured
Position ($w < 4\,\mathrm{cm}/\ 4\,\mathrm{cm} < w$)	$4.1/3.8\,\mathrm{mm}$	$2.4/3.6\,\mathrm{mm}$	$2.4/4.8\,\mathrm{mm}$
Energy ($w < 2\,\mathrm{cm}/\ 2\,\mathrm{cm} < w$)	$2.5\%/1.8\%$	$1.1\%/1.0\%$	$1.8\%/1.8\%$
Timing	$62\,\mathrm{ps}$	$76\,\mathrm{ps}$	$55\,\mathrm{ps}$

The planned branching ratio sensitivity of 5×10^{-14} can be achieved by extending the data-taking time. As shown in Table 11.6, the required data-taking time is 4.0–4.6 year depending on the PDE degradation speed in the future. This is still within a realistic time and the extension of the beam time is a significant option[*2]. It is notable that the longer data-taking time than the original MEG II plan is not a problem from the view point of the PMT lifetime because most of the PMTs are operatable for five years by reducing the gain (Section 5.1.3) and the reduced beam intensity will mitigate the PMT gain degradation.

[*2] Actually, MEG data-taking was performed for 4.5 years from 2009 to 2013

Table 11.5   Summary of the sensitivity improvement/degradation from MEG. A negative value in this table corresponds to a better performance of the experiment as defined in Section 11.1.3. The ambiguity comes from that of the PDE degradation speed in the future.

	MEG II design	MEG II measured
Position resolution	-23%	-20%
Energy resolution	-22%	-13%
Timing resolution	$+7\%$	-3%
Detection and analysis efficiency	-6%	-4%
PDE degradation	0%	$+0$–10%
AIF2γ reduction (MC)	0%	-12%
Total (without AIF2γ reduction) [*]	-32%	-32–-25%
Total [*]	-32%	-40–-34%

[*] Due to the effect of single event senstivity and the senstivity improvement by the RDC, the sum of each component is not equal to the overall improvement.

Table 11.6   Required time to achieve the branching ratio sensitivity of 5×10^{-14}

|	required time
MEG II design	3.0 year
MEG II LXe detector. Optimal PDE degradation saturated at PDE of 6%.	4.0 year
MEG II LXe detector. Pessimistic PDE degradation (Plan B).	4.6 year
MEG LXe detector + other MEG II detectors	7.6 year
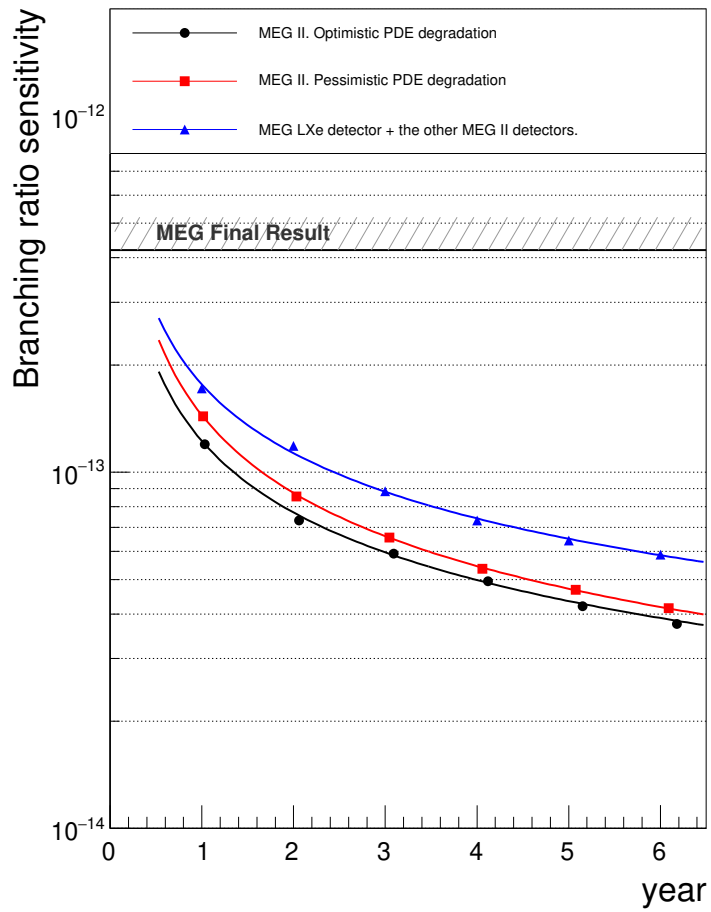
Figure 11.15   Branching ratio sensitivity as a function of time. (Black) With the MEG II LXe detector in the optimal PDE degradation saturated at PDE of 6%. (Red) With the MEG II LXe detector in the pessimistic PDE degradation.   DAQ at the halved beam intensity is assumed. (Blue) With the MEG LXe detector, and other MEG II detectors.

Chapter 12

Conclusion

Conclusion

MEG II experiment is planned to improve the branching ratio sensitivity of a charged lepton flavor violating decay of a muon, $\mu \to e\gamma$, by one order of magnitude. Improvements on the detector resolutions are mandatory in MEG II because the performance of the previous MEG experiment was limited by the number of accidental backgrounds. For this purpose, a new LXe γ-ray detector has been developed. It utilizes a large area VUV-sensitive MPPC newly developed to improve the granularity and the uniformity of the scintillation readout.

A series of the pilot runs was performed under the high intensity muon beam. Detector resolutions were evaluated from the obtained data. An improvement in the position resolution for the shallow events is confirmed. The timing resolution is estimated to be 55 ps, which is better than the resolutions in the previous studies thanks to an optimal threshold for the timing extraction. The energy resolution for the signal energy γ-ray is evaluated by fitting the energy spectrum of the background γ-rays. Thanks to the better uniformity of the readout, an improvement in the energy resolution for the shallow events ($w < 2\,\mathrm{cm}$) is confirmed. The energy resolution for the deep events ($w > 2\,\mathrm{cm}$) is measured to be worse than expected. This is probably due to an unknown contribution also observed in MEG.

A degradation correlated with the beam usage is found on the MPPC PDE for the xenon scintillation light. This kind of radiation damage was neither reported nor expected. A recovery of the damage by an annealing process is confirmed. In the most pessimistic scenario of the PDE degradation in the future, muon beam intensity in the MEG II data-taking has to be halved to keep a sufficient PDE for a sufficient resolution.

The branching ratio sensitivity of MEG II with this LXe detector is estimated to be 6.0–6.6×10^{-14} with three years of data-taking. The ambiguity of the sensitivity comes from that of the PDE degradation speed in the future. This is worse than the planned sensitivity of 5×10^{-14} mainly due to the worse energy resolution and the PDE degradation. Nonetheless, the planned sensitivity is found to be still achievable by a realistic extension of the beam time up to 4.6 years. Therefore, it is concluded that the LXe detector has a sufficient performance to search for the $\mu \to e\gamma$ decay with a branching ratio sensitivity of 5×10^{-14}.

Prospect

For a furthur improvement of the sensitivity, a faster annealing procedure should be tried in a future work, which can mitigate the effect of the PDE degradation. Future work should also measure the performance of the pileup rejection by the charge distribution with a full channel readout to confirm another 12% improvement on the sensitivity. For a better understanding of the detector, the source of the PDE degradation and the source of the unknown contribution on the energy resolution should also be investigated.

The MEG II experiment will start the physics data-taking from 2021 by utilizing the LXe detector developed in this thesis, to search for a charged lepton flavor violation and thus a physics beyond the Standard Model.

Appendix A

Data reduction algorithm

As mentioned in Section 1.8, to store the obtained data from the MEG II physics data-taking, a data size reduction by a factor of a few is needed before it is written in the disk. Two kinds of data reduction algorithms for the LXe detector are briefly shown in this chapter.

One is a re-binning of the waveforms. In this algorithm, peak regions are defined around peaks above a threshold (40 photoelectron) in each photosensor waveform, which are important for the γ-ray reconstruction. Only the signal amplitudes in the peak regions are stored as it is, and those in the other time regions are re-binned with adjacent time bins by a factor of 8 (Fig. A.1). Since the threshold is set sufficiently low, this method does not affect the performances of the γ-ray reconstruction. This algorithm reduces the number of sampling point, and the data size. The size of the LXe detector waveforms is expected to be reduced from $3.4\,\mathrm{MB/event}$ to $0.7\,\mathrm{MB/event}$ in the simulation, and thus this is a promising method.

Another reduction algorithm called "waveform clustering" is also considered as an option. This algorithm reduces the granularity of the MPPC readout where no γ-rays hit. The MPPCs on the inner face are grouped into the adjacent 4×4 MPPCs, and a pulse amplitude of a summed waveform of each group is calculated. If the pulse amplitude is below a given threshold, waveform of each MPPC in the group is discarded, and only the sum of them are stored. As shown in Fig. A.2, the granularity of the MPPC readout is reduced in the off-peak regions, while it is kept in the on-peak region needed for the hit position reconstruction. This reduces the data size by another 30% in addition to the waveform re-binning.

These algorithms were not applied in the pilot runs because only the MPPCs near the γ-ray hit position were read out by the limitted number of channels, and there was little room for the data reduction. The performances of these methods should be checked with data once the full readout channels gets available. Especially effects of the reduced granularity should be checked on the pileup rejection algorithm by charge distribution and on some possible analyses utilizing the MEG II granularity developed in the future.
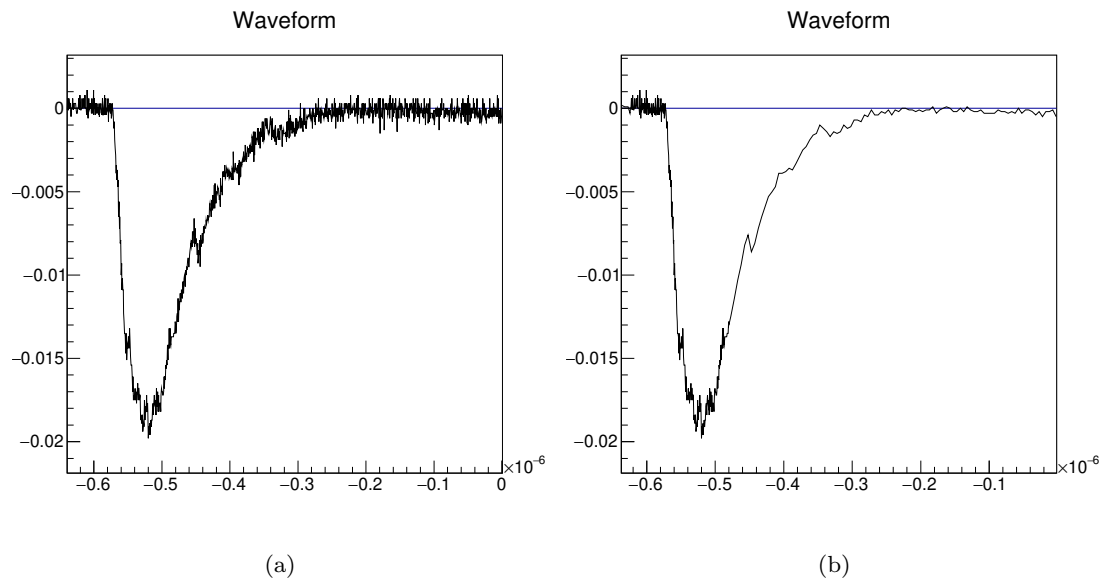
Figure A.1   Data reduction by the waveform re-binning in a simulated example channel. (a) Before reduction. (b) After reduction.
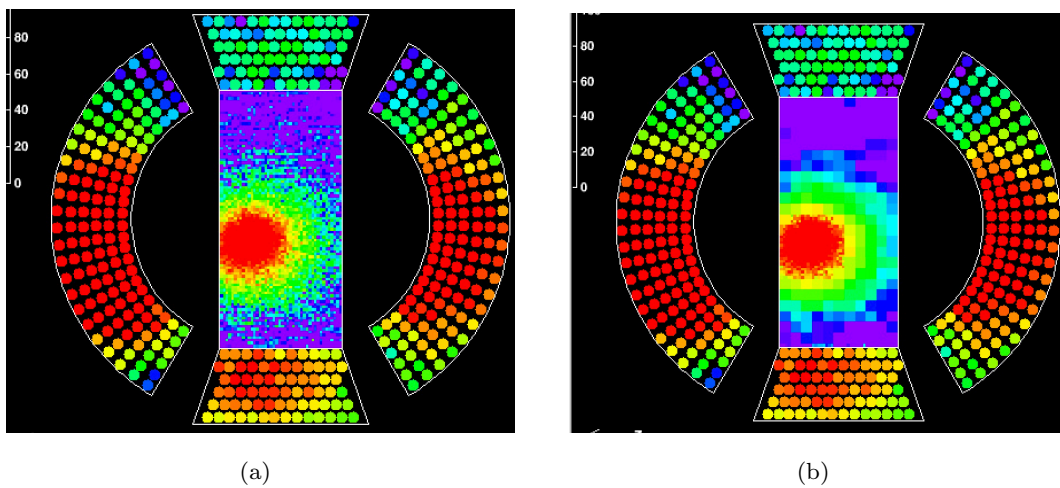

Figure A.2   Data reduction by the waveform clustering in a simulated example event. (a) Before reduction. (b) After reduction.

Appendix B

Threshold dependence of timing resolution of a channel

As disused in Section 8.3, and Fig. 8.5, better timing resolution can be achieved if we use lower threshold for the timing extraction from the waveforms. In this chapter, a simple model which explains this behavior is given.

In the scintillation of the signal γ-ray, many photons come to each photosensor. Emitted photons follow the time distribution of the scintillation (typically an exponential). For the timing reconstruction of the γ-ray, starting time of this distribution needs to be reconstructed from the photosensor waveforms.

First, let's start discussion when the scintillation time distribution is a constant distribution. In this case, photons come to a sensor at a constant frequency A [Hz]. Timing of the n-th arriving photon t_n from the start time of the scintillation follows a following relation

$$t_{i+1} = t_i + \delta_i$$

, where δ_i follows a probability distribution of $f(t) = A \exp{(-At)}$. Since $\delta_i (0 \leq i \leq n)$ is independent each other, event-by-event spread of t_n becomes,

$$\sigma(t_n) = \sqrt{\sum_{i=0}^{n} \sigma(\delta_i)^2} = \sqrt{n}\sigma(t_0) = \sqrt{n}/A$$

Fig. B.1(a) shows the spread of t_n estimated in a toy simulation, and it follows this expectation.

In reality, scintillation time distribution is not a constant, and $\sigma(t_i)$ will be different. Also in those cases, due to the stochastic fluctuation of δ_i, $\sigma(t_i + 1)$ becomes larger than $\sigma(t_i)$. Fig. B.1(b) shows the spread of the n-th photon timing for the exponential distribution of the xenon scintillation time constant.

The better timing resolution by the smaller threshold comes from this statistical fluctuation of the photon arriving timing. By using the smaller threshold, we can extract the timing of a photon coming earlier, and the better timing resolution can be achieved. Fig. B.2 shows timing resolution as a function of the constant fraction, where only the fluctuation of the photon arriving time is considered. It shows a roughly consistent dependence with that in Fig. 8.5.

(a)

(b)
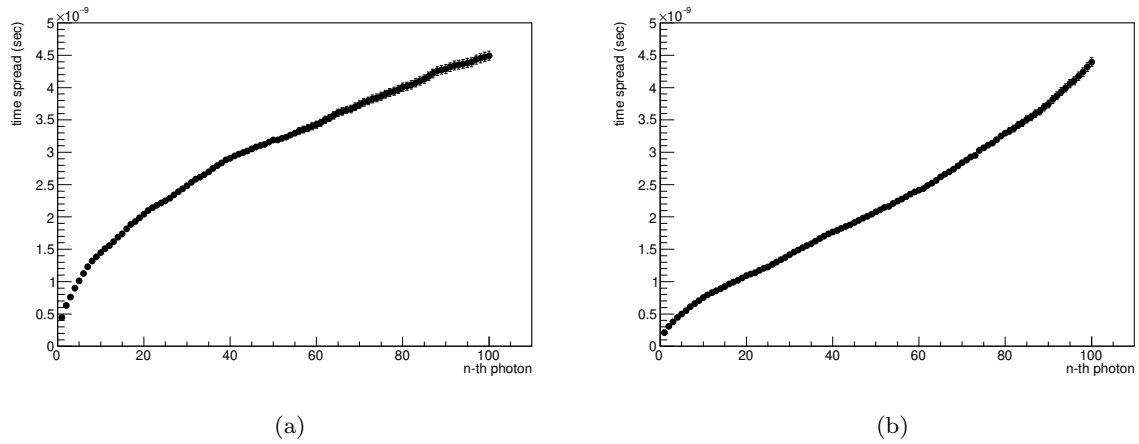
Figure B.1   Spread of n-th photon estimated from a toy simulation. Spread for 200 photoelectron signal. (a) Assuming a uniform (2.2 MHz) scintillation time distribution. (b) Assuming an exponential ($\tau = 45$ ns) time distribution.
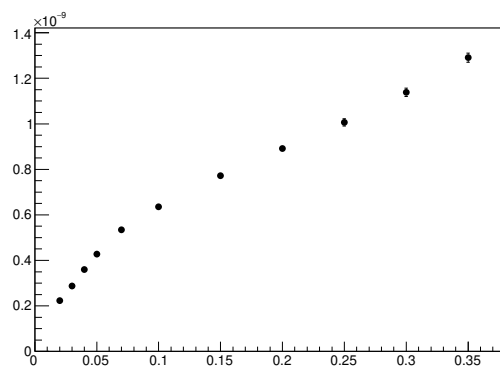

Figure B.2   Timing resolution from photon arriving time fluctuation for 200 photoelectron signal. Assuming xenon scintillation time constant, and single photoelectron MPPC waveform in Fig. 4.3.

Appendix C

List of abbreviations

AIF,AIF 1γ,AIF 2γ	annihilation in flight	Page.119
BTS	beam transport solenoid (magnet)	Page.9
CEX	charge exchange (reaction)	Page.51
COBRA	constant bending radius (magnet)	Page.9
CW, CW-Li	Cockcroft-Walton (accelerator)	Page.50
LXe	liquid xenon	Page.16
PDF	probability density function	Page.132
PSI	Paul Scherrer Institute	Page.5
RMD	radiative muon decay	Page.6
VUV	vacuum ultra violet	Page.17

photosensor

CE/QE	collection/quantum efficiency (of PMT)	Page.67
ECF	excess charge factor	Page.37
ENF	excess noise factor	Page.38
MPPC	multi-pixel photon counter	Page.22
PDE	photon detection efficiency (of MPPC)	Page.38
PMT	photomultiplier tube	Page.12
SiPM	silicon photo-multiplier	Page.13

electronics

DCB	data concentrator board	Page.27
DRS	domino ring sampler	Page.27
TCB	trigger concentrator boards	Page.27
WDB	WaveDREAM boards	Page.27

Acknowledgements

Bibliography

[1] A. M. Baldini et al. (MEG collaboration). Search for the lepton flavour violating decay $\mu^+ \rightarrow e^+\gamma$ with the full dataset of the MEG experiment. Eur. Phys. J. C, 76(8):434, 2016.

[2] T. P. Cheng and Ling-Fong Li. $\mu \rightarrow e\gamma$ in theories with dirac and majorana neutrino-mass terms. Phys. Rev. Lett., 45:1908–1911, Dec 1980.

[3] Yoshitaka Kuno and Yasuhiro Okada. Muon decay and physics beyond the standard model. Rev. Mod. Phys., 73:151–202, 2001.

[4] R. Barbieri and L.J. Hall. Signals for supersymmetric unification. Phys. Lett. B, 338(2):212 – 218, 1994.

[5] J. Hisano, T. Moroi, K. Tobe, and Masahiro Yamaguchi. Lepton flavor violation via right-handed neutrino Yukawa couplings in supersymmetric standard model. Phys. Rev. D, 53:2442–2459, 1996.

[6] Takeo Moroi, Minoru Nagai, and Tsutomu T. Yanagida. Lepton flavor violations in high-scale susy with right-handed neutrinos. Phys. Lett. B, 728:342–346, 2014.

[7] A. M. Baldini et al. (MEG II collaboration). The design of the MEG II experiment. Eur. Phys. J. C, 78(5), May 2018.

[8] Toichiro Kinoshita and Alberto Sirlin. Radiative corrections to fermi interactions. Phys. Rev., 113:1652–1660, Mar 1959.

[9] Daisuke Kaneko. The final result of $\mu^+ \rightarrow e^+\gamma$ search with the MEG experiment. PhD thesis, The University of Tokyo, 2016.

[10] D. Palo, M. Hildebrandt, A. Hofer, W. Kyle, D. Lad, T. Libeiro, and W. Molzon. Precise Photographic Monitoring of MEG II Thin-film Muon Stopping Target Position and Shape. Nucl. Instrum. Meth. A, 944:162511, 2019.

[11] Wataru Ootani, Wataru Odashima, Satoshi Kimura, Takayuki Kobayashi, Yasuhiro Makida, Toshiya Mitsuhashi, Shoichi Mizumaki, Roger Ruber, and Akira Yamamoto. Development of a thin-wall superconducting magnet for the positron spectrometer in the MEG experiment. IEEE Trans. Appl. Supercond., 14(2):568–571, 2004.

[12] Miki Nishimura. Positron Timing Measurement to Search for Lepton Flavor Violating Decay in MEG II. PhD thesis, The University of Tokyo, 2018.

[13] Particle Data Group. The Review of Particle Physics. Atomic and Nuclear Properties of Materials, 2019.

[14] Keiko Fujii, Yuya Endo, Yui Torigoe, Shogo Nakamura, Tomiyoshi Haruyama, Katsuyu Kasami, Satoshi Mihara, Kiwamu Saito, Shinichi Sasaki, and Hiroko Tawara. High-accuracy

measurement of the emission spectrum of liquid xenon in the vacuum ultraviolet region. Nucl. Instrum. Meth. A, 795:293 – 297, 2015.

[15] Akira Hitachi, Tan Takahashi, Nobutaka Funayama, Kimiaki Masuda, Jun Kikuchi, and Tadayoshi Doke. Effect of ionization density on the time dependence of luminescence from liquid argon and xenon. Phys. Rev. B, 27:5279–5285, May 1983.

[16] Tadayoshi Doke, Akira Hitachi, Jun Kikuchi, Kimiaki Masuda, Hiroyuki Okada, and Eido Shibamura. Absolute scintillation yields in liquid argon and xenon for various particles. Jpn. J. Appl. Phys, 41(Part 1, No. 3A):1538–1545, mar 2002.

[17] Tadayoshi Doke and Kimiaki Masuda. Present status of liquid rare gas scintillation detectors and their new application to gamma-ray calorimeters. Nucl. Instrum. Meth. A, 420(1):62 – 80, 1999.

[18] S Kubota, M Hishida, and J Raun. Evidence for a triplet state of the self-trapped exciton states in liquid argon, krypton and xenon. J. Phys. C, 11(12):2645–2651, jun 1978.

[19] Shinzou Kubota, Masahiko Hishida, Masayo Suzuki, and Jian-zhi Ruan(Gen). Dynamical behavior of free electrons in the recombination process in liquid argon, krypton, and xenon. Phys. Rev. B, 20:3486–3496, Oct 1979.

[20] A. Hitachi. Properties of liquid xenon scintillation for dark matter searches. Astropart. Phys., 24:247–256, 2005.

[21] Ryu Sawada. A Liquid Xenon Scintillation Detector to Search for the Lepton Flavor Violating Muon Decay with a Sensitivity of 10^{-13}. PhD thesis, The University of Tokyo, 2008.

[22] A. M. Baldini et al. (MEG collaboration). MEG Upgrade Proposal. arXiv:1301.7225, 2013.

[23] MPPC / Technical note. https://www.hamamatsu.com/resources/pdf/ssd/mppc_kapd9005e.pdf.

[24] MIDAS system. https://midas.triumf.ca/.

[25] Stefan Ritt, Roberto Dinapoli, and Ueli Hartmann. Application of the drs chip for fast waveform digitizing. Nucl. Instrum. Meth. A, 623(1):486 – 488, 2010.

[26] P.W. Cattaneo, M. De Gerone, F. Gatti, M. Nishimura, W. Ootani, M. Rossella, S. Shirabe, and Y. Uchiyama. Time resolution of time-of-flight detector based on multiple scintillation counters readout by sipms. Nucl. Instrum. Meth. A, 828:191 – 200, 2016.

[27] Marco Francesconi. The new trigger and data acquisition system for LFV searches in the MEG II experiment. PhD thesis, The University of Pisa, 2020.

[28] Y.Uchiyama for the MEG II collaboration. Preparation of the $\mu^+ \to e^+\gamma$ experiment MEG II towards the physics data taking. The Physical Society of Japan 2016 Annual Meeting.

[29] K. Ieki, T. Iwamoto, D. Kaneko, S. Kobayashi, N. Matsuzawa, T. Mori, S. Ogawa, R. Onda, W. Ootani, R. Sawada, K. Sato, and R. Yamada. Large-area mppc with enhanced vuv sensitivity for liquid xenon scintillation detector. Nucl. Instrum. Meth. A, 925:148 – 155, 2019.

[30] Acktar Black. http://www.acktar.com/category/BlackOpticalCoating.

[31] W. Ootani, K. Ieki, T. Iwamoto, D. Kaneko, T. Mori, S. Nakaura, M. Nishimura, S. Ogawa, R. Sawada, N. Shibata, Y. Uchiyama, K. Yoshida, K. Sato, and R. Yamada. Development of deep-UV sensitive MPPC for liquid xenon scintillation detector. Nucl. Instrum. Meth. A, 787:220–223, 2015.

[32] S. Vinogradov. Analytical models of probability distribution and excess noise factor of solid state photomultiplier signals with crosstalk. Nucl. Instrum. Meth. A, 695:247 – 251, 2012.

[33] C.H. Faham, V.M. Gehman, A. Currie, A. Dobi, P. Sorensen, and R.J. Gaitskell. Measurements of wavelength-dependent double photoelectron emission from single photons in VUV-sensitive photomultiplier tubes. JINST, 10(09):P09010, 2015.

[34] Satoru Kobayashi. Research on precise gamma-ray position measurement with meg ii liquid xenon detector. Master's thesis, The University of Tokyo, 2019. (in Japanese).

[35] Toyoda Gosei E1L49–3B1A–02. https://www-jlc.kek.jp/~tauchi/index/LXeTPC/meetings/d070524-components/LED/E1L49_xxxxx_JEA.pdf.

[36] Kingbright KA-3021QBS-D. https://www.kingbright.com/attachments/file/psearch/000/00/00/KA-3021QBS-D(Ver.9B).pdf.

[37] A. M. Baldini et al. A radioactive point-source lattice for calibrating and monitoring the liquid xenon calorimeter of the meg experiment. Nucl. Instrum. Meth. A, 565(2):589 – 598, 2006.

[38] Angela Papa. Search for the lepton flavour violation in $\mu^+ \to e^+\gamma$. The calibration methods for the MEG experiment. PhD thesis, The University of Pisa, 2009.

[39] J. et al. Adam. The MEG detector for $\mu^+ \to e^+\gamma$ decay search. Eur. Phys. J. C, 73(4), Apr 2013.

[40] Rina Onda. Research and development on time calibration and background reduction for -ray detection in meg ii experiment. Master's thesis, The University of Tokyo, 2019. (in Japanese).

[41] R. Onda, K. Ieki, T. Iwamoto, S. Kobayashi, N. Matsuzawa, Toshinori Mori, M. Nakao, M. Nishimura, S. Ogawa, W. Ootani, and Y. Uchiyama. Optimal design of plastic scintillator counter with multiple sipm readouts for best time resolution. Nucl. Instrum. Meth. A, 936:563 – 564, 2019. Frontier Detectors for Frontier Physics: 14th Pisa Meeting on Advanced Detectors.

[42] Paolo W. Cattaneo, Matteo De Gerone, Flavio Gatti, Miki Nishimura, Wataru Ootani, Massimo Rossella, and Yusuke Uchiyama. Development of High Precision Timing Counter Based on Plastic Scintillator with SiPM Readout. IEEE Trans. Nucl. Sci., 61(5):2657–2666, 2014.

[43] Yasuhiro Nishimura. A Search for the Decay $\mu^+ \to e^+\gamma$ Using a High-Resolution Liquid Xenon Gamma-Ray Detector. PhD thesis, The University of Tokyo, 2010.

[44] Satoru Kobayashi, Marco Francesconi, Luca Galli, Kei Ieki, Toshiyuki Iwamoto, Terence Libeiro, Nobuo Matsuzawa, William Molzon, Toshinori Mori, Mitsutaka Nakao, Shinji Ogawa, Rina Onda, and Wataru Ootani. Precise measurement of 3D-position of SiPMs in the liquid xenon gamma-ray detector for the MEGII experiment. Nucl. Instrum. Meth.

A, 936:189 – 191, 2019. Frontier Detectors for Frontier Physics: 14th Pisa Meeting on Advanced Detectors.

[45] Tomiyoshi Haruyama, K. Kasami, H. Inoue, Satoshi Mihara, and Y. Matsubara. Development of a high-power coaxial pulse tube refrigerator for a liquid xenon calorimeter. AIP Conference Proceedings, 710, 06 2004.

[46] CRYOMECH AL300 CRYOCOOLERS. https://www.cryomech.com/products/al300/.

[47] Adam Nepomuk Otte, Distefano Garcia, Thanh Nguyen, and Dhruv Purushotham. Characterization of three high efficiency and blue sensitive silicon photomultipliers. Nucl. Instrum. Meth. A, 846:106 – 125, 2017.

[48] S. Agostinelli et al. GEANT4–a simulation toolkit. Nucl. Instrum. Meth. A, 506:250–303, 2003.

[49] J. Allison et al. Recent developments in geant4. Nucl. Instrum. Meth. A, 835:186 – 225, 2016.

[50] ROOT based Object oriented Midas Extension. https://elog.psi.ch/rome/.

[51] Kazuki Toyoda. Research and Development on Calibration of MEG II Gamma Ray Detector. Master's thesis, The University of Tokyo, 2020.

[52] E. Garutti and Yu Musienko. Radiation damage of SiPMs. Nucl. Instrum. Meth. A, 926:69–84, 2019.

[53] Isamu Nakamura. Radiation damage of pixelated photon detector by neutron irradiation. Nucl. Instrum. Meth. A, 610(1):110 – 113, 2009. New Developments In Photodetection NDIP08.

[54] Yi Qiang, Carl Zorn, Fernando Barbosa, and Elton Smith. Radiation hardness tests of sipms for the jlab hall d barrel calorimeter. Nucl. Instrum. Meth. A, 698:234 – 241, 2013.

[55] M. Centis Vignali, E. Garutti, R. Klanner, D. Lomidze, and J. Schwandt. Neutron irradiation effect on sipms up to $\phi_{neq} = 5 \times 10^{14}$ cm^{-2}. Nucl. Instrum. Meth. A, 912:137 – 139, 2018.

[56] Tsunayuki Matsubara. Radiation damage of MPPC by gamma-ray irradiation with Co 60. PoS, PD07:032, 2008.

[57] D. Renker and E. Lorenz. Advances in solid state photon detectors. JINST, 4:P04004, 2009.

[58] E. H. Snow, A. S. Grove, and D. J. Fitzgerald. Effects of ionizing radiation on oxidized silicon surfaces and planar devices. Proceedings of the IEEE, 55(7):1168–1185, 1967.

[59] Flora M. Li and Arokia Nathan. CCD Image Sensors in Deep-Ultraviolet. Springer, Berlin, Heidelberg, 2005.

[60] Hamamatsu l9455. https://www.hamamatsu.com/resources/pdf/etd/5W_Xe-F_TLSZ1006J.pdf.

[61] Naoya Shibata. Development of hcal scintillator cell unit for ilc detector. Master's thesis, The University of Tokyo, 2016. (in Japanese).

[62] Glen Cowan, Kyle Cranmer, Eilam Gross, and Ofer Vitells. Asymptotic formulae for likelihood-based tests of new physics. Eur. Phys. J. C, 71(2), Feb 2011.